RADIATION RESPONSE, MECHANICAL PROPERTY CHANGES, AND CORROSION BEHAVIOR OF MOLTEN SALT REACTOR MATERIALS

A Dissertation

by

ANDRÉS MORELL-PACHECO

Submitted to the Graduate and Professional School of
Texas A&M University
in partial fulfillment of the requirements for the degree of

DOCTOR OF PHILOSOPHY

Chair of Committee,	Lin Shao
Committee Members,	Pavel V. Tsvetkov
	Karim Ahmed
	Homero Castaneda-Lopez
Head of Department,	Michael Nastasi

May 2022

Major Subject: Nuclear Engineering

ABSTRACT

Corrosion related failures pose risk to the integrity of routinely cycled and permanent reactor components long before radiation damage alone adversely impact reactor performance. Compared to Light Water Reactors (LWRs), Molten Salt Reactors (MSRs) have not enjoyed a history of continuous engineering development and refinement. Hastelloy N, a nickel superalloy developed at ORNL explicitly for molten fluoride salt conditions, and 316SS, a widely used austenitic alloy, are among the leading candidates for immediate deployment in MSR systems. Data collected during initial development of Hastelloy N suffered from limitations in available microscopy and spectroscopy techniques, obfuscating the role of radiation damage and mechanical stress in the microstructural evolution of the alloy. 316SS, considered a more economical alternative to the nickel superalloy, is restricted by lower corrosion resistance and strength at high temperature. The present work bridges some of the nuanced gaps in knowledge related to Hastelloy N microstructural evolution, as well as evaluating the feasibility of coating systems for enhanced corrosion resistance for 316SS. Hastelloy N was exposed to light ion irradiation, micromechanical testing, and immersion corrosion using FLiNaK molten salt after either irradiation or static strain mounting using the three-point bending technique. 316SS, either coated using a modified cathodic cage plasma nitriding technique or mounted under static strain, was exposed to heavy ion irradiation. Several evaluation techniques were used including scanning electron microscopy (SEM), electron dispersive x-ray spectroscopy (EDS), electron backscatter diffraction (EBSD),

transmission electron microscopy (TEM), and micromechanical pillar compression testing. The results show that, low-dose irradiation and subsequent elemental segregation and embrittlement, as well as tensile mechanical stress loading, have a deleterious effect on the corrosion resistance of Hastelloy N. Nickel coating on 316SS is demonstrated as highly radiation tolerant. Combination of irradiation and the three-point bending technique demonstrates a feasible pathway for further evaluation of alloys and coating systems for MSR applications.

DEDICATION

Dedicated to my parents and grandparents, whose love I build myself upon.

ACKNOWLEDGEMENTS

Many people deserve acknowledgements for making this work possible. First and foremost, I would like to thank my advisor Dr. Lin Shao, through whom I learned the value of persistence and the skills needed to succeed in scientific research. Secondly, I would like to thank Dr. Frank Garner, a towering lighthouse of knowledge and experience without whom I would fumble around in the dark endlessly. Additional thanks are given to Drs. Lingfeng He and Ruchi Gakhar who generously donated their time, knowledge, and use of their facilities at Idaho National Laboratory. I would also like to thank my advisory committee members Dr. Karim Ahmed, Dr. Pavel Tsvetkov, and Dr. Homero Castaneda-Lopez for lending their expertise and helping refine my work. I thank Rainbow Suh for her fount of affection and encouragement through the trials and tribulations throughout my degree. Finally, I thank all my friends and family whose support I could not have endured without, especially my loving parents Drs. Guillermo Morell and Susan Pacheco.

CONTRIBUTORS AND FUNDING SOURCES

Contributors

This work was supervised by a dissertation committee consisting of Professor Lin Shao of the Department of Nuclear Engineering and Professors Pavel Tsvetkov, Karim Ahmed, and Homero Castaneda-Lopez of the Departments of Nuclear Engineering and Materials Science.

For work presented in Chapter II, ion irradiation was performed with assistance by Robert Balerio and Adam Gabriel. Microscopy of irradiated samples and interpretation of data was assisted by Hyosim Kim and Ching-Heng Shiau. Frank Garner aided in editing and revision. Professor Lin Shao performed overall organization and assisted in writing.

For work presented in Chapter III, ion irradiation was performed with the assistance of Adam Gabriel, Laura Hawkins and Aaron French. Laura Hawkins also assisted in microscopy sample preparation and is credited with performance of transmission microscopy analysis. Zhihan Hu assisted in design of point-defect kinetics equation modeling.

For work presented in Chapter IV, lab facilities and support for performance of corrosion study was provided by Ruchi Gakhar. Data analysis and interpretation was assisted by Lingfeng He and Professor Lin Shao.

For work presented in Chapter V, ion irradiation was performed with the aid of Adam Gabriel, Aaron French, Miguel Peña, and Yongchang Li. Microscopy sample

preparation and transmission electron microscopy was performed by Boopathy Kombaiah. Professor Lin Shao and Lingfeng He assisted in data analysis and interpretation.

For work presented in Chapter VI, micropillar compression and data analysis was performed with the assistance of Miguel Peña. Data interpretation was performed with the help of Professor Lin Shao and Miguel Pena. Ion irradiation was performed with the aid of Adam Gabriel, Aaron French, Miguel Peña, Yongchang Li, Zhihan Hu, and Trevor Parker.

All other work conducted for the dissertation was completed by the student independently.

Funding Sources

Graduate study was supported by a fellowship from the Nuclear Energy University Program, awarded through the Integrated University Program office of the Department of Energy.

This work was also made possible in part by a Nuclear Science User Facilities (NSUF) Rapid Turnaround Experiment (RTE) grant office program under Grant Number RTE 2833. Its contents are solely the responsibility of the authors and do not necessarily represent the official views of the Department of Energy.

NOMENCLATURE

3PB	Three-point bending
AISI	American Iron and Steel Institute
AH	Age-hardenable
ANP	Aircraft nuclear propulsion
ARE	Aircraft Reactor Experiment
ART	Advanced Reactor Technology
ASME	American Society of Mechanical Engineers
ASTM	American Society of Testing and Measurements
CCPD	Cathodic cage plasma nitriding
CCV	Continuous calibration verification
CW	Cold worked
DFT	Density Functional Theory
DI	Deionized
DOE	Department of Energy
DPA	Displacements per atom
EBSD	Electron backscatter diffraction
ECT	Elastic Continuum Theory
EDS	Energy dispersive X-ray spectroscopy
EELS	Electron energy loss spectroscopy
FCC	Face centered cubic

FEA	Finite element analysis
FIB	Focused ion beam
FLiBe	$LiF\text{-}BeF_2\text{-}UF_4$
FLiNaK	LiF-NaF-KF
GB	Grain boundary
GBS	Grain boundary sliding
GND	Geometrically necessary dislocation
HAGB	High angle grain boundary
HCE	Hollow cathode effect
ICP-MS	Inductively coupled plasma mass spectroscopy
KAM	Kernel averaged misorientation
LAAMPS	Large-scale Atomic / Molecular Massively Parallel Simulator
LWR	Light water reactor
MOS	Mean orientation spread
MSR	Molten salt reactor
MSRE	Molten Salt Reactor Experiment
NaFZrF	$NaF\text{-}ZrF_4\text{-}UF_4$
NB	Norton-Bailey
NSUF	Nuclear Science User Facilities
ORNL	Oak Ridge National Laboratory
PIE	Post irradiation examination
PDKE	Point defect kinetics equations

RTE	Rapid turnaround experiment
SRIM	Stopping Range of Ions in Matter
SS	Stainless steel
SSTT	Small scale testing techniques
STEM	Scanning transmission electron microscopy
TEM	Transmission electron microscopy
VASP	Vienna Ab initio Simulation Package
σ	Standard deviation
σ_{EST}	Standard error of the estimate

TABLE OF CONTENTS

Page

LIST OF FIGURES

Page

LIST OF TABLES

Page

CHAPTER I

BACKGROUND

Reactor Development Experience

Light Water Reactors

Nuclear reactors represent some of the harshest environments in contemporary engineering. These systems challenge designers with radiation damage, high temperature and pressure aqueous flow conditions, and chemical control considerations. Additionally, nuclear reactors are expected to maintain integrity throughout their lengthy operation lifetime (often 40+ years). From the latter half of the 20th century up until the present, extensive experience has been amassed over construction and operation of nuclear reactors. This is especially true for light water reactors (LWRs), which account for most nuclear reactors built in the United States and around the world. In the United States alone, data have been compiled from tens of millions of hours of operational experience, thousands of fuel cycles, and roughly 100 commercial LWRs [1]. From these data, physical phenomena novel to reactor systems have been studied and operators and engineers have learned to manage engineering challenges unique to these radiation damage environments.

Many degradation phenomena observed in LWRs result directly from radiation and its interactions with materials in these systems. Neutron damage, which is metered in displacements per atom (DPA), results from either primary knock-on collisions or secondary collision cascades [2]. These collisions liberate point defects which diffuse

and aggregate diverse ways, fundamentally altering the microstructure of the original material. Direct radiation damage can be attention-grabbing in its severity. This was first famously demonstrated by severely swollen cold-worked (CW) AISI 316 fuel cladding removed from the EBR-II fast reactor after exposure to 75 DPA neutron damage [3]. Such severe swelling however is not of great concern in the fuel cycles or lifetime of the LWR [4]. More often, radiation effects are subtle, such as embrittlement causing cladding to crumble like graphite, restructuring and transmutation of uranium ceramic fuel, and accelerated creep deformation of pressure baring components [5-7].

Despite the alarming nature of these degradation modes, corrosion related failures are likely to occur long before radiation damage will adversely impact reactor performance [4, 8]. Corrosion affects both routinely cycled as well as permanent reactor structures, having amassed billions of dollars in damage since the advent of commercial nuclear energy [9]. Zircaloy cladding periodically suffer cracking and rupture, brought on by oxidation corrosion and stress corrosion cracking conditions. This corrosion attack can prove catastrophic in loss of coolant accidents [10, 11]. Neutronics control using boric acid, which is pivotal to power management in certain LWRs, can lead to dangerous pressure vessel degradation if improperly regulated [12, 13]. When combined with radiation damage, corrosion can take on new dimensions of aggression such as exacerbation through electrolysis of water coolant or irradiation-assisted stress corrosion cracking [8].

Molten Salt Reactors

While formidable, the encumbrances of radiation damage and corrosion in LWR operation have been surmounted through persistence and experience. Comparatively, Molten Salt Reactors (MSRs), have not enjoyed the same history of continuous engineering development and refinement. One of the advanced reactor designs which are being promoted by the Department of Energy (DOE) to eventually replace the aging LWR fleet in the United States, MSRs saw prolonged attention during the 50s and 60s but went largely understudied again until the beginning of the 21st century. Much of the engineering and design basis for contemporary MSRs derive from experiments performed as part of the Aircraft Nuclear Propulsion (ANP) program and the Molten Salt Reactor Experiment (MSRE) programs spearheaded by Oak Ridge National Laboratory (ORNL) [13].

MSR Design Features

Advantages

Several variations of MSRs designs exists reflecting different operational strategies and economic goals. These designs share key features which distinguish them from LWRs, the most important being primary coolant composed of a halide salt. Both fluoride and chloride salt-based designs are being considered, the former benefiting from the greatest historical database while the latter enabling epithermal and fast neutron spectrum designs. Additionally, both solid fuel and liquid circulating fuel designs exist (e.g., U(III) and U(IV) fluoride). Liquid fuel MSRs offer the most robust advantages

over LWRs and the design benefits are summarized here: 1) higher possible operation temperatures and lower pressures, simplifying safety engineering, improving thermodynamic efficiency, and enabling process heat applications, 2) negative temperature coefficient of reactivity, 3) core design simplification in the absence of solid fuel and supporting structures 4) Potential for high burnup in the absence of limiting solid fuel structures 5) potential for burning/breeding reactor configurations to reduce the waste stream and conserve fuel resources [14, 15].

Materials Challenges

Material degradations undermine the long-term structural integrity of MSR reactor designs.

Figure 1 illustrates the temperature range expected for a number of advanced reactor designs with emphasis added to highlight the position of MSR reactors.

Even for basic commercial power generation, MSRs are expect to reach radiation damage levels upwards of 200 DPA with peak hot-leg temperatures around 700°C [16]. Under these conditions, radiation hardening, halide corrosion, and creep deformation and restructuring become serious concerns for some, if not all, the alloy candidate considered for MSRs. The complexity of pyrochemical interactions between structural materials and fuel and coolant preclude a comprehensive discussion of all potential halide salt configurations, namely chloride MSR variations. Chloride MSR designs are being explored by several commercial entities [17] and are the subject of at least one private/public partnership aiming to fabricate a pilot test plant similar to the ORNL

MSRE [18]. Structural materials evaluation, systems design, and salt chemistry and purification technology for chloride systems require further development [19]. The proceeding discussion focuses on the more-mature fluoride MSR technology, which have more immediate viability for commercial application.

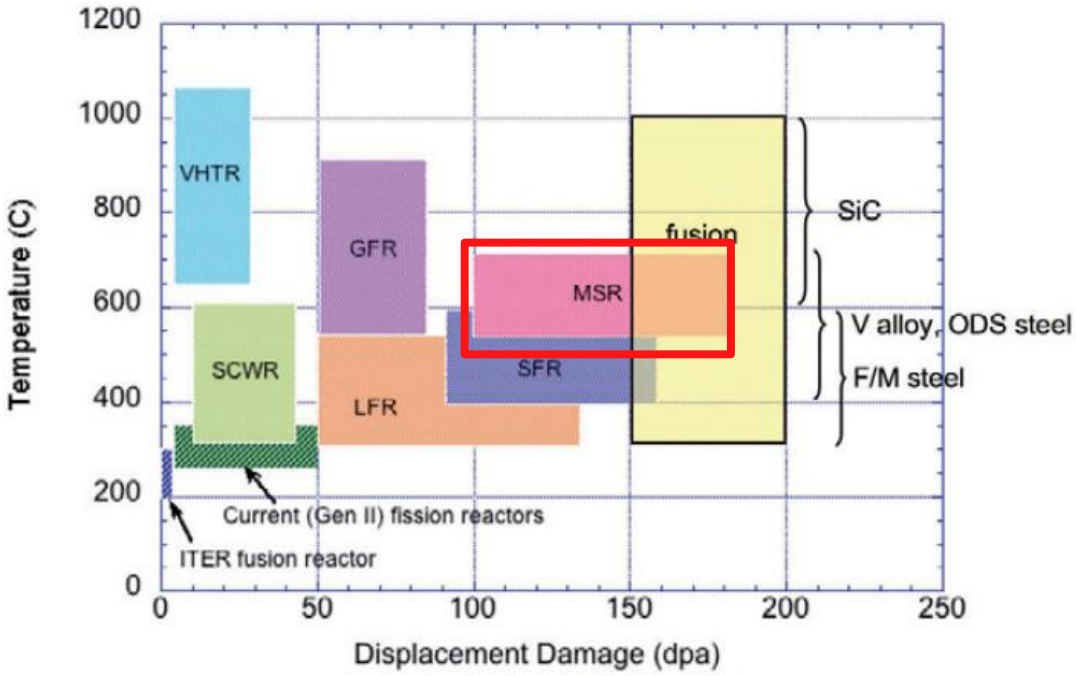

Figure 1. Infographic of damage/temperature regime for different advanced reactor designs with added emphasis. Reprinted from Zinkle and Busby [16].

Fluoride Salt Chemistry

Even within the category of fluoride salts, several coolant and fuel mixtures have been investigated in the literature. The compositions vary by specific application and

include considerations for reactor neutronics, interaction cross-sections, radiation stability, thermophysical properties, and corrosion chemistry [20, 21]. LiF-BeF_2-UF_4 (FLiBe) and NaF-ZrF_4-UF_4 (NaFZrF) are considered the most viable candidates as prospective MSR primary loop fuel salts. Of the two mixtures, FLiBe is currently the most popular option and the most heavily researched in contemporary studies. FLiBe benefits from historical precedent [22], as a variation of the mixture was used in the original MSRE campaign at ORNL. The salt fuel is highly resistant to radiation degradation, has manageable corrosion levels, and has superior neutronic properties (contingent on ^{7}Li enrichment) over NaFZrF [20, 23, 24].

For secondary coolant loop application in both MSRs and other high temperature reactor designs, the eutectic mixture LiF-NaF-KF (FLiNaK) is well-accepted as the leading candidate. FLiNaK is also routinely used as an experimental surrogate for FLiBe, offering near-identical thermophysical and corrosion characteristics without the personnel hazards associated with beryllium exposure. Regardless of exact composition, fluoride salts share some key characteristics which make them unique from a corrosion engineering standpoint, even within the extreme environmental regime of generation IV nuclear reactors. Passivation, where an alloy additive such as chromium forms a protective oxide layer and slows further corrosion, cannot be relied upon to protect structural materials in fluoride salt environments. Oxides tend to be completely soluble in high temperature fluoride salt mixtures and so corrosion can only be controlled by thermodynamic equilibrium and locomotive forces of diffusion and convection [25-27].

The standard free energy of formation for different fluoride corrosion products thus becomes one of the primary metrics for sensitivity of different elements to dissolution into fluoride salt melts. Table I highlights the Gibb's free energy of formation for common alloying elements [26]. Elements with the most negative free energy of formation (from the top downwards) most readily form fluoride compounds in the salt melt and thus are most sensitive to fluoride corrosion. Not included in the above table is the free energy of formation of UF_4, the primary fuel-carrying fluoride compound proposed for fluoride MSRs.

Table 1. Gibbs Free Energy of Formation for Common Elements in Fluoride Melts

Element	Most stable fluoride compound	Standard free energy of formation per gram atom fluorine (kcal/g-atom of F)	
		800°C	600°C
Al	AlF_3	-87	-92
Ti	TiF_3	-85	-90
V	VF_2	-80	-84
Cr	CrF_2	-72	-77
Fe	FeF_2	-66	-69
Ni	NiF_2	-59	-63
Nb	NbF_2	-58	-60
Mo	MoF_5	-57	-58
W	WF_5	-46	-48

Reprinted from DeVan [26].

In general, stability of the container material in contact with the salt is contingent on the thermodynamic stability of UF_4 in the melt. Corrosion of the container material first begins when the UF_4 fuel molecule undergoes a reduction reaction to form UF_3 (see Appendix A, eq. 1.b). This in turn enables the oxidation of the container material and production of one of the above stable fluoride compounds in the salt. The continued reduction of the UF_4 molecule facilitates continued dissolution of the container material. Under closed system equilibrium conditions, there is a stable proportion of UF_4/UF_3 which would ideally arrest the continued dissolution of the container material. The ingress of contaminants (e.g., atmospheric gas and moisture) however ensure that corrosion of the container alloy never ceases [28].

In the presence of contaminants, the corrosion in the fluoride salt melt becomes significantly more aggressive. Raiman and Lee highlighted the near-singular importance of salt purity, completing a comprehensive review of data from molten salt corrosion experiments performed in the 20^{th} and early 21^{st} century [29]. This work applied a statistical analysis to the variables of each experiment and highlighted which were most consequential for reducing the weight loss rate of the evaluated alloys. The results of the analysis, reproduced below in Figure 2 show that the purity of the fluoride salts is by far the most important variable to control. Oxygen and moisture both enable direct oxidation reactions and the deleterious production of HF in the melt. Additionally, contaminant metal fluorides present in the initial salt loading enable secondary redox reactions where these contaminant metals are deposited as solids in exchange for dissolution of alloy atoms (see Appendix A) [25]. The implication of this continuous ingress of contaminants

to the primary and secondary loops is twofold. First, online redox potential control will be crucial for maintaining corrosion to below an acceptable threshold over reactor lifetime. It has been shown that corrosion can be managed well by controlling the U-F_4/UF_3 ratio, thus maintaining a reducing redox potential in the melt [19, 28]. This in turn restricts the formation of fluoride compounds with the container material. There are several viable methods for accomplishing this task [28]. Second, localized purity

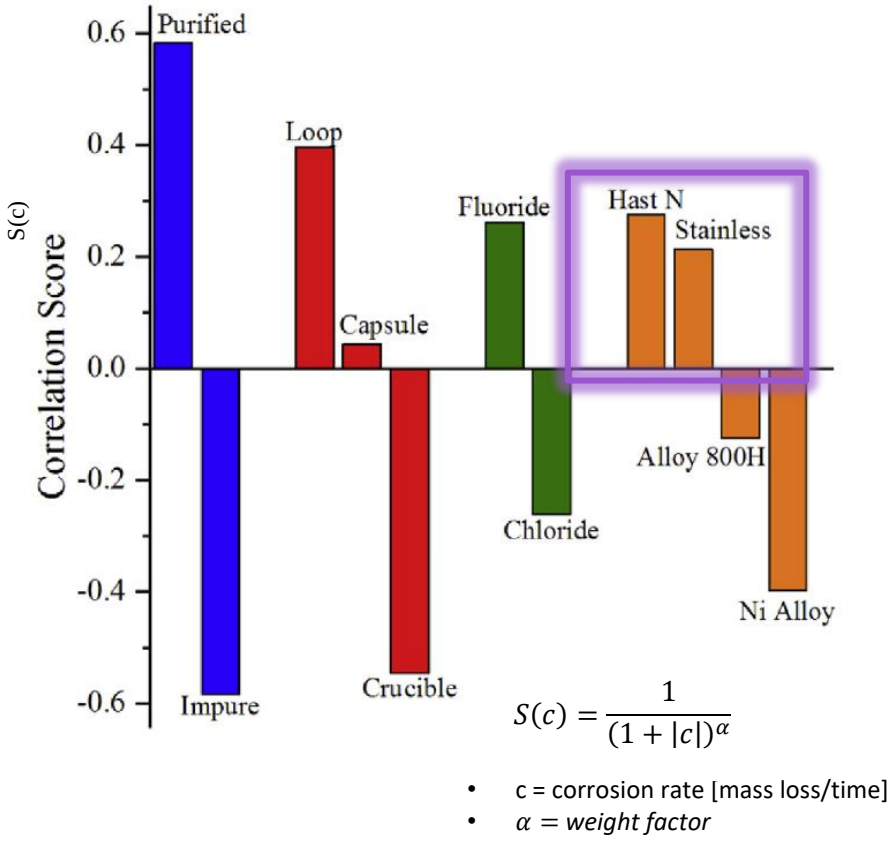

Figure 2. Correlation analysis results for the effect of different experiment parameters on corrosion rate in molten salt experiments performed in the 20th and 21st century. Reprinted from Raiman and Lee [29].

transients and gradients mean that the innate corrosion resistance and strength of the alloy is still important. Raiman and Lee also demonstrated a strong correlation between the evaluated alloy in each study and the severity of corrosion observed [29]. Hastelloy N, and to a lesser extent 316SS, performed better than the other alloys after normalizing for other experiment conditions. Both alloys have been evaluated extensively in fluoride MSR development and the proceeding discussion will highlight benefits and drawbacks for each.

Candidate Alloys

Hastelloy N

INOR-8, the alloy developed at ORNL and better known by its propriety name Hastelloy N (Haynes Stellite N) was developed specifically for fluoride MSR conditions. The alloy and variants featuring minor improvements to the original formulation are still considered top candidates for immediate MSR deployment [17]. Hastelloy N resulted from lengthy experimentation and failure analysis in early MSR systems. The Aircraft Reactor Experiment (ARE) under the ANP program highlighted the limitations of conventional reactor materials exposed to fluoride salt coolant and fuel. The NaF-ZrF_4-UF_4 fuel mixture caused significant weight loss and intergranular degradation throughout the coolant loop fabricated from Inconel 800H, an alloy which typically is known for its durability in high temperature and pressure heat exchangers [30]. A number of other alloys were tested with similarly poor results [31, 32].

Since fluoride salt mixtures completely preclude oxide passivation, efforts were made to design an alloy of exceptional thermodynamic stability in fluoride salt environments [25, 27, 33]. The composition of INOR-8/Hastelloy reflects this design objective, maximizing use of fluoride-hardy elements. Additionally, minor compositional adjustments were included to improve atmosphere-facing oxidation, high temperature strength, and impart good machinability and weldability characteristics [33]. The final alloy, approximately composed of XNi-16Mo-7Cr-5Fe-0.6Si, showed unparalleled corrosion performance compared to any previously tested alloys.

The MSRE was able to run for four years using a primary coolant loop fabricated from Hastelloy N and LiF-BeF-ZrF_4-UF_4 fuel [34]. While corrosion was managed evaluation of surveillance specimens placed at different points in the primary coolant loop revealed unique sensitivity to grain boundary embrittlement.

The aggregation of transmuted helium was identified as a challenge to prolonged use of Hastelloy N in fluoride salt systems, as the low-solubility of helium [35] causes accumulation and weakening at grain boundaries [34, 36]. Helium transmutation is initiated from neutron capture of ^{58}Ni and to a lesser extent, ^{10}B [37, 38]. While the latter reaction is limited the natural abundance of ^{10}B in contamination of forged alloys, the nickel transmutation pathway poses a continuous degradation risk for Hastelloy N over service lifetime. It has been shown that at moderate neutron fluences, helium embrittlement significantly diminishes alloy ductility [36, 38]. Tellurium uptake at from fission products circulating in the fuel coolant poses an additional embrittlement risk.

tellurium tends to form brittle telluride compounds along grain boundaries which ductility similarly to helium bubbles [34, 37, 39].

Studies performed towards the end of the MSRE program showed that the Te embrittlement issue was prospectively controlled with additions of between 1.5 and 2.0% niobium to the composition of Hastelloy N, or through redox control of the salt stabilizing the tellurium fluoride compound [39]. Use of Ti-modified Hastelloy N melts for strengthening and carbide helium-trapping is somewhat limited for high temperature service. Carbide coarsening and mechanical property degradation occur reliably with extended high temperature aging [37, 40]. Figure 3 illustrates typical fracture behavior of embrittled Hastelloy N following extensive aging. Additionally, Ti offers no alleviation to Te-driven embrittlement and even appears to negate the benefits of Nb additions under certain circumstances [37]. The limitations of microscopy and spectroscopy techniques in the 1960s and 1970s also obfuscated investigation into the role of naked radiation damage in the microstructural evolution of the alloy. It is thus not clear whether embrittlement is solely attributable to deleterious element aggregation at grain boundaries.

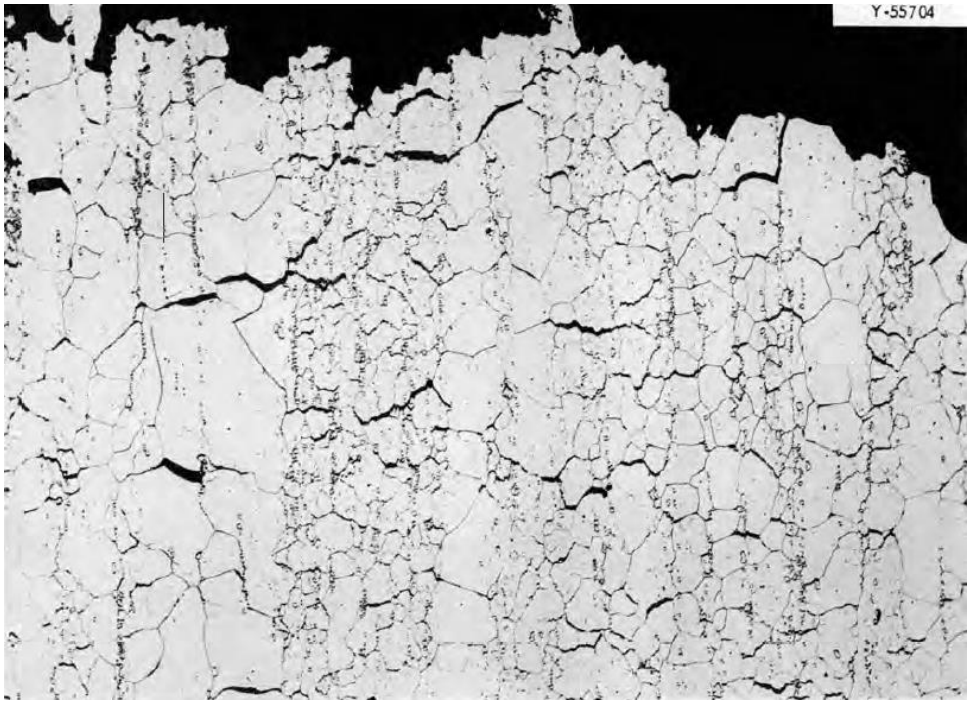

Figure 3. Fracture of Hastelloy N tested at 871 °C after 1 hour annealing at 1176 °C and 1000 hour aging at 593 °C. Reprinted from McCoy [41]

AISI 316SS

In the absence of radiation damage and corrosion concerns, Hastelloy N still suffers significant ductility and toughness losses above 700C [41, 42]. While the MSRE was able to operate 4 years without issue, such mechanical property decay may be unacceptable for commercial MSRs. In addition to its performance drawbacks, Hastelloy N presents an unattractive economic choice given its high cost and the limited fabrication experience. In order to mitigate costs, wrapper structural alloys may potentially be paired with an inner Hastelloy N container [17]. AISI 316 stainless steel (SS) is being considered as both a more practical MSR primary loop container material

and structural wrapper [17]. The alloy is already codified under the ASME BPVC standard for high temperature reactor use up to 425°C and the corrosion in fluoride salt environments is tolerable with careful purity and moisture control [29, 43].

While a promising alternative, 316SS is less resistant than Hastelloy N to prolonged radiation damage and high temperature exposure, suffering significant strength reduction, creep relaxation, swelling deformation, and embrittlement in the temperature regime of prospective MSR designs [44-46].

Figure 4 describes the influence of temperature on cold-worked 316SS, which is still subject to significant swelling in MSR temperature ranges [45]. While less so than in Hastelloy N, nickel-helium transmutation and embrittlement may still pose concerns for 316SS experiencing significant neutron fluence over reactor life [47]. Thus far, insufficient data exists to glean how these irradiation degradation phenomena will interplay with fluoride salt corrosion, especially in the event of purity transients.

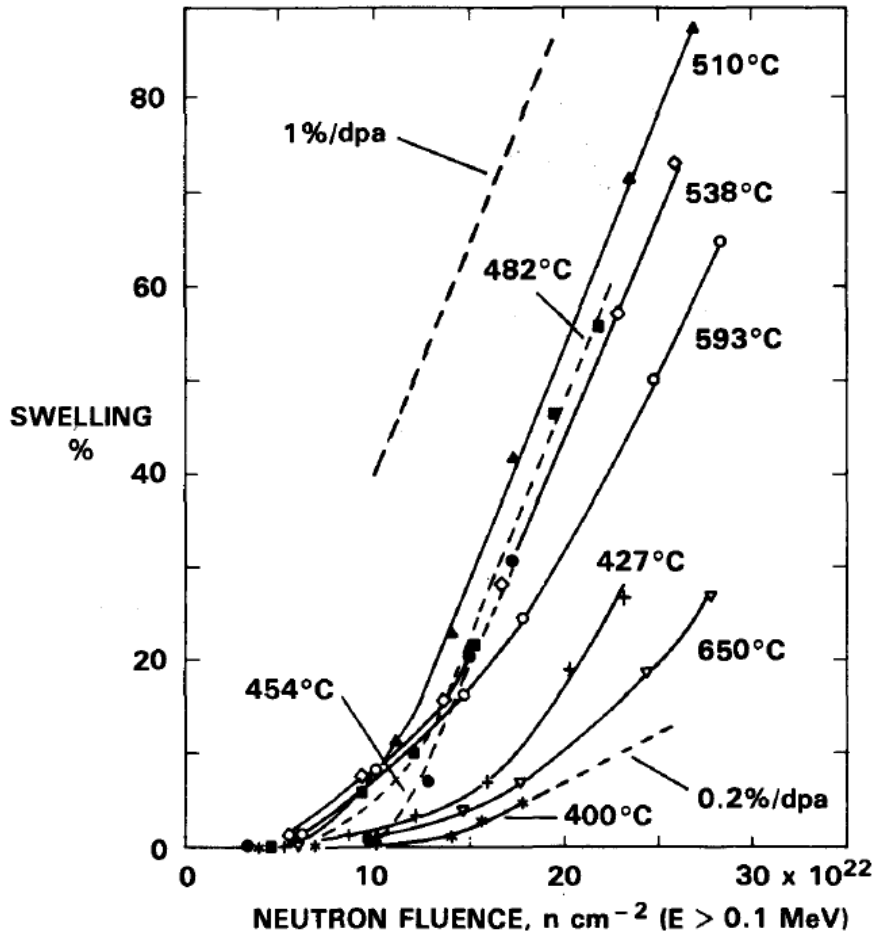

Figure 4. Void swelling in 20% CW AISI 316 versus neutron fluence. Reprinted from Garner and Gelles [45].

Problem Statement

The DOE is currently pushing for near-term commercial deployment of MSRs through the Molten Salt Reactor Campaign (MSRC) under the Advanced Reactor Technology Program (ART) [19]. The campaign aims to achieve a pilot test plant by 2025 and some ambitious goals shortly thereafter. This effort runs parallel to the dozens of commercial startups which are attempting to bring MSRs to market, along with

several international research efforts. Hastelloy N and AISI 316SS are the leading options for fluoride salt container materials, but additional work is still needed to ensure adequate performance for long-term application. Full-scale testing facilities for every new MSR design is costly and unrealistic. Making MSRs viable requires minimization of cost/risk with codification of new materials and licensing of novel MSR reactor designs. To this end, small scale vetting of prospective MSR materials is necessary before full scale testing can be carried out with mitigated economic risk.

The environment of MSRs present a complicated Multiphysics problem with a confluence of several mechanisms, each which can potentially aggravate materials degradation. Of primary importance is thus identifying which of the physical processes present in MSR environments poses the greatest and most immediate limitation on either Hastelloy N or 316SS. Figure 5 summarizes the most important processes which should be considered when making this assessment. Thermal aging and fission product management can reasonably be categorized as long-term concerns. thermal aging requires extended elevated temperature exposure and fission product interactions are contingent on a sufficient buildup of inventory to become chemically significant. Flow-loop dynamics are immediate, but flow erosion and solubility gradients are well-reported from MSRE data and serve as an exacerbating factor for these other mechanisms. In contrast, halide salt corrosion, radiation damage, and thermomechanical stress are each present at reactor startup and do not stop until end of service life. It is reasonable then to assert that these physical processes merit special attention. As previously mentioned, radiation damage in the context of historical MSR research was largely studied under the

assumption that embrittlement was dominated by helium aggregation alone. Little is understood about the effects of bare radiation damage on MSR facing materials for two reasons. First, any irradiation study performed using reactor-generated neutrons would be influenced by the presence of transmuted helium. Second, post-irradiation examination (PIE) techniques were not yet sufficiently refined to capture the minutia of early radiation damage induced microstructural changes. At its most basic, radiation damage behaves as a continuous nonequilibrium source of point defects.

The liberation of vacancies and interstitials should tend towards accelerating the microstructural transformations already underway, including those brought about by corrosion. The timescale at which these transformations occur however, and whether radiation damage phenomena or exacerbated corrosion become the dominant degradation mode, is still to be determined.

Figure 5. Summary of physical mechanisms affecting materials in MSRs.

Thermomechanical stress influences existing physical processes in several ways. Stress and heat can affect diffusion gradients, accelerate microstructural transformation towards equilibrium, or alter equilibrium conditions entirely for one or all phases. High stress and thermal energy can also enable dislocation movement, macroscopic deformation, and complete restructuring of the material. The thresholds where these different physical influences occur are typically dependent on the individual characteristics of the material under influence and are seldom well-understood. With all the above physical processes at work in MSR environments, it is difficult to separate their individual influence if they are studied simultaneously. Isolating each variable however does not properly illustrate the sensitivity of interdependence between them and can overlook important phenomena.

Objectives

In order to approach the full complexity of this Multiphysics problem, the work described here aims to study two or three of these variables together. The confluence of corrosion, thermomechanical stress, and radiation damage are chosen as the most relevant to immediate and impactful to MSR implantation. By studying these key processes simultaneously, this research attempts to describe and quantify the impact of radiation and stress conditions on the onset of molten salt corrosion in the prospective MSR materials Hastelloy N and AISI 316. Specifically, quantification is pursued of the impact of radiation damage and stress on 1) the embrittlement and corrosion onset in Hastelloy N and 2) the microstructural changes and surface defect sinking at the corrosion interface in AISI316. Figure 6 illustrates the overlap of these processes and will be used throughout this work to highlight the processes being investigated in each chapter.

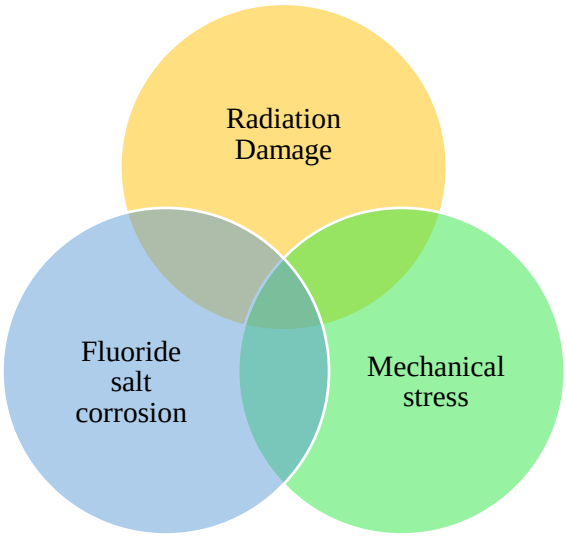

Figure 6. Physical mechanisms whose interactions are focused on in this work.

Additionally, the viability of protective coating for AISI 316 systems is investigated. The methodology consists of first conducting experiments to expose the two alloys to coupled stress corrosion, irradiation-assisted corrosion, and irradiation-assisted stress evolution which are reflective of MSR conditions. Experimentation is supported using finite element analysis (FEA) to capture nuanced mechanical and thermal stress evolution. Second, microscopy and spectroscopy evaluation and micromechanical testing are performed to probe the response of the alloys in the reproduced MSR environments. Third, the AISI 316 stress-irradiation investigation is coupled with molecular dynamics simulation to correlate stress-dependent defect/ dislocation sinking and migration energies to experiment observations, quantifying possible defect interplay with corrosion interface. The specific research objectives are summarized in the following list. The experiment matrix followed to accomplish these objectives is shown in Figure 7.

- Characterize elemental segregation and dislocation at low radiation damage levels in Hastelloy N
- Quantify the effect these microstructural changes have on macroscopic mechanical properties
- Determine the role that low dose microstructural changes have in the early onset of fluoride salt corrosion
- Quantify the physical mechanisms driving stress-accelerated corrosion in Hastelloy N

- Demonstrate the viability of corrosion resistant coating for AISI 316L in MSR environments through radiation damage testing and microstructural characterization
- Characterize the effect of mechanical stress on near-surface sinking and migration strength of point defects produced via radiation damage in AISI 316L
- Qualify the effect these point defect sinking and migration strength changes will have on corrosion interface evolution

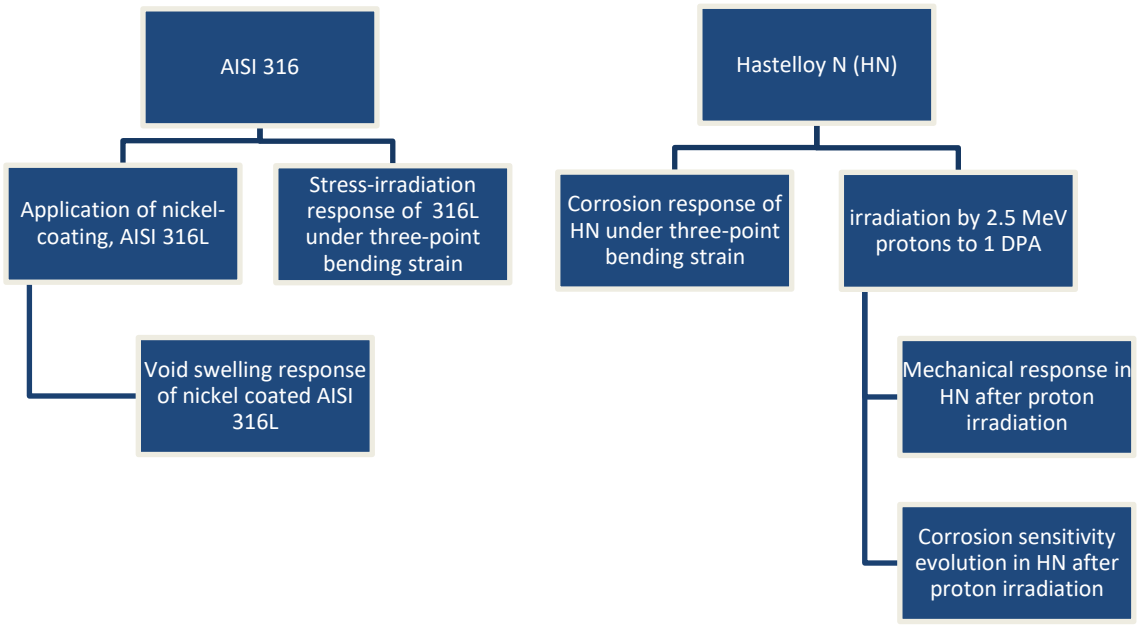

Figure 7. Matrix of experiments contained in this body of work.

References

[1] U.S.E.I.A. (EIA), Preliminary Monthly Electric Generator Inventory, 2021.

[2] G.H. Kinchin, R.S. Pease, The Displacement of Atoms in Solids by Radiation, Reports on Progress in Physics 18(1) (1955) 1-51.

[3] J.L. Straalsund, R.W. Powell, B.A. Chin, An overview of neutron irradiation effects in LMFBR materials, Journal of Nuclear Materials 108-109 (1982) 299-305.

[4] H.M. Chung, E. Technology, Assessment of void swelling in austenitic stainless steel PWR core internals, ; Argonne National Lab. (ANL), Argonne, IL (United States), 2006, p. Medium: ED.

[5] J.C. Wilson, Effects of Irradiation on the Structural Materials in Nuclear Power Reactors, in: R. Hurst, R.N. Lyon, C.M. Nicholls (Eds.), Progress In Nuclear Energy, Pergamon Press, New York, 1960, pp. 201-221.

[6] T.J. Gerczak, C.M. Parish, P.D. Edmondson, C.A. Baldwin, K.A. Terrani, Restructuring in high burnup UO2 studied using modern electron microscopy, Journal of Nuclear Materials 509 (2018) 245-259.

[7] D.L. Porter, F.A. Garner, Irradiation creep and embrittlement behavior of AISI 316 stainless steel at very high neutron fluences, Journal of Nuclear Materials 159 (1988) 114-121.

[8] H.M. Chung, W.J. Shack, Irradiation-Assisted Stress Corrosion Cracking Behavior of Austenitic Stainless Steels Applicable to LWR Core Internals, U.S. Nuclear Regulatory Commission, 2006.

[9] F. Cattant, D. Crusset, D. Féron, Corrosion issues in nuclear industry today, Materials Today 11(10) (2008) 32-37.

[10] S.A. Nikulin, V.G. Khanzhin, A.B. Rozhnov, V.A. Belov, Behavior of atomic reactor zirconium cladding fuel rod tubes under extreme operating conditions, Metal Science and Heat Treatment 51(5-6) (2009) 230.

[11] J. Stuckert, M. Veshchunov, Behaviour of Oxide Layer of Zirconium-Based Fuel Rod Cladding under Steam Starvation Conditions, 2008.

[12] G. Bibel, Significant wastage of a nuclear reactor pressure vessel head, Int. J. of Forensic Engineering 2 (2014) 1-14.

[13] J.-H. Park, O.K. Chopra, K. Natesan, W.J. Shack, Boric Acid Corrosion of Light Water Reactor Pressure Vessel Materials, U.S. Nuclear Regulatory Commission, 2005.

[14] J.A. Lane, H.G. McPherson, F. Maslan, Part II: Molten Salt Reactors, in: A.M. Weinberg (Ed.), Fluid Fueled Reactors, Addison-Wesley Pub. Co1958.

[15] M.W. Rosenthal, P.R. Kasten, R.B. Briggs, Molten-Salt Reactors—History, Status, and Potential, Nuclear Applications and Technology 8(2) (1970) 107-117.

[16] S.J. Zinkle, J.T. Busby, Structural materials for fission & fusion energy, Materials Today 12(11) (2009) 12-19.

[17] R.N. Wright, T.-L. Sham, Status of Metallic Structural Materials for Molten Salt Reactors, ; Idaho National Lab. (INL), Idaho Falls, ID (United States); Argonne National Lab. (ANL), Argonne, IL (United States), 2018, p. Medium: ED; Size: 34 p.

[18] L. Battelle Energy Alliance, TerraPower Molten Chloride Reactor Experiment TICAP Tabletop Exercise Report, Technology Inclusive Content of Application Project

For Non-Light Water Reactors, 2021.

[19] A.L. Qualls, Advanced Reactor Technology Program Molten Salt Reactor Campaign FY 2018 Summary, ; Oak Ridge National Lab. (ORNL), Oak Ridge, TN (United States), 2018, p. Medium: ED; Size: 44 p.

[20] R.R. Romatoski, L.W. Hu, Fluoride salt coolant properties for nuclear reactor applications: A review, Annals of Nuclear Energy 109 (2017) 635-647.

[21] J. Jerden, Molten Salt Thermophysical Properties Database Development: 2019 Update, ; Argonne National Lab. (ANL), Argonne, IL (United States), 2019, p. Medium: ED; Size: 30 p.

[22] R.C. Briant, A.M. Weinberg, Molten Fluorides as Power Reactor Fuels, Nuclear Science and Engineering 2(6) (1957) 797-803.

[23] W.R. Grimes, CHEMICAL BASIS FOR MOLTEN-SALT REACTORS, in: R.B. Briggs (Ed.) Molten-Salt Reactor Program Semiannual Progress Report, Oak Ridge National Laboratory, 1964, pp. 214-251.

[24] R.B. Briggs, Molten-Salt Reactor Program Semiannual Report, Oak Ridge National Laboratory, 1964.

[25] W.D. Manly, J.H. Coobs, J.H. DeVan, D.A. Douglas, H. Inouye, P. Patriarca, T.K. Roche, J.L. Scott, Metallurgical Problems In Molten Fluoride Systems, in: R. Hurst, R.N. Lyon, C.M. Nicholls (Eds.), Progress In Nuclear Energy, Pergamon Press, New York, 1960, pp. 201-221.

[26] J.H. DeVan, R.B.E. Ill, Corrosion Behavior of Reactor Materials In Fluoride Salt Mixtures, Oak Ridge National Laboratory, 1962, p. 14.

[27] J. Baes, C F, THE CHEMISTRY AND THERMODYNAMICS OF MOLTEN SALT REACTOR FLUORIDE SOLUTIONS, ; Oak Ridge National Lab., Tenn., 1965, p. Medium: ED; Size: Pages: 34.

[28] J. Zhang, C.W. Forsberg, M.F. Simpson, S. Guo, S.T. Lam, R.O. Scarlat, F. Carotti, K.J. Chan, P.M. Singh, W. Doniger, K. Sridharan, J.R. Keiser, Redox potential control in molten salt systems for corrosion mitigation, Corrosion Science (2018) Medium: ED; Size: p. 44-53.

[29] S.S. Raiman, S. Lee, Aggregation and data analysis of corrosion studies in molten chloride and fluoride salts, Journal of Nuclear Materials 511 (2018) 523-535.

[30] W.B. Cottrell, H.E. Hungerford, J.K. Leslie, J.L. Meem, OPERATION OF THE AIRCRAFT REACTOR EXPERIMENT, ; Oak Ridge National Lab., Tenn., 1955, p. Medium: ED; Size: Pages: 245.

[31] L.S. Richardson, D.C. Vreeland, W.D. Manly, Corrosion by Molten Fluorides, Oak Ridge National Laboratory, 1952, p. 24.

[32] W.D. Manly, J. Adamson, G. M., J.H. Coobs, J.H. DeVan, D.A. Douglas, E.E. Hoffman, P. Patriarca, AIRCRAFT REACTOR EXPERIMENT--METALLURGICAL ASPECTS, ; Oak Ridge National Lab., Tenn., 1958, p. Medium: ED; Size: Pages: 57.

[33] J.H. DeVan, I.R.B. Evans, CORROSION BEHAVIOR OF REACTOR MATERIALS IN FLUORIDE SALT MIXTURES, United States, 1962.

[34] J.W. Koger, Evaluation of Hastelloy N alloys after nine years exposure to both a molten fluoride salt and air at temperatures from 700 to 560C, ; Oak Ridge National Lab., Tenn. (USA), 1972, p. Medium: ED; Size: Pages: 39.

[35] W.G. Wolfer, C.D. Van Siclen, S.M. Foiles, J.B. Adams, Helium solubility in solid and liquid nickel, Acta Metallurgica 37(2) (1989) 579-585.

[36] J.H.E. McCoy, EVALUATION OF THE MOLTEN-SALT REACTOR EXPERIMENT HASTELLOY N SURVEILLANCE SPECIMENS: FOURTH GROUP, United States, 1971.

[37] J. McCoy, H. E., Status of materials development for molten salt reactors, ; Oak Ridge National Lab., TN (USA), 1978, p. Medium: ED; Size: Pages: 36.

[38] W.R. Martin, J.R. Weir, Postirradiation Creep and Stress Rupture of Hastelloy N, Nuclear Applications 3(3) (1967) 167-177.

[39] J.R. Keiser, Status of tellurium--hastelloy N studies in molten fluoride salts, United States, 1977.

[40] C.E. Sessions, E.E. Stansbury, Thermal Stability of Titanium-Modified Hastelloy N at 650C and 760C, Oak Ridge National Laboratory, Oak Ridge, Tennessee 1971.

[41] H.E. McCoy, The Influence of Several Metallurgical Variables on the Tensile Properties of Hastelloy N, Oak Ridge National Lab., Tenn., 1964.

[42] H.E. McCoy, D.T. Bourgette, Influence of aging on the impact properties of Hastelloy N, Haynes alloy No. 25, and Haynes alloy No. 188, ; Oak Ridge National Lab., Tenn. (USA), 1973, p. Medium: ED; Size: Pages: 33.

[43] T.A.S.o.M. Engineers, ASME Boiler and Pressure Vessel Code - An International Code, Section III: Rules for Construction of Nuclear Facility Components, ASME, New York, NY, 2019, p. 2.

[44] F.A. Garner, M.L. Hamilton, N.F. Panayotou, G.D. Johnson, The microstructural origins of yield strength changes in aisi 316 during fission or fusion irradiation, Journal of Nuclear Materials 104 (1981) 803-807.

[45] F.A. Garner, D.S. Gelles, Neutron-Induced Swelling of Commercial Alloys at Very High Exposures, in: P. Nicolas, S. Roger, K. Arvind (Eds.), STP-1046V2: Effects of Radiation on Materials: 14th International Symposium (Volume II), ASTM, Philadelphia, 1990, p. 673.

[46] F.A. Garner, 4.02 - Radiation Damage in Austenitic Steels, in: R.J.M. Konings (Ed.), Comprehensive Nuclear Materials, Elsevier, Oxford, 2012, pp. 33-95.

[47] L.K. Mansur, M.L. Grossbeck, Mechanical property changes induced in structural alloys by neutron irradiations with different helium to displacement ratios, Journal of Nuclear Materials 155-157 (1988) 130-147.

CHAPTER II

RADIATION TOLERANCE OF NICKEL COATING ON 316L STAINLESS STEEL APPLIED USING NOVEL CAGE PLASMA TREATMENT[1]

Introduction

Nitriding and carburizing, or the combined nitrocarburization, are well developed industry techniques for surface engineering of steels [1]. In plasma Nitriding (also called plasma immersion ion implantation), nitrogen atoms bombard an object from all directions, which make it feasible to treat materials of arbitrary shapes, e.g., cladding tubes or spacers. Different from gas nitriding or gas carbonization, plasma nitriding can be performed at relatively low temperatures, less than the last tempering temperature of steels. Additionally, plasma nitriding is less resource intensive once a system is built and uses relatively affordable gases which do not pose special personnel hazards [2, 3]. For austenitic stainless steels (316 and 304SS), an "S-phase" forms on the treatment surface. In literature, this term is confusingly used to describe both a compound layer of metal nitride (such as FCC γ' phase) and a layer of nitrogen-supersaturated and precipitation-free "expanded austenite". The latter is more preferred in many applications since chromium does not precipitate into CrN and corrosion resistance is largely sustained [1]. Nitrogen interstitials increase hardness through solution-strengthening and nitriding-

[1] *Reprinted with permission from "Ni coating on 316L stainless steel using cage plasma treatment: Feasibility and swelling studies" by Andres Morell-Pacheco, et. Al., 2020. J. Nucl. Mater., Volume 540, Page 152385, Copyright 2022 by Elsevier B.V.

introduced compressive stresses on the surface tend to close existing microcracks and further impede their formation [4-6]. Therefore, S-phase can sustain corrosion resistance, increase hardness and increase wear resistance [1].

Surface nitriding is not new for nuclear engineering and has been demonstrated to be economical and industrially viable. For in-core components requiring enhanced wear resistance, nitriding has been applied to improve their reliability and lifetimes. Examples include rod cluster control assemblies, in-core instrumentation flux thimbles and fuel assembly socket head screws [1, 4-7]. Nitruvid and Framatome developed commercial plasma nitriding techniques and instrument to modify surfaces of control rod clusters [7, 8]. The treated tubes show remarkably improved wear resistance in reactor testing and such treatment has been accepted in rod clusters control assembly design since 1992. The advanced nitriding instrument, developed by Framatome, can continuously treat tubes of >4 meter length at a capacity of >30 tubes at one time [9]. In comparison with other surface treatment techniques such as vapor deposition or sputtering deposition, plasma nitriding is well-suited for reactor applications, considering its accuracy, repeatability and high throughputs.

Plasma nitriding includes both “direct” plasma creation and “indirect” plasma creation on treated surfaces. In traditional plasma nitriding, plasma is created in close vicinity to metal surfaces. The technique sometimes has large spatial non-uniformity in treating materials having complicated geometry or sharp corners, due to the combined effects of particle diffusion, standing wave formation, and edge effects [10]. To mitigate the problem, the technique of Cathodic Cage Plasma Nitriding (CCPN) was developed, in

which a nitriding cage is introduced to create a hollow cathode effect (HCE) [11, 12]. Plasma is created on the cage holes and diffuse towards metal surfaces. The holes result in an optimal pressure depending on their size and spacing. In comparison with the traditional approach, the CCPN technique minimizes edge effects, increases temperature uniformity, and reduces arcing.

The present study aims to explore the feasibility of using CCPN for coating nickel onto 316L instead of direct nitriding of 316L. This is achieved by simultaneously (1) using a Ni cage to create plasma, (2) sputtering nickel from the cage by plasma bombardment on cage holes, (3) diffusing plasma towards 316L substrate, (4) Ni deposition onto 316L substrate. The proposed process is well-suited for combination with nitriding, which can improve the mechanical strength of the 316L substrate through solid solution and/or dispersion strengthening [13, 14]. The key is to float the 316L substrate at the same potential as the cage, hence minimizing sputtering of deposited nickel atoms from the 316L substrate while allowing nitrogen diffusion into the surface.

The motivation here is to develop a method to coat a nickel layer onto 316L for potential applications in molten salt reactors (MSR). Nickel and Ni-based alloys such as Hastelloy N have shown satisfactory compatibility and reasonable corrosion resistance in fluoride salts such as FLiNaK [15-17]. The cost of such nickel superalloys, however, makes them impractical for industrial-scale use. Stainless steels such as 316L have been proposed as a more economical alternative but do not resist corrosion as readily [18]. Recent comparison studies show that Ni-201 (which is almost pure nickel) has the lowest corrosion rate among the alloys including Ni-201, Hastelloy-B, 316S, 317L, Incoloy-

800H and Inconel-625) [18], while 316L has a corrosion rate about 20 times larger [18]. Early studies show that 316 stainless steel has intergranular corrosion attack and Cr depletion in FLiBe salt, with an expected corrosion attack depth about 16 μm for one year service at 700°C [19]. Although 316L is less ideal than Ni alloys in corrosion resistance, the welding and thermal-mechanical processing technology is more mature. Hence, Ni coated 316L can find unique applications in MSRs. The concept of Ni coating has been explored before on Incoloy-800H by using Ni electroplating technique, which shows improved corrosion resistance since nickel protects against chromium dissolution into the salt [20].

Here, the CCPN technique was used to coat a continuous Ni layer onto 316L for potential MSR applications, capitalizing on previously-demonstrated corrosion resistance of nickel and well-characterized 316L bulk properties. The study includes two sequential tasks. First, demonstrate the feasibility of using CCPN to apply Ni coating. Second, show that the Ni coating layer has satisfactory void swelling resistance. The second task is important since nickel belongs to a group of metals (including nickel, chromium, and copper) which easily swell at low damage levels. Pure nickel swells quickly, reaching 3.2% after 22 DPA as demonstrated by irradiation at 600°C in BOR-60 [21]. 316 stainless steel has reasonable swelling resistance. At irradiation temperatures of 575°, it shows a swelling incubation period of ~75 DPA. This is followed by a transition period and subsequent steady-state void growth stage at a rate of approximately 1% per dpa, as expected for FCC Fe-based steel [22]. In general, FCC metals have worse swelling resistance than BCC metals, and their void swelling needs to be considered in materials

design. If the Ni coating layer swells easily, stress created from volume expansion can cause debonding of the coating film. For the second task of swelling testing, Fe self-ion irradiation was used as a surrogate to neutron damage. The Fe ion penetration depth is limited. Therefore, ion irradiation is performed by bombarding Fe ions into the cross section of samples polished after plasma treatment, which allows comparison of swelling in different regions under the same ion irradiation condition.

Experiment Procedure

The present study consists of three steps. Firstly, 316L is plasma treated in a home-made CCPN system using 200 Nickel alloy (≥99% nickel) as the cage material. Second, the treated sample is cut and the newly created cross section is polished and irradiated by using 3.5 MeV Fe ions to 50 peak dpa at 600°C. Third, focused ion beam (FIB) is used to prepare lamellae specimens from different locations on the cross section, and transmission electron microscopy (TEM) is used to characterize void swelling and microstructures.

For the first step of the experiment, the sequence of the coating process is as follows: (1) The N_2/H_2 gas mixture is streamed into the vacuum chamber and fills up the volume to a prescribed pressure. (2) gas passing between the grounding plate and stage ionizes and accelerates towards the cage/stage in the electric field. The stage is held at a potential beyond the electrical breakdown voltage, leading to secondary ionization cascades and collisions which energize neutral gas atoms and sputter electrons from the cathode surface [23]. (3) Ions further energize by the HCE around the cage holes and form

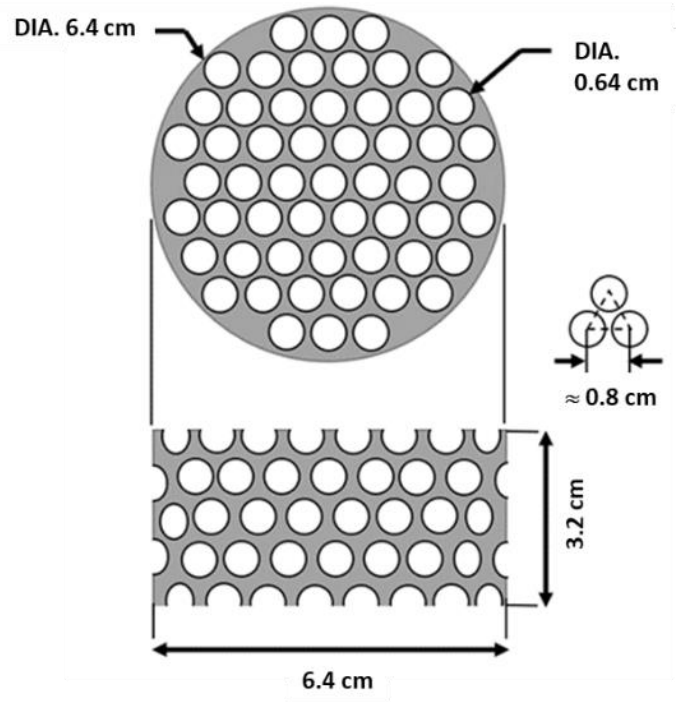

Figure 8. Diagram of plasma formation and sputtering around cathodic cage and dimensions of final cage design used for applying nickel coating.

a plasma field within and around the cage. The confined plasma heats the sample. Some ions and atoms impact the cage and sputter nickel away. (4) Nitrogen plasma within the cage diffuses into the sample and nickel is simultaneously deposited onto the sample.

The biased DC voltage between the grounding plate (positioned 7 cm away from the top of the cage) and the nickel anodic cage is 650 volts. The dimensions of the cage are shown in Figure 8. The cage was fabricated from 0.019 inch sheet. The 316L sample inside the cage was connected to the sample stage. The sample stage and the cage were at the same potential. Hence, the sample is floating with respect to the cage and plasma or sputtered Ni atoms from the cage diffuse towards the sample. This is important since, if a

bias is applied between the cage and the sample to increase bombarding energies of sputtered nickel atoms (depending on charge status and voltage direction), sputtering can be increased and remove deposition on the substrate (depending on nuclear stopping powers under specific bombarding energies). The stage is isolated from the stainless steel chamber walls via alumina ceramic standoffs.

The gas used is a mixture of 90 at. % nitrogen and 10 at.% hydrogen. Hydrogen is used, as a well-known practice, to minimize oxidation. Hydrogen ions in the plasma mixture serve as a reactive species, which liberate unwanted contaminants and the protective metallic-oxides from the surface and carry them away. This facilitates the nitrogen ions diffusing more readily into the alloy, as well as better adherence of the applied coating [2, 3, 24-26]. The absolute gas pressure during the plasma treatment is maintained at 1.5 torr during operation. After the plasma is ignited, both the pressure and voltage are slowly increased to the operation setup in order to avoid arching. The plasma creation, as reflected by purple color on the cage, shows satisfactory uniformity. No overheated spot (i.e., spots which are much brighter and which jump location) is apparent on the cage holes. The substrate temperature is controlled by gas pressure, bias and current, and is measured to be ~800°C. The sample was treated at high temperature deliberately in order to avoid Fe-Ni intermetallic compound or other modeling-suggested compounds [27, 28].

Numerous problems have been identified in the initial design and have been solved. Examples include severe arching when igniting plasma, metallic sputtering and deposition on inner ceramic insulators which cause electrical shortage and inconsistent

nitriding results. Various solutions have been found to eliminate or alleviate these issues. For example, the anode was redesigned for stable electrical grounding, multiple shielded sample holders are used to replace single isolation disk, and additional shields are used to isolate thermocouple feedthrough. Frequent abrasive cleaning was implemented on the system components and chamber to remove buildup of shorting pathways. In early testing, the HCE was only formed on one cage opening at a time and the location was unstable. This produced a variable temperature distribution inside the nitriding cage due to the localized plasma concentration. These small temperature differences produced large variations of the nitride layer in pure iron samples used for testing in preparation for this experiment. This variation was addressed by optimizing the cage hole size and gas flow rate to enable more uniform plasma distribution outside and within the cage, resulting in a completely uniform sample temperature in proceeding pure iron samples. After this correction, other sample materials tested showed uniform temperature distributions.

For the second step, the cross section of the nitrided sample is uniformly irradiated by using 3.5 MeV Fe ions to 50 peak dpa at 600°C. The temperature selected approximately coincides with the maximum swelling temperature of FCC Fe-based steels [22]. The SRIM-2013 code utilizing the Kinchin-Pease model is implemented for damage calculation using metallic displacement energy recommendations specified by ASTM International [29, 30]. As shown in Figure 9, peak damage occurs at ~1 μm and the implanted irons peak range occurs at ~1.2 μm. With limited ion penetration depth, studying the radiation response at the different regions of the nitride-layer requires performing irradiation on the polished cross-section of the sample. The ion irradiation is

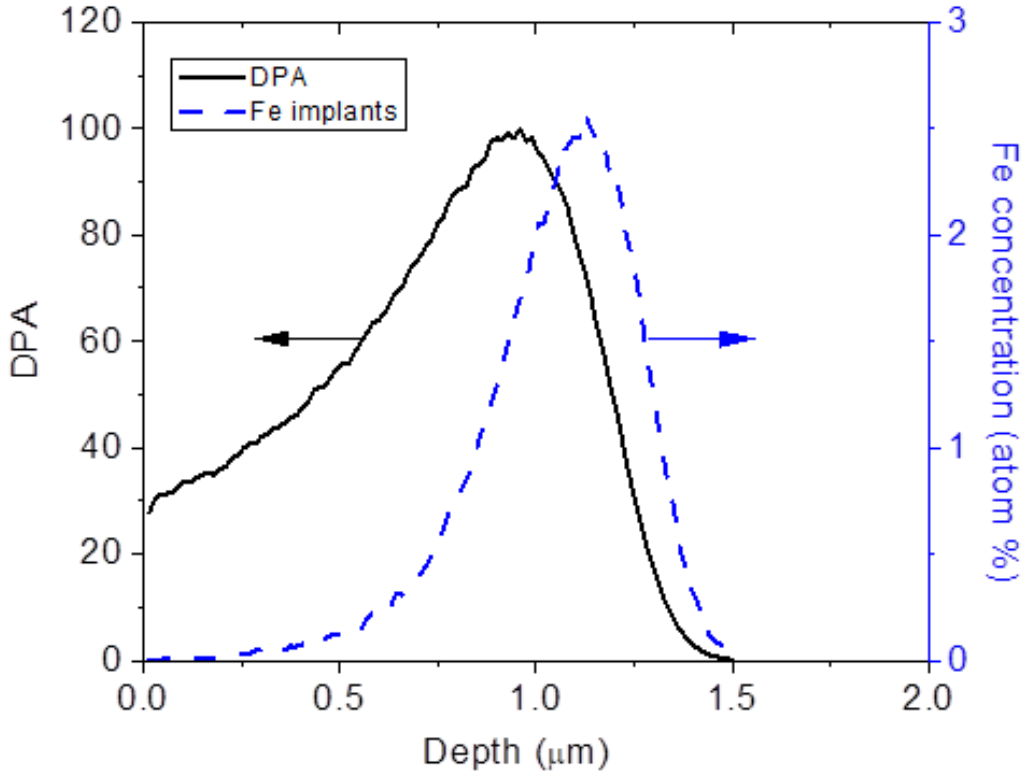

Figure 9. SRIM simulations of dpa damage and Fe implant distribution caused by 3.5 MeV Fe bombardment.

performed by using a defocused beam with a spot size of 6mm × 6mm, in order to avoid the pulsed beam effect [31, 32]. The technique of multiple-beam-deflection was applied to avoid carbon contamination. Our recently-developed ion beam filtering system using a series of deflecting magnets and a liquid nitrogen cold trap on the beamline is used to avoid beam-induced contamination (C-, N-, O-rich molecules) of the specimens during irradiation [33-35]. The target chamber pressure was maintained at 6×10^{-8} torr or better during irradiation and the temperature variation is less than ±3 ℃ throughout the irradiation. For the third step of structural characterization, scanning electron microscopy

(SEM), TEM, and localized diffraction analysis are performed. An SEM energy dispersive x-ray spectroscopy (EDS) line-scan analysis, spaced evenly every 7μm, is executed to profile the compositional changes on the polished cross section of plasma-treated sample. FIB is used to prepare TEM specimens from different locations of the cross section. TEM characterization was done using a FEI Tecnai F20 ST with an operating voltage of 200 kV.

Results and discussion

Figure 10.a shows an SEM image of the polished cross section. There are three distinctive regions. The surface layer is a dense precipitation-free layer of about 20 to 30 μm thickness, as marked as region 1 in the figure. Beneath is a thick layer of ~100 μm thickness, marked as region 2, which has high density precipitations, appearing white. The precipitation density decreases with increasing depth. Both intragranular and intergranular precipitates appear, but intergranular precipitates are dominant. At depth deeper than ~100 μm from the original surface, referred to as region 3, precipitation disappears, and the region is the least unaffected by nitrogen plasma treatment.

Figure 10.b shows schematics of the surface change. The dense region 1 results from Ni and Ni-containing molecule deposition due to plasma sputtering of the pure Ni cage. Sputtered atoms/molecules are mainly in the energy region of eVs. These atoms/molecules are presumably not energetic enough to cause sputtering of substrate.

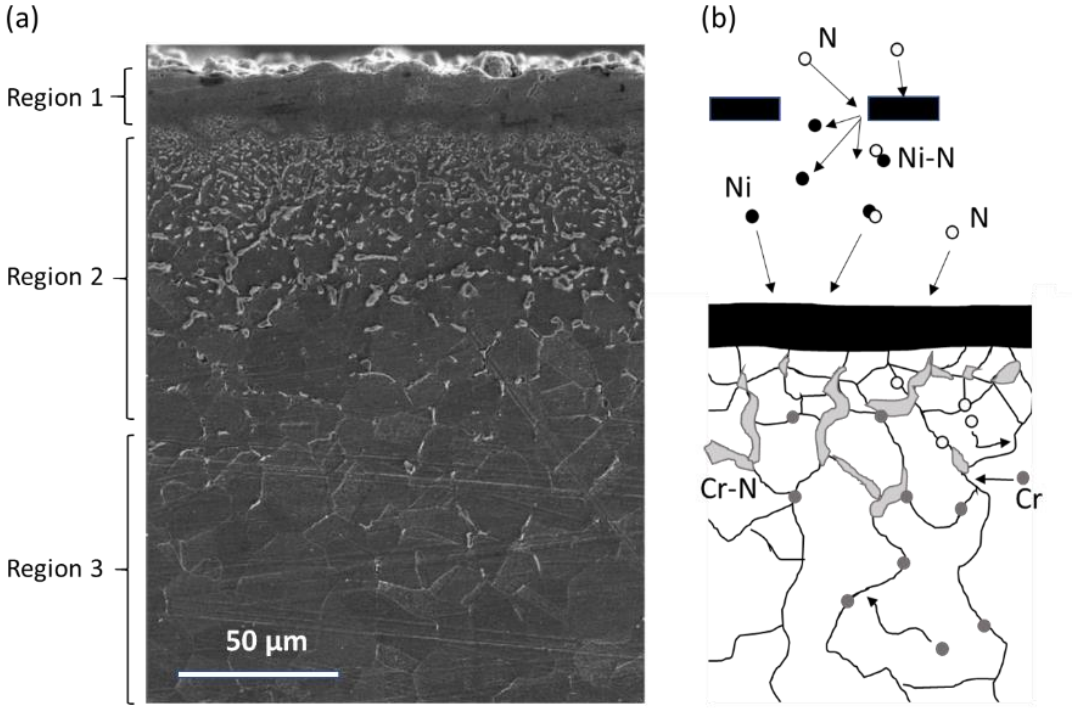

Figure 10. a) SEM image of the cross section polished 316L after plasma treatment and b) schematics of the layer formation. The surface of the sample is oriented upwards.

Instead, they are mainly deposited onto it, although some can be sputtered by the nitrogen/hydrogen plasma. This is different from the case in which the substrate is biased differently from the cage, which results in more energetic nitrogen bombardment and sputtering, instead of deposition. During the whole process, nitrogen plasma continuously interacts with substrates. The diffusing nitrogen atoms interact with chromium atoms which segregates along grain boundaries under such high temperature, forming boundary chromium-nitride precipitates.

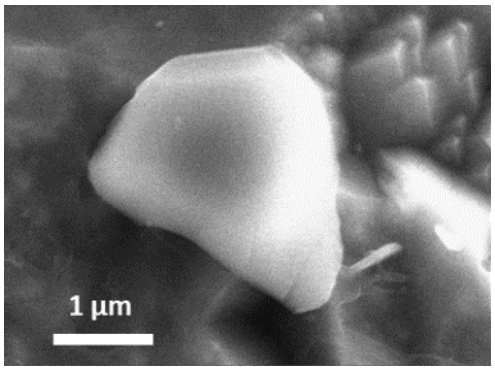

Composition	
Element	wt.%
Fe	39.34
Cr	32.08
N	12.99
Ni	6.25
C	5.73
Mo	2.37
Mn	1.35

Figure 11. SEM image of a boundary precipitate forming after plasma treatment and the corresponding EDS composition analysis.

Figure 11 shows an SEM image of one typical boundary precipitate. EDS composition analysis shows significant nitrogen signals. Since the particle size is less than 2 µm, the interference with the substrate is significant, leading to high iron yield.

The particle is presumably a nitride compound due to significant chromium and nitrogen yields. Note that boundary precipitates appear only within 100 µm from the surface, which is consistent with the limited diffusion range of nitrogen. Previous studies suggested that Cr_2N is unstable below 400°C [36]. Under high temperature, chromium diffusion towards grain boundaries would promote formation of Cr_2N via a Cr + CrN = Cr_2N eutectic reaction. Cooling down from high treatment temperature may lead to the subsequent

decomposition of Cr_2N. Such segregation and grain boundary precipitation may not occur at lower temperature treatment.

The result of EDS composition analysis is shown in Figure 12. Note that SEM-EDS is largely affected by the matrix due to big interaction volume under an electron analysis beam. This leads to relatively large uncertainty on composition analysis but the technique is appropriate to show elemental changes over a large area. Region 1, from the surface to a depth of ~20 μm, is a nickel-rich layer containing Fe as γ-(Fe, Ni) solution. No intermetallic layer and no precipitation are found. From depths of 30 μm to 40 μm, the SEM image in Figure 12 shows the beginning of a dense precipitant field which corresponds to the original surface and is significantly affected by nitrogen introduction. This is reflected in the EDS scan where at a depth of approximately 35 μm, there is a jump in the Fe, Cr and N signal strength resulting from measurement of a precipitate along the scan path.

This layer may correspond to FCC γ phase "expanded austenite", as S phase in nitrided austenite. This layer also has intense intergranular and intragranular Cr-N compound formation, with possible chromium migration from the bulk. Beneath this thin layer is a much thicker region, from depth ~40 μm to ~100 μm. This is the region affected by nitrogen diffusion along the grain boundaries as demonstrated by the EDS spectrum shown in Figure 11 Nitrogen yields in this region are very low, which is attributable to the

high treatment temperature (800°C). This has two implications. First, much of the superficially trapped nitrogen can escape soon after diffusing into the substrate surface.

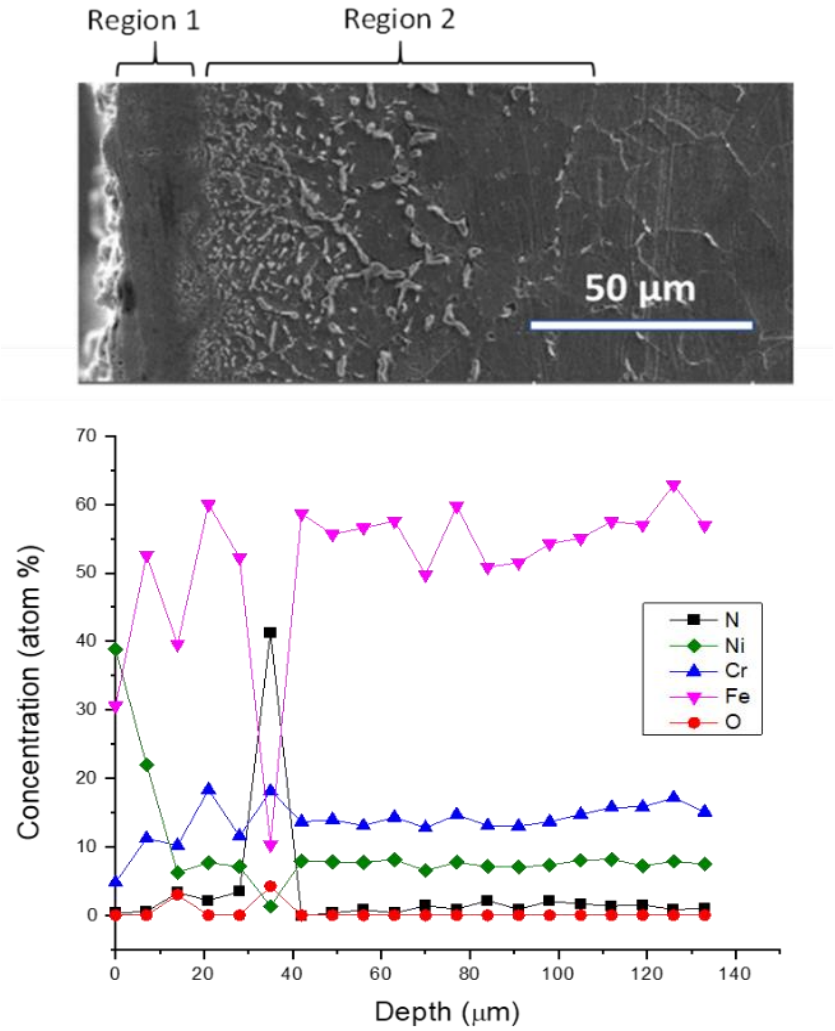

Figure 12. EDS line scans of the cross section of nitrided sample. The top is the SEM cross sectional image.

Second, the expanded austenite phase in stainless steel is widely documented as unstable above 400-450°C [37-42], decomposing into CrN and normal γ-phase [41, 42].

Nitrogen which does penetrate the sample will thus preferentially form Cr-N precipitates along grain boundaries instead of occupying interstitials within the bulk matrix. This reflects the results of the SEM and EDS analysis, which show that nitrogen is virtually absent in the intragranular regions but rich in the precipitates decorating the grain boundaries between ~40 μm and ~100 μm. Since both layers at 30 μm – 40 μm and 40 μm – 100 μm have FCC phase, they are together described as layer 2, or the nitrogen diffusion layer. Depths deeper than 100 μm is considered the bulk region which is the least affected by nitrogen. Small GB precipitates may exist in this region, but precipitate density is significantly less than the shallower region. Due to limited diffusion and much less grain boundary precipitation, chromium is largely retained within the bulk.

For aqueous applications, chromium is crucial for passivation against corrosion and thus precipitating chromium compounds during thermal treatments should be avoided. In molten fluoride environments however, chromium dissolves readily into the salt and molybdenum and nickel are the most thermodynamically stable alloying elements in 316L [43]. Precipitating chromium from the matrix would thus be less consequential, as the nickel coating applied to the surface of the 316L be responsible for corrosion inhibition.

Figure 13.a and b show the TEM image, high-resolution TEM image and its corresponding localized diffraction patterns from region 1 and region 2, respectively. In both regions, diffraction patterns show FCC γ phases. The interplanar distances match the expected spacing of γ-(Fe, Ni) or γ-Fe. Furthermore, twinning is frequently observed in

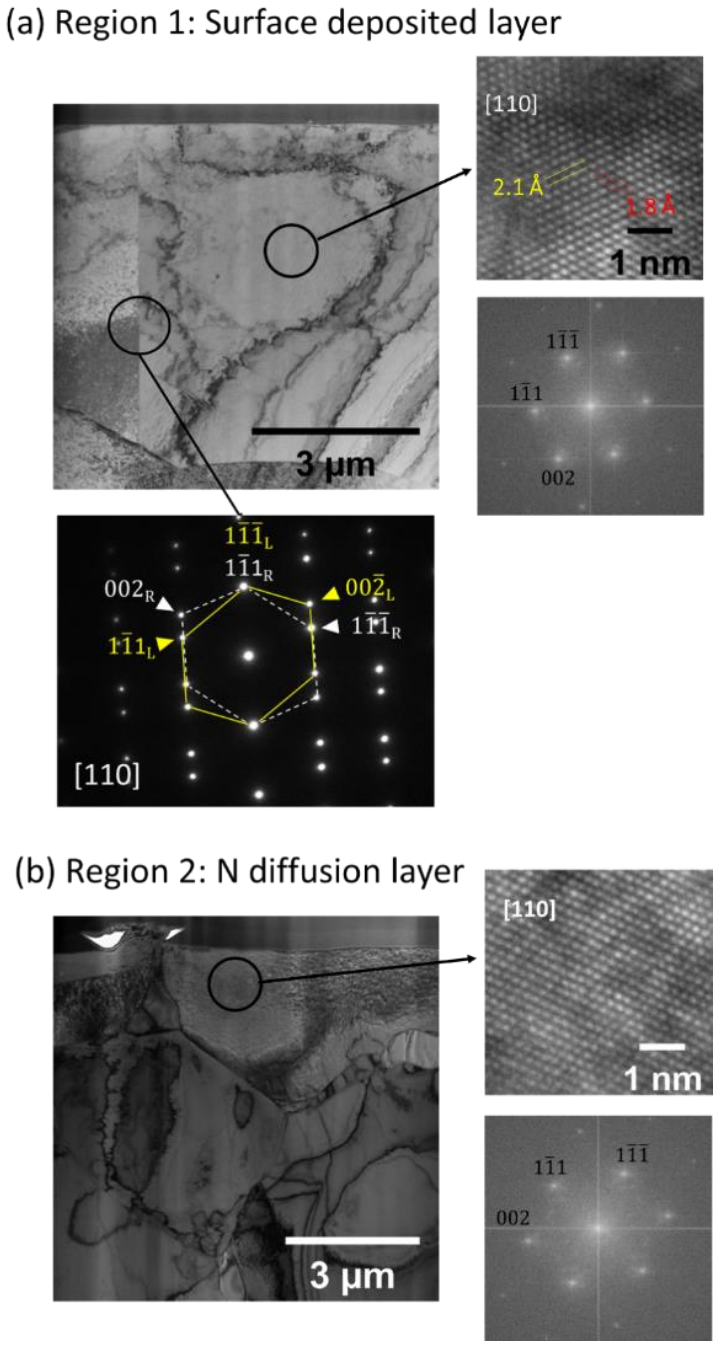

Figure 13. a) Cross sectional TEM image, high resolution TEM image, localized diffraction pattern, and corresponding FFT region 1, the Ni-deposited layer, and b) TEM image and high resolution TEM image, and localized diffraction pattern of region 2, the N-diffusion layer.

region 1, as shown in the vertical boundary in Figure 13.a. The bottom inset of Figure 13.a is the diffraction pattern taken from the twin boundary, with white dash and yellow dash lines corresponding to the left and right side of the boundary, respectively. There is no observation of cavity or microcracks, suggesting an excellent bonding and integrity with the original substrate and thorough Fe-Ni interdiffusion.

Figure 14.a1-a3 show cross sectional TEM images of different locations of region 1 after Fe-ion irradiation. The FIB lamella is lifted out from the cross section of the irradiated specimen, at a location corresponding to region 1. Therefore, the whole specimen corresponds to region 1, and the depth of 0 to ~1.2 μm corresponds to the ion bombarded region. No voids and phase changes are observed. The deposited Ni rich layer shows excellent radiation tolerance and structural integrity. Pure nickel swells easily, but the diffusion of iron from the substrate into the deposited nickel layer and formation of γ-(Fe, Ni) significantly increase swelling resistance in the present study. Nitrogen atoms may also help to suppress swelling through impurity-defect interaction in the lattice. There is no polygonization observed. This region has very large grains, although twins are frequently observed. The presence of nitrogen may reduce the stacking fault energy for the system and promote more frequent twining [44]. The lack of small grains or nanograins further suggests the swelling suppression is not from grain boundary defect sinking. Thus, swelling suppression is likely attributable to the interaction between nitrogen and point defects.

Figure 14.b1-b3 show cross sectional TEM images from region 2. No polygonization. A few voids, however, are observed. The void diameters range from 40

nm to 70 nm. The swelling was measured to be 0.1%. There are several possible mechanisms for the apparent swelling reduction. One is from N-defect interaction. Although nitrogen atoms are very limited within grains, a small amount below EDS detection thresholds may still be present and interact with either interstitials or vacancies. Both can lead to reduced void selling. Interstitial trapping by nitrogen can reduce interstitial mobility and thus reduce dislocation loop growth, which is required for dislocations to initiate biased interstitial trapping. The dislocation growth causes incomplete point defect recombination and vacancy supersaturation/clustering. On the other hand, possible nitrogen interactions with vacancies may include strain relaxation around interstitial solutes, reducing vacancy clustering. Another possible mechanism is the effect of nickel and chromium. It is well-known in early alloying engineering literature that nickel can suppress void swelling and chromium can promote swelling [45]. The deposition of the nickel layer, the nickel diffusion into the bulk, and reduced chromium concentration within grains due to migration towards grain boundaries will both lead to suppressed void swelling.

As a comparison, Figure 14.c1-c3 show TEM images from region 3 which is the least affected by nitrogen diffusion. The void diameters range from 15 nm to 120 nm. The void swelling was measured to be about 1.7%, which is much larger than 0.1% swelling of region 2. Voids are distributed from the surface up to ~1 μm, which is expected since the projected range of 3.5 MeV implanted iron is ~1.2 μm. The significant swelling in bulk 316L shows that the plasma treatment is effective for reducing swelling in region 1 and region 2. The slightly increased swelling resistance

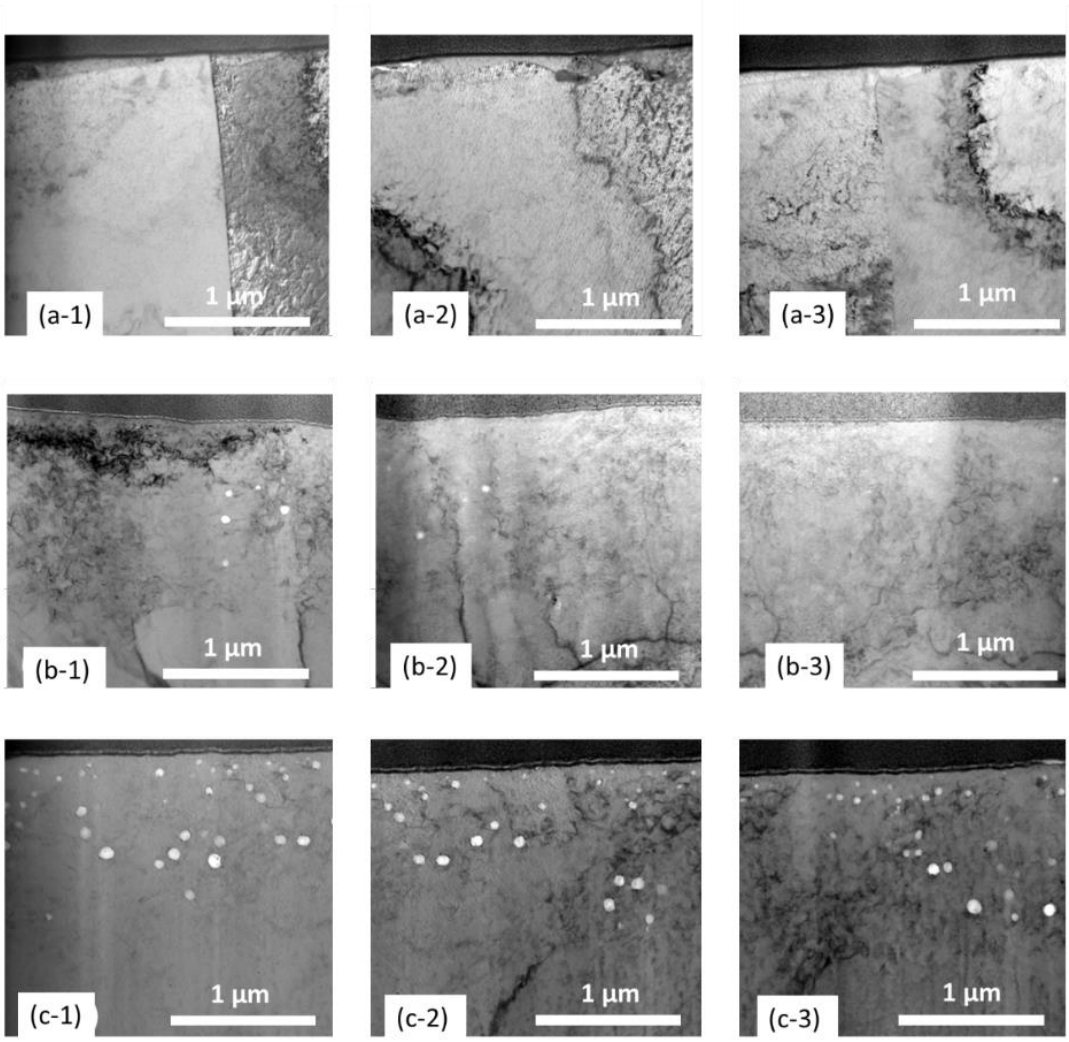

Figure 14. (a1-a3) TEM images of lamella taken from region 1 (nickel deposition region). (b1-b3) TEM image from region 2 (nitrogen diffusion region). (c1-c3) TEM image of region 3 (bulk region). All samples were ion-irradiated.

towards the surface, as a "graded swelling", is beneficial since it will reduce the stress caused by easy swelling of bulk 316L. If swelling response has a sharp change across an interface, debonding becomes likely. On the other hand, chromium nitride formation at grain boundaries may be an issue. The Ni protective layer however is expected to reduce

or stop Cr diffusion into the salt and to serve as the primary barrier for corrosion inhibition. It is expected that nitride formation will be significantly reduced at lower plasma treatment temperature due to limited diffusion and the threshold temperature for CrN precipitation. Sputtering is not affected by temperature. Hence, nickel deposition will still occur at lower plasma temperature.

The present study is mainly to demonstrate the feasibility of the technique, and materials selection is not optimized. The usage of 316L is stimulated by a series of previous corrosion testing to evaluate 316L as a potential MSR material [46], and by the finding that carbon plays a significant role in determining corrosion susceptibility [19]. 316L is good for its sensitization resistance, but its maximum allowable temperature (475°C), according to ASME-II-D, is low for MSR application. Hence, future studies are needed to extend to other stainless steels such as 316H, which is an alloy suitable for higher operation temperatures. The comparison of nitridation behaviors among different alloys, such as 316L and 316H, is meaningful, since high concentration carbon in 316H may consume Cr for carbide formation and reduce chromium nitride formation. Furthermore, systematic studies are needed to evaluate bonding strength and thermal fatigue resistance. The formation of nitride-rich layer between Ni layer and 316L may be problematic if there is a large mismatch of thermal expansion coefficients between different layers. The lack of void swelling in Ni layer and nitride-rich layer, as discovered from the present study, suggests that void swelling should not cause debonding. The present study shows that the surface layer is rich in Fe. The effect of Fe enrichment on corrosion resistance needs to be evaluated since Fe is not immune to corrosion attack. On

the other hand, the level of Fe enrichment can be adjusted by increasing the deposition layer thickness. Since nitriding is a low-temperature process, Fe diffusion can be further minimized by controlling temperature.

References

[1] H. Dong, S-phase surface engineering of Fe-Cr, Co-Cr and Ni-Cr alloys, International Materials Reviews 55(2) (2010) 65-98.

[2] D. Pye, Practical Nitriding and Ferritic Nitrocarburizing, ASM International2003.

[3] A. Bernal, Investigation on Nitriding with Enphasis in Plasma Nitriding Process , Current Technology and Equipment, Materials Processing, Royal Institute of Technology - KTH, Stockholm, 2006.

[4] W. Liang, X. Bin, Y. Zhiwei, S. Yaqin, The wear and corrosion properties of stainless steel nitrided by low-pressure plasma-arc source ion nitriding at low temperatures, Surface and Coatings Technology 130(2) (2000) 304-308.

[5] L. Shen, L. Wang, Y. Wang, C. Wang, Plasma nitriding of AISI 304 austenitic stainless steel with pre-shot peening, Surface and Coatings Technology 204(20) (2010) 3222-3227.

[6] W. Liang, Surface modification of AISI 304 austenitic stainless steel by plasma nitriding, Applied Surface Science 211(1) (2003) 308-314.

[7] J.P. Lebrun, L. Poirier, D. Hertz, C. Lincot, Stainless steel 2000 : proceedings of an International Current Status Seminar on Thermochemical Surface Engineering of Stainless Steel : held in Osaka, Japan, November 2000. edited by Tom Bell and Katsuya

Akamatsu, Manley Pub. for the Institute of Materials in association with the International Federation for Heat Treatment and Surface Engineering and the Japan Society for Heat Treatment, London, 2001.

[8] J.P. Lebrun, L. Poirier, D. Hertz, C. Lincot, Environmentally friendly low temperature plasma processing of stainless steel components for nuclear industry, Surface Engineering 18 (2002) 423-428.

[9] J. Pelletier, A. Lacoste, Y. Arnal, T. Lagarde, C. Lincot, D. Hertz, New trends in DECR plasma technology: applications to novel duplex treatments and process combinations with extreme plasma specifications, Surface and Coatings Technology 139(2) (2001) 222-232.

[10] M.E. Chabica, D.L. Williamson, R. Wei, P.J. Wilbur, Microstructure and corrosion of nitrogen implanted AISI 304 stainless steel, Surface and Coatings Technology 51(1) (1992) 24-29.

[11] C. Alves, F.O. de Araújo, K.J.B. Ribeiro, J.A.P. da Costa, R.R.M. Sousa, R.S. de Sousa, Use of cathodic cage in plasma nitriding, Surface and Coatings Technology 201(6) (2006) 2450-2454.

[12] R.R.M. de Sousa, F.O. de Araújo, J.A.P. da Costa, A. de S. Brandim, R.A. de Brito, C. Alves, Cathodic Cage Plasma Nitriding: An Innovative Technique, Journal of Metallurgy 2012 (2012) 385963.

[13] M.J. Schneider, M.S. Chatterjee, Introduction to Surface Hardening of Steels, in: J. Dossett, G.E. Totten (Eds.), ASM Handbook,Steel Heat Treating Fundamentals and Processes

ASM International2013.

[14] M.A.J. Somers, T.L. Christiansen, 14 - Low temperature surface hardening of stainless steel, in: E.J. Mittemeijer, M.A.J. Somers (Eds.), Thermochemical Surface Engineering of Steels, Woodhead Publishing, Oxford, 2015, pp. 557-579.

[15] N. Iwamoto, Y. Makino, K. Furukawa, Y. Katoh, H. Katsuta, Corrosion of hastelloy-N in molten flinak loop, Transactions of JWRI 9(2) (1980) 259-261.

[16] D. Sridharan, M. Anderson, M. Corradini, T. Allen, L. Olson, J. Ambrosek, D. Ludwig, Molten Salt Heat Transport Loop: Materials Corrosion and Heat Transfer Phenomena, (2008).

[17] L.C. Olson, J.W. Ambrosek, K. Sridharan, M.H. Anderson, T.R. Allen, Materials corrosion in molten LiF–NaF–KF salt, Journal of Fluorine Chemistry 130(1) (2009) 67-73.

[18] C.S. Sona, B.D. Gajbhiye, P.V. Hule, A.W. Patwardhan, C.S. Mathpati, A. Borgohain, N.K. Maheshwari, High temperature corrosion studies in molten salt-FLiNaK, Corrosion Engineering, Science and Technology 49(4) (2014) 287-295.

[19] G. Zheng, L. He, D. Carpenter, K. Sridharan, Corrosion-induced microstructural developments in 316 stainless steel during exposure to molten Li2BeF4(FLiBe) salt, Journal of Nuclear Materials 482 (2016) 147-155.

[20] L. Olson, K. Sridharan, M. Anderson, T. Allen, Nickel-plating for active metal dissolution resistance in molten fluoride salts, Journal of Nuclear Materials 411(1) (2011) 51-59.

[21] N.I. Budylkin, E.G. Mironova, V.M. Chernov, V.A. Krasnoselov, S.I. Porollo, F.A. Garner, Neutron-induced swelling and embrittlement of pure iron and pure nickel irradiated in the BN-350 and BOR-60 fast reactors, Journal of Nuclear Materials 375(3) (2008) 359-364.

[22] H. Kim, J.G. Gigax, J. Fan, F.A. Garner, T.L. Sham, L. Shao, Swelling resistance of advanced austenitic alloy A709 and its comparison with 316 stainless steel at high damage levels, Journal of Nuclear Materials 527 (2019) 151818.

[23] J.L. Vossen, W. Kern, Thin Film Processes II, Elsevier.

[24] M. Naeem, J. Iqbal, M. Abrar, K.H. Khan, J.C. Díaz-Guillén, C.M. Lopez-Badillo, M. Shafiq, M. Zaka-ul-Islam, M. Zakaullah, The effect of argon admixing on nitriding of plain carbon steel in N2 and N2-H2 plasma, Surface and Coatings Technology 350 (2018) 48-56.

[25] A. Ricard, Spectroscopy of flowing discharges and post-discharges in reactive gases, Surface and Coatings Technology 59(1) (1993) 67-76.

[26] A. Szasz, D.J. Fabian, A. Hendry, Z. Szaszne-Csih, Nitriding of stainless steel in an rf plasma, Journal of Applied Physics 66(11) (1989) 5598-5601.

[27] Y. Mishin, M.J. Mehl, D.A. Papaconstantopoulos, Phase stability in the Fe–Ni system: Investigation by first-principles calculations and atomistic simulations, Acta Materialia 53(15) (2005) 4029-4041.

[28] G. Cacciamani, J. De Keyzer, R. Ferro, U.E. Klotz, J. Lacaze, P. Wollants, Critical evaluation of the Fe–Ni, Fe–Ti and Fe–Ni–Ti alloy systems, Intermetallics 14(10) (2006) 1312-1325.

[29] Anon, Standard Practice for Investigating the Effects of Neutron Radiation Damage Using Charged-Particle Irradiation, ASTM International, West Conshohocken, PA, 2016.

[30] J. Ziegler, M.D. Ziegler, J. Biersack, The Stopping and Range of Ions in Mater, Nuclear Instruments and Methods in Physics Research Section B: Beam Interactions with Materials and Atoms 268 (2010) 1818-1823.

[31] J. Gigax, E. Aydogan, T. Chen, D. Chen, L. Shao, Y. Wu, W.-Y. Lo, Y. Yang, F. Garner, The influence of ion beam rastering on the swelling of self-ion irradiated pure iron at 450 °C, Journal of Nuclear Materials 465 (2015).

[32] E. Getto, Z. Jiao, A.M. Monterrosa, K. Sun, G.S. Was, Effect of irradiation mode on the microstructure of self-ion irradiated ferritic-martensitic alloys, Journal of Nuclear Materials 465 (2015) 116-126.

[33] J. Gigax, H. Kim, E. Aydogan, F. Garner, S. Maloy, L. Shao, Beam-contamination-induced compositional alteration and its neutron-atypical consequences in ion simulation of neutron-induced void swelling, Materials Research Letters 5 (2017) 1-8.

[34] L. Shao, J. Gigax, H. Kim, F. Garner, J. Wang, M. Toloczko, Carbon Contamination, Its Consequences and Its Mitigation in Ion-Simulation of Neutron-Induced Swelling of Structural Metals, 2018.

[35] J.G. Gigax, H. Kim, E. Aydogan, L.M. Price, X. Wang, S.A. Maloy, F.A. Garner, L. Shao, Impact of composition modification induced by ion beam Coulomb-drag effects on the nanoindentation hardness of HT9, Nuclear Instruments and Methods in Physics Research Section B: Beam Interactions with Materials and Atoms 444 (2019) 68-73.

[36] J.W. Seok, N.M. Jadeed, R.Y. Lin, Sputter-deposited nanocrystalline Cr and CrN coatings on steels, Surface and Coatings Technology 138(1) (2001) 14-22.

[37] Z.L. Zhang, T. Bell, Structure and Corrosion Resistance of Plasma Nitrided Stainless Steel, Surface Engineering 1(2) (1985) 131-136.

[38] E. Menthe, K.T. Rie, J.W. Schultze, S. Simson, Structure and properties of plasma-nitrided stainless steel, Surface and Coatings Technology 74-75 (1995) 412-416.

[39] S.K. Kim, J.S. Yoo, J.M. Priest, M.P. Fewell, Characteristics of martensitic stainless steel nitrided in a low-pressure RF plasma, Surface and Coatings Technology 163-164 (2003) 380-385.

[40] R. Djellal, A. Saker, B. Bouzabata, D.E. Mekki, Thermal stability and phase decomposition of nitrided layers on 316L and 310 austenitic stainless steels, Surface and Coatings Technology 325 (2017) 533-538.

[41] G.A. Collins, R. Hutchings, K.T. Short, J. Tendys, X. Li, M. Samandi, Nitriding of austenitic stainless steel by plasma immersion ion implantation, Surface and Coatings Technology 74-75 (1995) 417-424.

[42] T. Christiansen, M. Somers, Decomposition kinetics of expanded austenite with high nitrogen contents, International Journal of Materials Research 97 (2006) 79-88.

[43] J.H. DeVan, I.R.B. Evans, CORROSION BEHAVIOR OF REACTOR MATERIALS IN FLUORIDE SALT MIXTURES, United States, 1962.

[44] I.V. Kireeva, Y.I. Chumlyakov, Effect of nitrogen and stacking-fault energy on twinning in [$$\bar 1$$11] single crystals of austenitic stainless steels, The Physics of Metals and Metallography 108(3) (2009) 298-309.

[45] G.S. Was, Fundamentals of Radiation Materials Science: Metals and Alloys, Fundamentals of Radiation Materials Science: Metals and Alloys (2007) 1-827.

[46] G. Zheng, K. Sridharan, Corrosion of Structural Alloys in High-Temperature Molten Fluoride Salts for Applications in Molten Salt Reactors, JOM 70(8) (2018) 1535-1541.

CHAPTER III

EVALUATION OF IRRADIATION-STRESS RESPONSE OF 316L THROUGH COMBINATION OF ION IRRADIATION AND THREE-POINT BENDING TECHNIQUE

Introduction

Advanced nuclear fission and fusion reactors are being developed to fortify global energy supply with clean, reliable baseload power. The development of these reactors requires diverse alloys for a wide array of different components and system conditions. Safety considerations necessitate a thorough understanding of the durability of these alloys, which must be able to withstand extensive neutron radiation damage under high temperatures and stress fields [1]. Data over the effects of mechanical stress on the void size and swelling response of alloys is mostly non-existent. One notable exception is a limited number of stress studies on neutron and ion-irradiated austenitic steels for use in fission reactor environments, which ultimately concluded void swelling increases with stress [2-7]. The ability to evaluate the effect of stress on the radiation tolerance of advanced fission and fusion reactor materials in an efficient and economical manner thus proves imperative.

The scarcity of fast-fission test reactors has led to widespread implementation of ion accelerators to simulate neutron radiation damage. Charged particle irradiations are a cost-effective surrogate for neutron damage experiments, able to impart significant radiation damage in a fraction of the time [8]. With careful design and methodical

evaluation, these studies can replicate and predict neutron irradiation damage behavior under a wide array of conditions [9-11]. The flexibility and control offered by ion accelerator systems enables combining radiation damage with unique target sample configurations to evaluate complex multi-physics problems at cost-effective laboratory scale.

Small-specimen testing techniques (SSTT) are continuously refined with the aim towards, among other goals, reduction of testing size. Such efforts serve to minimize the cost and exclusivity of testing facilities, reduce the amount of valuable materials consumed, and enable direct evaluation of microstructural systems with high sensitivity to short-range property behavior [12]. Traditional SSTT techniques are standardized for the accurate and repeatable extraction of mechanical property data from a narrowly defined group of materials under specific preparation conditions [13]. The properties which can be extracted are limited to overall macroscopic behavior and not intended to capture localized mechanical response. Finite element analysis (FEA) in contrast is well-suited for mechanical members with complex boundaries and geometries and is capable of fine spatial resolution. FEA thus can make use of established SSTT testing techniques, maximizing the acquisition of useful data without rigorous adherence to dimensional and procedural standards.

The present study demonstrates a method for evaluating the microstructural response of a test material exposed to simultaneous irradiation and mechanical stress at elevated temperatures. Heavy ion implantation is combined with the three-point bending technique to characterize the effects of changing stress on void swelling using a single

sample of AISI SS316L. An FEA model constructed using the commercial software ABAQUS is used to map the stress distribution of the sample after deflection. A separate FEA model was produced using the Solidworks software to assess possible temperature gradients resulting from the complex geometry of the irradiation setup. Transmission electron microscopy (TEM) was performed for lamellae extracted from seven sites on the cross-section face of the bender sample. The sites were chosen to be regularly spaced across the stress gradient of the sample under stress, capturing a steady transition between extremes of compressive and tensile stress. Additional nanoindentation was performed to quantify the effect of the loading stress on the irradiation hardness response. Finally, point-defect kinetics equation (PDKE) modeling was performed to contextualize the results observed and provide explanation for the divergence in behavior between compressive and tensile stress regions.

Experiment Procedure

The A sample of AISI 316L was cut into a 20mm long bar, 1.4mm thick and roughly 5mm wide. The cross-section face was mechanically polished down to P4000 grit silicon-carbide and then subsequently electrochemically polished with 5% perchloric acid solution using a Tenupol-5 Twin Jet Electropolisher. The final width of the sample after polishing down the cross section was 4mm.

A three-point bender apparatus was used to pre-load the sample with static stress prior to irradiation. The apparatus was fabricated from stainless steel to the specifications detailed in Figure 15. The stress applied to the sample was adjusted by turning the 8-32 thread tensioning screw at the base of the apparatus. The tensioning screw pushes against a carriage tightly slotted into the center channel of the base of the device, forcing the pin at the top of the carriage to push into the center of the sample. The sample was deflected to a distance proportional to a desired stress by controlling the degree of

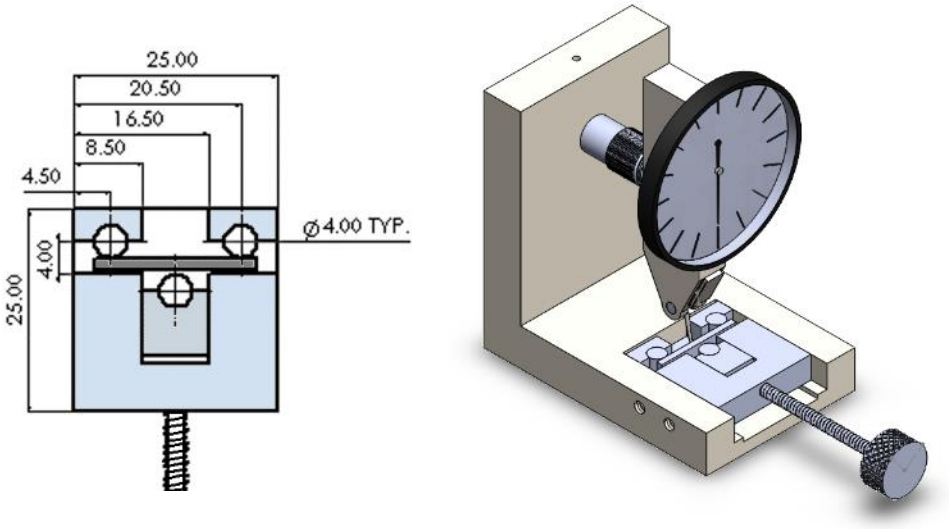

Figure 15. a) Drawing and dimensions of the three-point bender device assembly showing dimensions and loaded sample. b) Setup for measuring the sample deflection using a test dial indicator.

rotation applied to the screw. The thread count of the screw was used to calculate the displacement applied per full screw turn. A Mitutoyo model 513-403 horizontal dial test indicator was used to simultaneously monitor the displacement during tension

application to account for errors caused by tolerances in the device. The final displacement measured by the test dial indicator was used as the input deflection for the FEA model created in ABAQUS. The configuration of the three-point bender assembly and the test dial indicator used to measure the sample deflection is illustrated in Figure 15.

The displacement needed to induce the desired stress in the sample was determined using a finite element model in the software Abaqus/CAE version 12.0.0.1. The exact dimensions of the sample were input into the model, as well as the spacing and dimensions of three posts in the three-point bender apparatus. The elastic and plastic deformation properties for 316L were input into the model from tensile stress-strain test results obtained by Idaho National Laboratory on common variations of 300 stainless steels [14]. The region of maximum normal stress for materials under three-point bending conditions is located along the centerline of the sample which divides the longest dimension, as shown in Figure 16. 0.035mm hexahedra elements were chosen for the mesh size immediately around the center axis aligned with the stress-applying pin. This size subdivides the thickness of the bender sample into 40 cells for high space resolution and ease of data interpretation, as well as to minimize average effects between elements. Second order quadratic elements with reduced integration (C3D20R) were used per the recommendations in the Abaqus documentation [15]. This was done to avoid the phenomenon of sheer locking, which can be problematic for modeling systems with high anisotropic distortion such as bending.

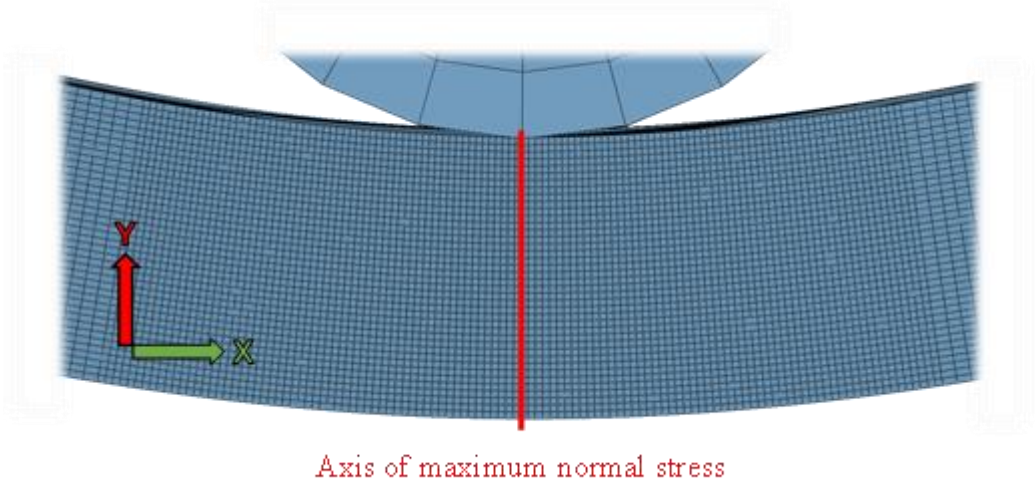

Figure 16. Diagram showing model mesh and location of maximum normal stress aligned with the bending pin after deflection of the sample with a deformation factor of 114.2 applied for emphasis.

The results of the analysis were loosely validated by comparing the predicted principle stress against the maximum principle stress of a beam under three-point bending derived from beam theory. The maximum stress at midspan in the elastic strain domain and when deflections are less than 10% of the thickness of the member is given Eq. 1 [16]. The model was deemed sufficiently accurate when the difference between the two predictions were less than 5%. Mises stresses are thereafter used as the primary stress metric in the system. ASTM E855-08, “Standard Test Methods for Bend Testing of Metallic Flat Materials for Spring Applications Involving Static Loading” details specimen dimensions for standardized three-point bending testing [17]. The dimension specifications of the standard, specifically the length-to-thickness ratio, were ignored to

$$\sigma = \frac{6Ety}{H^2} \qquad \textbf{Equation 1}$$

Where:

σ = maximum tensile stress

E = modulus of elasticity

t = thickness of the specimen

y = maximum deflection

H = distance between outer supports

increase the usable surface area on the irradiated face for data collection. Comparing the expected maximum stress predicted by the ASTM standard against the FEA simulation thus provides only an approximate validation of the realism of the model results. The model however provides a quantitative spatial stress distribution with sensitivity to local deformities, offsetting the tradeoff for direct comparability with standardized data. The center displacement pin was fabricated with a stainless-steel clip. This clip was oriented across the sample to hold down a 100-mesh copper TEM grid, with a hole width of 204 μm, against the polished surface of the sample. This was done to develop a clear grid of irradiated and unirradiated regions and thus facilitating post-irradiation analysis via electron microscopy. After applying the appropriate displacement to induce the desired stress into the 316L sample, the three-point bender holder was mounted onto a copper irradiation hot stage for ion irradiation. A K-type thermocouple was clipped to the front facing surface of the sample as close to the beam spot as possible to reduce the thermal gradient. The setup of the sample, the three-point bender holder, and the irradiation

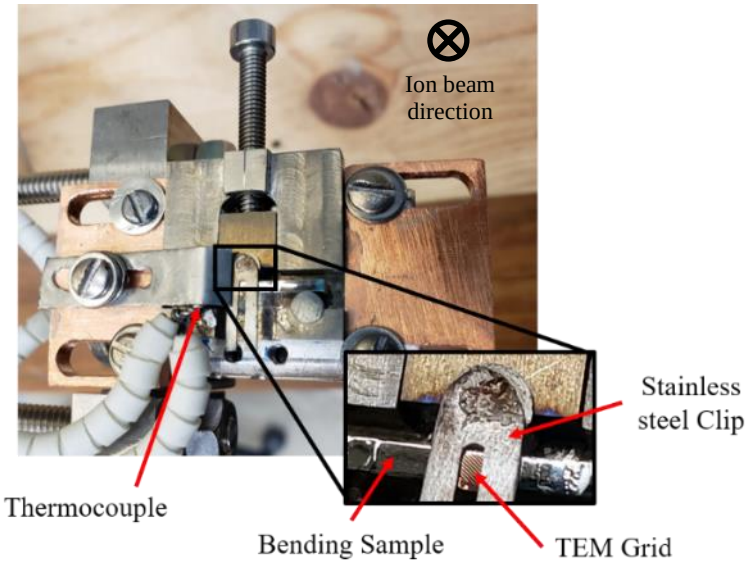

Figure 17. The final layout of the three-point bender mounted sample prior to irradiation.

hot-stage are shown in possible to reduce the thermal gradient. The setup of the sample, the three-point bender holder, and the irradiation

Figure 17.

The 316L sample was irradiated with 3.5 MeV Fe^{2}+ ions using a National Electrostatics Corporation 1.7 MV ion accelerator. The unrastered [18] and defocused beam spot of Fe^{2}+ ions was approximately 4 mm x 4 mm. The beam passed through multiple magnetic deflectors along the beamline to reduce carbon contamination and enable applicability for predicting neutron irradiation response [19]. Liquid nitrogen was used along the beam line and in the chamber to maintain high vacuum. The sample was irradiated at 475± 3 °C to an ion fluence equivalent to 100 peak DPA. This temperature is notably below the peak swelling temperature of the alloy [20] and was chosen to

coincide with the range of peak swelling temperatures documented for F-M alloys for use as comparison with future studies [21]. The temperature choice additionally minimizes the need for consideration of pure thermal creep in the bulk of the sample [22] as well as the diminished yield stress of AISI 316L at high temperatures [23-25]. The fluence/DPA ratio and the distribution of ions and damage penetrating into the sample surface was simulated using the Stopping and Range of Ions in Matter (SRIM-2013) in the Kinchin-Pease mode [26]. The displacement energy values used for the constituents of AISI 316L in SRIM were taken from the American Society of Testing and Measurements (ASTM) recommended values for radiation damage simulation [27]. The damage and ion distribution predicted by SRIM and produced using 100K particles is shown below in Figure 18. The predicted model resulted in an estimated peak ion depth of 1.12 μm from the surface and a peak damage at 0.95 μm.

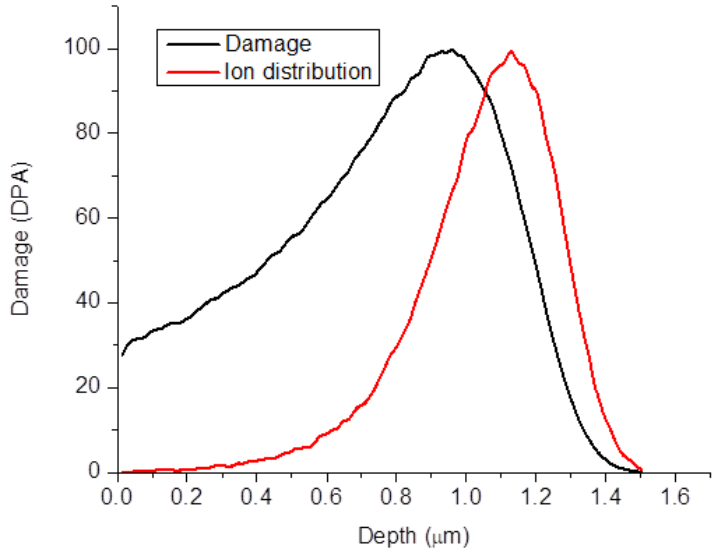

Figure 18. Damage and ion distribution 3.5MeV ions into AISI 316L sample as simulated by SRIM.

An FEA model was produced in Solidworks in order to identify possible thermal gradients in the SS316L three-point bender (3PB) sample when mounted to the irradiation stage [28]. The model comprised of a simplified representation of the irradiation hot stage as well as the three-point bender and 316L sample mounted therein. Of primary concern is a possible thermal gradient caused by the contact with the deflection pin on the compressive side of the sample, leading to a heat source effect not experienced by the tensile side. Materials properties documented in Solidworks library were used for the AISI316L sample, bender device and fastening screws, and the copper mounting clamps. Thermal properties for the hot stage composed of Inconel 625 were sourced from a datasheet provided by Special Metals Corp [29].

The irradiation hot stage is heated via a 550W cartridge heater inserted from the top into a cylindrical opening in the stage base. The power input of the heater can be varied using a 120V variable transformer. The thermal FEA model was evaluated by modeling the cartridge heater component as a uniformly distributed power source and varying the input power until the desired sample surface temperature was reached. Thermal resistances from imperfect surface contacts ignored as the surfaces of the stage and the sample in the three-point bender mount were tightly fixed together. The vacuum chamber surrounding the hot stage was assumed to limit heat loss from the hot stage to radiative loss. The full stage assembly including the sample was assumed to have a uniform heat emissivity of 0.7, approximately average for the model assembly composed primarily of nickel alloy and stainless steel [30]. The mesh for the model was generated

using Solidworks' automatic adaptive mesh protocol. The mesh comprised of trigonal elements ranging 0.315 mm to 3.11 mm based on the dimensions of different features of the assembly.

After the irradiation, scanning electron microscopy (SEM) was performed on the sample surface to confirm the coincidence of the beam spot with the stress region of interest. Figure 19 shows bright field SEM images taken for the sample before and after the clip was removed. A clear imprint is visible where the ion beam impacted the sample surface or was masked by the TEM grid and mounting hardware. TEM specimens were prepared using the focused ion beam (FIB) lift-out technique for several positions along the stress field. Each specimen was characterized to produce a correlation between void swelling and stress state. The Tescan Lyra-3 Focused Ion Beam was used for lamella preparation to create specimens with sizes approximate to 10 μm x 8 μm. The specimens were then further thinned to approximately 120 nm using a 5 keV Ga beam. The FEI Technai F20 was used for void imaging, producing cross-sectional bright field

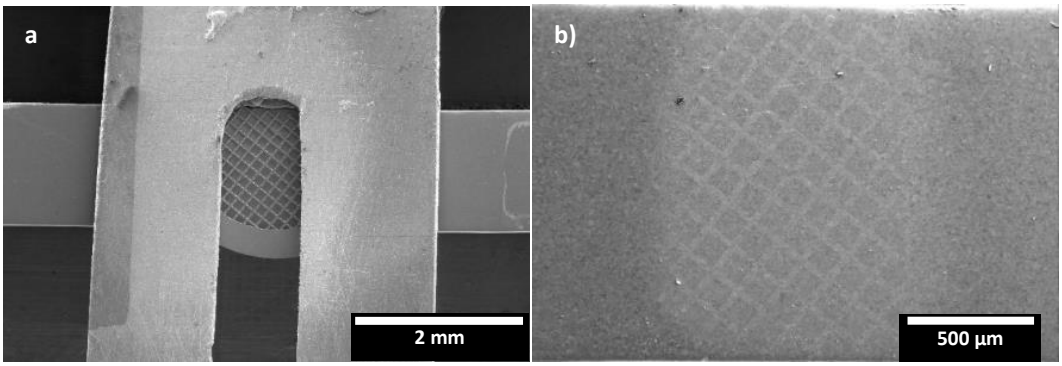

Figure 19. a) Bright field SEM of the stressed sample after irradiation with the TEM grid and clip still in place. b) the patterned imprint left by the ion beam caused by the obstructing TEM grid and stainless-steel clip.

micrographs of the various stress regions. Electron Energy Loss Spectroscopy (EELS) was performed on the FEI Technai G2 F20 Super-Twin to calculate the thicknesses of the TEM specimens.

After performing lift-out of the TEM lamella, nanoindentation was carried out to quantify the effect of simultaneous stress-irradiation on the hardness of the material. The technique has been previously demonstrated as capable of capturing mechanical property evolution resulting from microstructural changes induced by ion irradiation damage [31, 32]. The depth of the indentations was limited to 300nm using a Berkovich tip to roughly coincide with the depth of maximum void swelling observed under TEM. The indentation size effect cannot be ignored at these limited depths and will tend towards artificially increasing the measured hardness [33]. Additional indentations were thus performed on an unirradiated control sample cut and prepared identically to the irradiated sample for use as comparison, as well as at additional sites on the irradiated sample outside of the beam spot.

Finally, a computer model utilizing the PDKE procedure described by Golubov, Barashev, Stoller [34] was executed. The PDKE scheme was recently validated by Short et. Al. against experimental data for Fe ion implantation [35] and successfully replicated key features of the ion implantation void swelling profile. The model was reproduced for the present experiment and follows the procedure and input parameters described there. The calculations were used to qualitatively illustrate the influence of surface sinking and injected interstitial artifacts on the results of the present experiment. Sensitivity analysis was performed to assess the possible influence of the vacancy migration energy under

different stress conditions on the void nucleation distribution observed in the present data. The results of the PDKE modeling were contextualized with reviewed literature.

Results and discussion

Figure 20 shows a contour mesh plot of the resulting Mises stress distribution predicted by the ABAQUS model. Each element of the mesh is represented by an averaged stress value and reflects the influence of the 20 nodes at the corners and edges of the element. At the side closest to the pin, the sample experiences the highest amount of compressive stress. At the opposite side of the sample, the tensile stress is maximized. At the midpoint down the length of the centerline, the stress is at a local minimum and represents an inflection point between the tensile and compressive stress. The tensioning pin in contact with the compressive side of the sample is under a significantly lower stress than the bending sample. For this reason, it is assumed that the deformation of the pin is negligible.

The mesh of the pin was thus generated to be relatively coarse to save on computation time when solving the stress distribution of the model. Figure 21 shows the distribution of Mises stress down the face of the sample extracted from the contour plot. A geometric convention was applied to simplify interpretation of this plot and others proceeding it. The compressive stress is displayed as having a negative magnitude, as well as occurring at a negative position relative to the middle latitudinal axis of the sample. The stress distribution shows that for a displacement value of 0.0175mm, the peak Mises and principal stress experienced in any single node is 167.4MPa and

113MPa, respectively. Equation (1) predicts a maximum principal stress of 117.7 MPa, which represents a 3.99% difference from the stress predicted by the FEA model.

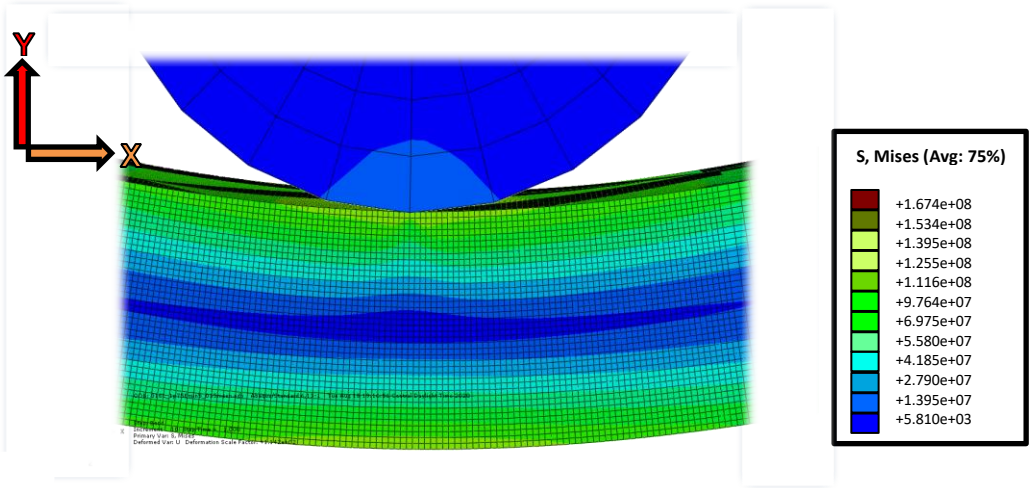

Figure 20. Colored contour plot shows stress distribution in 316L sample after three-point bender deflection. A deformation factor of 114.2 is applied for emphasis.

Nearly the entire sample is in an elastic strain state, the exception being the maximum compression region closest to the tensioning pin. Here, some highly localized plastic deformation is predicted at the contact point. This occurrence is partially due to the coarse mesh used for the tensioning pin, which contacts the sample with a wedge-shaped point rather than a rounded surface. This elastic strain condition is important to maintain to avoid the complexity of interpreting irradiation response under the influence of significant and heterogeneous dislocation density in the sample. To simplify the analysis, TEM lamellae were extracted along a vertical axis 245μm to the left of the deflection point. Here, the localized plastic deformation surrounding the pin contact

region is avoided without significantly affecting the overall magnitude of the stress gradient. A comparison of the centerline stress trend versus the 245µm stress trend is shown in Figure 21.

The TEM grid imprint along the stress profile, shown in Figure 22, was used as guide for selecting locations for TEM lamellas. The solid red vertical line represents the offset axis shifted 245 µm left of the deflection pin contact. The white X marks in the figure show the locations selected for TEM lamellae extraction and reflects a best attempt at distributing the sites evenly about the zero-stress x-axis. The fourth TEM lamella close to the center of the sample was selected slightly away from the 245µm y-

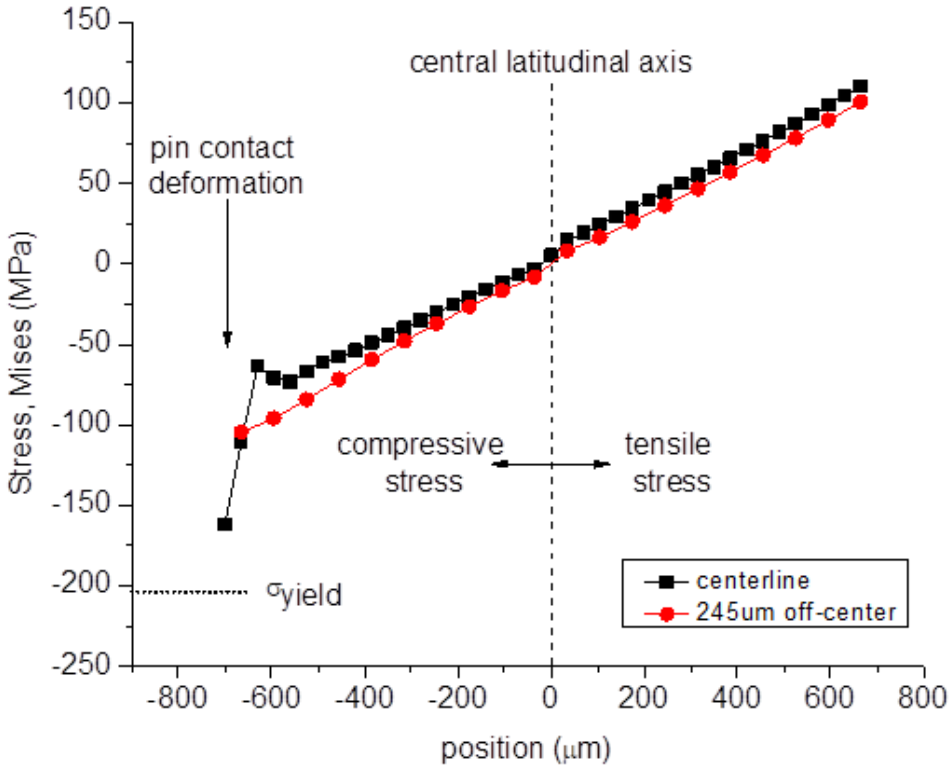

Figure 21. Plot of Mises stress down the center axis of from the pin (negative position) to the outer deflected surface (positive position).

axis due to spatial constraint of the grid imprint, as directly along the 245μm location resided in an unirradiated region masked by the TEM grid. Distances from the center were found and the stress at these locations were calculated using the ABAQUS software for comparison to the swelling profile.

SEM imaging performed on the surface of the sample illustrates the difference between the irradiated grain structure and the unirradiated grain structure shielded by the TEM

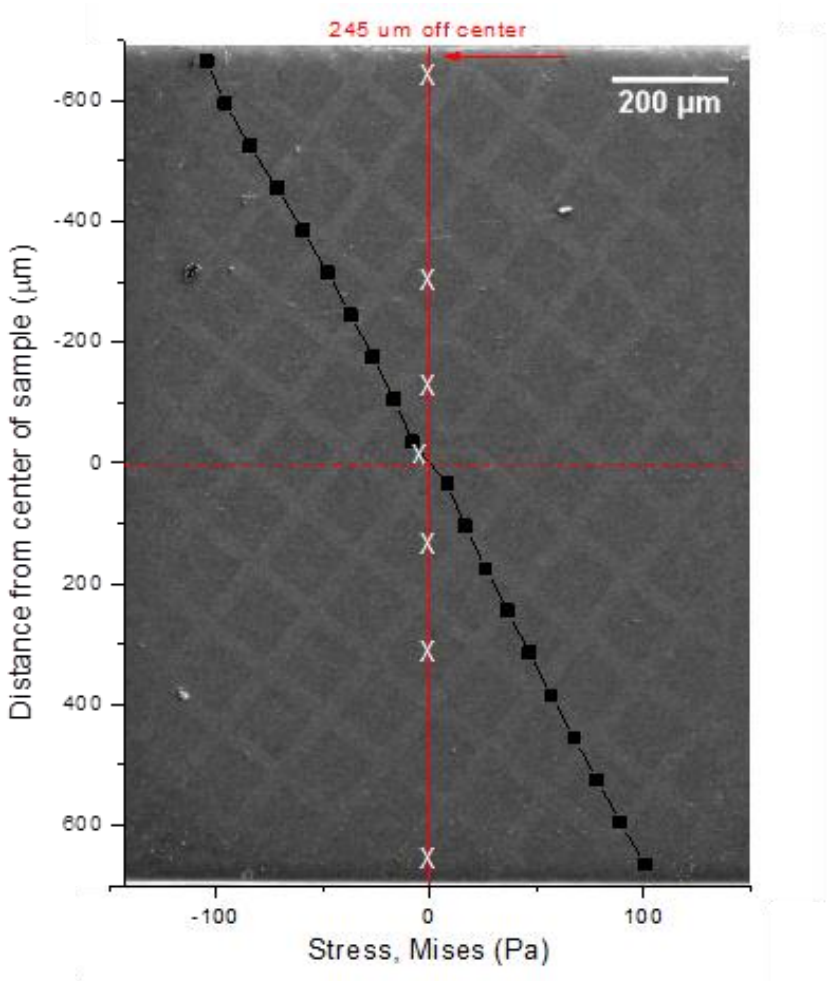

Figure 22. Stress across the surface of the sample, 245μm from the deflection point. X's represent the locations used for SEM imaging and TEM specimens.

grid. Figure 23 shows the structure of one of the squares created by the irradiation. Note the raised grain structure resulting from swelling in the sample, creating a clear delineation for useful analysis area. SEM images of the surface showed proof of voids in both the compressive and tensile regions, one of which is shown in Figure 24. Two noninvasive analysis methods were attempted to streamline the void swelling data acquisition and correlation with stress data. These techniques were carried out with the intention of calibrating the results against the reliable void swelling measurements collected via traditional TEM imaging, hopefully accelerating void data acquisition in

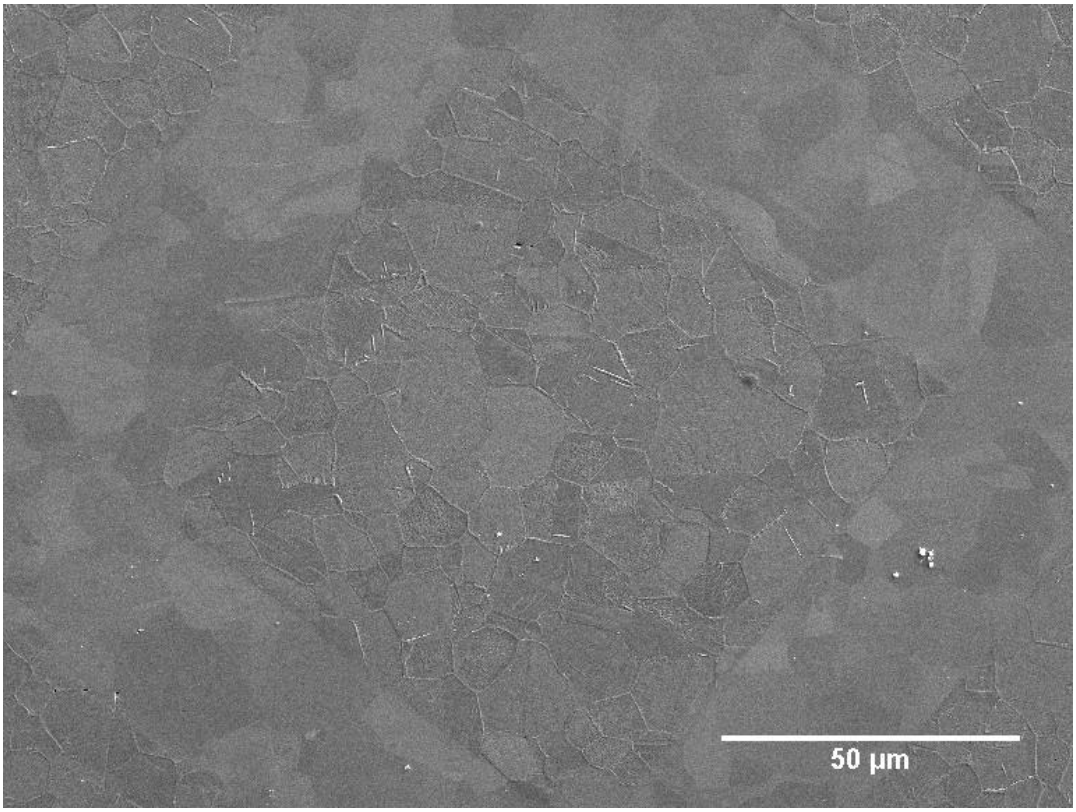

Figure 23. Irradiation of 316L resulted in raised grain structure in uncovered regions. Virgin grain structure represents regions covered by the TEM grid.

the future. The first consisted of calculating the swelling at the different sites using backscatter electron SEM surface imaging and a void-volume estimation model based on Monte Carlo simulation [36]. The second method followed an optical profilometry procedure described by Jin et. Al. using a Veeco Yko NT9100 3D optical profilometer [37].

The results of the noninvasive analysis did not accurately represent the swelling percentage of the sample. The backscatter electron SEM method was only able to account for voids on the surface, and not throughout the bulk of the ion irradiated depth. Similarly, surface irregularities and the subtle difference in heights between the irradiated and unirradiated regions confounded the profilometry results. The more

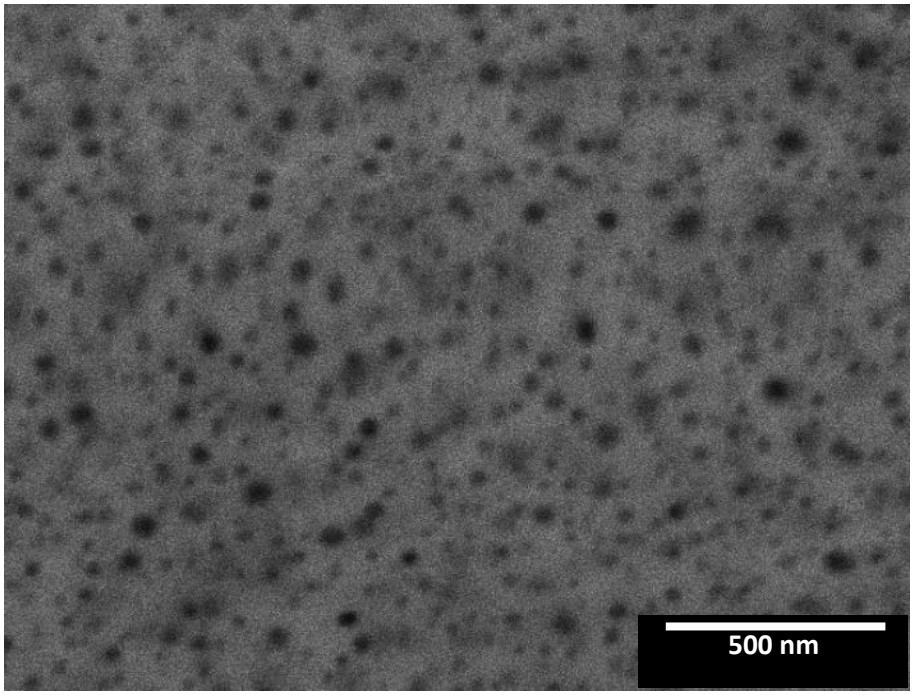

Figure 24. SEM image of the irradiated region of the 316L sample, showing pronounced subsurface voids and swelling.

traditional void measurement performed via FIB lift-out and TEM is thus relied upon as the sole measurement for swelling. Lamellas created using the FIB lift-out method at the locations represented in Figure 22 produced TEM micrographs of the cross-section ion irradiated depth. Figure 25 highlights the swelling behavior revealed via TEM at the extremes of the stress distribution. All three regions exhibit distinct characteristics which will be further highlighted in the statistical distribution of the voids described later. The compressive regions exhibited the largest volume of voids and the tensile region, the smallest. The region in the middle, with the minimum stress, lacked voids with small diameters – decreasing the void density. In contrast to the large and sparsely distributed voids of the neutral stress region, the regions under compressive and tensile stress host more small voids. Additionally, there is a clear shift in the density of the void volume towards the surface in the tensile stress region, whereas the void

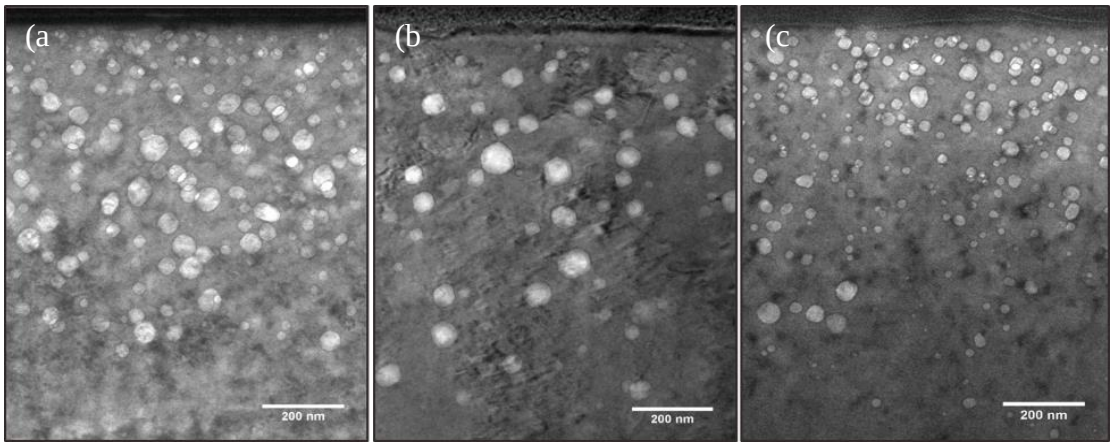

Figure 25. TEM micrographs of the regions with (a) the highest compressive stress, (b) the least approximate stress and (c) the highest tensile stress.

distribution exhibits the opposite behavior in the compressive region. The neutral stress region in the center region roughly exhibits a transition between these two behaviors, with the largest and most dense void distribution occurring in the center of the damage range.

Assessment of the overall void swelling in the seven evaluated regions revealed a decrease in swelling from the compressive to the tensile stress region, with a slight peak for the local minimum stress. Figure 27.a shows the total void swelling profile and the stress as a function of position across the analysis surface of the sample. Figure 27.b shows plots the swelling trend directly against the affecting stress at each position where

Figure 26.a and Assessment of the overall void swelling in the seven evaluated regions revealed a decrease in swelling from the compressive to the tensile stress region, with a slight peak for the local minimum stress. Figure 27.a shows the total void swelling profile and the stress as a function of position across the analysis surface of the sample. Figure 27.b shows plots the swelling trend directly against the affecting stress at each position where

Figure 26.b respectively show the change in the void diameter and void density versus position based versus the location of lamella extraction. The location of each lamella was correlated to the distance from the center of the sample, where the stress minimum occurs. Analysis of the voids following irradiation produced a data set for the average void diameter, density and swelling. The average void diameter decreased gradually from the compressive region to the tensile, with an abrupt peak in diameter near the minimum stress correlating to a sudden increase in size of the voids. Swelling in

all regions produced drastically different sizes of voids, resulting a large error for the average diameter over the ion irradiated depth. The average density of the voids roughly increased from the compressive region to the tensile, with the minimum density in the middle of the sample with approximately zero stress. Both the compressive and tensile regions produced a similar number of voids; however, the tensile region produced voids with smaller diameters resulting in an increased density. The minimum stress region has large voids and lacked many with small diameters, resulting in the lowest average void density.

Assessment of the overall void swelling in the seven evaluated regions revealed a decrease in swelling from the compressive to the tensile stress region, with a slight peak for the local minimum stress. Figure 27.a shows the total void swelling profile and the

stress as a function of position across the analysis surface of the sample. Figure 27.b shows plots the swelling trend directly against the affecting stress at each position where

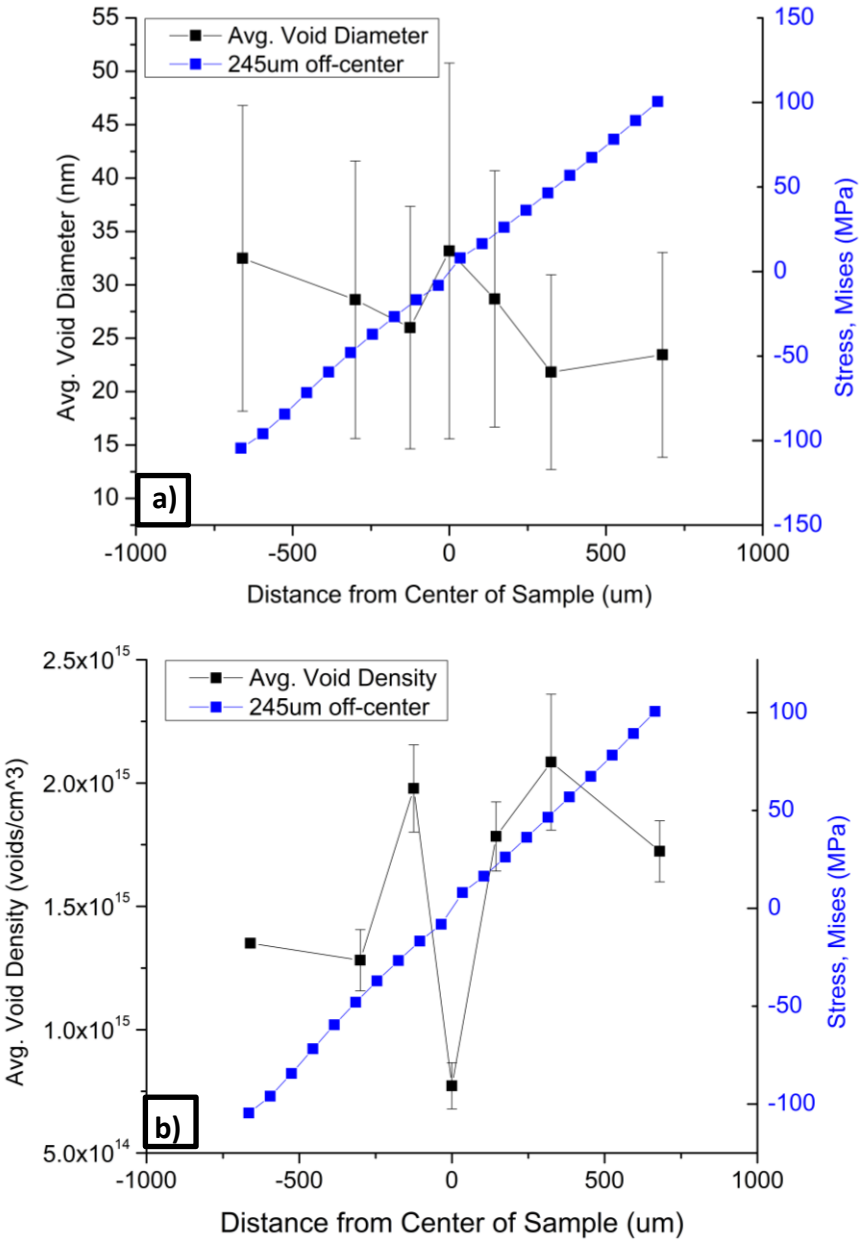

Figure 26. The stress profile vs. position is plotted alongside a) the average diameter of voids and b) the average void density.

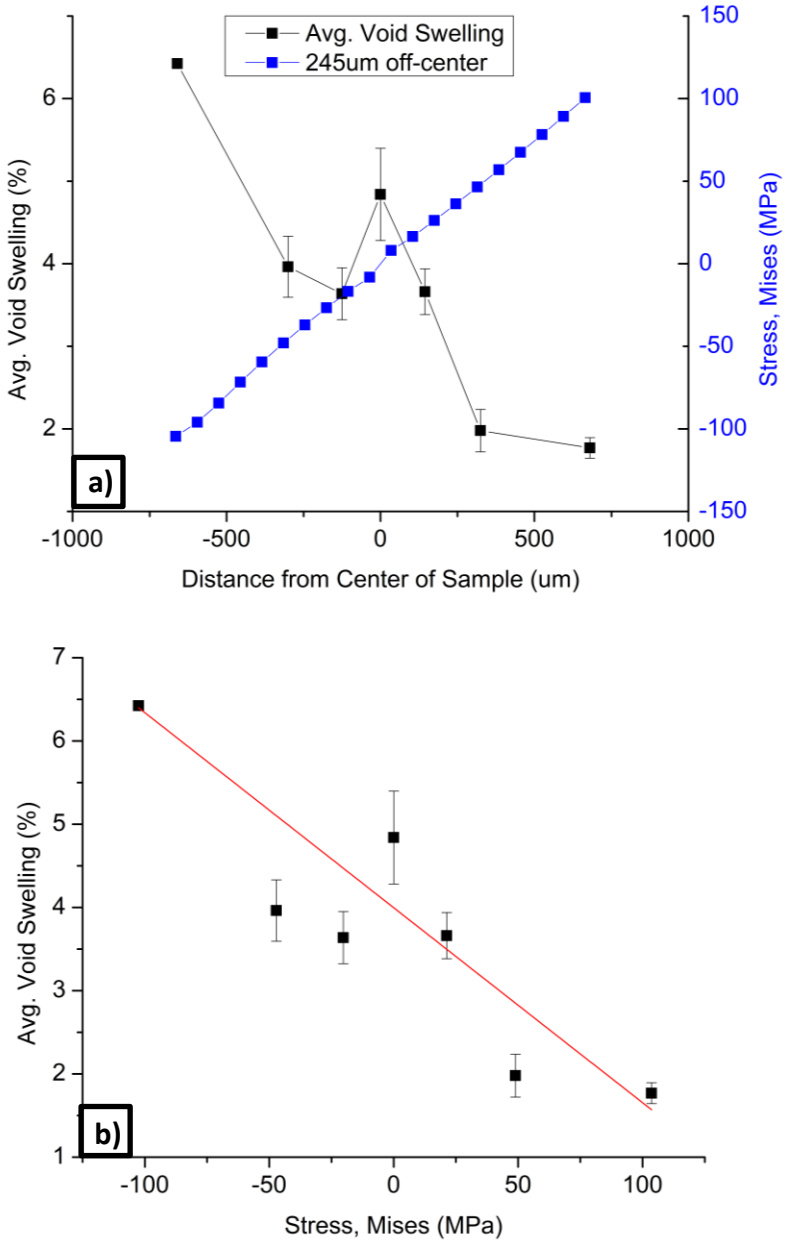

Figure 27. a) Average void swelling decreases from the compressive to the tensile region, with a slight peak for the local minimum stress. b) Average void swelling in the sample in direct correlation to the stress state.

a red linear trend line is applied to illustrate the overall behavior of the swelling data. Taken at face value, the trend shows that swelling increased under compressive stress and decreased under tensile stress in the bender sample. These results contradict a wide body of existing literature which show that the increase in void swelling should be symmetrical in both compressive and tensile states. Therefore, other factors in this experiment affected the swelling rate in the tensile region and prevented adequate swelling to match that of the compression region. The proceeding discussion explores other factors in this experiment which affected the swelling rate in the tensile region and prevented adequate swelling to match that of the compression region.

In contrast to the data presented here, the sign of stress direction has no significant difference on void diameter, density, and volume [2]. Stress is indeed important in the onset and rate of void growth [38], but such sensitivities should be restricted to the swelling incubation period and should have little effect when the total swelling is as high as in the present experiment. Swelling is increased by the application of stress but is independent of the tensile or compressive regime [3]. Sahu and Jung [2] and Lauritzen et. Al. [3] first showed that in ion and neutron irradiation studies, respectively, mechanical stress in the elastic regime serves to shorten the void swelling incubation period. The symmetry of the swelling response under compressive and tensile stress states pointed to the importance of the deviatoric stress component in the shortening of the swelling incubation period [39].

It is theorized that shear stress in FCC systems enables the unfaulting of sessile interstitial Frank loops, which once glissile can expand to form the interstitial-biased

defect sink network throughout the lattice [40, 41]. Recent molecular dynamics studies strongly support this theory with increasing confidence, demonstrating the role of shear stress in Frank loop unfaulting for binary and ternary FCC alloys [42-44]. The compositions of these alloys were tweaked to have stacking fault energies and interatomic potentials close to those of austenitic stainless steels. Further improvements to interatomic potential calculation models and computational power are still needed to model these phenomena directly in austenitic steel mixtures. The contribution of the normal stress component to the unfaulting process however cannot be fully disregarded, as Hall's most recent improvement to the continuum plasticity model suggests a contribution from both hydrostatic and deviatoric stress components to stress-affected swelling [45]. The model was shown to excellently fit newly produced stress-assisted swelling data from samples under a wide range of conditions and stress states [46], including preconditioned samples with irradiation history, stress history, both, or neither.

Consideration was given to other experiment parameters which may explain the deviation from expected stress/swelling response exhibited here, such as temperature, cold work, and initial metallurgy conditions. As mentioned in the previous section, a thermal gradient somewhere in the sample or stage assembly hypothetically could have resulted in a distinct temperature in the tensile region. Specifically, the contact of the deflection pin located near the heat source, on the compressive side of the sample may have resulted in a higher temperature near the deflection point. Effects on tensile swelling can be visible but small at temperatures below 550 C [19]; however, in

comparison to the compressive stress effect in this data set, they appear to be inconsequential.

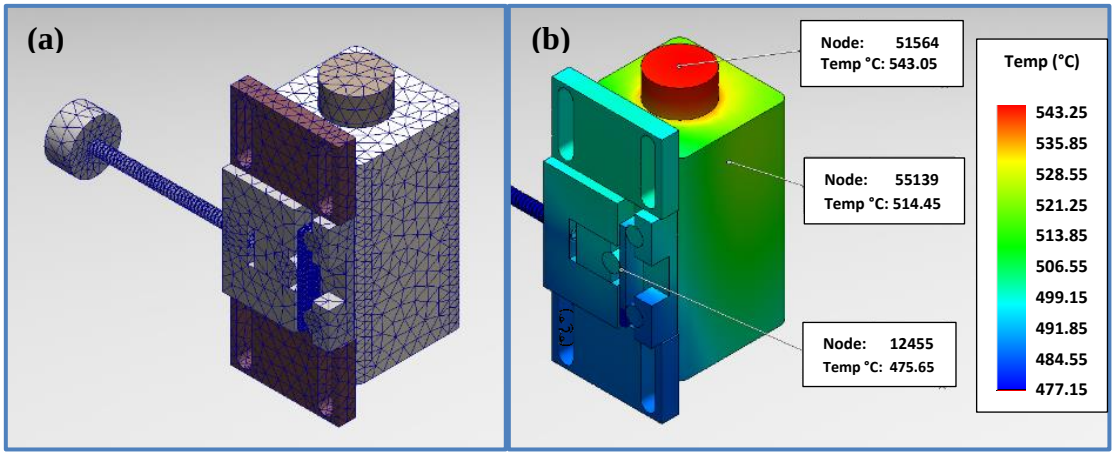

Figure 28. a) Mesh generated in Solidworks for thermal FEA model of irradiation hot stage. b) Colored contour plot showing the temperature distribution predicted by the FEA model.

Figure 28.a shows the final hot stage assembly model and the mesh generated for the thermal analysis. The results of the thermal analysis are shown in Figure 28.b. The final iteration of the model showed that an input power of 110W at the heater caused a surface temperature of 476°C, approximately the desired surface temperature of the sample. This power input was in good agreement with the power input which was needed to reach the desired surface temperature during the experiment. Closer inspection of the 316L sample section of the FEA model, illustrated in Figure 29, shows that no significant temperature gradient exists going from the left to right face of the sample. The tensioning pin, while slightly hotter than the sample, does not appear to transmit sufficient heat at its tangential contact with the sample to cause a noticeable temperature increase. A

significant gradient of approximately 10°C exists going from the top to bottom of the sample. This results from the cartridge heater channel not passing completely though the hot stage body and thus propagating less heat to the lower section of the stage.

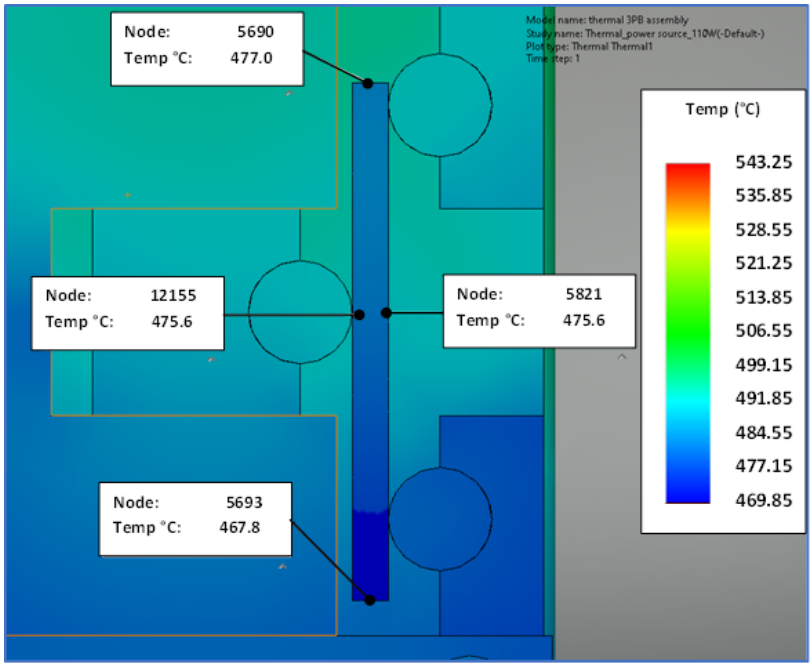

Figure 29. Predicted temperature distribution in the 316L three-point bender sample shows a uniform temperature distribution going across the sample from the compressive to tensile stress sides.

The results of the finite element analysis and its agreement with the thermocouple readings suggest that the sample remained below the diminished yield stress at 475°C, which is approximately 150 MPa [23-25]. The bulk of the sample (i.e., beyond the irradiation interaction region) is thus presumed to be under elastic stress

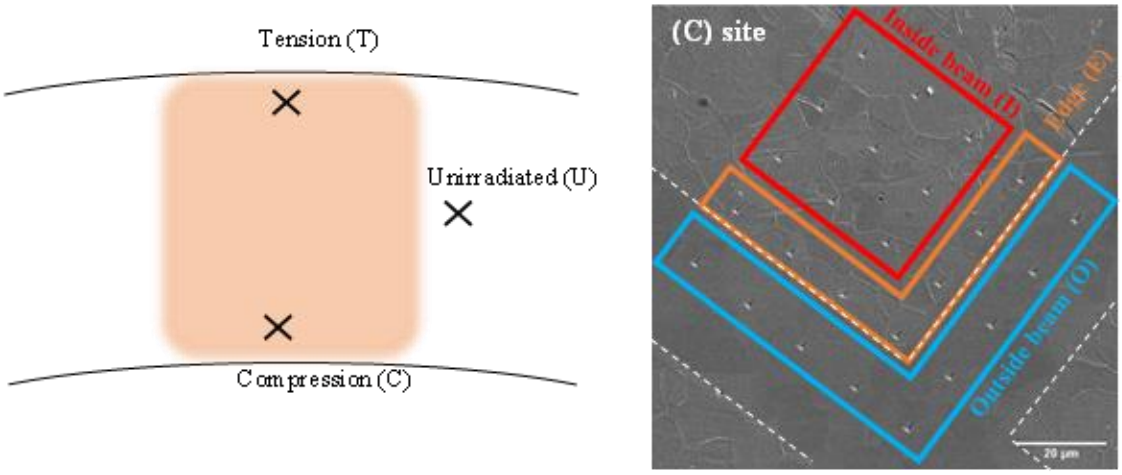

Figure 30. Map of nanoindentation sites on the irradiated sample and a diagram illustrating the subregion breakup of the tension (T) and compression (C) sites.

throughout the irradiation. Similarly, the creep relaxation in the bulk of the sample is presumed negligible [25, 47]. Irradiation creep must be considered in the target region of the ion beam however, as relaxation can be significant even at modest temperatures and radiation damage levels for 300 series stainless steels [39, 48, 49]. The departure from secondary irradiation creep at 475°C may occur at neutron damage levels as low as 20-25 dpa, though this cannot be directly compared to irradiation creep induced by heavy-ion bombardment [50]. Nanoindentation assists in qualifying the significance of the irradiation creep relaxation and contextualize the swelling response. This approach merits caution however as the results are complicated by irradiation hardening and void swelling effects.

Figure 30 illustrates the layout of nanoindentation sites on the irradiated sample. Four total sites were used in the indentation campaign, named irradiated tension (T),

irradiated compression (C), unirradiated-center (U), and control (not shown here). An SE-SEM image of the C site is also shown to illustrate the alignment of the indentation array relative to the slanted pattern left by the TEM grid. A 5x5 array of indentations was chosen for a total of 25 indentations. The beginning of the array was placed outside the boundary of the irradiated region to create additional subregions of the data at each region of the sample. Nine indentation sites are located outside of the irradiated region (O), seven sites at the edge of the irradiated region (E), and nine inside of the irradiated region (I). An identical indentation array was created on the T site. The control sample features a similar 25 indentation array but with no subregions given the uniformity of the sample. Five additional reference indentations were collected at the U site for comparison.

Figure 31 highlights the hardness results from the nanoindentation analysis. Six areas of interest are distinguished using the stress-state/region naming convention detailed in Figure 30: compression-outside beam (CO), compression-inside beam (CI), tension-outside beam (TO), tension-inside beam (TI), Control (C), and neutral stress-unirradiated (UN). Sites which fell into the edge (E) region were omitted from the analysis because they could not be clearly binned into either region straddling the boundary. The results show a distinct change in the hardness of the material in regions irradiated by the ion beam. Additionally, there appears to be a slight increase in hardness in the tension sites compared to the compression sites. The nanoindentation data does not refute the occurrence of advanced irradiation-creep but suggests other mechanisms at play in the microstructural evolution of the irradiated region. The tension region exhibits

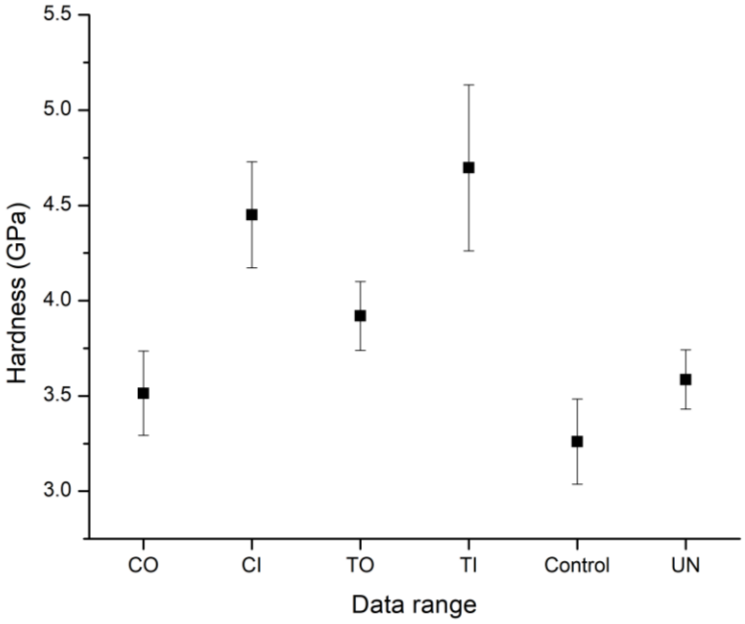

Figure 31. Comparison of hardness values from nanoindentation analysis performed at different sites on the irradiated and control sample.

a more pronounced hardness change which is not easily attributed to straightforward radiation embrittlement.

Asymmetric Cottrell atmosphere saturation around edge dislocations in the sample may explain this occurrence. Solute point defects liberated by ion beam mixing are driven towards edge dislocation cores to relieve the hydrostatic stress around these defects. The solute atoms increase the energy threshold for inducing movement, either by rigidly pinning the dislocations in place or by being dragged along as they migrate [51].The presence of another stress field alters the driving force of atmosphere production. A compressive stress field may reduce the saturation population of Cottrell atmospheres by lowering the hydrostatic stress exhibited at the dislocation cores. This in

turn would cause fewer pinned edge dislocations and a lower apparent hardness in the compressive region. This argument may also explain the difference in hardness observed at the CO and TO sites which were not irradiated but experienced opposite stress states. The tension stress field could cause an increased aggregation of solute atoms at edge dislocations. These solute atoms and their resultant atmospheres would be trapped upon cooling the sample, pinning a greater number of edge dislocations, and artificially increasing the hardness of the TO region compared to the CO region. Another possible

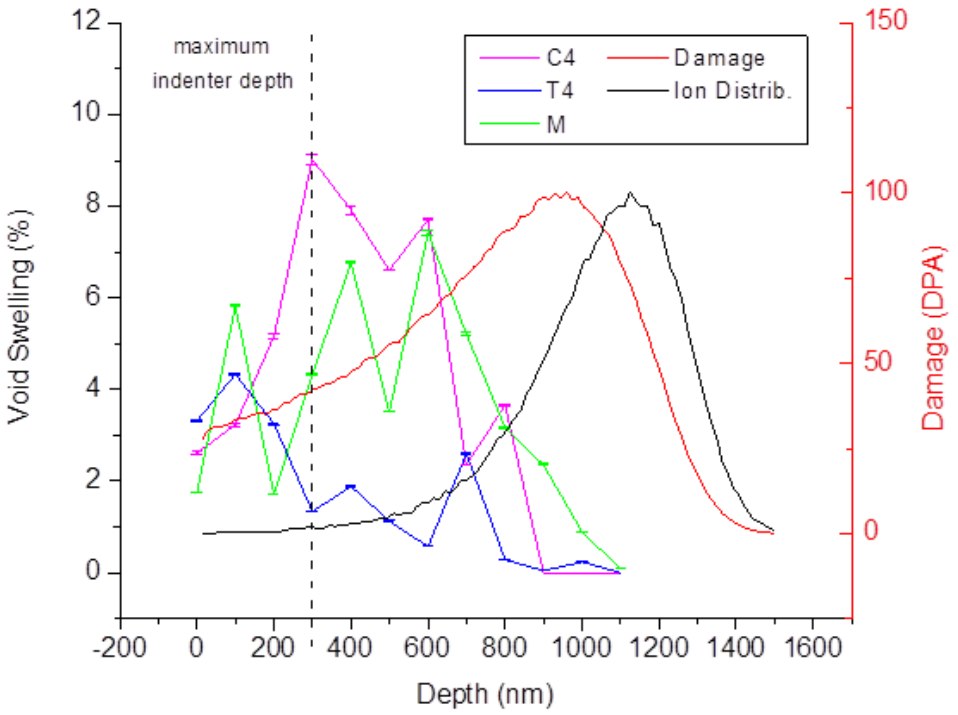

Figure 32. Comparison of typical nanoindentation depth at tension and compression sites versus void swelling profile and SRIM-predicted ion and damage distribution.

explanation for the discrepancy in hardness between the compressive and tensile regions is the irradiation “softening” effect observed for materials experiencing advanced levels of void swelling [39]. Neustrov. et. al. postulated that above a certain ratio of average void size to void-center distance, the material would experience an apparent mechanical softening due to heightened stress concentration and microcracks in the vicinity of voids [52]. These microscopic defects compound to a reduction in localized macroscopic strength and hardness. The effects would be more pronounced in the irradiated compressive region which exhibits higher void swelling than the tensile side (~2X greater). This explanation is furthered by the close coincidence of the nanoindenter penetration depth and the peak swelling profiles observed, illustrated in Figure 32. This is especially true in the compressive stress region (C4) where the peak swelling depth coincides with the maximum depth of indenter probe penetration. Irradiation softening however fails to explain the discrepancy between the hardness at the CO and TO sites. Softening effects would be highly localized around brittle void structure and are unlikely to propagate far outside the bounds of the irradiated region.

As highlighted in Figure 32, the void swelling distribution changes distinctly across the different stress extremes of the bender sample. the distribution of region M is the most erratic, oscillating significantly along the depth range evaluated. The C4 region of highest void swelling is the most uniformly distributed of the seven evaluated sites, with a centroid which is roughly centered midway along the length of the damage distribution. Region T4 exhibits the most distinctive behavior with a swelling distribution heavily weighted towards the surface of the sample. The observations here

require considering the role that surface sinking may be playing in the results, especially as it pertains to heavy ion irradiation studies where such effects are crucial. In general, The combined influence of the surface sinking effect [53, 54] and injected interstitial effect [55-58] result in a complicated void nucleation distribution which changes significantly depending on the point-defect mobility characteristics of a system.

Short et al. [35] evaluated the effect of several variables on void nucleation distribution in the ion implantation range using PDKE modeling described elsewhere [34]. The model and the ion irradiation experiment which served as the comparative basis for the results were based of the implantation of 3.5 MeV iron ions into a pure iron target [57]. While the results are for a relatively simple physical system compared to a single-phase alloy such as is discussed in the present paper, they demonstrate some important findings. The combined influence of the surface sinking effect and injected interstitial effect result in a complicated void nucleation distribution which changes significantly depending on the point-defect mobility characteristics of a system. Some of the variables evaluated which directly affect this mobility include temperature and dose rate and direct manipulation of vacancy activation energy, the latter of which showed those most profound impact on nucleation distribution [35]. Increase in the vacancy activation energy demonstrated a shift in void nucleation towards the ion incident surface which echoes the results demonstrated in the present study.

Fe and 316 have similarly low density of strong defect sinks, both systems being single phase solutions, and are thus comparably sensitive to small changes in vacancy migration energies. This similarity may explain the occurrence of the characteristic ion

irradiation double-peak phenomenon observed in both systems [58-60] and described by Short et. Al. [35]. For metallic systems in which impurities are present, it is also expected that the vacancy migration energy will increase because of solute binding. The sensitivity of vacancy migration energy to impurity concentration changes can vary greatly between monoatomic systems and complex alloys. Alpha Fe for example demonstrates sensitivity to even ppm levels of carbon contamination [61, 62] In contrast, AISI 316 shows relatively low sensitivity to alloying constituents [63]. Holzwarth et. Al. therefore reasoned that vacancy trapping by minor alloying elements are negligible in 316 [64], making them different to pure Fe systems in this regard. Moreover, the defect binding and migration characteristics of each system are different due to the BCC and FCC structures of Fe and austenitic steels, respectively. As previously stated, both pure Fe and 316SS systems have demonstrated the double-peak ion irradiation phenomenon. Despite structural differences in the two systems, it can be argued that using Fe as basic surrogate for 316SS is acceptable to illustrate qualitative behavior.

Connétable and Maugis [65] calculated several diffusion parameters for four FCC metals under the influence of different stress states. This was done using both density functional theory (DFT) and Elastic Continuum Theory (ECT) and through the VASP (Vienna *ab initio* simulation package) software. The results show that positive stress applied uniaxially (simulated along [001] and [111] individually) and biaxially (applied simultaneously to [100]+[010]) both result in a decrease in the formation and migration enthalpies in Al, Cu, Ni, and Pd [65]. For uniaxial stress, this results in a marked increase in the diffusivity of vacancies in the directions perpendicular to the

applied stress. These changes in enthalpy occurred alongside significant changes to the lattice parameter in each jump direction of the vacancies. The results of Connétable and Maugis are corroborated by Kang, who performed molecular dynamics simulations of BCC Fe lattices under stress using the Large-scale Atomic / Molecular Massively Parallel Simulator (LAMMPS) package. The results showed notable increase in vacancy diffusivity along axes perpendicular the applied tensile stress [66]. The opposite effect was also observed for compressive stress where vacancies tended to diffuse more

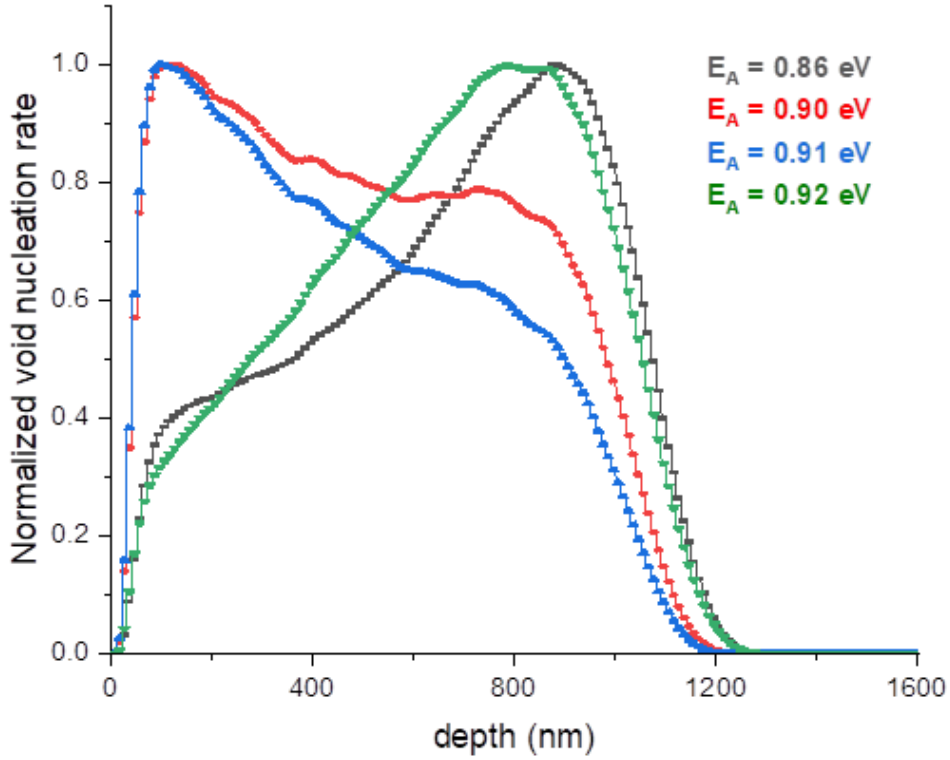

Figure 33. Results of point defects kinetics equations modeling showing change in the void nucleation distribution relative to the irradiated sample surface across different vacancy activation energies.

quickly along the axis of applied stress.

The PDKE scheme detailed by Short et. Al. [35] was replicated to illustrate the dramatic change in void nucleation which may occur under in Fe under ion irradiation and stress and by extension, changes in the void nucleation and migration enthalpies. Figure 33 shows the results of the computation, where the activation energies for point

d

e

f

e

c

t

m $$\boldsymbol{D_{v,i} = D_0 e^{\left(-\frac{E_{A_{(v,i)}}}{k_B T}\right)}}$$ **Equation 2**

i $$\boldsymbol{E_{total} = KE + PE + U = KE + PE + [H(S,p) - pV]}$$ **Equation 3**

g

Where:

r

D_o = diffusivity prefactor ($m^2 s^{-1}$)

a

E_A = activation energies for point defect migration (eV)

t

K_B = Boltzmann's constant ($eV K^{-1}$)

i

T = temperature (K)

o

KE = kinetic energy (eV)

n

(continued from previous page)

PE = potential energy (eV)

(

E

A

U = internal energy (eV)

(continued from previous page)

H(S,p) = enthalpy

p = specific pressure

V = volume

reflective of the powerful defect sinking of this interface. Notably, continually decreasing the activation energies results in the nucleation distribution again shifting deeper into the sample. While these results cannot be quantitatively applied to the present experiment, they illustrate the possible sensitivities of void nucleation and distribution to surface sinking and injected interstitial effects under the influence of stress. The above simulation results also mimic the change in void distribution observed in Figure 32. The misalignment of the results here with historical literature of uniform neutron irradiation data without directional dependencies thus can be attributed to experiment artifacts unique to heavy ion irradiation.

It is worth noting that such stress sensitivities were not observed by Sahu and Jung in their benchmark stress/ion irradiation study, where 316SS was irradiated using 6.2 MeV protons to a damage level of 0.4 dpa [2]. Protons at this energy will penetrate tens of micrometers into the sample and result in a much more uniform damage profile provided that void swelling measurement is not performed close to the sharp Bragg peak at the end of damage tail. Additionally, dose rates for proton irradiaiton are significantly lower than those of heavy ion irradiations [8]. With a larger void swelling sampling area

which is further from both the surface and injected interstitial regions, the double-peak nucleation distribution is likely suppressed [35] and the integrity of the results are preserved. The strong influence of surface sinking observed in the tensile stress region necessities isolating and evaluating the compressive stress data independently. The swelling behavior observed in the regions ranging from neutral stress to compressive stress were more typical of those observed in studies without applied stress. Reevaluating the swelling vs. stress distribution shown in Figure 27.b, the region exposed to the highest compressive stress shows a significant increase in swelling in agreement with literature. The lower compressive stress levels in contrast show an unclear influence, possibly not being of sufficiently high magnitude to significantly accelerate void nucleation.

References

[1] S.J. Zinkle, J.T. Busby, Structural materials for fission & fusion energy, Materials Today 12(11) (2009) 12-19.

[2] H.K. Sahu, P. Jung, Void swelling and irradiation creep in stainless steel under compressive and tensile stress, Journal of Nuclear Materials 136(2) (1985) 154-158.

[3] T. Lauritzen, S. Vaidyanathan, W.L. Bell, W.J.S. Yang, Irradiation-Induced Swelling in AISI 316 Steel: Effect of Tensile and Compressive Stresses, ASTM STP-955: Radiation-Induced Changes in Microstructure: 13th International Symposium (Part I), ASTM International, West Conshohocken, PA, 1987, pp. 101-113.

[4] J.F. Bates, E.R. Gilbert, Experimental evidence for stress enhanced swelling, Journal of Nuclear Materials 59(2) (1976) 95-102.

[5] J.F. Bates, E.R. Gilbert, Effects of stress on swelling in 316 stainless steel, Journal of Nuclear Materials 71(2) (1978) 286-291.

[6] J.E. Harbottle, VOLUMETRIC CREEP IN NICKEL: THE INFLUENCE OF STRESS ON SWELLING, in: M.R. Cundy, P. Von Der Hardt, R.H. Loelgen (Eds.), Measurement of Irradiation-enhanced Creep in Nuclear Materials, Elsevier1977, pp. 258-265.

[7] E.R. Gilbert, F.A. Garner, The influence of cold-work level on the irradiation creep and swelling of AISI 316 stainless steel irradiated as pressurized tubes in the EBR-II fast reactor, Journal of Nuclear Materials 367-370 (2007) 954-959.

[8] G.S. Was, Fundamentals of Radiation Materials Science: Metals and Alloys, Fundamentals of Radiation Materials Science: Metals and Alloys (2007) 1-827.

[9] L. Shao, J. Gigax, H. Kim, F. Garner, J. Wang, M. Toloczko, Carbon Contamination, Its Consequences and Its Mitigation in Ion-Simulation of Neutron-Induced Swelling of Structural Metals, 2018.

[10] G.S. Was, Challenges to the use of ion irradiation for emulating reactor irradiation, Journal of Materials Research 30(9) (2015) 1158-1182.

[11] J.C. Haley, S. de Moraes Shubeita, P. Wady, A.J. London, G.R. Odette, S. Lozano-Perez, S.G. Roberts, Microstructural examination of neutron, proton and self-ion irradiation damage in a model Fe9Cr alloy, Journal of Nuclear Materials 533 (2020) 152130.

[12] V.T. Srikar, S.M. Spearing, A critical review of microscale mechanical testing methods used in the design of microelectromechanical systems, Experimental Mechanics 43(3) (2003) 238-247.

[13] A. International, Standard Test Methods and Definitions for Mechanical Testing of Steel Products, ASTM International, 2021.

[14] R.K. Blandford, D.K. Morton, S.D. Snow, T.E. Rahl, Tensile Stress-Strain Results for 304L and 316L Stainless-Steel Plate at Temperature, United States, 2007.

[15] Abaqus 6.14 Online Documentation: Abaqus Theory Guide, 2014.

[16] A. International, Standard Practice for Preparation and Use of Bent-Beam Stress-Corrosion Test Specimens, 2016.

[17] A. International, Standard Test Methods for Bend Testing of Metallic Flat Materials for Spring Applications Involving Static Loading, 2013.

[18] J. Gigax, E. Aydogan, T. Chen, D. Chen, L. Shao, Y. Wu, W.-Y. Lo, Y. Yang, F. Garner, The influence of ion beam rastering on the swelling of self-ion irradiated pure iron at 450 °C, Journal of Nuclear Materials 465 (2015).

[19] J. Gigax, H. Kim, E. Aydogan, F. Garner, S. Maloy, L. Shao, Beam-contamination-induced compositional alteration and its neutron-atypical consequences in ion simulation of neutron-induced void swelling, Materials Research Letters 5 (2017) 1-8.

[20] H. Kim, J.G. Gigax, J. Fan, F.A. Garner, T.L. Sham, L. Shao, Swelling resistance of advanced austenitic alloy A709 and its comparison with 316 stainless steel at high damage levels, Journal of Nuclear Materials 527 (2019) 151818.

[21] C. Cabet, F. Dalle, E. Gaganidze, J. Henry, H. Tanigawa, Ferritic-martensitic steels for fission and fusion applications, Journal of Nuclear Materials 523 (2019) 510-537.

[22] O.D. Sherby, Factors affecting the high temperature strength of polcyrystalline solids, Acta Metallurgica 10(2) (1962) 135-147.

[23] R.K. Desu, H. Nitin Krishnamurthy, A. Balu, A.K. Gupta, S.K. Singh, Mechanical properties of Austenitic Stainless Steel 304L and 316L at elevated temperatures, Journal of Materials Research and Technology 5(1) (2016) 13-20.

[24] An Evaluation of the Yield, Tensile, Creep and Rupture Strengths of Wrought 304, 316, 321, and 347 Stainless Steels at Elevated Temperatures, ASTM International.

[25] V.K. Sikka, B.L.P. Booker, M.K. Booker, J.W. McEnerney, Tensile and creep data on type 316 stainless steel, ; Oak Ridge National Lab., TN (United States), 1980, p. Medium: ED; Size: 132 p.

[26] J. Ziegler, M.D. Ziegler, J. Biersack, The Stopping and Range of Ions in Mater, Nuclear Instruments and Methods in Physics Research Section B: Beam Interactions with Materials and Atoms 268 (2010) 1818-1823.

[27] S. E10.08, Standard Practice for Investigating the Effects of Neutron Radiation Damage Using Charged-Particle Irradiation, ASTM Book of Standards, American Society of Testing and Materials, United States, 2016.

[28] SOLIDWORKS Help: Thermal Analysis, 2019. https://help.solidworks.com/2019/english/SolidWorks/cworks/c_Thermal_Analysis.htm?id=0869d95e9c4e464899d2a427349b9e03#Pg0. (Accessed October 07 2020).

[29] Inconel Alloy 625, in: S.M. Corporation (Ed.) 2013.

[30] J.M. Jones, P.E. Mason, A. Williams, A compilation of data on the radiant emissivity of some materials at high temperatures, Journal of the Energy Institute 92(3) (2019) 523-534.

[31] P. Hosemann, J.G. Swadener, D. Kiener, G.S. Was, S.A. Maloy, N. Li, An exploratory study to determine applicability of nano-hardness and micro-compression measurements for yield stress estimation, Journal of Nuclear Materials 375(1) (2008) 135-143.

[32] P. Hosemann, C. Vieh, R.R. Greco, S. Kabra, J.A. Valdez, M.J. Cappiello, S.A. Maloy, Nanoindentation on ion irradiated steels, Journal of Nuclear Materials 389(2) (2009) 239-247.

[33] J.G. Swadener, E.P. George, G.M. Pharr, The correlation of the indentation size effect measured with indenters of various shapes, Journal of the Mechanics and Physics of Solids 50(4) (2002) 681-694.

[34] S.I. Golubov, A.V. Barashev, R.E. Stoller, Radiation Damage Theory, in: R.J.M. Konings, T.R. Allen, R.E. Stoller, S. Yamanaka (Eds.), Comprehensive Nuclear Materials, Elsevier Science & Technology, Oxford, UNITED KINGDOM, 2012, pp. 358-389.

[35] M.P. Short, D.R. Gaston, M. Jin, L. Shao, F.A. Garner, Modeling injected interstitial effects on void swelling in self-ion irradiation experiments, Journal of Nuclear Materials 471 (2016) 200-207.

[36] Q. Yan, J. Gigax, D. Chen, F.A. Garner, L. Shao, Monte Carlo modeling of cavity imaging in pure iron using back-scatter electron scanning microscopy, Journal of Nuclear Materials 480 (2016) 420-428.

[37] K. Jin, C. Lu, L.M. Wang, J. Qu, W.J. Weber, Y. Zhang, H. Bei, Effects of compositional complexity on the ion-irradiation induced swelling and hardening in Ni-containing equiatomic alloys, Scripta Materialia 119 (2016) 65-70.

[38] F.A. Garner, E. Gilbert, D. Porter, Stress Enhanced Swelling of Metals During Irradiation, Effects of Radiation on Materials, ASTM International, West Conshohocken, PA, 1981, pp. 680-697.

[39] F.A. Garner, Irradiation Performance of Cladding and Structural Steels in Liquid Metal Reactors, in: B.R.T. Frost (Ed.), Materials Science and Technology: A Comprehensive Treatment, VCH Publishing1994, pp. 419-543.

[40] S.J. Zinkle, P.J. Maziasz, R.E. Stoller, Dose dependence of the microstructural evolution in neutron-irradiated austenitic stainless steel, Journal of Nuclear Materials 206(2) (1993) 266-286.

[41] K.E. Sickafus, 1.05 - Radiation-Induced Effects on Material Properties of Ceramics (Mechanical and Dimensional), in: R.J.M. Konings (Ed.), Comprehensive Nuclear Materials, Elsevier, Oxford, 2012, pp. 123-139.

[42] T. Kadoyoshi, H. Kaburaki, F. Shimizu, H. Kimizuka, S. Jitsukawa, J. Li, Molecular dynamics study on the formation of stacking fault tetrahedra and unfaulting of Frank loops in fcc metals, Acta Materialia 55(9) (2007) 3073-3080.

[43] T. Nogaret, C. Robertson, D. Rodney, Atomic-scale plasticity in the presence of Frank loops, Philosophical Magazine 87(6) (2007) 945-966.

[44] D. Terentyev, A. Bakaev, Interaction of a screw dislocation with Frank loops in Fe–10Ni–20Cr alloy, Journal of Nuclear Materials 442(1) (2013) 208-217.

[45] M.M. Hall, Stress state dependence of in-reactor creep and swelling: Part I: Continuum plasticity model, Journal of Nuclear Materials 396(1) (2010) 112-118.

[46] M.M. Hall, J.E. Flinn, Stress state dependence of in-reactor creep and swelling. Part 2: Experimental results, Journal of Nuclear Materials 396(1) (2010) 119-129.

[47] S. Holmström, Negligible creep temperature curve verification for steels 10CrMoV9-10 and X2CrMoNiMo17-12-2, Institute for Energy and Transport, 2016.

[48] Y. Ishiyama, R.B. Rogge, M. Obata, Radiation-induced stress relaxation in high temperature water of type 316L stainless steel evaluated by neutron diffraction, Journal of Nuclear Materials 408(2) (2011) 153-160.

[49] J.P. Foster, E.R. Gilbert, K. Bunde, D.L. Porter, Relationship between in-reactor stress relaxation and irradiation creep, Journal of Nuclear Materials 252(1) (1998) 89-97.

[50] J.P. Foster, K. Bunde, M.L. Grossbeck, E.R. Gilbert, Temperature dependence of the 20% cold worked 316 stainless steel steady state irradiation creep rate, Journal of Nuclear Materials 270(3) (1999) 357-367.

[51] A.H. Cottrell, B.A. Bilby, Dislocation Theory of Yielding and Strain Ageing of Iron, Proceedings of the Physical Society. Section A 62(1) (1949) 49-62.

[52] V.S. Neustroev, V.N. Golovanov, V.K. Shamardin, Radiation embrittlement of the materials of fuel assemblies in the temperature range corresponding to maximum swelling, Soviet Atomic Energy 69(4) (1990) 833-837.

[53] W.G. Wolfer, F.A. Garner, Swelling-induced stresses in ion-bombarded surfaces: Effect of crystalline orientation, Journal of Nuclear Materials 85-86 (1979) 583-589.

[54] F. Garner, G. Wire, E. Gilbert, Stress Effects in ion bombardment experiments, Hanford Engineering Development Lab., Richland, WA (United States), 1975.

[55] E.H. Lee, L.K. Mansur, M.H. Yoo, Spatial variation in void volume during charged particle bombardment — the effects of injected interstitials, Journal of Nuclear Materials 85-86 (1979) 577-581.

[56] F.A. Garner, Impact of the injected interstitial on the correlation of charged particle and neutron-induced radiation damage, Journal of Nuclear Materials 117 (1983) 177-197.

[57] L. Shao, C.C. Wei, J. Gigax, A. Aitkaliyeva, D. Chen, B.H. Sencer, F.A. Garner, Effect of defect imbalance on void swelling distributions produced in pure iron irradiated with 3.5MeV self-ions, Journal of Nuclear Materials 453(1) (2014) 176-181.

[58] J. Bucky Badger, D.L. Plumton, S.J. Zinkle, R.L. Sindelar, G.L. Kulcinski, R.A. Dodd, W.G. Wolfer, Experimental Investigation of the Effect of Injected Interstitials on Void Formation, in: J.S. Perrin (Ed.) Effects of Radiation on Materials: Twelfth International

Symposium,, ASTM International, 1985, pp. 297-316.

[59] T. Aruga, Y. Katano, K. Shiraishi, Double peak of voidage depth profile in carbon or nitrogen ion irradiated 316 stainless steel, Journal of Nuclear Materials 122(1) (1984) 191-195.

[60] A. Bhattacharya, Ion irradiation effects on high purity bcc Fe and model FeCr alloys, Universite de Paris XI, 2014.

[61] S. Takaki, J. Fuss, H. Kuglers, U. Dedek, H. Schultz, The resistivity recovery of high purity and carbon doped iron following low temperature electron irradiation, Radiation Effects 79(1-4) (1983) 87-122.

[62] A. Vehanen, P. Hautojärvi, J. Johansson, J. Yli-Kauppila, P. Moser, Vacancies and carbon Impurities in alpha-iron: Electron irradiation, Physics Review B 25 (1982) 762-780.

[63] B.D. Sharma, K. Sonnenberg, G. Antesberger, W. Kesternich, Electrical resistivity of electron-irradiated concentrated Fe-Cr-Ni alloys during isochronal annealing, Philosophical Magazine A 37(6) (1978) 777-788.

[64] U. Holzwarth, A. Barbieri, S. Hansen-Ilzhöfer, P. Schaaff, M. Haaks, Positron annihilation studies on the migration of deformation induced vacancies in stainless steel AISI 316 L, Applied Physics A 73(4) (2001) 467-475.

[65] D. Connétable, P. Maugis, Effect of stress on vacancy formation and diffusion in fcc systems: Comparison between DFT calculations and elasticity theory, Acta Materialia 200 (2020) 869-882.

[66] C. Kang, Atomistic Scale Sudies of the Stress Effects on Defect Kinetics and Damage Evolution of Irradiated Fe, Nuclear Engineering, Texas A&M University, College Station, TX, 2018.

CHAPTER IV

FLINAK CORROSION RESPONSE OF HASTELLOY N UNDER VARIABLE STRESS CONDITIONS USING THREE-POINT BENDING TECHNIQUE

Introduction

MSRs are receiving increasing attention for potential near-term commercial application. These reactor designs boast numerous advantages over current LWRs, including but not limited to simplified design and safety features [1], potential process heat applications [2], and burner/breeder design permutations [3]. Of all prospective MSR designs, reactors utilizing fluoride salts have enjoyed the longest history of development [3, 4] and are thus the most viable for near-future commercial power generation. While fluoride MSR technologies host several attractive features, corrosion in these systems must be regulated via careful metallurgical design [5], redox potential control[6], and imposed operation limits.

Fluoride salt reactors coolants are typically comprised of eutectic mixtures of ionic salt compounds to achieve desirable thermophysical properties. FLiBe is a mixture of primary interest for fuel-bearing salt in primary coolant loops. The FLiBe salt has advantageous neutronic properties [7] but poses a greater personnel hazard. FLiNaK is routinely used to surrogate for FLiBe due to similar thermohydraulic and chemical characteristics [8, 9]. FLiNaK is additionally considered a viable candidate for secondary coolant loop circulation [2]. Like the extensively studied FLiNaK and FLiBe salts, research on prospective MSR reactor materials since the late 50s have been highly

focused on a few alloys. Hastelloy N (designated Alloy N hereafter), developed by ORNL under the name INOR-8, was specifically designed to meet the thermomechanical and corrosion challenges of fluoride salt systems [5, 10]. Alloy N and its variants are still considered some of the best alloy options for implementing commercial fluoride MSRs [11].

Comprehensive research was performed in studying the macroscopic creep rupture and corrosion properties of Alloy N under the influence of several variables. These including He and Te embrittlement [11-13], metallurgical aging [14, 15], and variations in composition [5, 10]. Microscale processes at the core of corrosion response went largely understudied however, likely due to limitations in microscopy and spectroscopy techniques. One such process is the impact of complex stress states on the corrosion response of Alloy N. Such Multiphysics interaction would affect salt-facing reactor components such as fasteners, heat exchangers, or components with residual stress from manufacturing. Contemporary works [16, 17] have significant made significant contributions in the understanding of creep under tensile stress and corrosion. As of now, no investigators have directly explored the impact of compressive stress/strain on corrosion.

In the present work, the high temperature stress relaxation behavior of Alloy N in FLiNaK salts is explored by combining the three-point bending technique with static immersion testing of a sample. Specifically, the bender sample was deflected to a maximum Von Mises stress ~0.55 σ_y and immersed in high-purity FLiNaK salt alongside a control sample for 50 hours at 700°C under an argon atmosphere. The

consequences of subjecting Alloy N immersed in FLiNaK to compressive and tensile stress are assessed via cross-section examination of the bent bar and control samples using SEM techniques, including EDS and EBSD. Parallels are drawn between stress-corrosion behavior observed here and contemporary literature to explain the disparate corrosion response between regions under compressive or tensile stress.

Procedure

Experiment Design

A sample of Hastelloy N was prepared from a coupon sourced from Haynes International. The sample was cut to the shape of a long bar using a low-speed diamond saw and the cross-section face of the sample prepared by mechanical polishing. 0.04um colloidal silica was used for the last step to expose grain structure. The sample was subsequently sonicated in acetone and rinsed in methanol. The final dimensions of the sample were measured to be 15.98 mm X 4.01mm X 0.446mm after polishing. The Hastelloy N sample was mounted under stress using a three-point bending apparatus fabricated using 200/201 Nickel alloy. The dimensions of the three-point bending device base are shown in sonicated in acetone followed by methanol, rinsed in DI water, and dried using nitrogen gas. The components were then outgassed under high vacuum at 300°C for two hours to remove material adsorbed during the machining and cleaning process.

Figure 34.a. Nickel 200/201 pins were used to fabricate the three 4mm contact pins of the bending apparatus, as well as the center carriage. The tensioning screw in contact with the center carriage pin was a commercially-sourced 6-32 5/8” long screw made of Monel 400 alloy. The entire assembly including the final polished sample is shown in sonicated in acetone followed by methanol, rinsed in DI water, and dried using nitrogen gas. The components were then outgassed under high vacuum at 300°C for two hours to remove material adsorbed during the machining and cleaning process.

Figure **34**.b. All components of the three-point bending apparatus were sonicated in acetone followed by methanol, rinsed in DI water, and dried using nitrogen gas. The components were then outgassed under high vacuum at 300°C for two hours to remove material adsorbed during the machining and cleaning process.

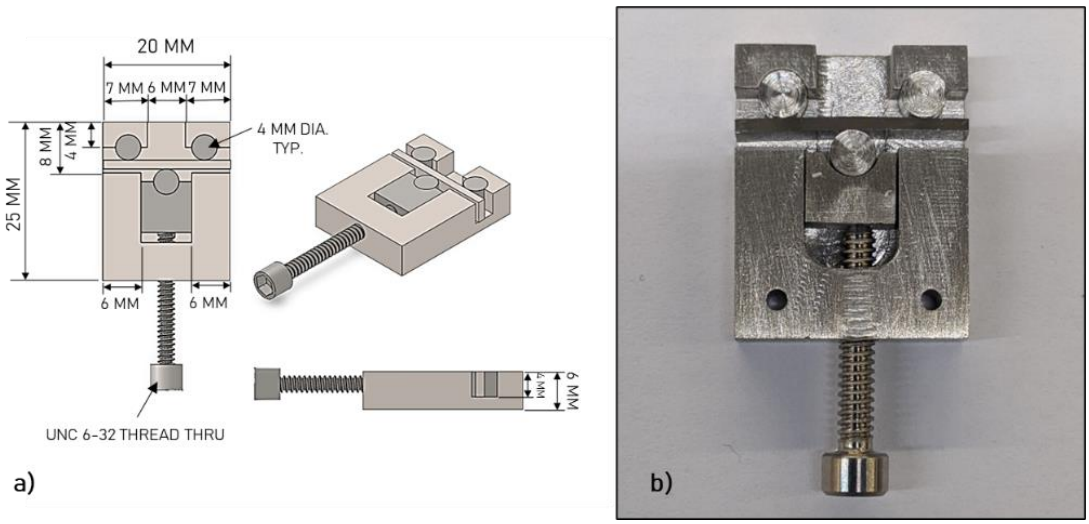

Figure 34. a) Schematic of three-point bending apparatus base used for mounting Hastelloy N sample under stress. b) Final configuration of sample mounted and tensioned in three-point bending device.

Several considerations were made when deciding the conditions to which the stressed sample would be exposed. Ultimately, the parameters of the corrosion test were driven by the temperature of the experiment. MSR designs typically quote hot-leg temperatures ≥700°C, benefiting from improved thermodynamic efficiency over LWRs and enabling integration of process heat applications [2, 8]. The corrosion temperature of the experiment was thus selected as 700°C. In turn, the corrosion exposure time and the stress applied to the sample were limited by the mechanical and thermal elongation behavior of the material at the chosen temperature. Additional constraints were imposed due to the limited availability of comprehensive thermal elongation data for Hastelloy N. Based on tabulated data collected by Haynes International at temperatures ≥ 700°C, the stress selected for the study was restricted to between 138-241 MPa [18].

The final two constraints imposed on the system were that a) the maximum stress experienced anywhere in the sample would not exceed the elevated-temperature yield stress of the material and that b) the sample would not be corroded too long as to induce full relaxation in the sample. The latter constraint was important to ensure the full coupling of creep and corrosion were reflected in the results. Computer modeling was performed to ensure satisfaction of the design constraints. Using the thermal elongation data for Hastelloy N, an iterative parametric variation scheme was performed using a Python script to solve for the constants of the time-based Norton-Bailey (NB) creep power law equation shown in Eq. 4 [19]. This simple model is appropriate for primary and secondary creep response and when the stress of the system does not exceed the

$$\boldsymbol{\varepsilon = (A\sigma^{n})t^{m}} \qquad \textbf{Equation 4}$$

Here,

$\varepsilon = strain$

$A = creep\ strain\ hardening\ coefficient\ [seconds^{-1}MPa^{-1}]$

$n = stress\ constant$

$m = time\ constant$

yield stress [19, 20]. The constants were iterated until the error between the modeled strain and the training data were less than two percent at the stress and time of interest. The standard error of the estimate was also calculated for the entire fitted trend against the training data. This was used as a secondary benchmark to ensure that the fit was globally accurate and behaved realistically throughout the history of the system. FEA model was created using the Abaqus/Standard commercial software to predict the stress distribution and creep relaxation in the sample over time. The results of the power law parametric variation procedure were input to the Abaqus model, along with any other relevant temperature-dependent mechanical properties available for Hastelloy N [18]. The FEA model consisted of a quadradic, hexahedral mesh (C3D20R) chosen for greatest accuracy for systems under bending conditions in the elastic regime [21]. The final model mesh contained 174960 cells. The cells at the center of the sample, the region of maximum deflection under the tensioning pin, were partitioned and locally seeded to a size of 0.0446mm to maximize local spatial resolution and accuracy. The displacement applied to the tensioning pin in the model was iterated to determine the

deflection needed to induce the desired maximum stress at the beginning of corrosion test. Once the necessary deflection was identified, the full creep simulation was executed to predict the total relaxation observed.

The FEA model was roughly validated by comparing the maximum principal stress at room temperature predicted by the simulation to an analytical prediction using beam theory. For a bent beam where the deflection experienced is less than 10% of the thickness of the member and which does not experience plastic deformation, the stress at mid-length is given by$\boldsymbol{\sigma = \frac{6Ety}{H^2}}$ Equation 5 Eq. 5 [22].

A final applied stress and corrosion time were selected for the experiment based on the results of the FEA model and the deviation of the results to the beam theory stress prediction.

$$\boldsymbol{\sigma = \frac{6Ety}{H^2}} \qquad \textbf{Equation 5}$$

Here,

σ = maximum tensile stress

E = modulus of elasticity

t = thickness of the specimen

y = maximum deflection

H = distance between outer supports

Experiment Execution

Once the desired stress was determined, tension was applied to the sample by tightening the tensioning screw on the bending apparatus and measuring the displacement experienced at the sample midpoint. The displacement was monitored using a Mitutoyo model 513-403 horizontal dial test indicator fixed with its sensor lever against the top face of the sample. Following stress mounting, wire composed of 200/201 nickel alloy was strung through the holes drilled into the base of the three-point bending apparatus (see Fig. 34.b). These wires were used to suspend the mounted sample from an alumina ceramic lid upside down into the corrosion crucible. A control sample with the same quality of mechanical polish and with a 2 mm hole drilled through its center was suspended on a separate wire to the same lid. A larger 1/4-20 nickel plated screw and nut set were used to secure the wire attached the bending apparatus, while a smaller ceramic 6-32 screw and nut set were used to secure the wire of the control sample. Two different sets of hardware were necessary due to the limited space available when machining the ceramic lid and the differences in weight between the two samples. The mounting holes in the ceramic lid were sufficiently far apart to avoid contact between the two samples. The alumina ceramic lid minimized the potential for electrochemical coupling between the two samples.

The samples were suspended from the ceramic lid into a glassy carbon crucible. Prior to the experiment, the crucible had been cleaned with methanol and outgassed at 200°C in an argon glovebox for one hour. The crucible was loaded with 30g of FLiNaK eutectic salt mixture. The FLiNaK salts used were high purity hydrogen fluoride-sparged

salts sourced from Oak Ridge National Laboratory. A small sample of the as-received salt was kept for inductively coupled plasma mass spectroscopy (ICP-MS). The amount of salt added to the crucible was determined based on the temperature dependent density correlation of FLiNaK salts recommended by Romatoski and the known dimensions of the crucible [8]. 30g reflects the amount of the needed to immerse the surface of the samples completely at a known distance from the base of the crucible. For conservancy of resources, the entire bending apparatus was not immersed.

Figure 35 illustrates the complete assembly of the corrosion crucible and samples. The assembly was placed inside a Thermo-scientific Thermolyne furnace residing within an MBraun Labmaster DP atmosphere-controlled argon glovebox. The glovebox maintained nominal oxygen and moisture levels <0.1 ppm. The furnace was heated to 700°C and left at temperature for 50 hours. The condition of the furnace and atmosphere in the glovebox were periodically monitored to ensure no deviation in the experiment conditions occurred. After 50 hours, the crucible was removed from the furnace while hot and the ceramic lid lifted off to remove the suspended samples from the salt. This was done to allow as much salt to drip off the samples as possible before resolidifying, simplifying the cleaning process. Once cooled, a second sample of salt was collected from the crucible and analyzed via ICP-MS to assess the accumulation of corrosion products after the experiment. Chemicals used in the ICP-MS analysis were Optima grade acid reagents from Fisher Scientific and Nanopure water produced using a

Barnstead/Thermolyne Nanopure lab water system meeting ASTM type 1 water standards. All labware was washed and leached using a 25% NO_3 solution and rinsed

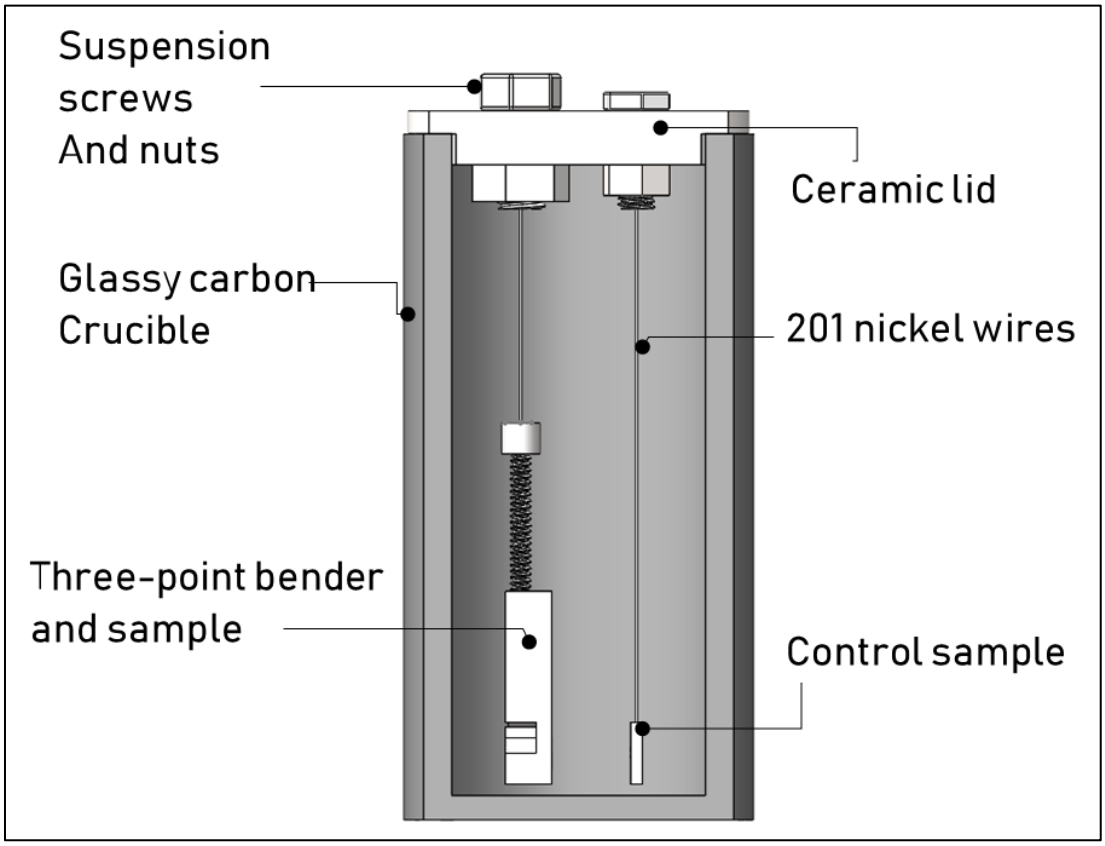

Figure 35. Schematic of the corrosion crucible and sample assembly.

in Nanopure water. Samples (pre and post corrosion experiment) were digested using a 1:1:2:4 H_2O/HCL/HF/HNO_3 volumetric solution in 25 ml Teflon beakers covered with Teflon watch glass. A method blank was also prepared using 1.0 ml of H_2O and the same proportions of digestion acids. Following full dissolution, the sample solutions were diluted to volume and passed through a 0.45µm filter. Following analysis, results from the salt samples were normalized using the method blanks.

After removal from the salt melt, the stressed and control samples were rinsed liberally with deionized (DI) water to remove loose chunks of salt. The samples were then submerged in individual glass beakers filled with DI water. The samples were removed and liberally rinsed again after 24 hours, and then submerged in clean DI water again. This soaking procedure was carried out three times to soften the salt as much as possible. After the third soak and rinse, the samples were sonicated for 10 minutes and then rinsed with DI water a final time. The samples were then rinsed in methanol and allowed to dry. Following cleaning, the samples were prepared for cross-section analysis. To protect the delicate corrosion structure at the surface, the samples were electroplated in copper. The electroplating was performed using a one molar DI water solution of Cu_2SO_4 and a pure copper anode. The plating was performed at room temperature using a mixing plate at 100 rpm for 15-25 minutes. Following electroplating, the samples were cut using a low-speed diamond wafering saw using a water-soluble cutting fluid. The stressed sample was bifurcated halfway along the length of the sample to expose the region directly under the center tensioning pin of the three-point bending mount. The samples were then mounted via hot compression mounting with the cut cross-section of the samples exposed. The samples were then mechanically polished with 0.04μm colloidal silica solution used to expose the grain structure of the samples at the final step.

The samples were next analyzed via SEM, EDS, and EBSD to observe the corrosion, elemental depletion, and restructuring at the sample surface. SEM, EDS and EBSD were performed using a Tescan Fera3 FIB-SEM electron microscope system

featuring Oxford Instruments NordlysNano EBSD detector and X-Max 50 EDS detector. Both analyses we performed using a 20keV electron beam energy for optimal backscatter resolution and x-ray excitation of Hastelloy N constituents. The analysis was performed on the stressed sample at six sites along the stress profile, half of the sites residing in the compressive stress region and the other half in the tensile stress region. The six sites selected for analysis were those which were best preserved after the mounting and polishing procedure. At each of the sites, a scan area was defined to perform five parallel line scans 2μm apart and perpendicular to the corrosion interface. These signals were averaged together to represent the site. Each individual scan was also repeated five times to average out random signal spikes during collection.

Results and Discussion

Results

The cross-section of the stressed Hastelloy N sample after mechanical polishing is shown in Figure 36. and is annotated to illustrate key features. The thickness of the sample is divided in two parts by the yellow midline, each half representing a region which experienced either compressive (top) or tensile (bottom) stress throughout corrosion test. This midline also represents the latitude along which the stress is effectively zero. The spaced sites were out as regularly as possible with slight deviations allowed where morphological features or corrosion damage inhibited accurate measurement. The sites are each given an identifier depending on their stress state and

proximity to the midline, where C indicates compression, T indicates tension, and N/C and N/T represent the sites on either the C or T side near the neutral (N) midline.

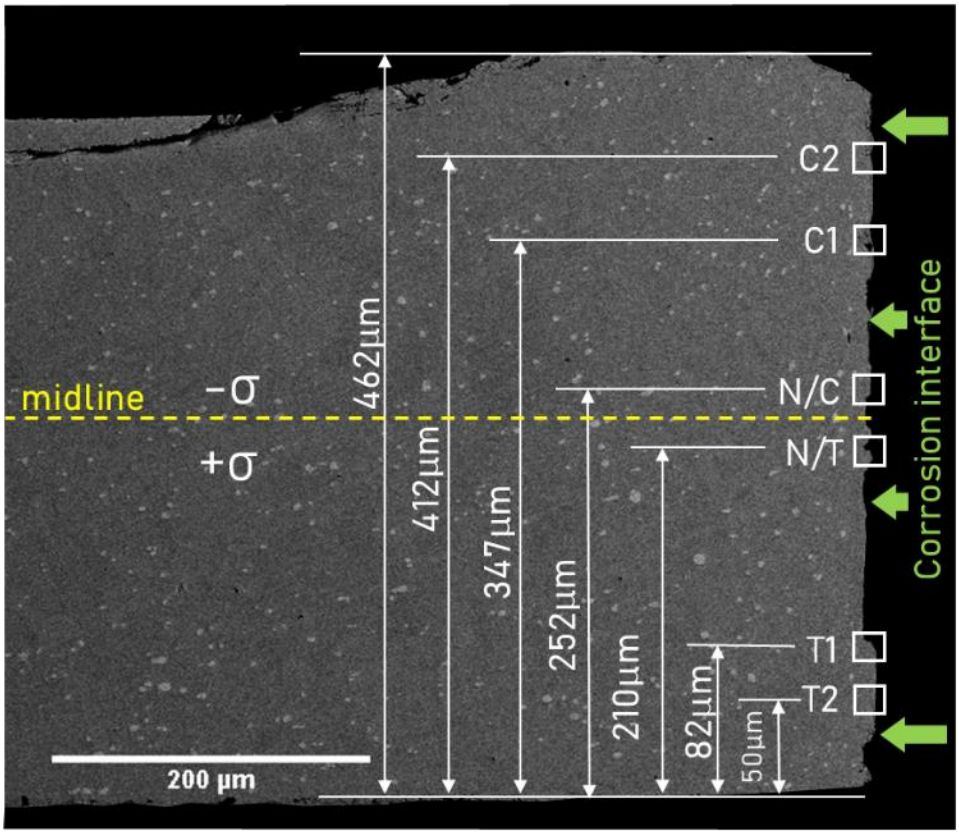

Figure 36. SEM image of Hastelloy N sample bisected and cross-section polished after corrosion to expose the stress gradient along the corrosion interface.

The FEA model-predicted stress distribution of the sample after initial bending is shown in model results in Figure 37. The cross-section view frame shown has been programmed to illustrate the Von Mises stress in each element. The deflection of the sample mesh is referred to as the “one-second” distribution. Von Mises stress is used as the primary metric for evaluating the approach to yield in the model. This quantity is

derived from the interaction of local maximal sheer stresses to the material yield stress, and is well-suited for systems under complex, non-uniaxial loading conditions [23].

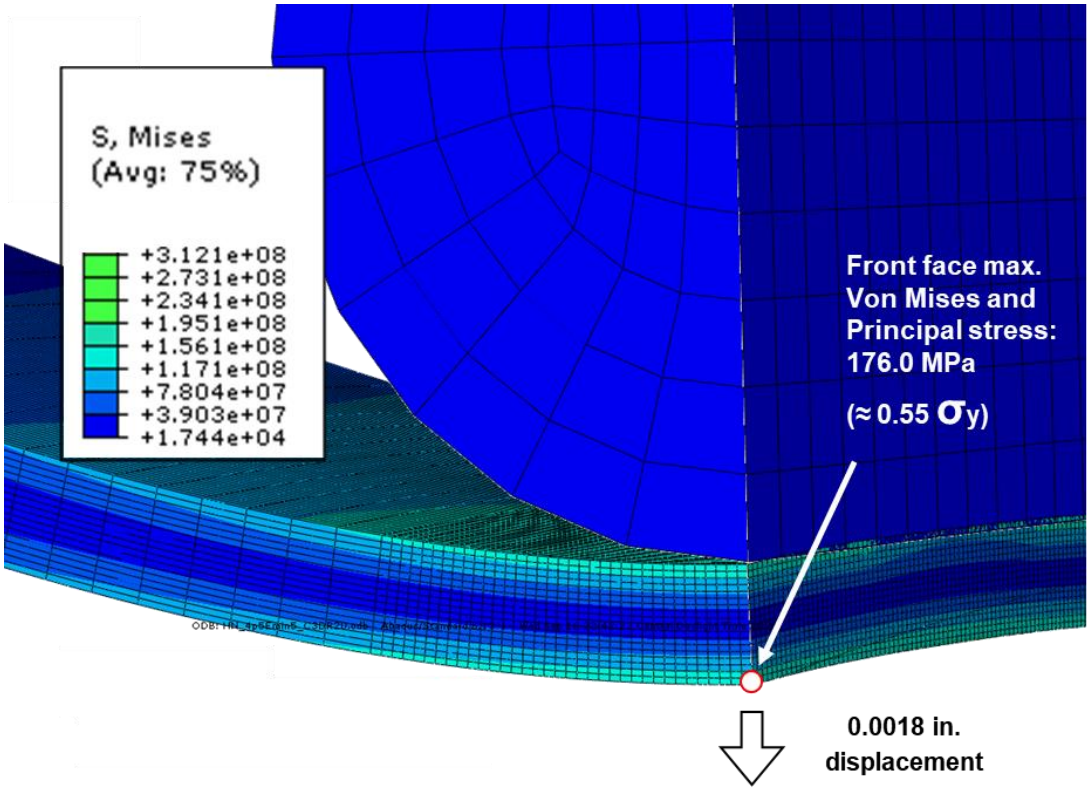

Figure 37. Output stress distribution of Hastelloy N after initial deflection under a 201-nickel pin as predicted by Abaqus FEA model. An 140X exaggerated mesh deflection is shown for clarity.

After carrying out the displacement iteration procedure, the maximum principal stress and Von Mises stress solved for the experiment was 176.0 MPa. This value falls within the range of available mechanical and thermal deformation data, ensuring that the subsequent creep step of the simulation behaves in a physically realistic manner.

Additionally, this stress value is below the elevated temperature yield stress of the material [18, 24] (and thus the room temperature yield stress as well) and so plastic deformation does not need to be accounted for. The final displacement value which achieves a stress of 176.0 MPa was 0.0018 inches. The one-second stress distribution in

The FEA model-predicted stress distribution of the sample after initial bending is shown in model results in Figure 37. The cross-section view frame shown has been programmed to illustrate the Von Mises stress in each element. The deflection of the sample mesh is referred to as the “one-second” distribution. Von Mises stress is used as the primary metric for evaluating the approach to yield in the model. This quantity is derived from the interaction of local maximal sheer stresses to the material yield stress, and is well-suited for systems under complex, non-uniaxial loading conditions [23].

Figure **37** shows that the maximum stress occurs on the cross-section face and at the mid-length of the sample on the sample side opposite tensioning pin. The stress observed in the tensioning pin is several orders of magnitude lower than in the sample. It is thus assumed that the compression experienced by the 201 Nickel tensioning pin during the sample loading is negligible and the sample is effectively acted on through a ridged body. The analytical beam theory model predicted a maximum stress 183.1 MPA in the sample. The difference between the analytical and FEA model one-second stress prediction is approximately 3.9%. It should be noted that the sample bar is outside the dimension range suggested by ASTM to ensure accuracy of the analytical model.

Despite this, the predictions of the two models agree well, ensuring that the FEA model is realistically depicts beam deflection as it occurs at room temperature.

The results of the creep power law parametric variation summarized are shown in Figure 38.a. The time-based BN power law is best fitted against several stress trends simultaneously to capture the sensitivity of primary and secondary creep behavior under different loads. Some flexibility exists in the shape of the fit depending on which stress trend is selected to fit the power law equation most closely. The tabulated experimental data used for the fitting scheme featured three stress data sets at 706°C, which are represented in Figure 38.a as the solid line trends with geometric symbols. 172.4 MPa, representing the middle trend, is closest to the estimated maximum principle stress of 176.0 MPa experienced by the sample at the one-second room temperature stress distribution. The accuracy of the fitted power-law trend in replicating the experimental creep strain data at different loadings is quantified using the standard error of the estimate ($\sigma_{\underline{EST}}$). A 95% confidence interval around the fitted trend at a specific stress can be approximated by multiplying the $\sigma_{\underline{EST}}$ value by 1.96. A smaller confidence interval indicates a better fit between the experimental data and the fitted trend. The SE value was calculated for each pair of experimental and fitted data at a particular stress level. The fitted data was only tabulated out to 50 hours for SE calculation to reflect the quality of the fit within the bounds of the corrosion experiment time. The SE for fits of the 137.9, 172.4, and 241.3 MPa sets were 0.000492, 0.00132, 0.0108 (values of strain). This spread of SE values indicate that the parameters solved for the time-based NB creep power law equation are more well-fitted at lower stresses within the 50-hour time frame

of the corrosion experiment. This is a beneficial quality as the initial stress loading will decay quickly upon high temperature corrosion exposure under fixed strain loading. Figure 38.b illustrates the stress relaxation estimated by the FEA model using the parameters derived for the NB creep power law equation. Each trend corresponds to one of the six sites detailed in The spaced sites were out as regularly as possible with slight deviations allowed where morphological features or corrosion damage inhibited accurate measurement. The sites are each given an identifier depending on their stress state and proximity to the midline, where C indicates compression, T indicates tension, and N/C and N/T represent the sites on either the C or T side near the neutral (N) midline.

Figure 36. At the sites experiencing the most initial strain the one-second distribution, (i.e., C2 and T2), the stress experienced is predicted to decay rapidly in the first few hours. In all the trends, the relaxation becomes more and more gradual as the initial stress decays and the driving force for further creep deformation is diminished. The stress trend for the C1 exhibits exceptional behavior in that the stress

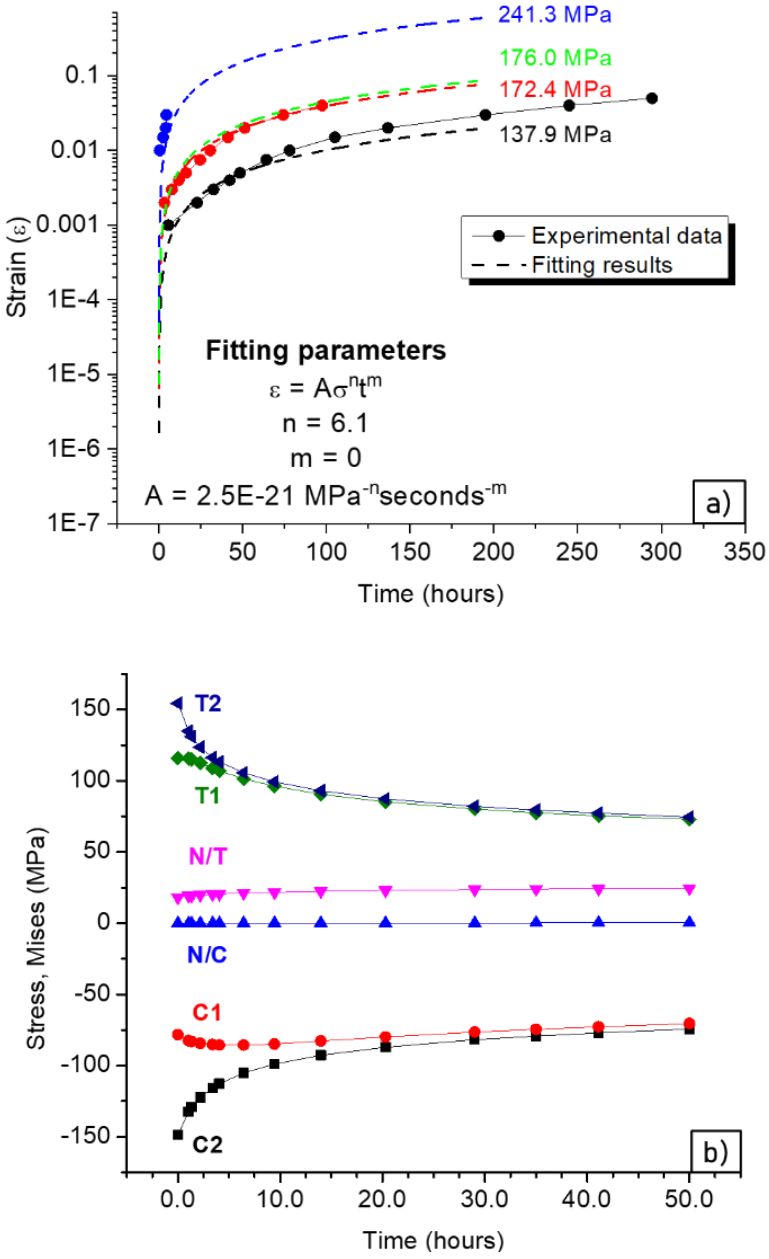

Figure 38. a) results of creep data fitting analysis against the Norton-Bailey creep power law function for the three strain versus time trends representing different experimental loading stresses at 706°C. b) Stress transformation and relaxation over time experienced at the different sites along the stress gradient of the sample.

appears to increase slightly (i.e., becomes more negative) in the first three hours before proceeding to relax.

This behavior is believed to arise due to the physical constriction of the compressive stress side of the sample. Stress on the tensile side will tend towards stretching the material in the long direction of the bender sample along the y-axis (see Figure 37). Compressive stress in contrast is limited by the resistance of the material towards being constrained into a smaller volume at the center of the sample. The interior of the sample on the compressive side, which has no free surface towards which to shift strained material, will thus experience an initial increase in stress as the surrounding material shifts and relaxes. A similar, but inverse effect appears to occur at the N/T site, which exhibits a slight and continuous increase of stress throughout the model history. Material in the N/T region is likely being pulled along by the adjacent material of the sample as it stretches towards the long dimension.

The ICPMS analysis is summarized in Table 2 and details the assay for key metallic constituents for FLiNaK and Hastelloy N. Continuous Calibration Verification (CCV) samples were evaluated during the analysis run to provide error estimation limits. These limits are typically within 10% of the real values. Three CCV check samples were used for the duration of the analysis, and some elements were not present in any of the CCV samples (e.g., Mo). The bulk of the detectable metallic constituents are comprised of lithium, sodium, and potassium. Contaminant metals are only present in trace amounts in the initial salt melt, the most significant of which are described in Table 1. For several of the elements here, the mean percent error values derived from the CCVs are

larger than the measured concentrations change between the samples before and after corrosion. The changes were thus too low to be used as a reliable quantification of the severity of corrosion over the 50-hour experiment.

The detected levels of metallic elements in the salt, while not indicative of quantitative corrosion severity, reflects low metallic contamination. This excludes the significant contribution of contaminate fluorides to overall corrosion. Such compounds are shown to undergo reduction reactions leading to surface deposition and oxidation of less thermodynamically stable alloy constituents such as chromium [25]. The small change in the metallic constituents detected also indicates that a) the experimental salt volume was sufficiently large to prevent corrosion product saturation during the experiment and b) minimal moisture contamination in the salt, reflective of the quality of the purification process. Both features are critical to avoid confoundment of the influence of stress on corrosion under ideal reactor operation conditions. Salt moisture purity is shown to be especially important for controlling the corrosion rate in fluoride salt environments and performing corrosion experiments [26]. The elimination of moisture and oxygen limits corrosion severity, preventing the production of deleterious chemical species such as HF or forming oxides with alloy constituents which freely dissolve into the melt [25, 27-32].

Table 2. Trace element analysis of FLiNaK salt before and after corrosion experiment via ICP-MS.

Element	Concentration before corrosion (mg/g)	Concentration after corrosion (mg/g)	Max. CCV mean percent error*
K	375.62	356.28	-45.1 ± 24.44
Li	73.4	77.23	34.42 ± 42.82
Na	57.44	56.79	7.90 ± 10.65
Cr	0.01	0.03	4.64 ± 1.83
Fe	0.049	0.001	-1.03 ± 0.48
Ni	0.174	0.017	6.73 ± 2.85
Mo	0.00022	0.00042	N/A
Rb	0.056	0.052	2.17 ± 0.69
Al	0.006	0.017	6.41 ± 2.00
Mg	0.018	0.02	5.92 ± 2.17

**a total of three Continuous Calibration Verification (CCV) assays performed throughout the analysis*

Upon initiation of the EDS, a calibration spectrum was collected at each of the six cross-section analysis sites detailed in The spaced sites were out as regularly as possible with slight deviations allowed where morphological features or corrosion damage inhibited accurate measurement. The sites are each given an identifier

depending on their stress state and proximity to the midline, where C indicates compression, T indicates tension, and N/C and N/T represent the sites on either the C or T side near the neutral (N) midline.

Figure **36**. An example calibration spectrum is shown in Figure 39.a, which was gathered over a square 100 μm^2 area at the T2 site and adjacent to the corrosion interface. The elements corresponding to the numbered peaks are listed in Table 3 alongside the characteristic x-ray and predicted weight distribution. Interference peaks were identified from oxygen, which interacted with the metallic sample and residual fluorides as atmospheric O_2 and water during mechanical polishing. Peak two, which is attributed to oxygen, is straddled closely on both sides by minor L band excitation peaks for chromium and so the purported weight percent contribution tends to be distorted. The oxygen peaks are thus removed from the assay for a more representative elemental analysis. Fluorine and carbon peaks are also identified, the former introduced from the corrosion ingress and the latter primarily from the carbon-based hot press mounting powder used for preparing the cross-section sample.

While carbon has a distinct peak at position one, fluorine occurs close to position three which is dominated by LI excitation band of nickel. Both carbon and fluorine are treated as surface contaminants similarly as oxygen and are removed from the calibration assay. Factoring in the corrections for these low mass elements, the resulting weight percent estimation closely replicates the nominal composition of

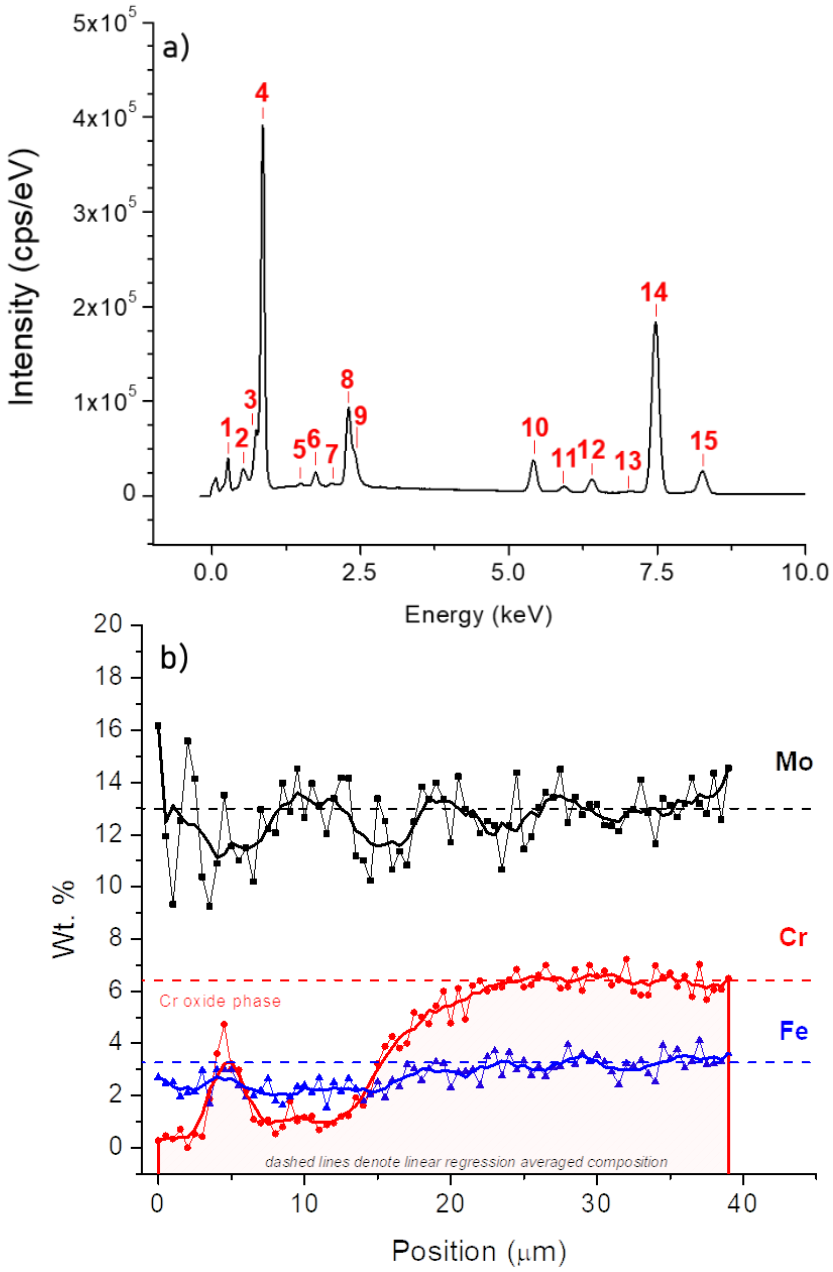

Figure 39. a) Example EDS calibration spectrum and characteristic peaks of detected elements from site T2. b) EDS line scan profile at T2 site of corrosion interface where the area under the Cr profile is integrated to calculate the depletion area change.

Hastelloy N [33]. Molybdenum and nickel are slightly higher and chromium and iron lower than in the stock material. This is reflective of the sensitivity of chromium and iron to corrosion in fluoride melts [28] and so a relative increase in molybdenum and nickel is expected given the normalization of the weight percent measurement to reflect a 100 percent composition. Figure 39.b illustrates the results of the EDS line scan routine performed at site T2 and highlights the elemental profile for three elements. The left side of the spectrum represents the region closest to the corrosion interface and so elemental depletion is expected to be most extreme here and become more gradual towards the right. Molybdenum, iron, and chromium are focused on as the main alloying constituents of Hastelloy N. The 25 raw spectra collected at each site (geometric icons connected by thin lines) were further processed using an adjacent average binning

Table 3. Characteristic peaks of example EDS calibration spectrum and measured weight percent distribution of Hastelloy N sample.

Peak no.	Element	X-rays	Weight %	σ
1	C	Ka1,2	N/A	-
2	O	Ka1	N/A	-
3,4,14,15	Ni	Ll,La1&2,Kb1	72.40	0.04
5	Al	Ka1	0.36	0.01
6	Si	Ka1	1.28	0.01
7-9	Mo	Ll, La1, Kb1	16.33	0.04
10,11	Cr	Ka1, Kb1	6.27	0.02
12,13	Fe	Ka1&2,Kb1	3.35	0.02

procedure to smooth the elemental profiles (thick continuous lines). The dashed lines represent the nominal local composition obtained from averaging a 15μm length of each elements profile towards the end of the scan path. These values, represented by the horizontal dashed lines in Fig.39.b, agree well with the estimated weight percent derived from the calibration map spectra when applicable. Molybdenum cannot be directly compared in this manner due to its limited solubility in the bulk matrix of Hastelloy N (approximately 12%) [34].

An accurate bulk weight percent measurement can only be accomplished by scanning a large area encompassing many of the Mo-rich secondary phases such as was performed for the calibration spectra. These nominal local average values are used as the basis for comparison to estimate elemental depletion experienced at each site. Fluctuation of the line scan profiles and the intersection of the scan paths with secondary phases was observed in the spectra collected despite the averaging of several scans. This prohibited a clear delineation of the corrosion depth of each element. To quantify the magnitude of depletion at the six sites, reduction from normal of the area under each of the element signal profiles is calculated. This was done by integrating under the entire smooth-averaged signal profile and calculating the difference between this area and the area under the rectangle defined by the nominal local average line. This area reduction calculation results in a single depletion quantity for each element and at each of the six analysis sites. The trends of these area depletion values are plotted in Figure 40 against the position of each site to illustrate the change in element depletion versus position on

the sample. Molybdenum, chromium, and iron are again highlighted, and a trend line is affixed to the data for each element to emphasize the behavior of each elemental trend.

The depletion area change calculations demonstrate a distinct increase in chromium corrosion moving from the compressive to tensile stress side of the sample. Iron appears to be slightly affected as well, but the magnitude of the change is small and possible attributable to systematic error. Molybdenum appears unaffected by the stress gradient overall. The line spectra collected demonstrated some variability, especially

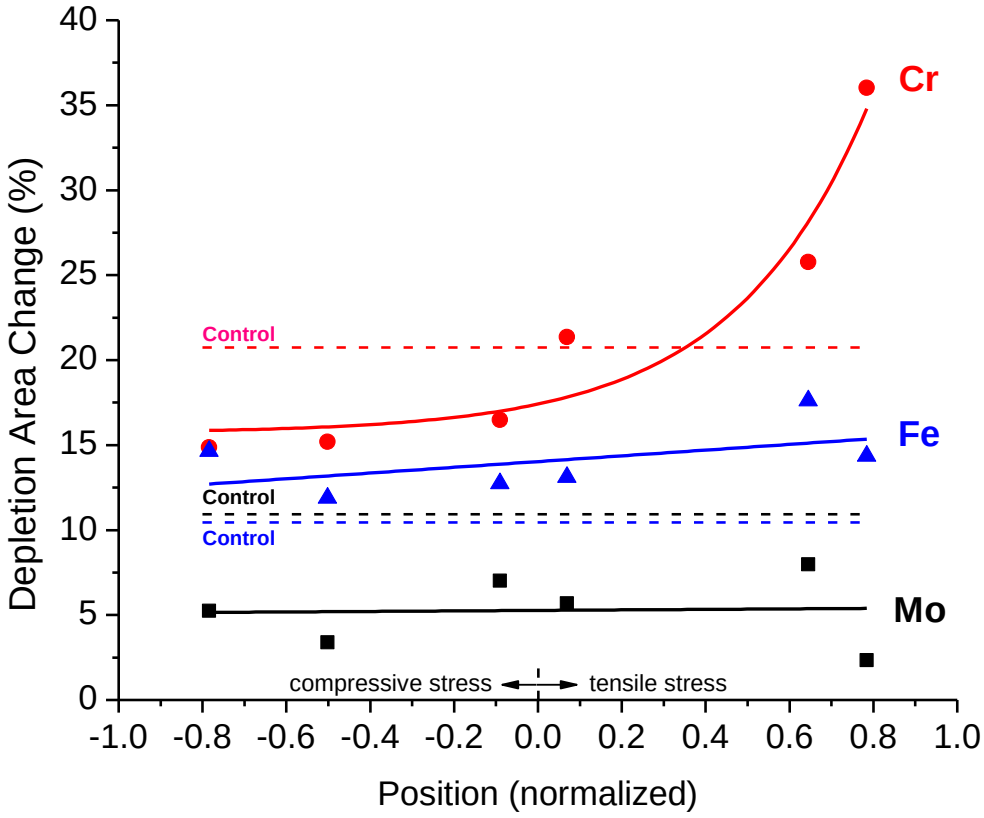

Figure 40. Trend of depletion area changes for chromium, iron and molybdenum measured at the six sites along the stress gradient of the sample.

close to the corrosion interface and for the sites in the tensile stress region (see Figure 39.b). The depletion area changes measured in the control sample are shown as horizontal dashed lines. The chromium depletion measured in the control sample is close to the level detected at the N/T site at ~ 0.1 of the normalized position. Similar to the T2 site (see Figure 39.a), carbon peaks from the hot press mounting material may be inflating the level of detected chromium due to the close coincidence of these peaks. The Fe and Mo depletion levels detected in the control sample are notably different from those observed across the stress sample.

The exact reason for this discrepancy is unknown. Signal intensity for all the spectra collected in the control sample were notably weaker and required longer collection time than with the stressed sample. Self-shadowing effects could possibly explain this occurrence if the polished surface of the control sample or the surround mounting material exhibited height gradients relative to the EDS detector. This would cause disproportionate self-absorption of secondary electrons relative to the detector, which might distort the overall weight percent assay [35, 36]. While not reliable as a perfect quantitative metric, the EDS trends still illustrate a clear increase in chromium depletion in the tensile stress region. The following discussion will focus instead on qualitatively describing the physical processes which led to the selective increase in chromium depletion.

The sensitization of chromium in the tensile stress region can be attributed to multiple factors. Cross referencing the model results in

Figure 38, the sample will have likely only experienced the onset of primary creep where strain hardening has not developed sufficiently to decelerate initial deformation [37]. The stress history over the course of the experiment and away from the sample center is however still a significant portion of the yield stress for Hastelloy N and so continuous loading effects should be considered. Recent work by Zhu, et. Al. observed that diffusion creep modes will dominate in Hastelloy N deformed under tensile stress at 100 MPa In Hastelloy N and 700°C [17]. In general, diffusion-driven creep predominates at lower stresses and across a wide range of temperatures [38]. It can thus be inferred that such deformation modes would drive creep in the deflected sample examined here, since all the evaluated sites are predicted to have experienced stress at or below 100 MPa for most of the experiment history.

In optimal conditions of moisture free salt, chromium tends to be the most thermodynamically sensitive to dissolution in the fluoride salt melt [28, 39]. One way which tensile stress could exacerbate chromium corrosion could be to increase the surface area of alloy exposed to the salt, such as through cleaving of grain boundaries and enabling salt ingress. Chromium has also been demonstrated to diffuse more quickly than other elements in nickel alloy mixtures [40, 41]. The enhanced chromium depletion therefore could be the result of augmented diffusion driven by creep restructuring or strong stress gradients. It has been shown that creep deformation is strongly dependent on the ease with which atoms may diffuse through a metallic system [42]. Enhanced chromium depletion therefore may be symptomatic of stress-driven changes in

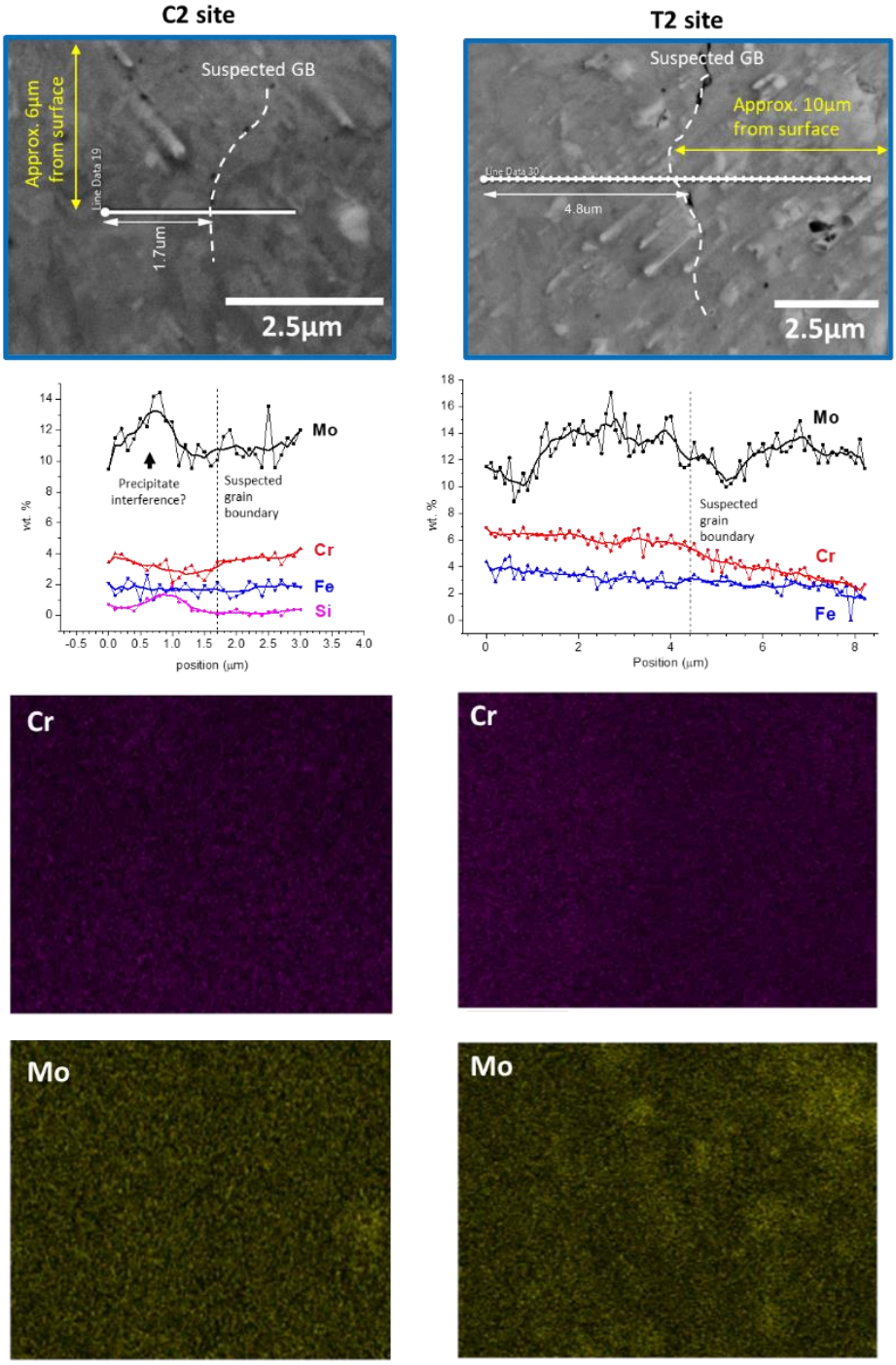

Figure 41. EDS line scans performed across grain boundaries at C2 and T2 sites near the corrosion interface to identify possible localized segregation and corrosion depletion.

diffusional potential for all constituents of Hastelloy N, which would sensitize chromium especially.

Additional EDS line scan and mapping analysis was performed at four sites (C2, C1, T1, and T2) to identify possible grain boundary depletion sensitivity changes at the different stress extremes. Figure 41 highlights the results of the grain boundary analysis at sites C2 and T2, the respective extremes of compressive and tensile stress. Grain boundaries were partially obscured by surface features, complicating analysis. The line scan paths were chosen to be as close to the surface as possible and selection relied on the presence of small voids as indication of grain boundaries. These trails of voids become more densely packed closer to the corrosion interface which suggests profound grain boundary salt ingress close to the sample surface. The line scan at the C2 site runs parallel to the corrosion interface of the sample while that of the T2 site is oriented perpendicularly to the site. The line scan data does not appear to identify a clear difference in grain boundary segregation behavior between the two sites, although some differences are apparent. The suspected grain boundaries denoted by white dashed lines in Figure 41 do not coincide closely with significant features in the elemental spectra. It is possible that electron beam drift and shadowing effects have limited the spatial accuracy of the microscope for EDS analysis, leading to shifting of features such as local spikes or dips of the detected elements. The spectra collected for the T2 site, especially that for molybdenum, exhibits a high degree of variability and is likely attributed to the presence of small secondary phases which litter the T2 site surface and occur near the line scan path. The elemental maps for the T2 site confirm that these are Mo-rich phases.

The difference in orientation of the two-line scans relative to the surface may explain the subtly distinct chromium signal behavior. The chromium trend across the grain boundary at the T2 site follows a steady depletion gradient in the direction of the corrosion interface, which follows the general corrosion trend at this site. The chromium gradient appears to become steeper after traversing the grain boundary, indicating that the grain boundary may serve to slow chromium diffusion out of the sample when oriented parallel to the corrosion interface. Conversely, the grain boundary at the C2 roughly coincides with a minimum in the Cr line scan spectrum. The perpendicularly oriented grain boundary here may therefore be enabling accelerated diffusion of chromium out of the sample. The observations made in Figure 41 do not clearly support nor refute the possibility of GB cleaving. A complication to observing such a phenomenon is the orientation of the stress relative to the corrosion interface and cross-section cut of the sample on the xy plane. The deflection of the sample will tend to pull apart the material on the tensile side in the direction of the length of the sample along the y-axis (see Figure 37). Such cleaving may not be obvious on the selected cross-section analysis plane along xz and a 90-degree change in observation orientation would be needed.

EBSD data taken at the C2 and T2 sites, shown in Figure 42, highlight several grain features at the corrosion interface. Dashed lines denoting the sample surface and two different chromium depletion thresholds demonstrate a coincidence between significant chromium depletion and surface grain boundary morphology change. As shown in the IPF-X map (Figure 42.a), grains in the compressive stress region appears

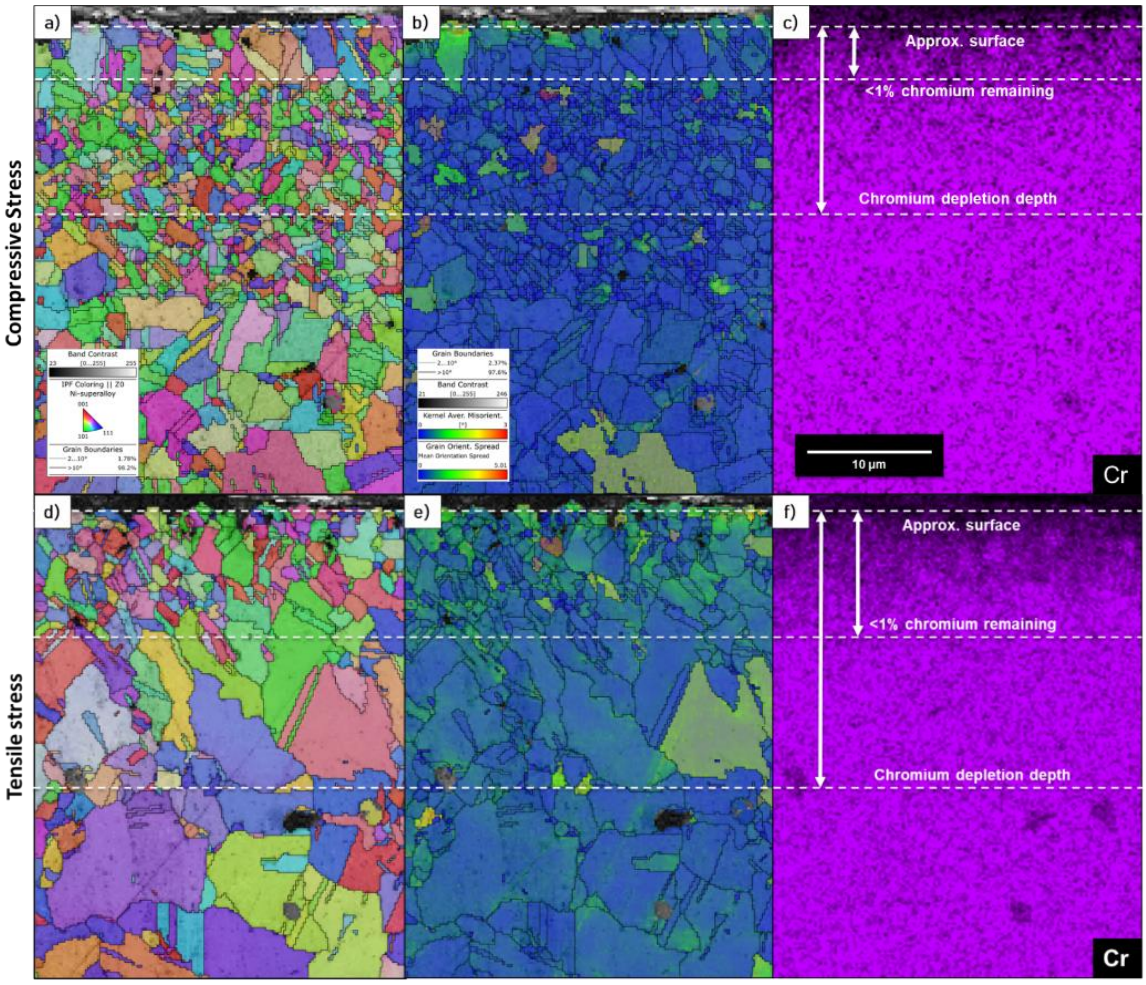

Figure 42. EBSD data collected at C2 and T2 sites, representing the extremes of compressive and tensile stress and deformation experienced by the sample. a-c): IPF-X, MOS + KAM, and EDS Cr signal collected at the compressive site. d-f) IPF-X, MOS + KAM, and EDS Cr signal collected at the tensile site.

coarser than the surrounding grains at the near surface where chromium depletion is most extreme (a threshold of <1% is denoted) Conversely, grains in the tensile stress region shown in IPF-X (Figure 42.d) are noticeably finer than in the rest of the evaluated region. The approximate coincidence of the <1% chromium depletion

threshold and the change in grain morphology may be indicative of a restructuring effect. The egress of chromium could cause solubility changes for the rest of the alloy constituents, especially Mo which has a distinct solubility limit in Hastelloy N [34]. This would explain the presence of the near surface microphases observed at the two sites, especially in the tensile stress region, shown in Figure 41. The presence of these phases may also be indicative of polygonization as a mode of stress relief [43, 44], as Hastelloy N already exhibits a tendency to precipitate molybdenum-rich $M_{12}C$ carbides along grain boundaries [45].

Mean orientation spread (MOS) and Kernel Averaged Misorientation (KAM) are overlaid for the compressive and tensile stress regions in Figure 42.b and Figure 42.e, respectively. The combination of these two maps are used to quantify the degree of deformation and recrystallization experienced by individual grains. The MOS+KAM maps further emphasize the differences in the near-surface grain morphology between the two sites. At both compressive and tensile stress sites, the near surface chromium depleted region exhibits a higher degree of grain misorientation on average. As previously mentioned, the observation plane here likely underemphasizes the true degree of deformation experienced at each of these sites. The misorientation observed on this plane is reactionary to the dominant stresses operating along the y-axis. Most of the deformation and recrystallization therefore should be along y-axis and thus obscured from view.

Evaluation of the change in grain size distribution and prevalence of twin boundaries at the two sites suggests distinct deformation/relaxation modes having

occurred in the tensile and compressive stress regions. As shown in Fig. 43.a through Fig. 43.c, the compressive stress region exhibits both a densification in grain boundaries and significant accumulation of twin boundaries

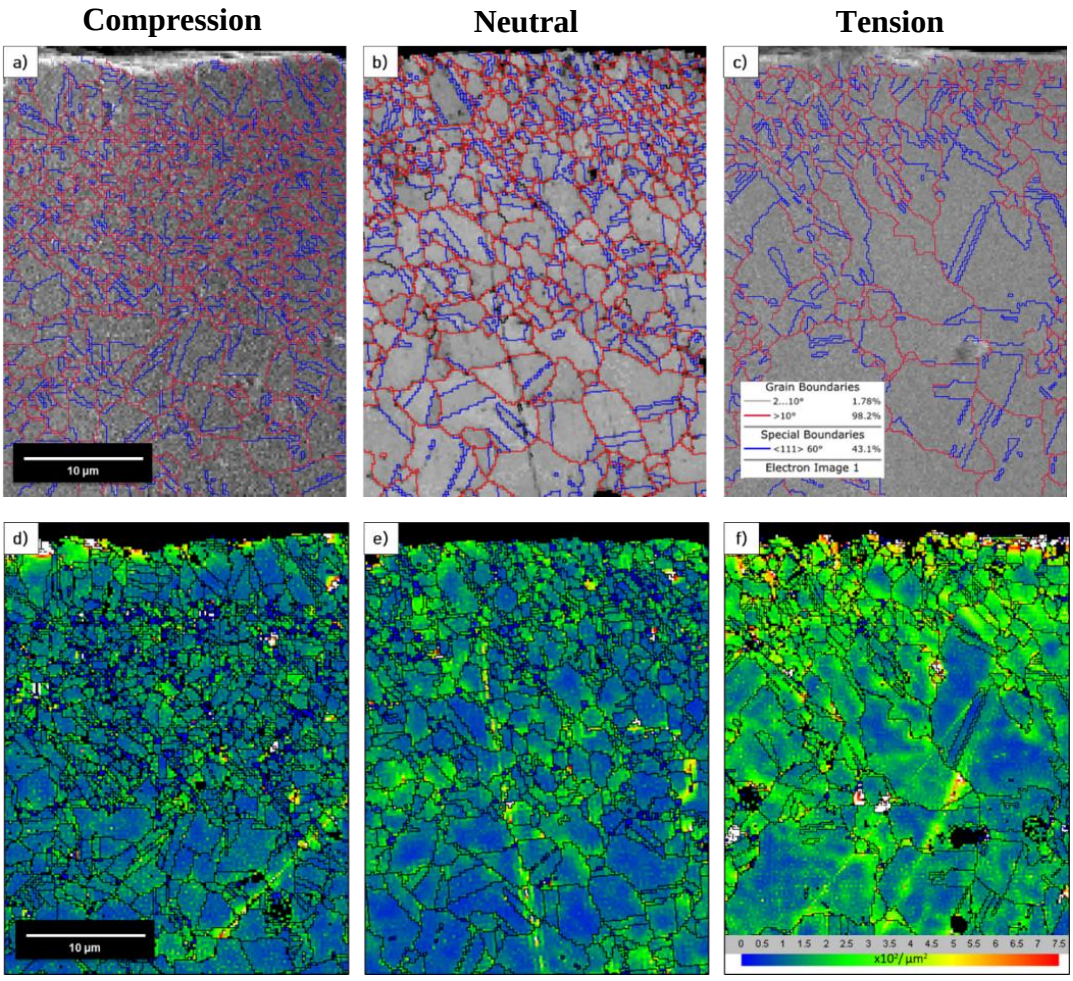

Figure 43. Maps of grain boundary and twin boundary distributions at the a) tensile (T2) stress site and b) compressive (C2) stress site. c) Comparison of grain size distribution and twin boundary density between C2 and T2 sites.

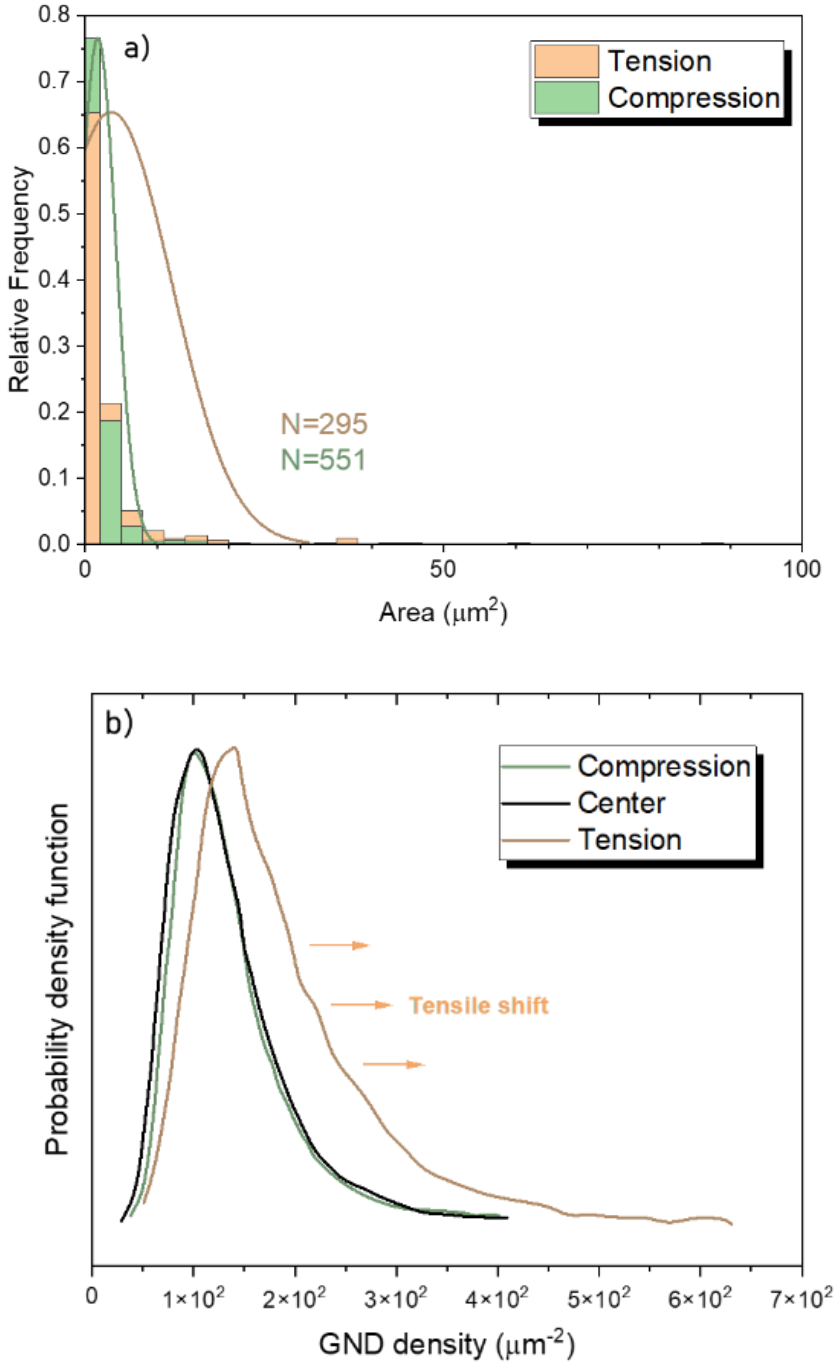

Figure 44. a) Distribution of grain size for tensile and compressive stress regions. b) Comparison of GND density observed at the three sites evaluated in Figure 43.

.

Table 4. Summary of 60°<111> twin boundary density measurements

Stress region	Twin boundary density ($\mu m/\mu m^2$)
Tension	0.1253
Center	0.6299
Compression	0.7184

compared to the neutral stress and tensile stress sites. The quantitative assessment of twin density and grain boundary area distribution is summarized in Figure 44.d through Figure 44.f. These maps illustrate the differences in density of geometrically necessary dislocations (GNDs) detected using EBSD [46, 47] which occurred in the three evaluated regions shown. GNDs are necessary for accommodation of lattice distortions in alloys and multiphase materials where stress gradients exhibit local inhomogeneity [48]. Measuring GND density thus provides a useful measurement of local distortions in lattice curvature accommodated by dislocation accumulation.

The GND maps show a noticeable increase in density in the tensile stress region. The compressive stress region in contrast appears to have experienced very fine dislocation cell formation as evidenced by the presence of small grains containing lower GND densities than the surrounding structures. [44] GNDs across all three evaluated sites tend to be denser in and around grain boundaries, as well as closer to the corrosion and Figure 44 combined highlight the disparity in twin boundary density, the grain size distribution, and the GND density in the evaluated area for the three stress sites chosen. The twin boundary density is nearly six times as high in the compressive stress region

versus the tensile stress region. The neutral stress region also exhibits a comparably high density of twin boundaries.

Discussion

Tensile stress appears to advance the depletion of chromium in the tensile stress region but exactly how requires more consideration. The data suggests a few possible processes to account for the sensitization. One possibility is enhanced depletion resulting from the stress-driven stabilization of secondary phases. Stress aging is a phenomenon receiving increasing attention to enhance the mechanical properties of age-hardenable (AH) aluminum alloys. Tensile and compressive stress are both shown cause preferential precipitation in AH alloys at grain boundaries oriented perpendicularly to loading direction [49, 50]. Tensile stress is also understood to reduce aging time of certain precipitates by reducing critical threshold energies needed to initiate nucleation [51, 52]. Hastelloy N is well-documented as precipitating secondary phases, likely a $M_{12}C$ carbide structure, along its grain boundaries with continued high temperature service [24, 34, 53-55]. These phases, like the native, globular M_6C carbide phases, are rich in molybdenum, chromium, carbon, and silicon [45]. Studies have shown that the after prolonged thermal exposure at temperatures ≥700 C, Hastelloy N structure evolves towards coexistence of primary M_6C carbide phase alongside secondary $M_{12}C$ phase grain boundary precipitates or complete dissolution of the M_6C phase in favor of $M_{12}C$ [56-59].

Stress aging treatments however are usually performed at significantly lower temperatures and stress thresholds than were exerted on the bender sample, and so creep is not usually a serious consideration. Had enhanced secondary phase precipitation occurred, the compressive and tensile stress regions of the sample would have been equally affected and the neutral stress site and control sample conversely unaffected. Survey of the density of grain boundary precipitates far away from the corrosion interface however yielded statistically similar measurements at the stressed and unstressed sites and was therefore inconclusive. Moreover, a concentration and egress of chromium via stress-enhanced grain boundary precipitation would have been evident in the analysis highlighted in Figure 41. This observation also undermines the role of stress-driven grain boundary cleaving having enabled more aggressive corrosion in the tensile stress region.

Different creep/stress relaxation processes having occurred between the two regions is left as a viable explanation for the observed results and is considered further. Creep in metallic systems encompasses several complex mass redistribution processes which are highly sensitive to stress, temperature, and individual material properties. In the temperature range of the stress corrosion experiment ($T \sim 0.5\ T_{melt}$, $\frac{\sigma}{G} \sim 10^{-4} - 10^{-3}$), a diffusion-based creep mode is likely the primary deformation mechanism of the tensile stress region of the 3PB-2 sample. Nabarro-Herring creep typically requires high temperatures ($T \sim T_M$) to facilitate significant grain elongation in the loading direction via intragranular diffusion [38, 60]. At intermediate temperatures such as were used in this experiment, Coble creep (i.e., grain boundary diffusion-facilitated) is more

likely a significant factor. Diffusion creep modes causes fluxes of vacancies in the plane(s) perpendicular to the maximum principal stress. Surplus vacancies flowing in the plane aligned with the corrosion gradient may enable enhanced diffusion of the Hastelloy N alloying elements, especially Cr which exhibits comparatively high mobility in nickel alloys [40]. Egress of Cr may thus be accelerated by the surplus of vacancies in the region of high tensile stress.

Naked stress effects were considered as a possible explanation to the observed results. Diffusion through the lattice cannot be enhanced or inhibited by long-range uniform stress by itself but can be affected under the influence of stress gradients [61-63]. These gradients are often localized, such as through lattice distortions caused by interface with secondary phases or dislocations via Cottrell atmospheres [64, 65]. Long-range stress gradients were also considered as a possible driving force for asymmetric chromium depletion [66-68] but are unable to explain the apparent retention of chromium in the compressive stress region. Apart from the distinct stress states experienced at the different regions of the sample, the compressive and neutral stress regions exhibit a similar density in twin boundaries and near identical density of GNDs. The presence of fine cells and greater grain and twin boundary density does not seem to have enhanced depletion of chromium in the neutral and compressive stress regions. Bulk diffusion of chromium through the lattice tends to dominate corrosion for alloys exposed to purified fluoride salts [27, 30]. Salt purity thus appears to overshadow any corrosion enhancement via altered grain texture in the compressive and neutral stress regions.

The accommodation of high creep strain in Hastelloy N exposed to 700°C and sub σ_{yield} stresses has been previously demonstrated to require GNDs accumulation [16, 17]. The higher density of GNDs observed in the tensile stress region may be the key to explaining the observed results. Higher GND density in grains and around grain boundaries is accompanied by more numerous Cottrell atmospheres [64], which would cause local tensile stress gradients and promote diffusion of interstitial/substitutional atoms. Chromium diffusion to high stress GB regions would be enhanced, acting as an intermediary which would accelerate chromium transport through corrosion depletion pathways overall. This enhanced diffusion around GNDs may be too rapidly equilibrated or the detection resolution too coarse to be able to detect clear chromium diffusion gradients at grain boundaries, as was attempted in Figure 41.

Recent work corroborates the importance of GND formation in the creep evolution of Hastelloy N. Zhu, et. Al. demonstrated that high stress (~150 MPa) creep and significant creep strain in Hastelloy N are mediated by dislocations as evident through accumulation of GNDs [17]. This was especially evident in the vicinity of high angle grain boundaries (HAGB) and carbides where lattice distortion from creep were highest. Creep at lower stress (~100 MPa) was shown to be mediated by both dislocation motion and diffusion as evidenced by more modest GND accumulation and grain boundary sliding (GBS) [17]. Merensky et. Al. also demonstrated a linear relation between creep strain and accumulated GND density at intermediate creep stress and temperature conditions (135 MPa/700C) in Hastelloy N [16]. The overall mass loss experienced was similarly shown to be linearly proportional to creep strain, and by

extension the GND density. Their data also showed increased accumulation of Cr in dislocation rich regions, lending credence to importance of Cottrell atmospheres around GNDs in the depletion pathway.

Despite theoretically experiencing similar thresholds of creep strain, the compressive stress region compares most closely to the neutral stress region in terms of chromium depletion. If the compressive region of the sample accommodated stress primarily via twinning rather than GND formation as in the tensile stress region, then it may explain the disparity in chromium depletion observed. Comparison of the GND and chromium depletion maps for the tensile stress region (Figure 43.f and Figure 42.f respectively) demonstrates close coincidence between the most severe chromium depletion and where GND density is highest. The compressive region thus may have avoided the most severe corrosion by relaxing via twinning rather than GND evolution. In general, twinning as a deformation mode occurs in direct competition to slip when temperatures are too low to support significant atomic diffusion and dislocation flow needed for slip [69, 70]. Twinning is often energetically unfavorable in single phase or monoatomic FCC materials due to high stacking fault energies and availability of several slip systems [69, 71]. Twinning can be activated however at intermediate temperatures and strains by stacking faults generated in secondary phases such as in γ/γ’ nickel superalloys [72, 73] or by mechanical shocks such as by significant and/or sudden stress loading [69, 71]. It has been previously demonstrated that FCC materials subjected to compressive stress at room temperature will accumulate twin boundaries at lower strain thresholds and at a higher volume fraction than under tensile stress [74].

Deformation twins have also been observed with greater frequency in nickel superalloys under compressive versus tensile loads and even at elevated temperatures [75] where diffusion-enabled deformation is more prevalent. The accumulation of twin boundaries can be more pronounced still under complex stress states combining tension, compression, torsion, and in the vicinity of free surfaces [74].The disparity of twinning behavior between tensile and compressive stress states lies in the geometric constrictions imposed on material under compressive strain, which cannot easily deform or compact to accommodate external stress. Twinning under compressive stress thus becomes highly sensitive to grain orientation and the critical resolved shear stress, as well as the availability of unrestrained planes of motion [76].

References

[1] J. Serp, M. Allibert, O. Beneš, S. Delpech, O. Feynberg, V. Ghetta, D. Heuer, D. Holcomb, V. Ignatiev, J.L. Kloosterman, L. Luzzi, E. Merle-Lucotte, J. Uhlíř, R. Yoshioka, D. Zhimin, The molten salt reactor (MSR) in generation IV: Overview and perspectives, Progress in Nuclear Energy 77 (2014) 308-319.

[2] D.F. Williams, Assessment of Candidate Molten Salt Coolants for the NGNP/NHI Heat-Transfer Loop, ; Oak Ridge National Lab. (ORNL), Oak Ridge, TN (United States), 2006, p. Medium: ED; Size: 44 p.

[3] A.L. Qualls, Advanced Reactor Technology Program Molten Salt Reactor Campaign FY 2018 Summary, ; Oak Ridge National Lab. (ORNL), Oak Ridge, TN (United States), 2018, p. Medium: ED; Size: 44 p.

[4] M.W. Rosenthal, P.R. Kasten, R.B. Briggs, Molten-Salt Reactors—History, Status, and Potential, Nuclear Applications and Technology 8(2) (1970) 107-117.

[5] J.H. DeVan, I.R.B. Evans, CORROSION BEHAVIOR OF REACTOR MATERIALS IN FLUORIDE SALT MIXTURES, United States, 1962.

[6] J. Zhang, C.W. Forsberg, M.F. Simpson, S. Guo, S.T. Lam, R.O. Scarlat, F. Carotti, K.J. Chan, P.M. Singh, W. Doniger, K. Sridharan, J.R. Keiser, Redox potential control in molten salt systems for corrosion mitigation, Corrosion Science (2018) Medium: ED; Size: p. 44-53.

[7] J.A. Lane, H.G. McPherson, F. Maslan, Part II: Molten Salt Reactors, in: A.M. Weinberg (Ed.), Fluid Fueled Reactors, Addison-Wesley Pub. Co1958.

[8] R.R. Romatoski, L.W. Hu, Fluoride salt coolant properties for nuclear reactor applications: A review, Annals of Nuclear Energy 109 (2017) 635-647.

[9] J. Jerden, Molten Salt Thermophysical Properties Database Development: 2019 Update, ; Argonne National Lab. (ANL), Argonne, IL (United States), 2019, p. Medium: ED; Size: 30 p.

[10] T.K. Roche, THE INFLUENCE OF COMPOSITION UPON THE 1500 F CREEP-RUPTURE STRENGTH AND MICROSTRUCTURE OF MOLYBDENUM-CHROMIUM-IRON-NICKEL BASE ALLOYS, United States, 1958.

[11] R.N. Wright, T.-L. Sham, Status of Metallic Structural Materials for Molten Salt Reactors, ; Idaho National Lab. (INL), Idaho Falls, ID (United States); Argonne National Lab. (ANL), Argonne, IL (United States), 2018, p. Medium: ED; Size: 34 p.

[12] J.R. Keiser, Status of tellurium--hastelloy N studies in molten fluoride salts, United States, 1977.

[13] J. McCoy, H. E., Status of materials development for molten salt reactors, ; Oak Ridge National Lab., TN (USA), 1978, p. Medium: ED; Size: Pages: 36.

[14] H.E. McCoy, D.T. Bourgette, Influence of aging on the impact properties of Hastelloy N, Haynes alloy No. 25, and Haynes alloy No. 188, ; Oak Ridge National Lab., Tenn. (USA), 1973, p. Medium: ED; Size: Pages: 33.

[15] J.H.E. McCoy, EVALUATION OF THE MOLTEN-SALT REACTOR EXPERIMENT HASTELLOY N SURVEILLANCE SPECIMENS: FOURTH GROUP, United States, 1971.

[16] O. Muránsky, I. Karatchevtseva, A.E. Danon, R. Holmes, P. Huai, Z. Zhang, Impact of dislocations and dislocation substructures on molten salt corrosion of alloys under plasticity-imparting conditions, Corrosion Science 176 (2020) 108915.

[17] H. Zhu, O. Muránsky, T. Wei, J. Davis, E. Budzakoska-Testone, H. Huang, M. Drew, The effect of applied stress on the high-temperature creep behaviour and microstructure of NiMoCr Hastelloy-N® alloy, Materialia 16 (2021) 101069.

[18] Hastelloy N Alloy, Haynes International, 2020.

[19] D. May, A. Gordon, D. Segletes, The Application of the Norton-Bailey Law for Creep Prediction Through Power Law Regression, 2013.

[20] J.T. Maximov, G.V. Duncheva, A.P. Anchev, M.D. Ichkova, Modeling of strain hardening and creep behaviour of 2024T3 aluminium alloy at room and high temperatures, Computational Materials Science 83 (2014) 381-393.

[21] C. Veyhl, I.V. Belova, G.E. Murch, A. Öchsner, T. Fiedler, On the mesh dependence of non-linear mechanical finite element analysis, Finite Elements in Analysis and Design 46(5) (2010) 371-378.

[22] A. International, Standard Practice for Preparation and Use of Bent-Beam Stress-Corrosion Test Specimens, 2016.

[23] H. Ford, Advanced mechanics of materials, Wiley, New York, 1963.

[24] H.E. McCoy, The Influence of Several Metallurgical Variables on the Tensile Properties of Hastelloy N, Oak Ridge National Lab., Tenn., 1964.

[25] W.D. Manly, J.H. Coobs, J.H. DeVan, D.A. Douglas, H. Inouye, P. Patriarca, T.K. Roche, J.L. Scott, Metallurgical Problems In Molten Fluoride Systems, in: R. Hurst, R.N. Lyon, C.M. Nicholls (Eds.), Progress In Nuclear Energy, Pergamon Press, New York, 1960, pp. 201-221.

[26] S.S. Raiman, S. Lee, Aggregation and data analysis of corrosion studies in molten chloride and fluoride salts, Journal of Nuclear Materials 511 (2018) 523-535.

[27] F.-Y. Ouyang, C.-H. Chang, B.-C. You, T.-K. Yeh, J.-J. Kai, Effect of moisture on corrosion of Ni-based alloys in molten alkali fluoride FLiNaK salt environments, Journal of Nuclear Materials 437(1) (2013) 201-207.

[28] J.H. DeVan, R.B.E. Ill, Corrosion Behavior of Reactor Materials In Fluoride Salt Mixtures, Oak Ridge National Laboratory, 1962, p. 14.

[29] J. Baes, C F, THE CHEMISTRY AND THERMODYNAMICS OF MOLTEN SALT REACTOR FLUORIDE SOLUTIONS, ; Oak Ridge National Lab., Tenn., 1965, p. Medium: ED; Size: Pages: 34.

[30] F.-Y. Ouyang, C.-H. Chang, J.-J. Kai, Long-term corrosion behaviors of Hastelloy-N and Hastelloy-B3 in moisture-containing molten FLiNaK salt environments, Journal of Nuclear Materials 446(1) (2014) 81-89.

[31] K.-i. Fukumoto, R. Fujimura, M. Yamawaki, Y. Arita, Corrosion behavior of Hastelloy-N alloys in molten salt fluoride in Ar gas or in air, Journal of Nuclear Science and Technology 52(10) (2015) 1323-1327.

[32] K. Sridharan, T.R. Allen, 12 - Corrosion in Molten Salts, in: F. Lantelme, H. Groult (Eds.), Molten Salts Chemistry, Elsevier, Oxford, 2013, pp. 241-267.

[33] Hastelloy N Alloy: Nominal composition. URL: www.haynesintl.com/alloys/alloy-portfolio_/Corrosion-resistant-Alloys/hastelloy-n-alloy/nominal-composition. 2021).

[34] R.E. Gehlbach, H.E. McCoy, Phase Instability In Hastelloy N, International Symposium on Structural Stability in Superalloys, 1968, pp. 346-366.

[35] P. Schiffman, S. Roeske, N. Botto, Electron Microprobe Analysis of Minerals, 2013.

[36] T. Salge, M. Falke, N. Musat, G. Stryganyuk, A. Ball, G. Broad, A. Kearsley, W. Müller, Characterization of biomaterials using energy dispersive spectrometry (EDS) at sub-micrometer spatial resolution, 2014.

[37] M.E. Kassner, 1.1 Description of Creep, Fundamentals of Creep in Metals and Alloys (2nd Edition), Elsevier.

[38] H.J. Frost, M.F. Ashby, Deformation-mechanism maps : the plasticity and creep of metals and ceramics. by H.J. Frost and M.F. Ashby. 1st ed, 1st ed. ed., Pergamon Press1982.

[39] L.C. Olson, J.W. Ambrosek, K. Sridharan, M.H. Anderson, T.R. Allen, Materials corrosion in molten LiF–NaF–KF salt, Journal of Fluorine Chemistry 130(1) (2009) 67-73.

[40] T.-F. Chen, G. Tiwari, nbsp, Prasad, Y. Iijima, K. Yamauchi, Volume and Grain Boundary Diffusion of Chromium in Ni-Base Ni-Cr-Fe Alloys, MATERIALS TRANSACTIONS 44(1) (2003) 40-46.

[41] I.R.B. Evans, J.H. DeVan, G.M. Watson, SELF-DIFFUSION OF CHROMIUM IN NICKEL-BASE ALLOYS, United States, 1961.

[42] O.D. Sherby, Factors affecting the high temperature strength of polcyrystalline solids, Acta Metallurgica 10(2) (1962) 135-147.

[43] R.W. Cahn, A New Theory of Recrystallization Nuclei, Proceedings of the Physical Society. Section A 63(4) (1950) 323-336.

[44] D. Kuhlmann-Wilsdorf, Theory of plastic deformation: - properties of low energy dislocation structures, Materials Science and Engineering: A 113 (1989) 1-41.

[45] J. Li, S.L. Shrestha, Y. Long, L. Zhijun, Z. Xintai, The formation of eutectic phases and hot cracks in one Ni–Mo–Cr superalloy, Materials & Design 93 (2016) 324-333.

[46] B.S. El-Dasher, B.L. Adams, A.D. Rollett, Viewpoint: experimental recovery of geometrically necessary dislocation density in polycrystals, Scripta Materialia 48(2) (2003) 141-145.

[47] O. Muránsky, L. Balogh, M. Tran, C.J. Hamelin, J.S. Park, M.R. Daymond, On the measurement of dislocations and dislocation substructures using EBSD and HRSD techniques, Acta Materialia 175 (2019) 297-313.

[48] M.F. Ashby, The deformation of plastically non-homogeneous materials, The Philosophical Magazine: A Journal of Theoretical Experimental and Applied Physics 21(170) (1970) 399-424.

[49] W.F. Hosford, S.P. Agrawal, Effect of stress during aging on the precipitation of θ′ in Al-4 Wt pct Cu, Metallurgical Transactions A 6(3) (1975) 487.

[50] A.W. Zhu, J. Chen, E.A. Starke, Precipitation strengthening of stress-aged Al–xCu alloys, Acta Materialia 48(9) (2000) 2239-2246.

[51] S. Fu, D.-q. Yi, H.-q. Liu, Y. Jiang, B. Wang, Z. Hu, Effects of external stress aging on morphology and precipitation behavior of θ″ phase in Al-Cu alloy, Transactions of Nonferrous Metals Society of China 24(7) (2014) 2282-2288.

[52] W. Guo, J. Guo, J. Wang, M. Yang, H. Li, X. Wen, J. Zhang, Evolution of precipitate microstructure during stress aging of an Al–Zn–Mg–Cu alloy, Materials Science and Engineering: A 634 (2015) 167-175.

[53] J. Yang, Y. He, C. Qin, W. Zhao, S. Chen, Z. Gao, Microstructure evolution in a Ni–Mo–Cr superalloy subjected to simulated heat-affected zone thermal cycle with high peak temperature, Materials & Design 86 (2015) 230-236.

[54] Y. He, J. Yang, C. Qin, S. Chen, Z. Gao, Characterization of the Ni–Mo–Cr superalloy subjected to simulated heat-affected zone thermal cycle treatment, Journal of Alloys and Compounds 643 (2015) 7-16.

[55] W. Wang, C. Li, L. Jiang, X.-X. Ye, K. Yu, S. Chen, Z. Li, X. Zhou, Evolution of carbide precipitates in Hastelloy N joints during welding and post weld heat treatment, Materials Characterization 135 (2018) 311-316.

[56] T. Liu, J.S. Dong, L. Wang, Z.J. Li, X.T. Zhou, L.H. Lou, J. Zhang, Effect of Long-term Thermal Exposure on Microstructure and Stress Rupture Properties of GH3535 Superalloy, Journal of Materials Science & Technology 31(3) (2015) 269-279.

[57] F. Han, L. Jiang, X. Ye, Y. Lu, Z. Li, X. Zhou, Carbides Evolution in a Ni-16Mo-7Cr Base Superalloy during Long-Term Thermal Exposure, Materials (Basel), 2017.

[58] T. Liu, J.S. Dong, G. Xie, L. Wang, L.H. Lou, Effect of silicon on microstructure and stress rupture properties of a corrosion resistant Ni-based superalloy during long term thermal exposure, Materials Science and Engineering: A 656 (2016) 75-83.

[59] X.-X. Ye, H. Ai, Z. Guo, H. Huang, L. Jiang, J. Wang, Z. Li, X. Zhou, The high-temperature corrosion of Hastelloy N alloy (UNS N10003) in molten fluoride salts analysed by STXM, XAS, XRD, SEM, EPMA, TEM/EDS, Corrosion Science 106 (2016) 249-259.

[60] M.E. Kassner, 3. Diffusional Creep, Fundamentals of Creep in Metals and Alloys (2nd Edition), Elsevier.

[61] Diffusion and External Driving Forces, Diffusion in Solids: Fundamentals, Methods, Materials, Diffusion-Controlled Processes, Springer Berlin Heidelberg, Berlin, Heidelberg, 2007, pp. 179-190.

[62] M.J. Aziz, Dopant diffusion under pressure and stress, International Conference on Simulation of Semiconductor Processes and Devices, 2003. SISPAD 2003., 2003, pp. 137-142.

[63] W. Gong, P. Trtik, S. Valance, J. Bertsch, Hydrogen diffusion under stress in Zircaloy: High-resolution neutron radiography and finite element modeling, Journal of Nuclear Materials 508 (2018) 459-464.

[64] A.H. Cottrell, B.A. Bilby, Dislocation Theory of Yielding and Strain Ageing of Iron, Proceedings of the Physical Society. Section A 62(1) (1949) 49-62.

[65] J. Völkl, G. Alefeld, Diffusion of hydrogen in metals, in: G. Alefeld, J. Völkl (Eds.), Hydrogen in Metals I: Basic Properties, Springer Berlin Heidelberg, Berlin, Heidelberg, 1978, pp. 321-348.

[66] W.S. Gorski, Physikalische Zeitschift der Sowjetunion (8) (1935) 457.

[67] J. Völkl, The Gorsky effect, Berichte der Bunsengesellschaft für physikalische Chemie 76(8) (1972) 797-805.

[68] Mechanical Spectroscopy, Diffusion in Solids: Fundamentals, Methods, Materials, Diffusion-Controlled Processes, Springer Berlin Heidelberg, Berlin, Heidelberg, 2007, pp. 237-251.

[69] J.W. Christian, S. Mahajan, Deformation twinning, Progress in Materials Science 39(1) (1995) 1-157.

[70] G.E. Dieter, D.J. Bacon, Mechanical metallurgy, McGraw-hill New York1976.

[71] J. Wang, C.N. Tome, I.J. Beyerlein, A. Misra, N. Mara, Deformation twinning mechanisms in FCC and HCP metals, United States, 2011.

[72] M.G. Ardakani, M. McLean, B.A. Shollock, Twin formation during creep in single crystals of nickel-based superalloys, Acta Materialia 47(9) (1999) 2593-2602.

[73] L. Kovarik, R.R. Unocic, J. Li, P. Sarosi, C. Shen, Y. Wang, M.J. Mills, Microtwinning and other shearing mechanisms at intermediate temperatures in Ni-based superalloys, Progress in Materials Science 54(6) (2009) 839-873.

[74] J.-K. Hwang, Effect of Stress States on Twinning Behavior in Twinning-Induced Plasticity Steel, Journal of Materials Engineering and Performance 28(8) (2019) 4811-4825.

[75] J.-B. le Graverend, F. Pettinari-Sturmel, J. Cormier, M. Hantcherli, P. Villechaise, J. Douin, Mechanical twinning in Ni-based single crystal superalloys during multiaxial creep at 1050 °C, Materials Science and Engineering: A 722 (2018) 76-87.

[76] G.Y. Chin, W.F. Hosford, D.R. Mendorf, G.I. Taylor, Accommodation of constrained deformation in f. c. c. metals by slip and twinning, Proceedings of the Royal Society of London. A. Mathematical and Physical Sciences 309(1499) (1969) 433-456.

CHAPTER V

EVALUATION OF CORROSION RESPONSE OF HASTELLOY N IN FLINAK SALT AFTER PROTON IRRADIATION

Introduction

Several challenges persist in the use and interpretation of data from the early development of fluoride MSRs, especially that which was collected during the time of the MSRE experiments. These efforts, while invaluable for its thorough characterization of embrittlement, creep rupture properties, and fission-product-accelerated cracking corrosion, were unable to isolate the microstructural processes associated with early onset of irradiation-assisted corrosion. Indeed, it is unclear whether Hastelloy N suffers from neutron-accelerated corrosion in the absence of fission-product and transmuted helium embrittlement. Additionally, the manner which experiments during the MSRE and ARE projects were carried out inadvertently divided the data set in the two categories. The first type of studies focused on bare corrosion behavior in the absence of radiation through static immersion and were usually carried out via static immersion or corrosion loop testing. The second type of studies consisted of evaluating corrosion and mechanical response in the presence of radiation *as well* as fission product interaction. The latter variable is an important distinction, as the presence of embrittling fission products and the resulting cracking behavior tended to dominate the attention of investigators.

The direct influence of radiation damage on corrosion response in the absence of fission product influence thus requires further investigation. Illuminating this neglected facet of fluoride MSR materials research has immediate importance as certain MSR configurations would suffer from the very conditions captured in this neglected field of research. For example, primary coolant loops in MSRs using prismatic fuel, where fission products are theoretically locked up from circulating in the salt but around which core radiation in still significant, would be affected by radiation and corrosion, but not tellurium and europium embrittlement. Moreover, structural material activation will ensure that self-irradiation in the coolant loops will persist beyond the primary coolant loop. Secondary salt loops, especially the heat exchangers and other components closest to the core volume will still experience radiation damage regardless of the primary loop or core configuration.

Proton irradiation offers a compromise between the damage rates possible through heavy ion implantation and the penetration depth possible with electron irradiation [1]. While the damage rates are significantly lower than heavy ions, the damage profiles produced through protons are much flatter and produce a larger usable analysis region. Additionally, protons can most closely reproduce the microstructural damage caused by neutron irradiations [2, 3]. Additionally, protons (i.e., hydrogen) exhibits decent solubility in most metallic systems whereas alloys helium has virtually no solubility in nickel [4] and causes significant bubbling at low doses. Figure 45 highlights the damage and implantation profiles of different ion projectiles into Hastelloy N.

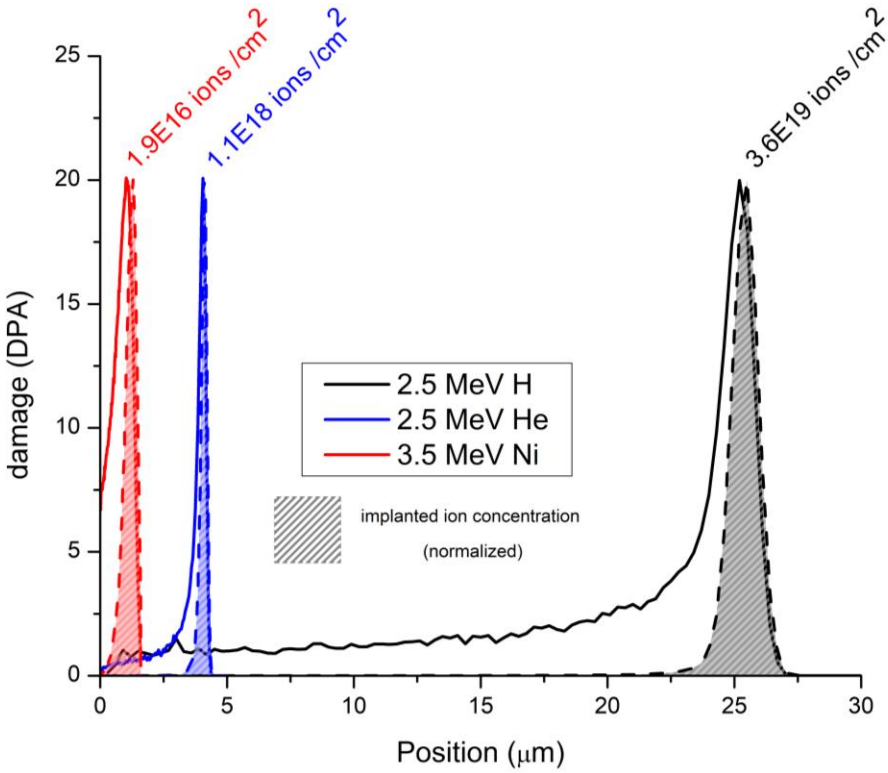

Figure 45. Comparison of damage profiles for different ions into a Hastelloy N target, as well as ion fluence needed to produce 20 DPA of damage.

Procedure

Sample preparation

Four sample of Hastelloy N were prepared from a 3mm thick coupon sourced from Haynes International. The samples were cut into 5mm x 5mm square pieces using a low-speed diamond saw. The samples were polished using a procedure identical to that which is described in Chapter V. The polished quality was verified using SE-SEM to ensure proper grain exposure.

Ion irradiation

The polished samples were irradiated using 2.5 MeV protons produced using a National Electrostatics Corporation 1.7 MV tandem ion accelerator. The samples were mounted using silver conductive paste to an Inconel hot stage fitted with an adjustable resistive heater. The samples were irradiated in a vacuum chamber maintained at pressures in the 1E-8 torr and featuring a liquid nitrogen cold trap for contamination control. High energy proton implantation has a narrow range of useful energy, balancing between limited range and damage at lower energies and nuclear activation reactions at higher energies [1]. These activation reactions tend to cause the release of significant short-term gamma excitation and decay heat which causes a significant increase in sample temperature. To mitigate this effect, the ion beam was rastered to allow some heat dispersal and to make the damage application across the sample more uniform. The samples were maintained at 500°C through a combination of the proton gamma heating, current control, and application of the resistive heater on the implantation stage. The samples were irradiated to 1 local DPA of damage, which was approximately equivalent to 1.3E19 ions·cm^{-2}. The fluence of ions needed was estimated using SRIM in the quick damage Kichin Pease mode [5].

After the irradiation was completed, the samples were left in the vacuum chamber at room temperature for two days. This was done to allow significant activation caused by the proton irradiation to decay away. The rough activity of the sample was

measured using live monitoring via a Geiger counter placed outside of the irradiation chamber at 18 inches. The activity of the sample was also modeled using MCNP to

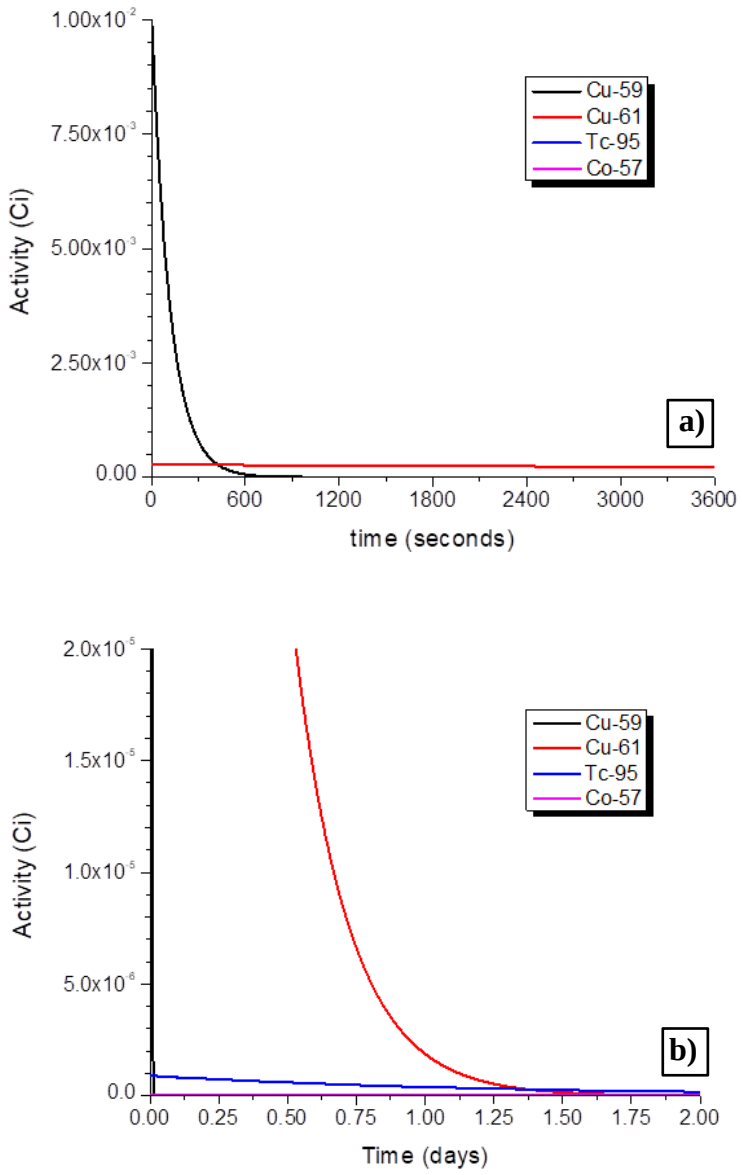

Figure 46. Activity over time of four largest contributors to proton activation in Hastelloy N samples after a) one hour and b) two days.

predict the isotopic breakdown of the radioactive inventory. The estimated radioactive inventory over time is illustrated in Figure 46, which shows that the greatest contributors to the activity decay to below 1μCi within a day. The most significant radioactive isotope, ^{59}Cu, decays away almost completely after 10 minutes. The remaining activity consists largely of ^{61}Cu and decays away in approximately 1.5 days. The remaining activity is a small and slow-decaying quantity of ^{95}Tc and ^{57}Co, both beta emitters through electron capture decay chains. The two isotopes combined were estimated to have an activity of roughly 1μCi after two days of decay and were deemed safe for removal. Following the two days spent in the vacuum chamber, the samples were removed and stored in a desiccator for an additional two weeks before regular handling for the next steps inf the experiment. FIB liftout was performed to produce TEM lamellae from each of the two irradiated and two control samples. These lamellae were evaluated later at the same time as those extracted from samples after corrosion.

Corrosion

After two weeks of storage, the samples were wrapped with 200 Nickel wire around their periphery. The wire wrap was applied to be able to submerge and suspend the samples in FLiNaK salt. Careful attention was paid to keeping track of the irradiated surface and ensuring that the surface was unobstructed from wire wrapping. The appearance of the wrap sample is shown in

Figure 47. This procedure was carried out identically for two irradiated samples and two control samples. Once prepared, the four samples were corroded via submersion

in molten HF-purified FLiNaK salt. The procedure followed for preparation, corrosion, and cleaning of the samples was identical to that carried out in Chapter IV. Two differences to the procedure detailed there are that 1) the corrosion was done by dividing the salt volume into two glassy carbon crucibles, each with their own alumina ceramic lid fitted to suspend one control sample and one irradiated sample, and 2) a different batch of HF purified salt, also sourced from ORNL, was used for the experiment. The salt was divided into two parts for immersion of the samples in the two separate crucibles. The experiment conditions and sample naming convention are summarized in Table 5.a through 5.c.

Table 5. a) sample naming conventions and irradiation conditions

Sample names	Condition	Material	Origin	Dimensions (mm)	Final polish
IRR1	1 local DPA H+	Hastelloy N	Haynes International	~6 x 6 x 3	0.04um colloidal silica
IRR2	1 local DPA H+	--	--	--	--
C1	Control	--	--	--	--
C2	Control	--	--	--	--

b) Corrosion crucible materials

Crucible material	Crucible lid	Wire material
Pyrolitic Glassy Carbon	Alumina Ceramic	200 Nickel alloy

c) Salt corrosion conditions

Salt	Temperature (°C)	Corrosion Time (hours)	Environment gas (mBarr gauge)	Nominal H_2O/O_2 levels (ppm)
FLiNaK, ORNL HF purified	700	500 hours	Ar gas, ≈1.3mBarr	≈ 0.1/0.1

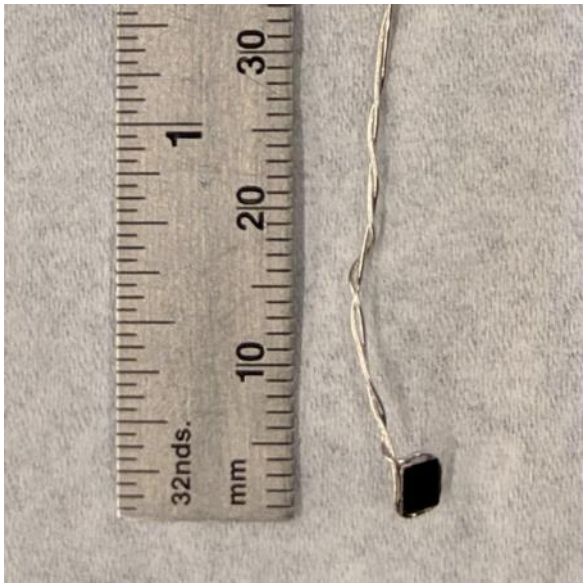

Figure 47. Example of Hastelloy N sample which is wire-wrapped after irradiation.

Post-corrosion analysis

Following cleaning, the samples were analyzed in two steps. First, FIB liftout was performed using a Tescan Lyra-3 Focused Ion Beam to prepare lamellae specimens with sizes approximate to 10 μm x 8 μm to extract TEM lamella from the irradiated/corroded surface of IRR1 and IRR2, and the corroded surfaces of C1 and C2. Two lamellae were prepared from each sample for a total of 8 lamellae. These lamellae and those produced from the samples after irradiation but before corrosion were analyzed using a using a 200 kV Thermo Scientific Talos F200X TEM. Elemental mapping was collected from the TEM specimens in the scanning transmission electron microscopy-energy dispersive X-ray spectroscopy (STEM-EDS) mode an Oxford Instruments SDD EDS detector. TEM and STEM-EDS at this step were used to evaluate

very fine microstructural evolution in the samples following corrosion. After completion of STEM/EDS analysis, the samples were coated in copper, bisected, and polished in the same manner as the sample described in Chapter IV. Following polishing, SEM-EDS and SEM-EBSD were performed to assess the gross depth of corrosion relative to the interaction surface of the samples. Experiment parameters used at this step replicate those described and carried out in chapter IV.

Results and Discussion

The results of the TEM/STEM-EDS the control sample (C1) after irradiation are shown in Figure 48. Figure 49 similarly highlights the TEM/STEM-EDS analysis performed on the first irradiated sample (IRR1) after proton implantation. Comparison of the microstructure and elemental distribution between the two samples reveals distinct features between the two conditions. Both sets of TEM/STEM-EDS data focused on a grain boundary in each respective sample. The micrographs show an accumulation of dislocations in proximity to the grain boundary. Dislocation loops and dislocation pileup are also evident as highlighted by white and yellow arrows, respectively. These dislocations are accompanied by select segregation of silicon. The metallic constituents evaluated in contrast do not appear to segregate towards the dislocations nor grain boundaries observed, either appearing depleted in regions rich in silicon (Cr,Fe) or with an unaffected distribution (Mo). Nickel is the exception, which appears to interact weakly with the dislocation structure, showing slight enrichment along some of the

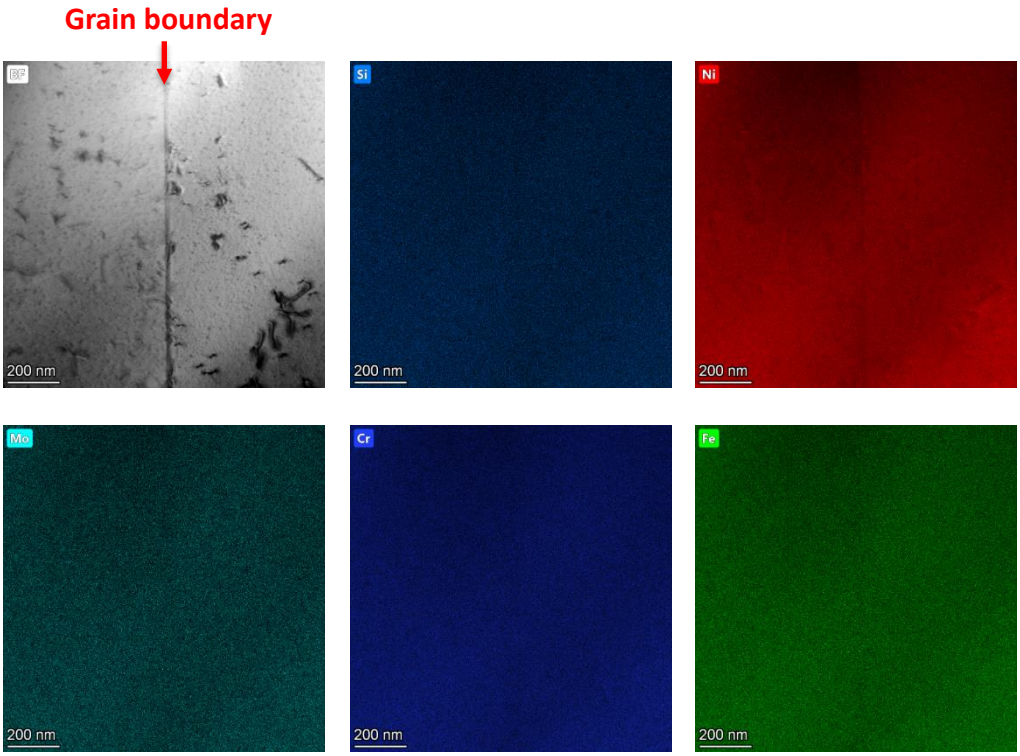

Figure 48. Highlight of STEM/EDS analysis performed along a typical grain boundary in control sample with same thermal history as irradiated sample.

larger network features. In C1 (Figure 48), which experienced the same thermal history as the irradiated sample, the dislocation structure is sparsely distributed and lacks the order of that observed in IRR1. Similarly, the STEM-EDS did not identify any elemental segregation at this step of the experiment for C1.

Secondary phase precipitation along grain boundaries is well documented in Hastelloy N after lengthy temperature exposures as low as 400°C [6, 7] But likely requires higher temperatures to develop in short to intermediate lengths of time [8]. This is unlikely to occur with the short thermal exposure experienced by the control sample

and is reflected in the results here. The accumulation of excess dislocations in IRR1 (and presumable IRR2) compared to the control sample is thus indicative of the effect of radiation damage on the microstructure of Hastelloy N after only modest radiation damage. Moreover, the liberation of point defects through radiation damage [1] enhances mobility of fast diffusing solutes in the alloy, which are attracted to the tensile strain fields around dislocations via Cottrell atmospheres [9, 10]. Silicon being the

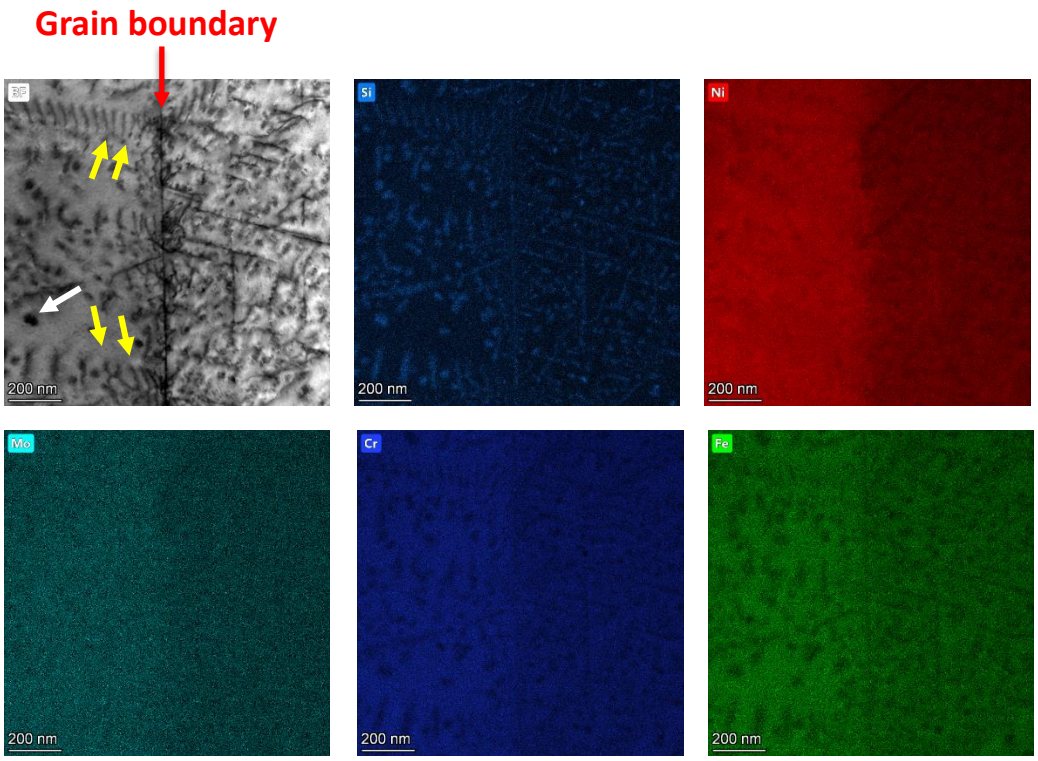

Figure 49. highlight of STEM/EDS analysis performed on proton irradiated sample and before corrosion. Evaluation in the midrange of the damage profile and along a grain boundary shows distinct silicon segregation and ordering interacting with dislocation structure.

smallest atom in the constituents of Hastelloy N will preferentially diffuse and segregate to these accumulated dislocations, explaining the segregation observed in Figure 49.

Similar microstructural changes are observed away from grain boundaries. Figure 50 highlights BF-TEM and the silicon EDS signal collected from an intragranular region. The BF-TEM micrograph shows several prominent features, including overlapping dislocations edge lines, randomly dispersed as well as ordered dislocation loops, and dislocation pileups. Similar to the behavior observed in Figure 49, the EDS signal shows Si segregation overlapping with the dislocation structures shown in the BF-TEM micrograph. Si does not discriminate against any type of defect structure observed, as it appears to distribute evenly amongst all identified dislocations.

Figure 51, Figure 52, and Figure 53 summarize some of the BF-TEM and STEM/EDS data collected from control samples 1 and 2 (C1, C2) and irradiated samples

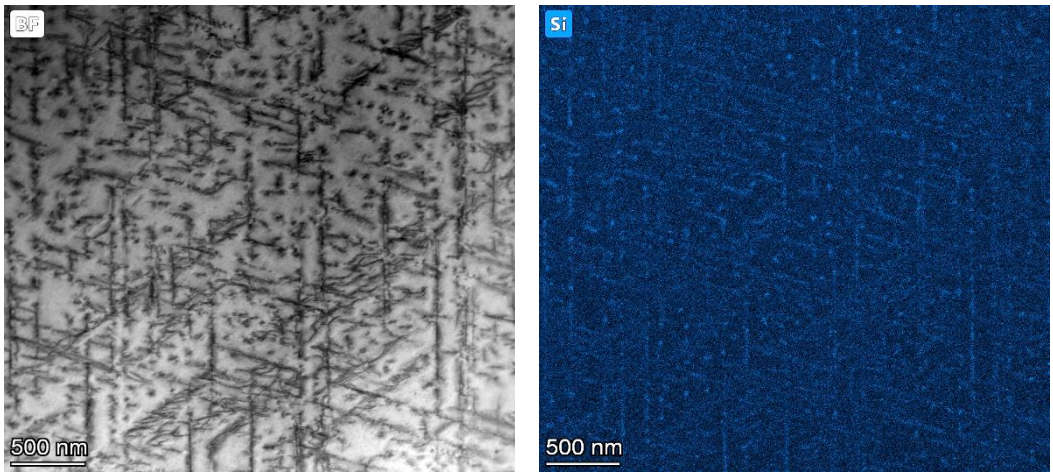

Figure 50. Additional STEM/EDS image away from grain boundaries shows similar ordering of segregated silicon structure.

1 and 2 (IRR1, IRR2) following the corrosion portion of the experiment. Ion damage and distribution after irradiation peaks at approximately 25 μm, which is notably beyond the range of the viewfield chosen for TEM and STEM/EDS analysis. The BF-TEM micrographs and EDS signals therefore are independent of the influence of hydrogen accumulation at the max depth of implantation and the significantly higher damage which occurs at the Bragg peak. Comparing the TEM and STEM/EDS data between the four samples reveals a few basic and persistent trends. Mo and Cr were chosen for display in the figures due to their importance in the corrosion resistance and susceptibility. In all four samples, Cr was always accompanied by O. Similarly, Mo was always accompanied by Si. For these reasons, O and Si maps are not shown independently but their presence can be inferred through the occurrence of Cr and Mo respectively. Oxygen is not a native constituent of Hastelloy N but is a commonly found contaminant due to the hydroscopic nature of ionic fluoride salts. Short corrosion studies must often divide corrosion measurements to distinguish between non-equilibrium and steady state corrosion rates, the transition between the two occurring when highly reactive contaminants such as oxygen are completely exhausted [11]. The steady ingress of contaminants is considered by some to be inevitable, which has spurred significant efforts in developing online salt purification systems for MSRs [12, 13]. Oxide phases observed in the samples are small and restricted to the near-surface region and are not considered to have significantly affected gross corrosion behavior.

In all four samples (Figure 51 a & b), Figure 52, and Figure 53), Cr and O rich phases can be observed close to the surface. In IRR1 (Figure 52), these phases are found

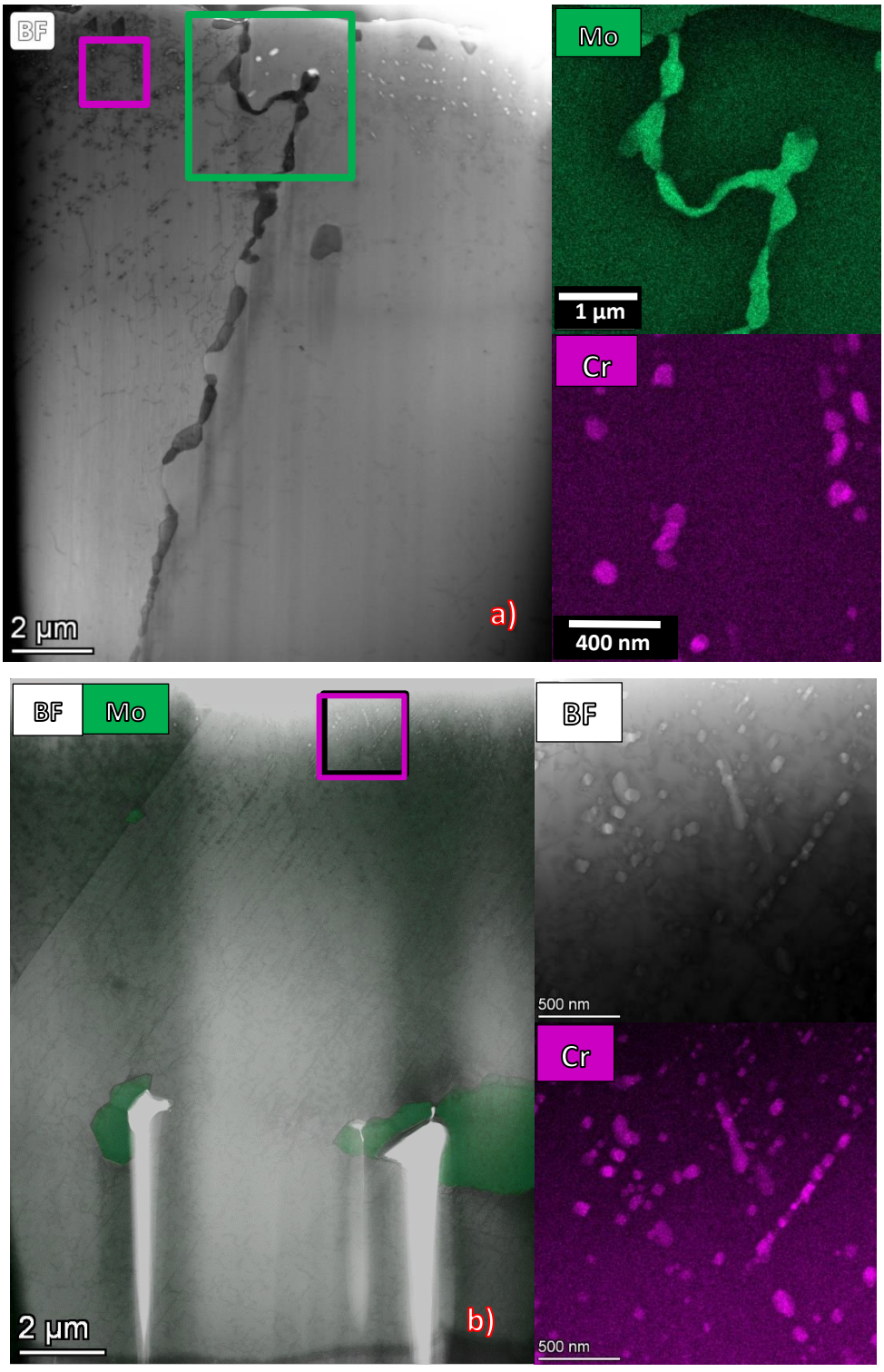

Figure 51. Post-corrosion BF-TEM micrographs and select Cr and Mo EDS data for control samples a) C1 and b) C2.

slightly deeper into sample near a grain boundary. The Cr-O phases are also slightly larger and more globular in IRR1. For all four samples the Cr-O phases are as small as 10s of nanometers and as large as 100s of nanometers. Additionally, the Cr-O rich phases are entangled with dislocation networks present in each of the four samples. With the control samples, these dislocation networks are confined to the surface whereas in the IRR1 sample at least, the network appears to extend outward from one of the inward-facing grain boundaries. These dislocation structures are highly ordered but overall, do not cross in the same manner as observed in the irradiated sample in Figure 50. The dislocations instead are largely aligned along one plane, possibly the dominant slip plane of the FCC system. The precipitates follow the same alignment, their formation likely catalyzed by the dislocation network.

The crisscrossing dislocation structure in the irradiated samples described in Figure 49 and Figure 50 are largely absent in the samples following the corrosion regimen. The enhanced defect gradient under dissolution of alloy constituents into the salt, as well as higher diffusion rates at 700°C would have caused in increased defect mobility. This dynamic environment likely drove the system towards a new thermodynamic equilibrium and enabled the dissolution of the original silicon-rich dislocation networks. Observation of the Mo distribution in IRR1 and IRR2 as illustrated in Figure 52, and Figure 53 suggests that the crossing Si-rich dislocation networks catalyzed the formation of, and was eventually replaced by, dispersed Mo-Si rich phases. In all four phases, the secondary phases which typically precipitate along grain

boundaries in Hastelloy N are present, presumably the well document $M_{12}C$ type Mo-Cr-Si rich pseudocarbides.

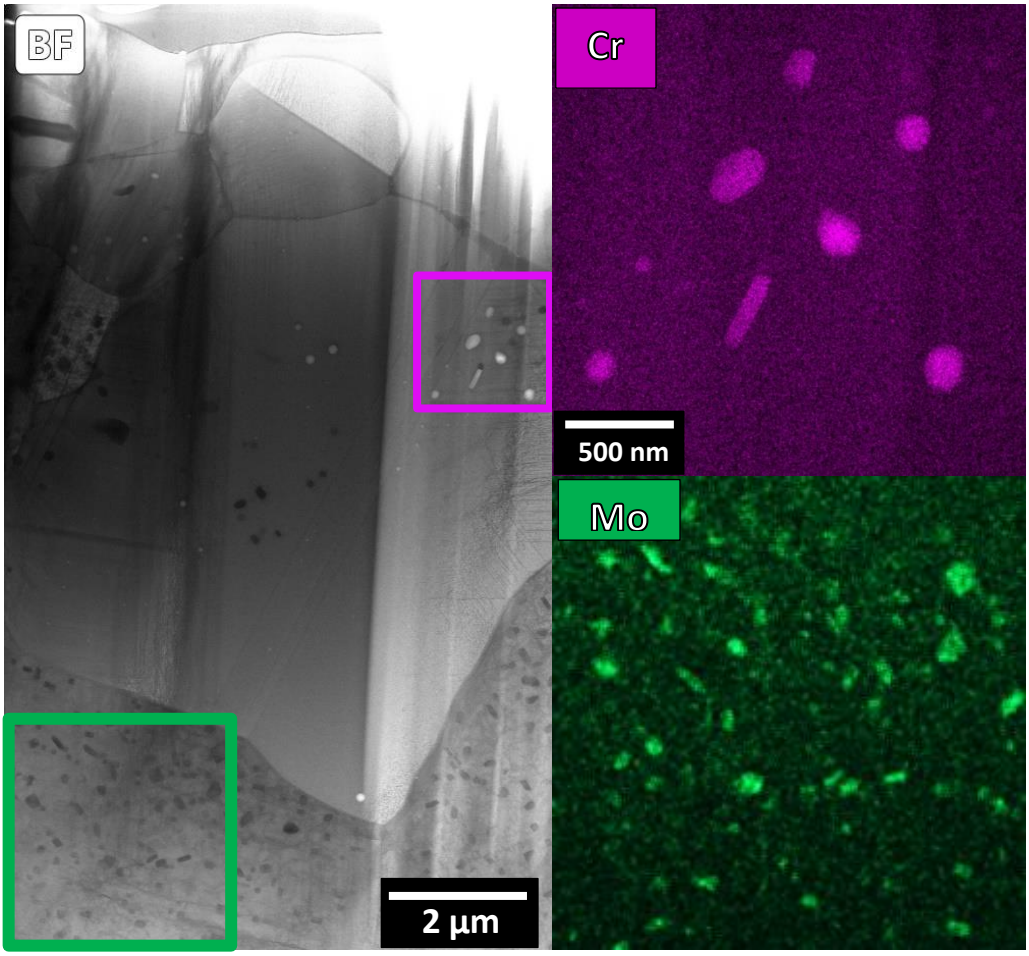

Figure 52. BF-TEM and Cr and Mo EDS spectra collected in the IRR1 sample.

Only in the irradiated samples however are new intragranular Mo-Si rich phases present, an atypical occurrence in the high temperature thermal evolution of Hastelloy N. Grain boundaries tend to preferentially enable precipitation of secondary phases due to the lower energy barriers at these interfaces. The presence of intragranular precipitates in

the irradiated region suggests that the dislocation network and surplus point defects resulting from proton irradiation, combined with the heightened defect mobility during

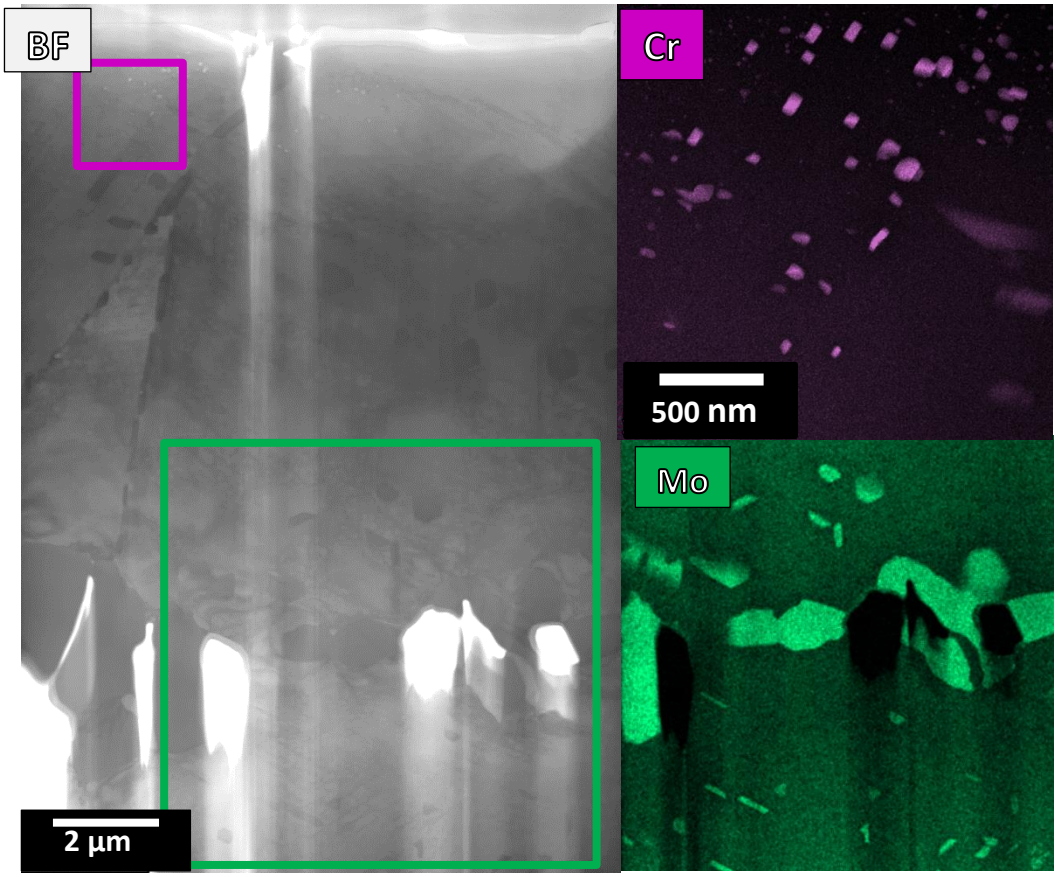

Figure 53. IRR2 post C.

corrosion, enabled the precipitation of these unique Mo-Si rich phases. The intragranular Mo-Si phases are quite fine and evenly distributed in the first irradiated sample (Figure 52) whereas they are more sparse and significantly larger in the second irradiated sample (Figure 53). The intragranular phases can be seen spaced away from the grain boundaries on the lower half of the second sample and are almost overshadowed by the

damage to the TEM lamella and large M_6C stringers which are native to Hastelloy N after annealing treatment.

Results of the SEM-EDS analysis performed on the cross-section face of the corroded samples show typical features of Hastelloy N corroded in fluoride molten salts and/or exposed to elevated temperatures. Data collected on all four samples did not

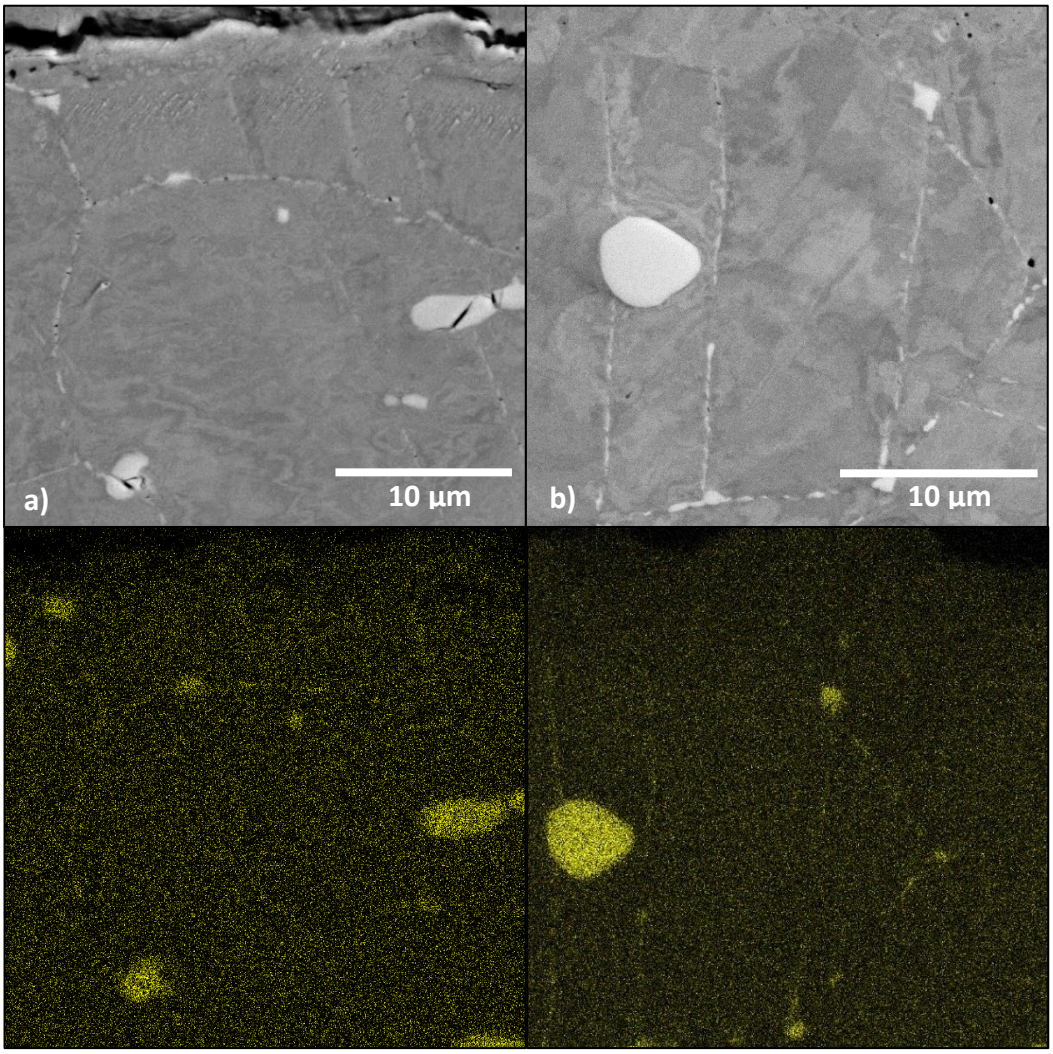

Figure 54. BSE-SEM images of near-surface grain morphology of Hastelloy N samples after corrosion testing for samples a) C1 b) IRR1. Mo EDS maps are shown below each BSE-SEM image.

include detectable levels of oxygen and so it was assumed that contaminant oxygen incursion was negligible despite its appearance in STEM-EDS results. Both the control samples and irradiated samples shown precipitation of secondary grain boundary phases. Figure 54 shows BSE-SEM images taken near the surface for a) control sample 1 (C1) and b) proton irradiated sample 1 (IRR1). Both samples show typical grain boundary precipitation which is endemic of Hastelloy N subjected to high temperatures for extended periods. The BSE images provide some elemental contrast due to energy loss and scatter efficiency caused by backscatter with heavy and light elements. Light features are more richly populated in heavy elements for which backscatter energy loss is lower and so it can be deduced that the globular M_6C precipitates and the newly formed grain boundary precipitates are of similar composition.

The high contrast of the BSE enabled identification of precipitate formations which appear to extend perpendicularly from the main grain boundaries towards the interior of the grains. These features are more prevalent in the irradiated samples as shown in Figure 54.b but are also observed with slightly less intensity in the control sample in Figure 54.a. It is speculated, but cannot be verified at this time, that these precipitate structures are following the pathways of annealing twin boundaries left over from the manufacturing of the alloy. These twin boundaries may serve as additional aggregation and diffusion pathways which merit further investigation in a separate study. Figure 54.c and Figure 54.d highlight the EDS signal for Mo distribution corresponding to the regions illustrated in Figure 54.a and Figure 54.b respectively. The Mo

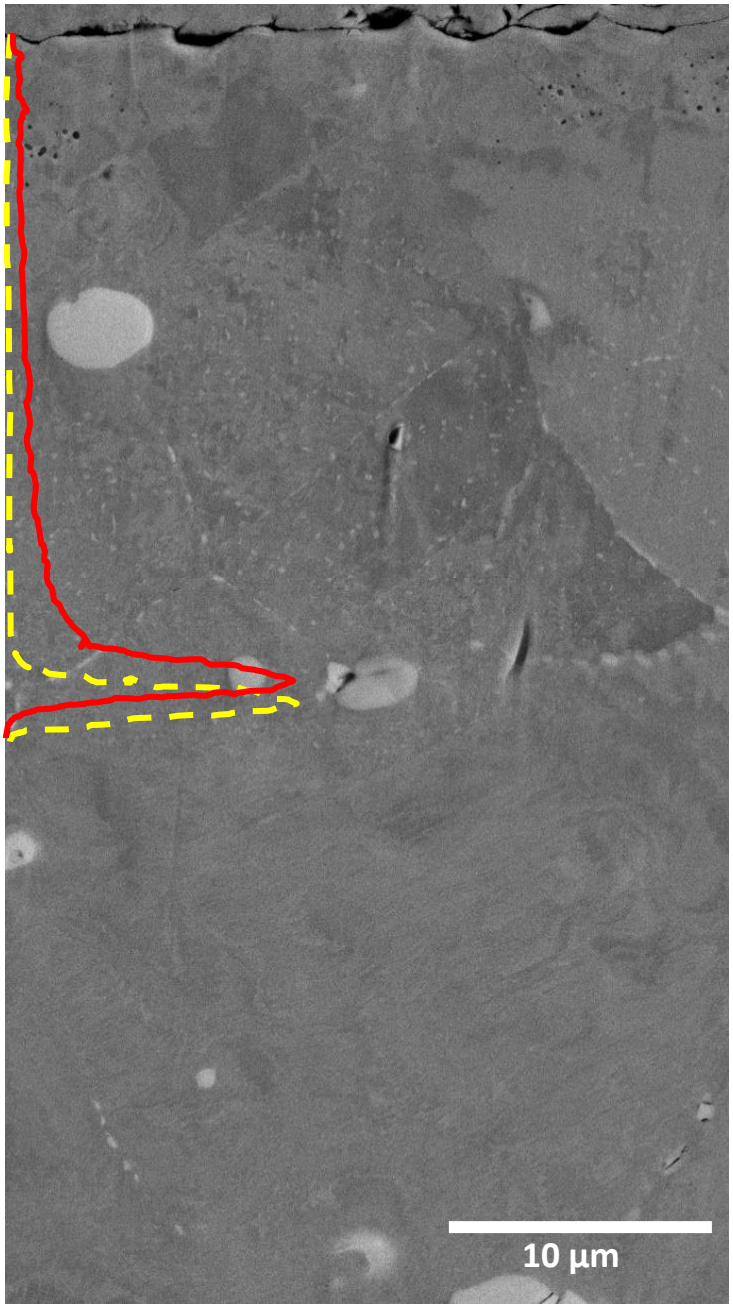

Further observation revealed the presence of fine intragranular "speckling" features on the irradiated samples close to the corrosion interface which were absent in Figure 55. BSE-SEM image of IRR2 sample showcasing intragranular "speckling" features which do not extend past the range of ion damage.

distribution for IRR1 (Figure 54.d) shows clearly that the linear precipitate formations extending into the grains are indeed rich in the heavy element Mo. The same is observed for the C1 sample (Figure 54.c) although the phases do not appear as well-resolved as in the irradiated sample. the control samples.

Figure 55 shows the BSE-SEM image of a near-surface region of IRR1. A fine white phase can be observed dotting across the upper half of the image, especially against the darkly colored grain which spans most of the upper image. These speckles disappear abruptly past the SRIM-predicted ion range which is superimposed onto the image, and it is likely that these features are a direct result of the pre-irradiation. Closer to the corrosion interface at the top of the sample, the speckling becomes more and more sparse and eventually disappears. Dark voids are also observed close to the surface which are presumably empty volumes. These voids are both intragranular and disconnected from one another and might be the remnants of the speckling features having been preferably depleted through corrosion kinetics. The BSE contrast demonstrates a similar composition between the grain boundary precipitates, the native M_6C carbides, and the speckling features. These features are possibly the same intragranular Mo-Si rich phases observed in the TEM and STEM/EDS micrographs (Figure 52 and Figure 53).

Results of the SEM-EDS line scan analysis show that the irradiated samples suffer more significant depletion of Cr, Mo, and Si than their control counterparts. Figure 56 illustrates the line scan data collected for Cr and Mo at each of the four samples. Si was excluded from the figure for brevity but follows similar trends. Each

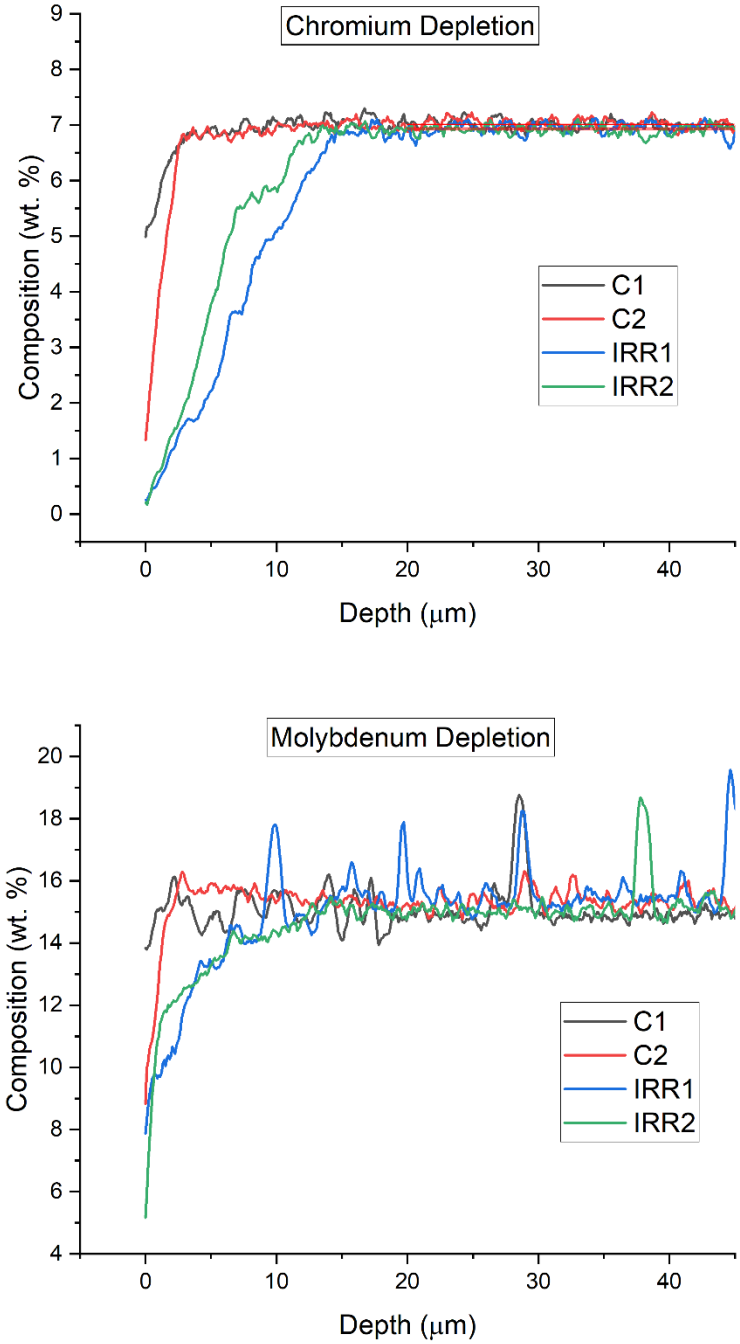

Figure 56. EDS line scan results for the four samples for chromium (top) and molybdenum (bottom) show clear enhanced depletion for these alloy-critical elements after irradiation.

line represents the average of 10 parallel scans consisting of 500 data points each along a 50μm path. Each signal is also smoothed using a 5-point adjacent averaging scheme to remove noise and clarify the overall depletion trends. While there is some variably in the depth of depletion in the samples, the results are consistent in showing irradiation-enhanced corrosion, especially in the chromium signals. The Mo trends are less smooth than those for chromium. Line scan paths were chosen which minimized interaction with secondary phases as much as possible, but these phases were often unavoidable. The EDS signal is thus influenced by the presence of grains boundary precipitates in all samples and the intragranular phases in the irradiated samples which are possibly Mo-rich. Fe tended to be enriched reciprocally to where Mo and Cr were most severely

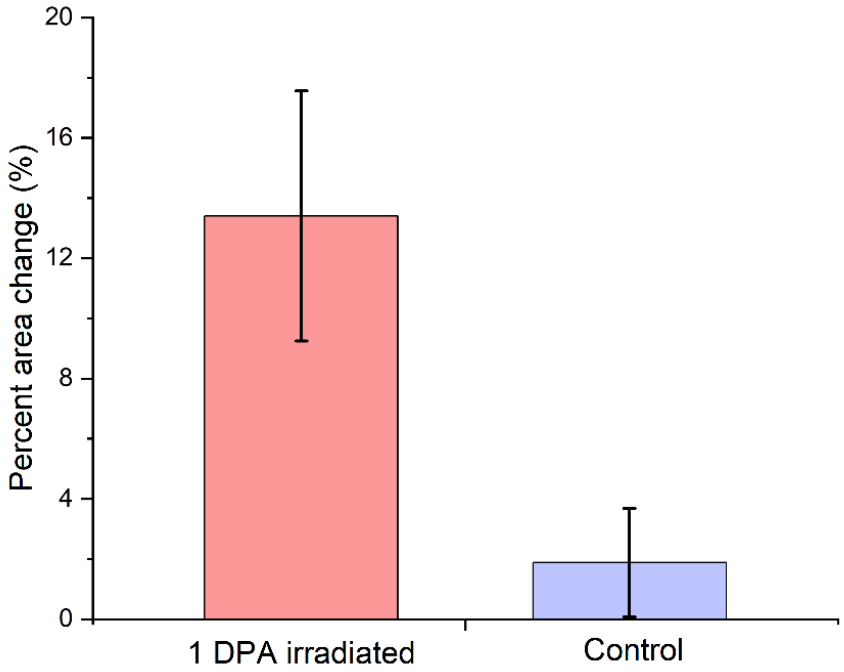

Figure 57. Comparison of percent area change calculated as a metric for Cr depletion in the irradiated and control sample sets (two data points each). Error bars signify a 2σ confidence interval.

depleted, a result of the weighted averaging and normalization of the EDS signals. Further statistical analysis was focused on the results of the Cr EDS signals using the methodology described in Chapter IV for Hastelloy N corroded under static strain loading (see Figure 40). The percent area depletion calculated for each sample was treated as an individual data point. Using these points, the mean corrosion depletion and standard deviation was calculated for the control and irradiated sample sets. While each set only contained two data points, the close grouping of the data in each set gives high confidence in the results. Figure 57 summarizes the area depletion analysis for Cr in the irradiated and control samples. The lack of overlap in the 2σ confidence intervals shown support the conclusion of unambiguous corrosion enhancement after irradiation.

Studies on the effect of irradiation on corrosion draw a variety of conclusions which depend greatly on the methodology used to approach the phenomenon. When subjecting Ni-20Cr binary alloy foils to simultaneous irradiation and corrosion in FLiNaK with EuF_3 additive, Zhou et. Al found that irradiation appeared to hinder the onset of corrosion [14]. Relative corrosion between the portions of the sample exposed or protected from the proton beam was measured via penetration depth of void volume along grain boundaries. It was hypothesized that the point defect surplus resulting from irradiation enhanced interstitial movement towards grain boundaries of both Cr and Ni atoms, which enabled the "self-healing" recombination of Ni and Cr with corrosion-injected interstitials. In doing so, Cr could not be depleted despite its preferential dissolution into the fluoride salt melt [15], as both atoms of Ni and Cr were piped to grain boundaries for recombination. This conclusion works heavily towards explaining

the change in grain boundary void volume and crack penetration depth observed in the Ni-20Cr sample. Uniform corrosion of Cr through the bulk volume of the sample outwards into the melt was not discussed in the results of this study. Cr dissolution through the grain volume has been noted to be of high importance in Hastelloy N [16], especially in pure salts where grain boundary attack is less prevalent [17, 18]. Relying on grain boundary crack depth as the sole metric of corrosion likely overlooked important bulk diffusion mechanisms. It is thus unclear whether corrosion was inhibited under irradiation or that only the main pathway for Cr egress was altered.

Other studies have shown mixed effects of irradiation on corrosion. Ezell, et. Al evaluated in-situ irradiation corrosion with chloride salts but showed no change in the susceptibility of Hastelloy N after 21 hours of exposure to a neutron fluence of ~10^{12} $n \cdot cm^{-2}s^{-1}$ [19]. This relatively low fluence was likely insufficient to cause significant change in the salt-tolerant alloy but was shown to exacerbate corrosion in 316SS exposed to wet salts. Bakai combined electron irradiation with simultaneous corrosion of Hastelloy N in $NaFZrF_4$ salt and showed a definite exacerbation in corrosion [20]. The exact cause of this increase however was likely an electrolysis effect due to surplus electron injection. While electron irradiation can penetrate deeply provide similar volumetric interaction distributions as neutron irradiation [1], they fail to cause similar damage rates and defect structures as irradiation via heavier particles. Ex-situ helium irradiation is shown to accelerate Cr depletion in Hastelloy N [21-23] but isolating the effects of radiation damage from those of migration and accumulation of helium is challenging due to low solubility in nickel systems [4].

As demonstrated in Figure 49, an extensive dislocation network was formed in the irradiated samples. “Pipe diffusion”, where diffusion of point defects is facilitated through dislocation networks [24] may explain the accelerated egress of Cr through the in the irradiated samples. The energy field of the dislocation cores results in a localized region with lower activation barriers for diffusion [25, 26]. The increase to diffusion rates can be profound. Legros et. Al showed that diffusion rates of Si in an Aluminum thin film increased by ≈3 orders of magnitude when facilitated by dislocations [27]. The STEM-EDS data collected in the irradiated samples seems to support the hypothesized role of irradiation dislocation networks in enhancing Cr diffusion through the bulk lattice.

Figure 58 highlights complex interactions between several microstructural features observed in the IRR1 STEM-EDS data. The highlighted grain incudes dozens of small, circular Mo-Cr rich features which appear to be pinning a dense tangle of dislocations. The circular features are depleted in Fe and Ni which is otherwise normally distributed around this and the adjacent grains. The circular features are speculated to be secondary phases due to their globular shape and distinct elemental makeup.

The coincidence of the dense dislocation network and surrounding Cr enrichment in Figure 58 is believed to be remnant evidence of pipe diffusion in the irradiated samples. Pipe diffusion has also been documented to enable fine $M_{23}C_6$ carbide phase precipitation and coarsening in René 88DT nickel superalloy [28]. Such dislocation-

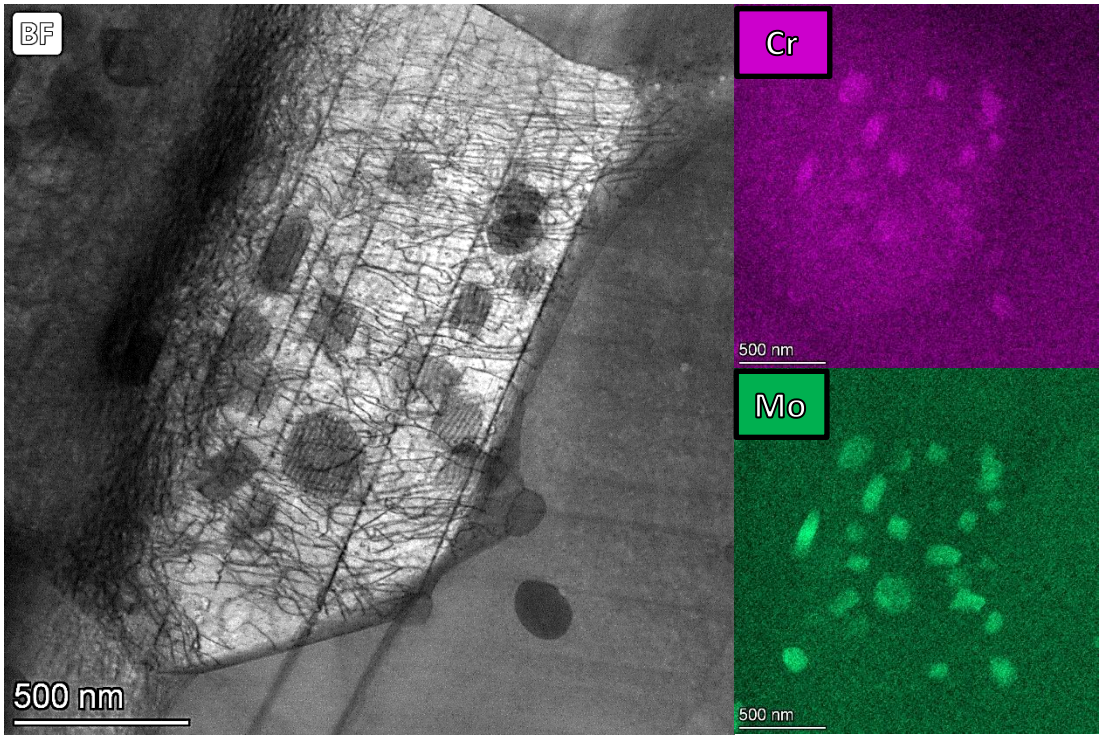

Figure 58. STEM-EDS data collected from IRR1 lamella showcases small grain with dense accumulation of dislocations and well as significant Cr enrichment.

facilitated precipitation may have been at work in the formation of the Mo-Si rich intragranular phases present in the irradiated samples. If dislocation network formation and pipe diffusion are indeed responsible for the accelerated egress of Cr, the magnitude of their effect here is significant. Irradiation induced segregation is understood to result from the flow of surplus vacancy towards defect trapping sites such as grain boundaries known as the inverse Kirkendall effect, resulting in a counterflow of fast-diffusing elements [29]. Theoretically, this phenomenon should force diffusion of Cr inwards towards grain interiors and inhibit dissolution into the salt.

For ex-situ irradiation/corrosion such as was performed in the present study, the pre-irradiation step causes damage leaving dislocations and surplus vacancies in the near-surface region. These surplus defect features suddenly come under the influence of new forces when exposed to corrosion at higher temperatures than the initial irradiation, driving the system towards a new equilibrium. It is thus unclear whether the behavior observed here is indicative of typical irradiation-corrosion behavior or unique to irradiation damage pre-loading conditions. Point defect equilibrium may be completely different under in-situ corrosion/irradiation and under different temperatures to prevent the formation of these dislocation networks at all. Alternatively, if dislocation networks are stable under simultaneous corrosion/irradiation, the exacerbation of corrosion enabled by pipe diffusion may be constant and severe.

References

[1] G.S. Was, Fundamentals of Radiation Materials Science: Metals and Alloys, Fundamentals of Radiation Materials Science: Metals and Alloys (2007) 1-827.

[2] J.C. Haley, S. de Moraes Shubeita, P. Wady, A.J. London, G.R. Odette, S. Lozano-Perez, S.G. Roberts, Microstructural examination of neutron, proton and self-ion irradiation damage in a model Fe9Cr alloy, Journal of Nuclear Materials 533 (2020) 152130.

[3] L. Tournadre, F. Onimus, J.L. Béchade, D. Gilbon, J.M. Cloué, J.P. Mardon, X. Feaugas, O. Toader, C. Bachelet, Experimental study of the nucleation and growth of c-

component loops under charged particle irradiations of recrystallized Zircaloy-4, Journal of Nuclear Materials 425(1) (2012) 76-82.

[4] W.G. Wolfer, C.D. Van Siclen, S.M. Foiles, J.B. Adams, Helium solubility in solid and liquid nickel, Acta Metallurgica 37(2) (1989) 579-585.

[5] J.F. Ziegler, M. Ziegler, J.P. Biersack, SRIM The stopping and range of ions in matter (2010), Nuclear Instruments & Methods in Physics Research Section B-beam Interactions With Materials and Atoms 268 (2008) 1818-1823.

[6] R.E. Gehlbach, H.E. McCoy, Phase Instability In Hastelloy N, International Symposium on Structural Stability in Superalloys, 1968, pp. 346-366.

[7] F. Han, L. Jiang, X. Ye, Y. Lu, Z. Li, X. Zhou, Carbides Evolution in a Ni-16Mo-7Cr Base Superalloy during Long-Term Thermal Exposure, Materials (Basel), 2017.

[8] H.E. McCoy, The Influence of Several Metallurgical Variables on the Tensile Properties of Hastelloy N, Oak Ridge National Lab., Tenn., 1964.

[9] J. Völkl, G. Alefeld, Diffusion of hydrogen in metals, in: G. Alefeld, J. Völkl (Eds.), Hydrogen in Metals I: Basic Properties, Springer Berlin Heidelberg, Berlin, Heidelberg, 1978, pp. 321-348.

[10] A.H. Cottrell, B.A. Bilby, Dislocation Theory of Yielding and Strain Ageing of Iron, Proceedings of the Physical Society. Section A 62(1) (1949) 49-62.

[11] S.S. Raiman, S. Lee, Aggregation and data analysis of corrosion studies in molten chloride and fluoride salts, Journal of Nuclear Materials 511 (2018) 523-535.

[12] A.L. Qualls, Advanced Reactor Technology Program Molten Salt Reactor Campaign FY 2018 Summary, ; Oak Ridge National Lab. (ORNL), Oak Ridge, TN (United States), 2018, p. Medium: ED; Size: 44 p.

[13] J. Zhang, C.W. Forsberg, M.F. Simpson, S. Guo, S.T. Lam, R.O. Scarlat, F. Carotti, K.J. Chan, P.M. Singh, W. Doniger, K. Sridharan, J.R. Keiser, Redox potential control in molten salt systems for corrosion mitigation, Corrosion Science (2018) Medium: ED; Size: p. 44-53.

[14] W. Zhou, Y. Yang, G. Zheng, K.B. Woller, P.W. Stahle, A.M. Minor, M.P. Short, Proton irradiation-decelerated intergranular corrosion of Ni-Cr alloys in molten salt, Nature Communications 11(1) (2020) 3430.

[15] L.C. Olson, J.W. Ambrosek, K. Sridharan, M.H. Anderson, T.R. Allen, Materials corrosion in molten LiF–NaF–KF salt, Journal of Fluorine Chemistry 130(1) (2009) 67-73.

[16] I.R.B. Evans, J.H. DeVan, G.M. Watson, SELF-DIFFUSION OF CHROMIUM IN NICKEL-BASE ALLOYS, United States, 1961.

[17] F.-Y. Ouyang, C.-H. Chang, J.-J. Kai, Long-term corrosion behaviors of Hastelloy-N and Hastelloy-B3 in moisture-containing molten FLiNaK salt environments, Journal of Nuclear Materials 446(1) (2014) 81-89.

[18] F.-Y. Ouyang, C.-H. Chang, B.-C. You, T.-K. Yeh, J.-J. Kai, Effect of moisture on corrosion of Ni-based alloys in molten alkali fluoride FLiNaK salt environments, Journal of Nuclear Materials 437(1) (2013) 201-207.

[19] N.D.B. Ezell, S.S. Raiman, J.M. Kurley, J. McDuffee, Neutron irradiation of alloy N and 316L stainless steel in contact with a molten chloride salt, Nuclear Engineering and Technology 53(3) (2021) 920-926.
[20] A.S. Bakai, Combined Effect of Molten Fluoride Salt and Irradiation on Ni-based Alloys, in: V. Ghetta, D. Gorse, D. Mazière, V. Pontikis (Eds.) Materials Issues for Generation IV Systems, Springer Netherlands, Dordrecht, 2008, pp. 537-557.
[21] G. Lei, C. Li, Z. Jiang, H. Huang, Irradiation accelerated fluoride molten salt corrosion of nickel-based UNS N10003 alloy revealed by X-ray absorption fine structure, Corrosion Science 165 (2020) 108408.
[22] M. Liu, J. Hou, F. Han, R. Liu, X. Zhou, Effects of He ion irradiation on the corrosion performance of alloy GH3535 welded joint in molten FLiNaK, Corrosion Science 146 (2019) 172-178.
[23] G. Lei, S. Yang, H. Huang, Q. Huang, R. Liu, W. Zhang, G. Yu, L. Yan, Corrosion-driven outward migration and growth of helium bubbles in a nickel-based alloy in high-temperature molten salt environment, Corrosion Science 153 (2019) 47-52.
[24] J. Pelleg, Diffusion in Dislocations, in: J. Pelleg (Ed.), Diffusion in Ceramics, Springer International Publishing, Cham, 2016, pp. 87-94.
[25] J. Huang, M. Meyer, V. Pontikis, Is pipe diffusion in metals vacancy controlled? A molecular dynamics study of an edge dislocation in copper, Physical Review Letters 63(6) (1989) 628-631.

[26] J. Rabier, M.P. Puls, Atomistic calculations of point-defect interaction and migration energies in the core of an edge dislocation in NaCl, Philosophical Magazine A 59(3) (1989) 533-546.

[27] M. Legros, G. Dehm, E. Arzt, T.J. Balk, Observation of Giant Diffusivity Along Dislocation Cores, Science 319(5870) (2008) 1646-1649.

[28] Y. Gu, J.C. Stinville, P.G. Callahan, M.P. Echlin, T.M. Pollock, J.A. El-Awady, Slip delocalization and diffusion mediated carbide formation during fatigue of a nickel-base superalloy, International Journal of Fatigue 145 (2021) 106077.

[29] A. Marwick, Segregation in irradiated alloys: The inverse Kirkendall effect and the effect of constitution on void swelling, Journal of Physics F: Metal Physics 8 (2001) 1849.

CHAPTER VI EVALUATION OF MECHANICAL PROPERTY EVOLUTION IN HASTELLOY N AFTER ION IRRADIATION VIA MICROPILLAR COMPRESSION

Introduction

Although Hastelloy N has shown promise for MSR application, systematic studies considering the influence of irradiation damage are needed for further performance testing and continuous structural and composition optimization. Unlike other FCC alloys such as AISI 316SS, Hastelloy N belongs to the group of swelling resistant materials in which self-ion-irradiation does not induce void swelling (if helium is not co-injected). Early studies used various gas ion irradiations to simulate reactor environments. For Hastelloy N irradiated at room temperature using Ar ions, irradiation induced black dot-like defects at a very low dose (0.4 DPA), and high-density dislocation loops were found at higher dpa. With increasing dpa, dislocation networks developed [1].

For Hastelloy N irradiated by Xe ions and characterized by nanoindentation, it was found that irradiation hardening is correlated with creep plasticity [2]. When irradiated by He, Xe, and a combined He + Xe irradiation, a synergistic effect in hardening mechanisms due to various types of defects has been reported [3]. These early studies have shown the unique irradiation responses of Hastelloy N in comparison with other alloys, such as easy dislocation network development at room temperature irradiations and at low damage levels. The usage of gas ion irradiations at relatively low energy however, makes both structural characterization and mechanical property testing challenging due to surface effects and a mixture of irradiation defect and gas bubbles. Irradiations at room temperature also have difficulties resembling reactor environments [1].

To further understand the performance changes caused by irradiation damage on Hastelloy N, motivation arose to study irradiation hardening and deformation mechanisms. For such investigations, the size of the irradiated region is important. Proton irradiations of a few MeV have been widely used during the past due to its capability to damage a region up to tens of microns [4, 5], large enough for micron-scale mechanical testing. A large grain was selected to prepare multiple pillars on the cross-sections of the irradiated sample to study compression responses of regions at different damage levels. Since the crystal orientation of the selected domain is known, resolved shear stress on the gliding planes of each pillar could be determined. Micropillar compression testing is a mature technique and similar approaches of testing pillars of the same orientation have been reported before with success [6, 7].

Procedure

Irradiation

A small, square sample of Hastelloy N, approximately 3mm on each side, was mounted and mechanically polished down to 0.04μm silica solution on one face to expose the grain structure. After polishing the first surface (henceforth referred to as surface A), the sample was remounted at a 90-degree angle so that a perpendicular face relative to the first (surface B) could be polished identically. The polished sample was evaluated via SE-SEM using a Tescan Lyra-3 SEM and Focused Ion Beam system. This was done to ensure that the meeting place of the two polished surfaces was sufficiently sharp and well-defined for the subsequent analyses. Figure 59 shows the sample under

SE-SEM after polishing and prior to irradiation. The two polished samples are shown by tilting the SEM stage 45° at an angle to see the two surfaces at once, which are perpendicular to each other. The SEM clearly shows the primary and secondary phase structure of the polished sample, as well as some annealing twins characteristic of the alloy.

After ensuring the quality of the polish, the sample was irradiated with 2.5 MeV protons at 500°C using identical irradiation parameters and configuration as described in Chapter V. The sample for pillar compression was irradiated simultaneously with the samples used for the corrosion testing in Chapter V and so conditions and evaluation of the samples are considered equivalent. The sample was irradiated with surface A oriented towards to the beam. The irradiation was carried out to a damage level of 1

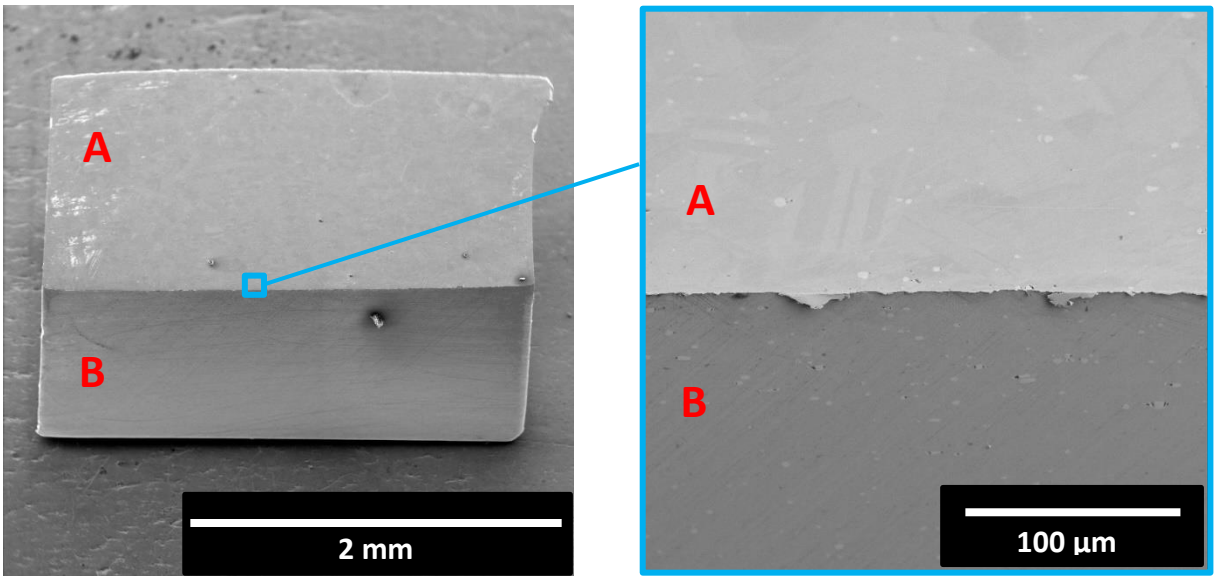

Figure 59. SE-SEM showing exposed grains of Hastelloy N sample prepared by mechanically polishing two adjacent and perpendicular faces, labeled A (irradiated face) and B (pillar face).

DPA local (approximately 3.27×10^{19} ions·cm^{-2}), corresponding to a peak damage of approximately 18 DPA occurring at 25.5μm. The fluence to achieve the desired damage was estimated using SRIM-2013 in the Kichin-Pease quick damage mode [8]. Local DPA reflects the total damage occurring at half the ion range, where the distribution is relatively flat. A control sample was also mounted to the irradiation stage but kept outside of the beam spot. This sample experienced the same thermal history as the irradiated sample.

Pillaring

After completing the irradiation, SEM-EBSD was performed on side B close to the A-B edge to map the grain morphology. The EBSD data was used to identify grains large enough along the A-B edge so that four pillars could be milled on a single grain.

The grain orientation map of the final location is illustrated in Figure 60. The grain chosen for pillar compression is approximately of orientation [1 4 6]. Due to the hot-rolling finish used by the manufacturer to shape the Hastelloy N coupon, many of grains were fragmented or featured annealing twin boundaries. The pillar sites were chosen to avoid the annealing twin bands crossing the entire diagonal length. The orientation data collected were also used to calculate Schmid factors and thus the critical resolved shear stress present during compression of the micropillars. This ensured that all pillars would have the same crystallographic orientation and would deform in an identical manner. This also ensured that they data collected from the four pillars were directly comparable.

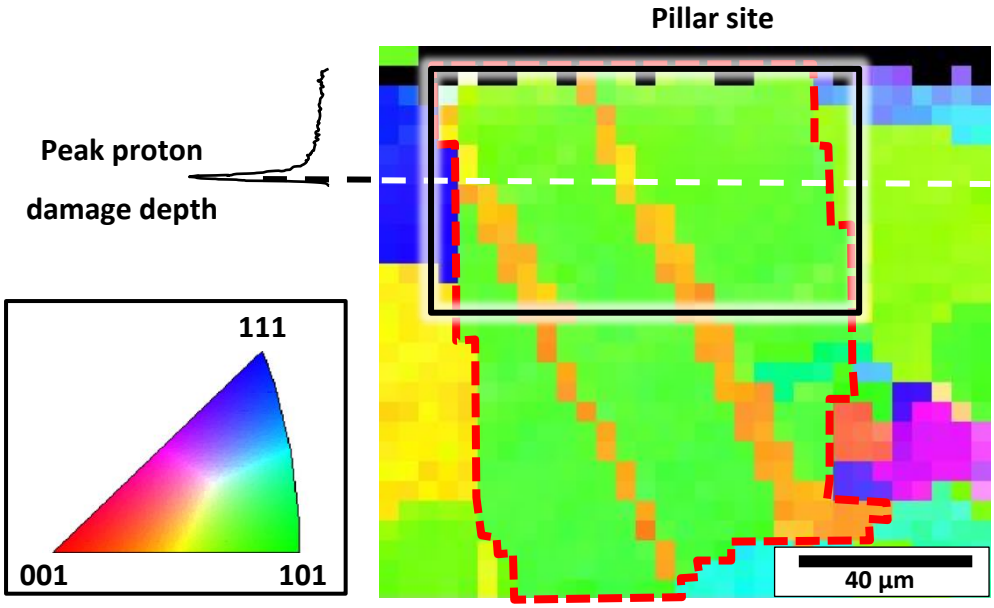

Figure 60. SEM-EBSD polar orientation map illustrating the grain selected for milling compression pillars.

The location of the pillars on surface B were distributed at different depths along surface B to reflect different average DPA levels. The positions of the fabricated pillars relative to the proton damage and ion distribution is illustrated in Figure 61. FIB was performed to fabricate mechanical pillars into surface B, perpendicular to the direction of ion irradiation. Four total pillars of dimensions 3µm × 3µm × 6µm were fabricated using a combination of xenon and gallium FIB at different steps. The final pillars after FIB milling and before compression testing are shown in Figure 62. The image features an overlay of the EBSD data shown in Figure 60 to emphasize the location of the pillars relative to the grain selected for analysis. Pillar compression was next performed using a Hysitron PI-85 Picoindenter inside a Tescan LYRA-3 Model GMH. The strain rate of each compression was 0.001 s^{-1}.

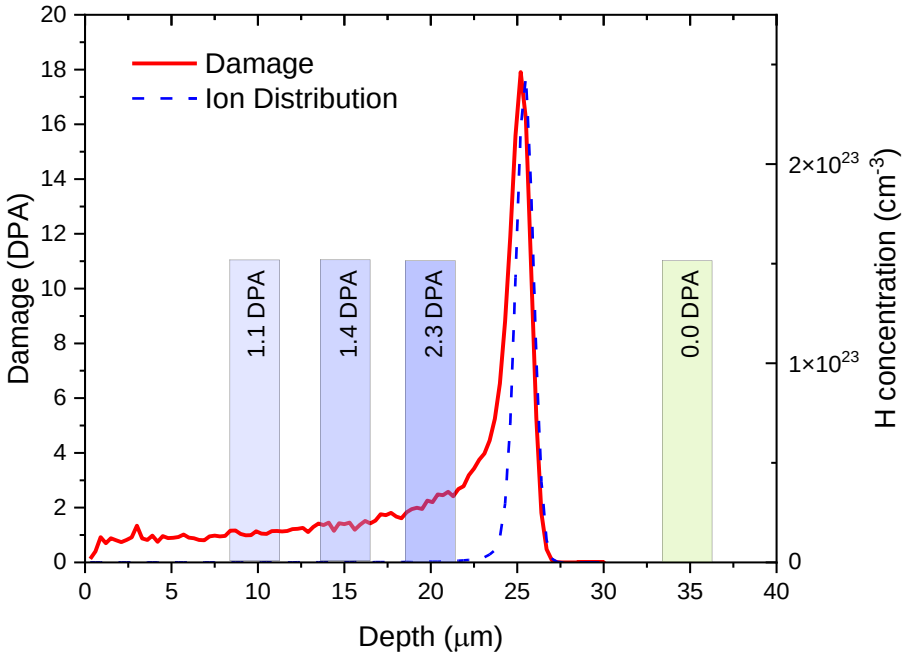

Figure 61. map of damage and ion distribution resulting from proton irradiation into Hastelloy N overlayed with position and average representative damage at the site of each fabricated pillar.

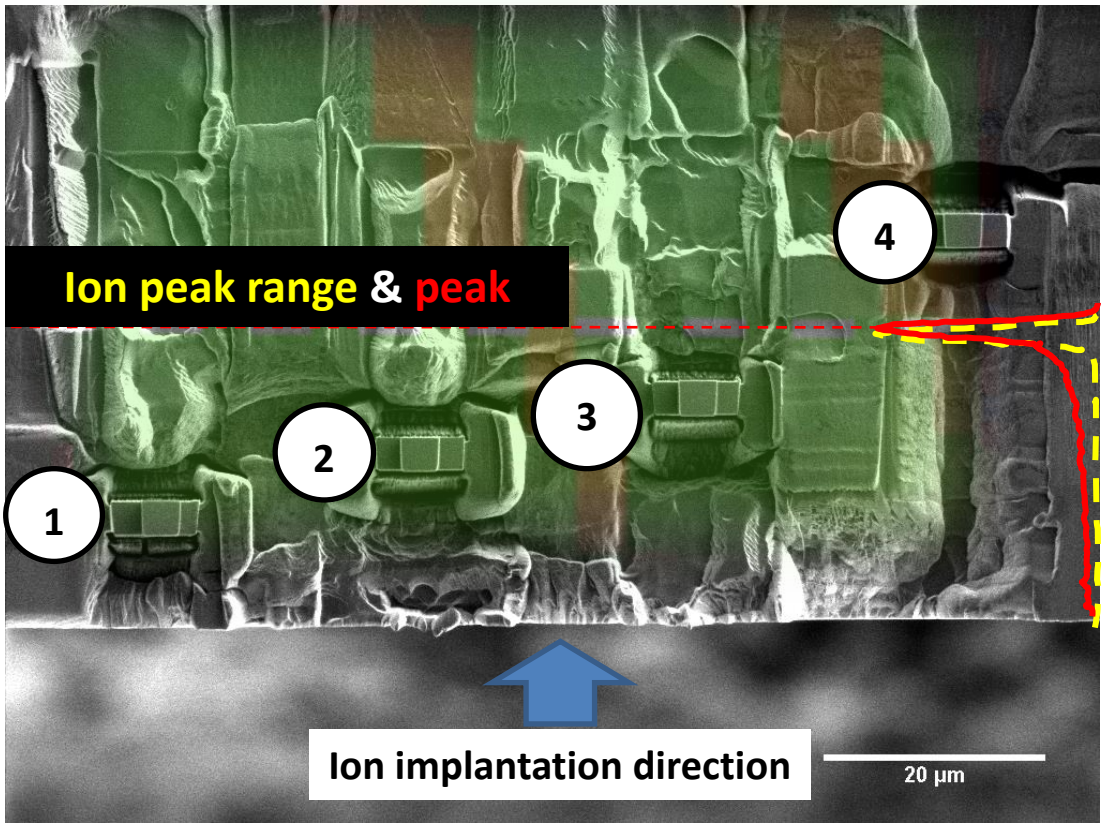

Figure 62. SE-SEM image illustrating final form of micropillars and overlay of EBSD grain map. Pillar locations were carefully chosen to avoid bisection by annealing twin boundaries.

Post-irradiation analysis

For experimental simplicity and brevity, FIB lamellae and TEM used as a comparison baseline for the pillar compressed sample was extracted from sample IRR1 described in the corrosion experiment in Chapter V. The TEM data, while not reflective of the specific pillar compression sample or grain where pillars were milled and tested, still illustrates gross microstructural changes resulting from proton irradiation and was used

to contextualize the results of the micropillar compression. STEM was performed by using a 200 kV Thermo Scientific Talos F200X TEM. Compositional maps were collected from the TEM specimens in the scanning transmission electron microscopy-energy dispersive X-ray spectroscopy (STEM-EDS) mode.

Results and Discussion

The microstructural changes resulting from irradiation are discussed in depth in Chapter V and summarized here. Comparing the control and irradiated lamellae shows that proton irradiation has enabled the formation of complex dislocation networks. These dislocation networks consist of edge dislocations which both crisscross and appear to pileup close to grain boundaries, dislocation loops, and corduroy dislocation loop structures. The Cottrell atmospheres around the dislocations have also caused select segregation of Si and Ni, the former which is strongly enriched along these dislocation features. Mo and Cr do not appear greatly affected by the irradiation while Fe appears to be slightly depleted in the vicinity of these dislocation features.

Figure 63 shows the engineering stress-strain behavior of the 1.1 local dpa pillar, the shallowest and least damage within the ion range. To reiterate, the pillars were all carved from the same [1 4 6] family grain and oriented in the same crystallographic direction. The load drops appear to occur during the pillar compression which correspond to strain levels of 4.7%, 9.3%, and 13.2%. Three images above the stress-strain curve in Figure 63 correspond to the live SE-SEM captured during these load drops in the pillar compression and are connected to their respective drop via dashed lines. The load drops

are clearly correlated to formation of major slip bands and are visible in the SEM images spanning the entire width of the pillar. The major slip bands occur in different locations during the three major load drops but were determined to be along the {111} plane family in each case. Additionally, a major slip band forms at the base of the pillar midway through the compression and continues to develop throughout the entire test.

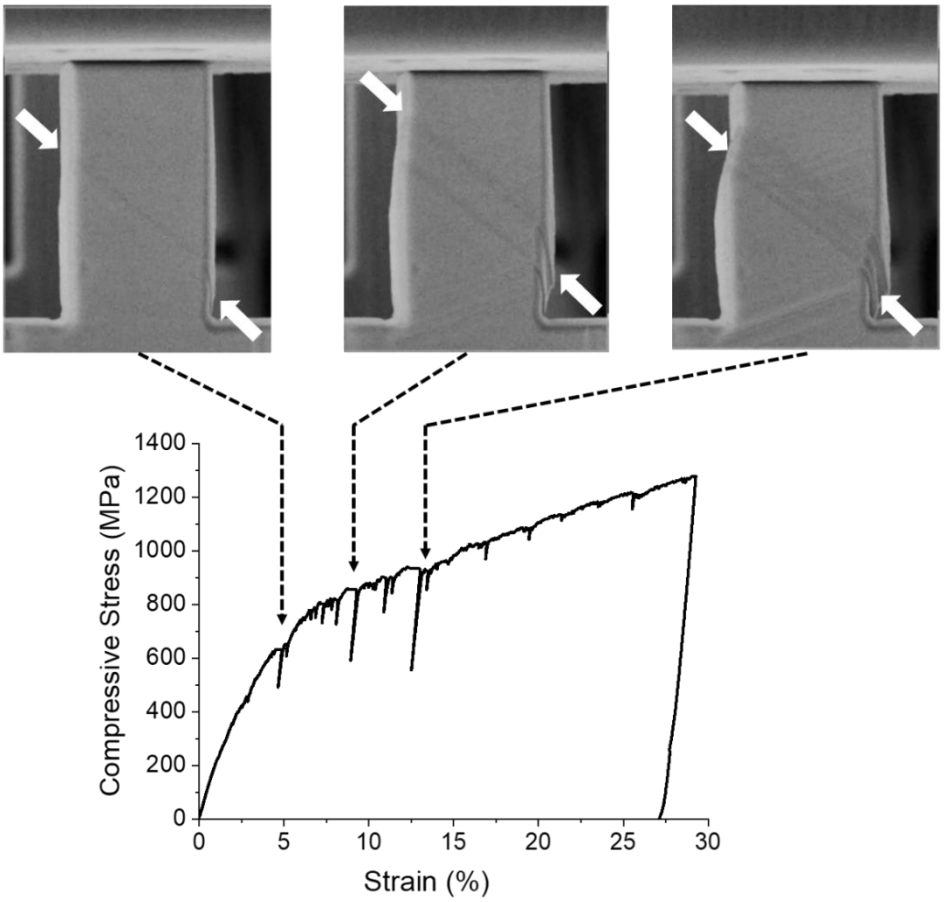

Figure 63. Engineering stress-strain curve extracted from pillar compression of site 1, corresponding to 1.1 local average DPA. Major slip bands are observed via SEM to coincide with load drops.

Figure 64 illustrates an example grain orientation and slip plane evaluation extracted from one of the compression pillars using a combination of SEM data collected during compression and EBSD data collected for pillar site selection. This figure illustrates the procedure as it was carried out for the second pillar, corresponding to 1.4 local DPA. The 1.4 DPA pillar experienced a double slip system in two directions during the compression testing, which gives the final pillar the impression of having been toppled preferentially in one direction. ESBD data allowed identification of grain orientation relative to compression direction as well as extraction of Schmid factors for critical resolved sheer stress. Two {111} gliding planes were identified as hosting the highest critical resolved sheer stresses and were responsible for forming the deformation bands. These bands were measured as occurring at 41° (top slip system) and 20° (bottom slip system).

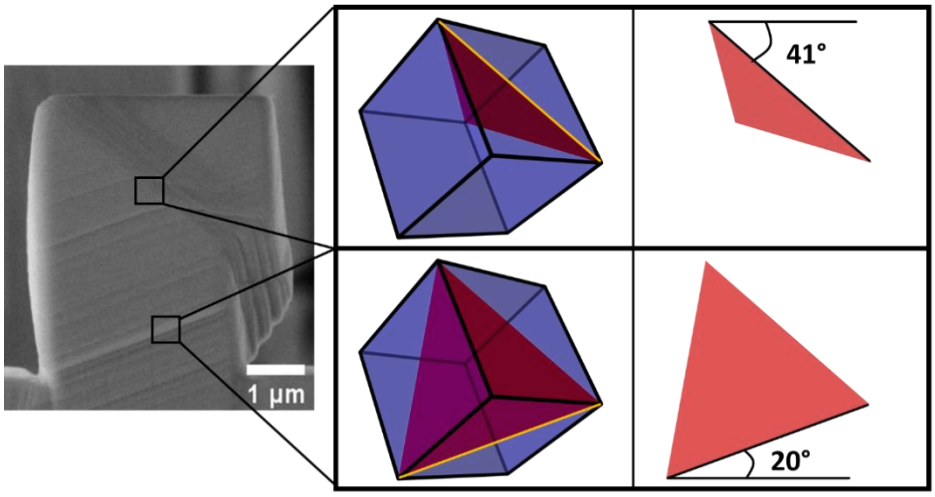

Figure 64. SE-SEM of 1.4 local DPA pillar and two slip systems which develop during compression test correlated to an illustration of respective slip planes derived from EBSD Schmid factor data.

Figure 65.a-d shows the engineering stress-strain curves and SEM images before and after the compression testing of pillars corresponding to 0, 1.1, 1.4, and 2.3 local dpa, respectively. Parallel slips bands were observed in all pillars after the compression. All four pillars showed the same dislocation gliding directions (corresponding to two {111} planes). The primary direction is denoted by a solid line and the secondary direction is denoted by a dashed line; primary meaning sliding on this planar direction occurred first. The consistency of gliding directions in all four pillars was expected since all pillars were prepared from the same domain.

The strain-stress curve of the unirradiated pillar (Figure 65.a) shows unique features and deformation behavior when compared with the other (irradiated) pillars. First, the load drops associated with major gliding events were much deeper for the unirradiated pillar, suggesting relatively large deformation and stress energy release. This could be explained by less resistance for dislocation migration in the unirradiated pillar. Second, the number of major load drops is the highest for the unirradiated pillar, which could be indicative of easier dislocation unpinning, allowing more plastic flow directions. Note that the unirradiated pillar had nine major load drops, while other three irradiated pillars had about three each. Third, the number of serrated stress fluctuation is the highest (>20) for the unirradiated pillar, which again would be explained by easier dislocation unpinning in this pillar. These observations suggest that dislocation unpinning was easiest and dislocation migration friction was the lowest in the unirradiated pillar. The strain hardening exponents were obtained by fitting stress-strain curves using Hollomon's

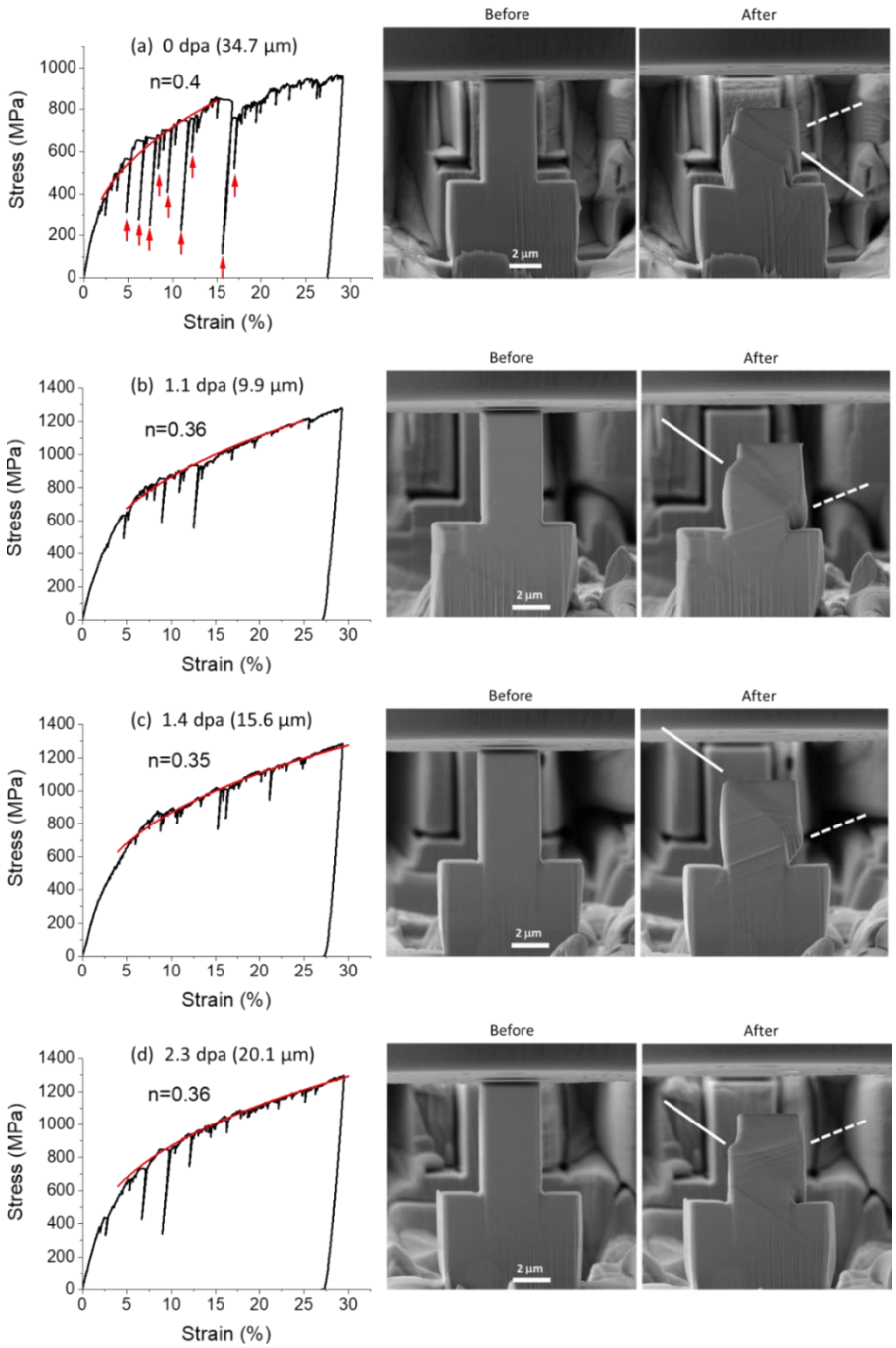

Figure 65. In situ micropillar compression test of pillars corresponding to (a) 0 local dpa, (b) 1.1 local dpa, (c) 1.4 local dpa, and (d) 2.3 local dpa. SEM images are taken before and after the compression testing.

equation [9], $\sigma = K\varepsilon^n$, where σ is the stress, ε is the strain, and K is the strength coefficient. The fitting lines are plotted in red in **Figure 65**.a-d. The extracted hardening exponents were 0.4, 0.36, 0.35, and 0.36 for dpa of 0, 1.1, 1.4, and 2.3. Most metals have a value between 0.1 and 0.5 [9]. A decreasing exponent means a transition from a elastic solid to a plastic solid. The exponent reduction observed can be explained due to increasing obstacles to dislocation motion [10].

Figure 66 plots the resolved shear stress vs. strain for all pillars. Since all pillars were made from a single domain and all plastic deformation began on the same sliding plane direction (judged by in situ SEM imaging), the projected forces on the dislocation

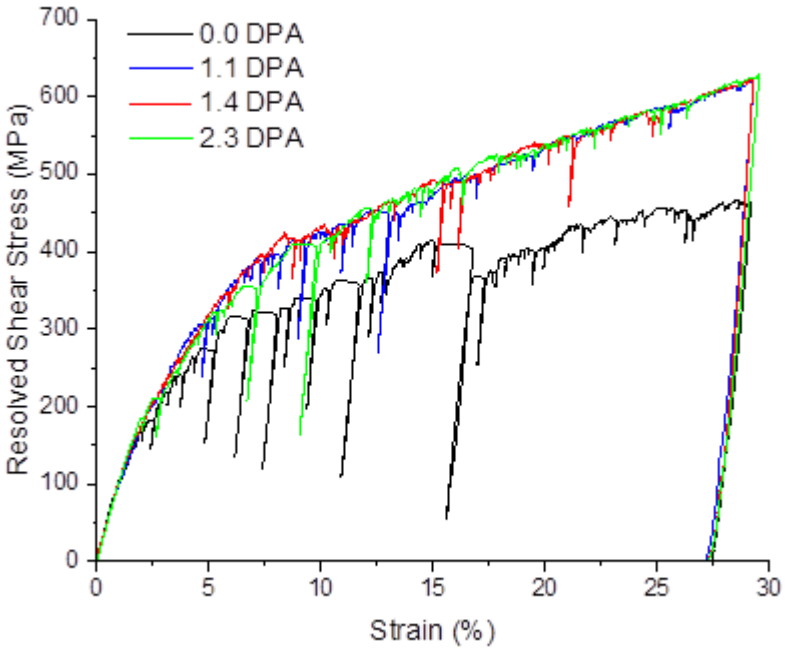

Figure 66. Engineering stress-strain curves illustrating resolved shear stress for each of the four compression pillars.

Table 6. Resolved critical shear stress obtained from pillar compression tests.

Average DPA	τ_{crss} (MPA)
0.0	115.72 ± 0.24
1.1	133.97 ± 0.15
1.4	161.46 ± 0.15
2.3	184.79 ± 0.15

gliding direction are the same for all pillars. The conversion from yield stress to the resolved critical shear stress (the projection of the force loading onto one <110> direction on {111} plane) was calculated by using the Schmid factor (m) determined from EBSD mapping according to $\tau_{crss} = \sigma_y cos\lambda cos\phi = \sigma_y m$, where τ_{crss} is the critical resolved shear stress. Table 6 summarizes the measured critical resolved shear stress τ_{crss}. Before applying the Schmid factor, the yield stress σ_y was measured by a 0.2% offset using the engineering strain-stress curves from Figure 65.a-d.

Figure 67 shows the normalized τ_{crss} (normalized to the value of unirradiated pillar). At the highest local dpa of 2.3, the τ_{crss} increased by 60%. Although the strain-stress curves of all irradiated pillars seem to be closely grouped together in Figure 66, the 0.2% offset measurements showed a significant shift with increasing dose.

Little diffusivity data exists on solute atoms in Hastelloy N. That which does consists of self-diffusion studies using ^{51}Cr tracers under different conditions. Evans III, DeVan and Watson performed some of the earliest work using a novel methodology where tracer atoms were introduced to Hastelloy and Inconel test samples in the form of enriched CrF_2 dissolved in NaF-ZrF molten salt [11]. Corrosion from this mixture was deemed

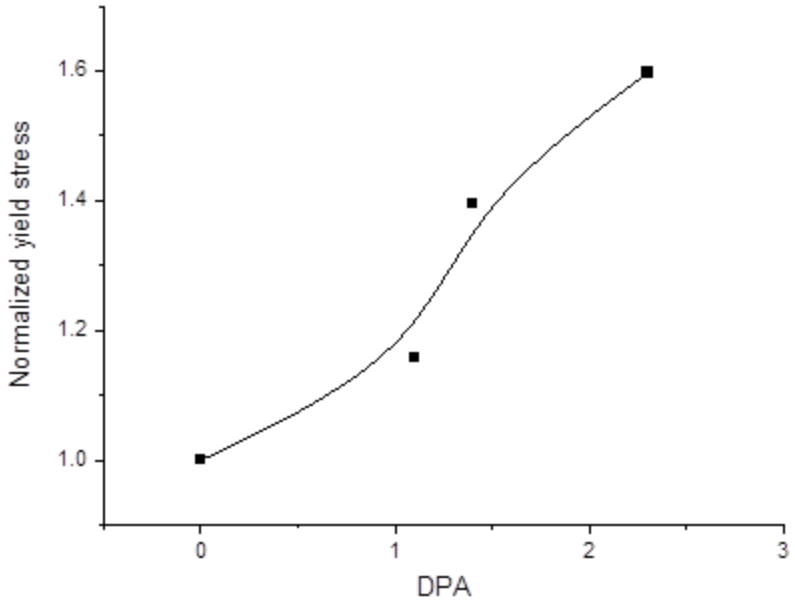

Figure 67. Yield stress vs. DPA extracted from pillar compression testing and normalized against the unirradiated pillar.

negligible and so the equilibrium reaction with chromium at the alloy surface and the doped fluoride proceeded without complication from unwanted alloy dissolution. The results of the findings showed that Inconel and Hastelloy N exhibited near-identical ^{51}Cr diffusivities in the range of 600-900 °C and 2) the transition between grain boundary and bulk dominated diffusion happens at approximately 800°C for these nickel alloy systems [11] Extrapolating the findings of these experiments to lower temperatures thus offer a reasonable prediction of the diffusivity of Hastelloy N, which is $\propto$ to 1×10^{-18} cm^2/s.

The findings by Evans III, DeVan and Watson disagree with more contemporary studies using traditional diffusion couple annealing to introduce ^{51}Cr tracers into Hastelloy N and Inconel. Findings by Chen, et. Al., and Pruthi, Anand, and Agarwala for Hastelloy

N and Inconel respectively show Cr diffusivity values several orders of magnitude lower. This discrepancy suggests a unique diffusivity augmentation resulting from tracer introduction via molten salts rather than solid metal coupling. Extrapolating the datasets from Chen, et. Al. and Pruthi, et. Al. gives bulk Cr diffusivity values of approximately 1.9×10^{-29} cm^2/s for Hastelloy N [12] and 4.6^{-27} cm^2/s in Inconel [13]. It is worth noting that the similarity in diffusivity behavior between Inconel and Hastelloy N which was noted by Evans III, DeVan and Watson holds approximately true in the high temperature regime between the Chen, et. Al. and Pruthi, et. Al. data sets. This is despite grossly different annealing treatments and grain size distributions described by each experiment [12, 13]. Inconel can thus be considered a rough surrogate description of Hastelloy N diffusion behavior.

Despite the importance of Cr to the corrosion behavior of Hastelloy N, the absence of strong Cr segregation suggests that Si segregation is more important singularly important to the microstructural evolution under irradiation. No diffusivity data exists for diffusion of Si atoms in Hastelloy N, but intensive data exists for Si in pure nickel or dilute Ni alloys. Early studies are consistent in showing that Si diffuses quickly in Ni or Ni alloys. First principle calculations obtained a Si diffusivity of 4×10^{-19} cm^2/s at 500 °C [14]. In comparison, the diffusivity of Cr is about 2.3×10^{-21} cm^2/s, and the diffusivity of Fe is 6.2×10^{-21} cm^2/s at the same temperature [14]. Experimentally measured diffusivities of Si [15, 16], Fe [17-19], and Cr [20-23] are slightly above the modeling results, but consistently show that Si diffusivity is a few orders of magnitudes higher than other solute atoms, including Mn and Mo. The above diffusivity difference is for an equilibrium

condition. Under irradiation, if all solute atoms diffuse preferably by one diffusion mechanism (generally vacancy-mediated diffusion), diffusivity would be enhanced, with the enhancement being proportional to the supersaturation ratio of point defects. Hence, the large difference in diffusivity of Si and other solute atoms still exists under irradiation. This could explain why Si would easily migrate to the stress fields around dislocation lines and loops.

The effect of Si on both defect development and mechanical properties is expected to be significant, although there are many unknowns at this point. First, all fast diffusers will promote defect migration through the solute-vacancy exchange in a vacancy diffusion mechanism. Being a fast-diffusing atom in nickel systems, Si will locally enhance vacancy mobility, and in turn is expected to influence both defect clustering processes and dislocation migration. No further evidence can be provided at this point. Second, Si can be expected to drag dislocations and thus facilitate migration, a result of its small atomic size and the tensile Cottrell atmosphere which will occur in its vicinity. The strength of the pining effect is unclear however, and the intensive dislocation networks observed suggest dislocations are quite mobile and the pinning effect weak. Alternatively, a Si Cottrell atmosphere may form after dislocations have already developed.

It is well-document that Si plays an important role in carbide evolution in Hastelloy N at high temperatures [15,32]. The effect of Si is complex, including (a) changing precursors to form M_6C carbide, (b) influencing M_6C carbide morphology changes, and (c) influencing M_6C carbide phase stability. Since carbides and carbide phase changes are critical to mechanical properties, Si is an important addition to influence high-temperature

fracture toughness. For case (a), an early comparison study showed that silicon containing GH3535 superalloy (the Chinese surrogate for Hastelloy N) can induce the formation of stable grain boundary carbides at high temperatures. The exact microstructure of these carbides is unclear [24] and they have been identified as either M_6C or $M_{12}C$ carbides. It is possible that the latter carbide becomes more stable and dominate with prolonged high temperature exposure [25, 26]. Regardless, these carbides are typical of air annealed Hastelloy N. In comparison, silicon-absent variants prepared via vacuum annealing, where Si-facilitated oxygen gettering is not necessary, form M_2C carbides first, and then M_2C carbides transform into coarse planar M_6C carbides at a later stage [27, 28]. For case (b), it was found that increasing Si increases the amount of M_6C at the expense of $M_{23}C_6$ in nickel superalloys. The M_6C flakes appear to be interconnected like a semi-continuous film, which causes severe embrittlement. With further increased Si, M_6C evolves into particles with reduced embrittling effects [29]. For case (c), early studies show that Si can stabilize carbides, and prevent carbides from being taken into the solid solution at high annealing temperatures [30]. Such stabilization effect causes carbides to transform into a high temperature phase such as δ-NiMo intermetallic compounds, which are likely responsible for embrittlement at high annealing temperatures [30].

Since Si is removed from the solution and enriched at the regions with dislocations and loops, it is questionable whether they still can act as carbide stabilizers when the irradiated samples are annealed at higher temperatures or for a prolonged time. The results of the corrosion test (see Chapter V) conducted at 700°C suggest that despite this pronounced segregation, Si-mediated secondary phase formation is still possible. This

agrees with literature showing segregation sensitivity after hundreds of hours of exposure to temperatures at or above 700°C, either under normal annealing or corrosion conditions [25, 26, 31, 32]. Gehlbach and McCoy showed precipitation sensitivity in hastelloy N at temperatures as low as 400°C for air-annealed (i.e., Si-containing) Hastelloy N, but these results have not be reproduced in contemporary literature [30]. A post-irradiation annealing experiment is proposed as a following study. Carbides have been proposed as trapping sites to reduce helium bubble formation, which is important to mitigate the issue of helium embrittlement for Hastelloy-N [33].

Although Hastelloy-N is generally considered the most promising candidate for MSRs (see Chapter I discussion), the gap between design needs and current performance is still large. Hastelloy N is shown in the present study to succumb to embrittlement at even modest damage levels above 2 or 3 dpa and at face value, would appear only usable at low-neutron-flux regions in reactors. It is unclear whether such embrittlement would occur under operation conditions, radiation damage and corrosion influence on point defect equilibrium will likely alter the segregation behavior of Si. The results of the ex-situ irradiation/corrosion study (see Chapter V) in fact challenge the assumption that these Si rich defect structures are stable at higher temperatures at all. The ASME has authorized use of Hastelloy-N for boilers and pressure vessels, but not for nuclear components. Although the present study is limited to low dpa damage levels, the knowledge is important for further evaluation and development of Hastelloy-N. Further evaluation is necessary, and it is suggested that the study be repeated at 600°C and 700°C.

The present study used 3 μm × 3 μm micro-pillars. The size selection considered both the needs to have multiple pillars within the proton irradiated region for dpa dependence (which favors small sizes) and the size effect (which favors large sizes). For the latter, it is documented that τ_{crss} values obtained from single crystal micropillars decrease with increasing pillar sizes, following an inverse power law trend in FCC and BCC metals [7, 34-37]. The decrease continues with increasing pillar size until a critical pillar size is reached, after which the τ_{crss} value matches the bulk value. The size effects vary among different materials. The size effects are limited for materials of hardening exponents between 0.21 to 0.48, and are almost ignorable for strong solids of, i.e. n ≈ 0.1 [6]. The critical pillar size for Hastelloy N is unknown, but it is believed that the size effect is small in the present study based on the criterion from the previous studies [6].

For materials with a FCC structure, the yield stress of a polycrystal is observed as roughly 3 times that of the τ_{crss} for a single crystal [38]. Earlier studies observed a yield stress of 331 MPa in unirradiated, polycrystal Hastelloy N [39]. The corresponding τ_{crss} is approximately 108 MPa, which is in close agreement with the τ_{crss} of 116 MPa observed in the unirradiated pillar in the present study. This would further suggest that the effects from the size of the pillars were minimal. The observed Young's modulus was an order of magnitude lower previously published values for bulk Hastelloy-N [40]. Previous studies show similar observations, with the deformation of the base of the pillar being the likely cause of the large difference [41]. The same phenomenon could possibly explain the observation in the current study.

References

[1] M. Liu, Y. Lu, R. Liu, X. Zhou, TEM investigation on the microstructural evolution of hastelloy N induced by Ar+ ion irradiation, Microscopy Research and Technique 77(2) (2014) 161-169.

[2] Z. Zhu, H. Huang, J. Liu, L. Ye, Z. Zhu, Nanoindentation Study on the Creep Characteristics and Hardness of Ion-Irradiated Alloys, Materials 13(14) (2020) 3132.

[3] J. Liu, H. Huang, J. Gao, Z. Zhu, Y. Li, Defects evolution and hardening in the Hastelloy N alloy by subsequent Xe and He ions irradiation, Journal of Nuclear Materials 517 (2019) 328-336.

[4] G.S. Was, J.T. Busby, T. Allen, E.A. Kenik, A. Jensson, S.M. Bruemmer, J. Gan, A.D. Edwards, P.M. Scott, P.L. Andreson, Emulation of neutron irradiation effects with protons: validation of principle, Journal of Nuclear Materials 300(2) (2002) 198-216.

[5] C.-H. Shiau, M.D. McMurtrey, R.C. O'Brien, N.D. Jerred, R.D. Scott, J. Lu, X. Zhang, Y. Wang, L. Shao, C. Sun, Deformation behavior and irradiation tolerance of 316 L stainless steel fabricated by direct energy deposition, Materials & Design 204 (2021) 109644.

[6] R. Soler, J.M. Molina-Aldareguia, J. Segurado, J. Llorca, R.I. Merino, V.M. Orera, Micropillar compression of LiF [111] single crystals: Effect of size, ion irradiation and misorientation, International Journal of Plasticity 36 (2012) 50-63.

[7] Z.M.T. Chen, N.L. Okamoto, M. Demura, H. Inui, Micropillar compression deformation of single crystals of Co3(Al,W) with the L12 structure, Scripta Materialia 121 (2016) 28-31.

[8] J.F. Ziegler, M. Ziegler, J.P. Biersack, SRIM The stopping and range of ions in matter (2010), Nuclear Instruments & Methods in Physics Research Section B-beam Interactions With Materials and Atoms 268 (2008) 1818-1823.

[9] J.H. Hollomon, Tensile Deformation, Transactions of Metallurgical Society of AIME 162 (1945) 268-290.

[10] S.J. Zinkle, J. Steven, Radiation-Induced Effects on Microstructure, 2012, pp. 65-98.

[11] I.R.B. Evans, J.H. DeVan, G.M. Watson, SELF-DIFFUSION OF CHROMIUM IN NICKEL-BASE ALLOYS, United States, 1961.

[12] T.-F. Chen, G. Tiwari, nbsp, Prasad, Y. Iijima, K. Yamauchi, Volume and Grain Boundary Diffusion of Chromium in Ni-Base Ni-Cr-Fe Alloys, MATERIALS TRANSACTIONS 44(1) (2003) 40-46.

[13] D.D. Pruthi, M.S. Anand, R.P. Agarwala, Diffusion of chromium in Inconel-600, Journal of Nuclear Materials 64(1) (1977) 206-210.

[14] C.Z. Hargather, S.-L. Shang, Z.-K. Liu, Data set for diffusion coefficients and relative creep rate ratios of 26 dilute Ni-X alloy systems from first-principles calculations, 20 (2018).

[15] H.W. Allison, H. Samelson, Diffusion of Aluminum, Magnesium, Silicon, and Zirconium in Nickel, 30 (1959).

[16] R.A. Swalin, A.E. Martin, R.L. Olson, Diffusion of magnesium, silicon, and molybdenum in nickel, JOM 9 (1957) 936-939.

[17] H. Bakker, J. Backus, F. Waals, A Curvature in the Arrhenius Plot for the Diffusion of Iron in Single Crystals of Nickel in the Temperature Range from 1200 to 1400°C, physica status solidi (b) 45(2) (1971) 633-638.

[18] Guiarldenq, Comptes Rendus de l'Acadmie des Sciences 254(1994) (1962).

[19] M. Badia, A. Vignes, Diffusion du fer, du nickel et du cobalt dans les metaux de transition du groupe du fer, Acta Metallurgica 17(2) (1969) 177-187.

[20] K. Monma, H. Suto, H. Oikawa, Diffusion of 63-Ni and 185-W in Nickel-Tungsten Alloys, Journal of the Japan Institute of Metals 28(4) (1964) 197-200.

[21] J. Růžičková, B. Million, Self-diffusion of the components in the F.C.C. phase of binary solid solutions of the Fe□Ni□Cr system, Materials Science and Engineering 50(1) (1981) 59-64.

[22] A.D. Tutunnik, G.E. Estoulin, Fiz. Met. I 4(558) (1957).

[23] M.D. Glinchuk, D.F. Kalinovich, I.I. Kovenskii, M.D. Smolin, Inzhernerno-Fiz Zh. 9(78) (1960).

[24] J. Li, S.L. Shrestha, Y. Long, L. Zhijun, Z. Xintai, The formation of eutectic phases and hot cracks in one Ni–Mo–Cr superalloy, Materials & Design 93 (2016) 324-333.

[25] T. Liu, J.S. Dong, L. Wang, Z.J. Li, X.T. Zhou, L.H. Lou, J. Zhang, Effect of Long-term Thermal Exposure on Microstructure and Stress Rupture Properties of GH3535 Superalloy, Journal of Materials Science & Technology 31(3) (2015) 269-279.

[26] T. Liu, J.S. Dong, G. Xie, L. Wang, L.H. Lou, Effect of silicon on microstructure and stress rupture properties of a corrosion resistant Ni-based superalloy during long term thermal exposure, Materials Science and Engineering: A 656 (2016) 75-83.

[27] L. Jiang, W. Yinling, R. Hu, R. Liu, X.-X. Ye, Z. Li, X. Zhou, Formation of nano-sized M2C carbides in Si-free GH3535 alloy, Scientific reports, 2018, p. 8158.

[28] L. Jiang, Z. Xu, Z. Li, Y. Lu, G. Wu, X. Zhou, The Effect of Silicon Additions on the Thermal Stability and Morphology of Carbides in a Ni-Mo-Cr Superalloy, in: F. Marquis (Ed.) Proceedings of the 8th Pacific Rim International Congress on Advanced Materials and Processing, Springer International Publishing, Cham, 2016, pp. 485-492.

[29] X.M. Guan, H.Q. Ye, Intergranular embrittlement caused by the precipitation of M6C carbide containing silicon, Journal of Materials Science 15(11) (1980) 2935-2937.

[30] R.E. Gehlbach, H.E. McCoy, Phase Instability In Hastelloy N, International Symposium on Structural Stability in Superalloys, 1968, pp. 346-366.

[31] F. Han, L. Jiang, X. Ye, Y. Lu, Z. Li, X. Zhou, Carbides Evolution in a Ni-16Mo-7Cr Base Superalloy during Long-Term Thermal Exposure, Materials (Basel), 2017.

[32] X.-X. Ye, H. Ai, Z. Guo, H. Huang, L. Jiang, J. Wang, Z. Li, X. Zhou, The high-temperature corrosion of Hastelloy N alloy (UNS N10003) in molten fluoride salts analysed by STXM, XAS, XRD, SEM, EPMA, TEM/EDS, Corrosion Science 106 (2016) 249-259.

[33] J. Busby, L. Garrison, L. Lin, S.S. Raiman, S. Sham, C.M. Silva, H. Wang, R. Iyengar, G. Tartal, Technical Gap Assessment for Materials and Component Integrity Issues for Molten Salt Reactors, 2019.

[34] M.D. Uchic, P.A. Shade, D.M. Dimiduk, Plasticity of Micrometer-Scale Single Crystals in Compression, Annual Review of Materials Research 39(1) (2009) 361-386.

[35] J.R. Greer, J.T.M. De Hosson, Plasticity in small-sized metallic systems: Intrinsic versus extrinsic size effect, Progress in Materials Science 56(6) (2011) 654-724.

[36] T.A. Parthasarathy, S.I. Rao, D.M. Dimiduk, M.D. Uchic, D.R. Trinkle, Contribution to size effect of yield strength from the stochastics of dislocation source lengths in finite samples, Scripta Materialia 56(4) (2007) 313-316.

[37] D.M. Dimiduk, M.D. Uchic, T.A. Parthasarathy, Size-affected single-slip behavior of pure nickel microcrystals, Acta Materialia 53(15) (2005) 4065-4077.

[38] W.F. Hosford, Mechanical Behavior of Materials, Cambridge University Press2005.

[39] J. McCoy, H E, AN EVALUATION OF THE MOLTEN-SALT REACTOR EXPERIMENT HASTELLOY N SURVEILLANCE SPECIMENS: THIRD GROUP, United States, 1970, p. Medium: X; Size: Pages: 88.

[40] T.A.S.o.M. Engineers, ASME Boiler and Pressure Vessel Code - An International Code, Section III: Rules for Construction of Nuclear Facility Components, ASME, New York, NY, 2019, p. 2.

[41] K.H. Yano, M.J. Swenson, Y. Wu, J.P. Wharry, TEM in situ micropillar compression tests of ion irradiated oxide dispersion strengthened alloy, Journal of Nuclear Materials 483 (2017) 107-120.

CHAPTER VII OVERALL CONLCUSIONS

Summary of results

Figure 68 updates the original experiment matrix described in the introduction chapter of

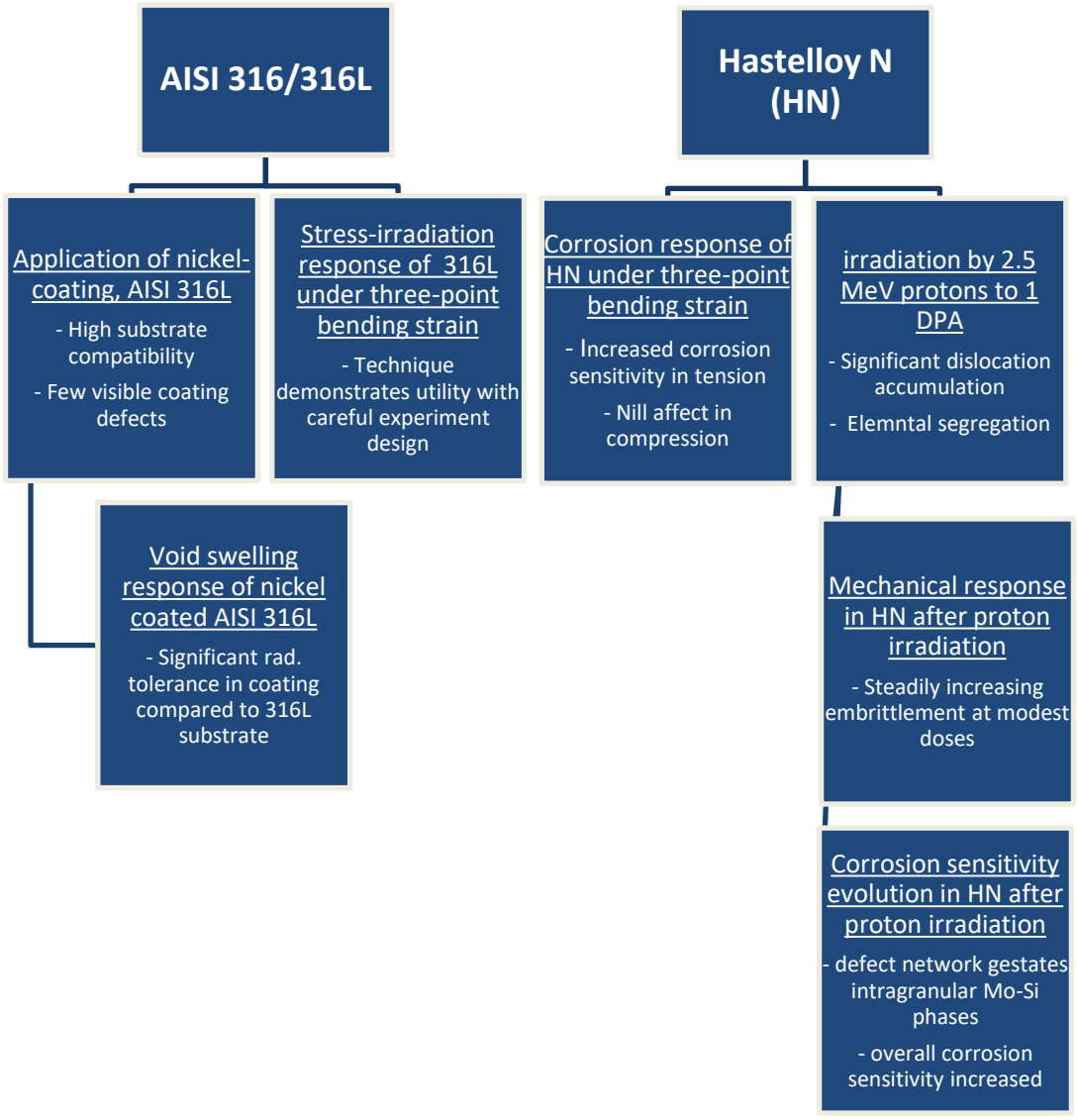

Figure 68. The original experiment matrix is presented again with a bulleted summary of significant findings.

this document with a bulleted summary of the findings herein. The most important result for each experiment is listed. A more detailed summary of the results is included in the proceeding text, which evaluates the degree of success achieved in addressing the bulleted objectives listed at the end of Chapter I. Additionally, the utility of the findings and suggestions for future studies are discussed.

Radiation Tolerance of Nickel Coating on 316L Stainless Steel Applied Using Novel Cage Plasma Treatment

The results of the study show that the surface plasma treatment in a modified CCPN configuration using nickel as a cage material can deposit a high-quality Ni film on 316L. At a high temperature processing at 800°C, no Ni-Fe intermetallic compound layer is formed. The deposited layer has no precipitation, cavities or cracks. Nitrogen plasma treatment introduced a high density of Cr nitride precipitation at grain boundaries some distance away from the surface. The shallower the depth into the surface, the higher the grain boundary nitride density. Cross sectional ion irradiation at 600°C shows that the top nickel-deposited layer has excellent swelling resistance. No voids are observed after 50 peak dpa irradiation. In comparison, for the nitrogen diffusion layer beneath the original surface, limited void swelling is observed. At much deeper depth in the bulk unaffected by nitrogen, significant void swelling is observed. Such “graded” swelling is beneficial to reduce the stress build up due to volume expansion under high damage-level irradiation. Moreover, the swelling did not appear to adversely affect the adhesion of the coating layer,

which was likely attributable to the graduation of swelling through the large nitrogen affected zone. The study suggests the feasibility of using CCPN to coat Ni protective layer on austenite steels to improve corrosion resistance, especially but not limited to applications in molten fluoride salt systems.

The viability of corrosion resistant coating for AISI 316L in MSR environments from the perspective of radiation damage was successfully demonstrated in the study presented here. The possibility of using of a nickel coating for fluoride salt-facing alloys has been previously explored with Inconel 800H [1], 316L [2], and Hastelloy N [3-5]. The results of Olson, et. Al results suggest significant corrosion improvement could be imparted in MSR systems, provided that the diffusion of chromium through the outermost nickel layer could be mitigated. Wang, et. Al showed that introduction of a nitride interlayer between Hastelloy N and the outer nickel coating can effectively arrest this chromium diffusion through the coating while simultaneously improving mechanical properties and adhesion of the coating [4, 5]. This two-layer coating system was able to effectively reduce the corrosion rate when the coating was perfectly intact, but complications may arise in the event of coating failure which exposures of the bare nitride substrate to fluoride salt.

In general, utilization of coating technology will require meticulous quality control, as defects in application can lead to detriment in conditions of fluoride salt coolant loops. The work of Zhu et. Al and Yadavalli et. Al. showed that Hastelloy N and 316L respectively benefit significantly from Ni coating in fluoride salt systems, but care must be taken to mitigate the introduction of oxidation during the coating process. The

introduction of these oxides, which are susceptible to dissolution in the fluoride salt, risk sensitization of the system by changing the redox potential of the melt.

The radiation tolerance and the compatibility of the nickel coating with 316L demonstrated in Chapter II bodes well for application of coating systems in MSR reactors. As previously discussed, commercial systems are expected to accumulate ~200 DPA over the course of their operational lifetime [6] Peak void swelling temperatures for 316SS are well characterized. Ion and neutron irradiation studies place the peak swelling temperatures for 316SS at 575°C and 510°C respectively [7, 8]. The latter temperature is most directly applicable for predicting MSR performance where hot and cold leg temperatures are expected to range between 600°C and 700°C. 316SS thus can be expected to benefit from radiation damage at MSR operation temperatures above its peak swelling region, where recovery and defect recombination will be enhanced. Ni coating on 316SS substrate can be expected to benefit from a more gradual increase swelling stress through the void nucleation period of the material, lowering the risk of coating interface degradation.

Evaluation of irradiation-stress response of 316L through combination of ion irradiation and three-point bending technique

316/316L SS was subjected to simultaneous stress and heavy ion irradiation conditions utilizing the three-point bending technique to impart a static loading condition. The results of the study show distinct change in void size, density, and overall swelling

volume between the regions of the sample exposed to neutral, compressive, and tensile stress. Overall, a decrease in swelling was observed transitioning from the compressive to tensile stress sides of the sample. Swelling response in the tensile stress region therefore deviated from results documented in literature. It is hypothesized that suppressed swelling here resulted from increased defect sinking at the sample surface made possible by changes to migration energy changes under tensile stress. This conclusion is supported by point-defect kinetics equations modeling on a simplified surrogate system.

The swelling results of the present work do not contribute significantly to the body of data which already exists for 316SS. The methodology followed in this work however, with some minor changes, is valuable for continued to investigation into the performance of 316SS or any other alloy as a viable alternative to Hastelloy N in MSR applications. Information on high temperature stress-swelling sensitivity, especially when historical literature suggests unilateral swelling increase under these conditions, will be crucial for vetting MSR reactor materials in the near-future. This will be especially true if MSR design develops to utilize coating systems, as coating interfaces are already susceptible to elevated stress. Moreover, complex components or those exposed to static or cyclical stresses thus invite greater chance for coating failure. The technique laid out in this study can be applied with little change to evaluate the combined stress-irradiation tolerance of coating systems and thus ensure coating durability for future MSR systems.

The complexity of the stress distribution in the three-point bender sample can be alleviated somewhat by implementing a four-point bending system for future studies. Eliminating the macroscopic lateral stress induced through three-point bending will help simplify interpretation of the local normal and deviatoric stress distributions and their correlation to swelling response.

FLiNaK Corrosion Response of Hastelloy N Under Variable Stress Conditions Using Three-Point Bending Technique

The corrosion response and stress relaxation of Hastelloy N under static strain was evaluated by combining the three-point bending technique with submersion in molten FLiNaK salt at 700°C for 50 hours. Stress application and creep relaxation were estimated using a finite element model constructed in the ABAQUS software. Initial stress loading was estimated as 176 MPa, or approximately 0.55 σ_y. The bent sample enabled simultaneous evaluation of the effect of compressive and tensile stress states and their respective effect on corrosion response. The sample was subdivided into six evaluation regions representing distinct stress states. These sites were evaluated using EDS and EBSD techniques. The physical mechanisms driving stress-accelerated corrosion in Hastelloy N were successfully identified and the results show that:

1. Corrosion as measured by the depletion of chromium at the surface of the six evaluated sites on the stress sample showed more severe corrosion at the site of

highest tensile stress. Compressive stress in contrast did not appear to accelerate chromium depletion compared to the neutral stress sites or the control sample.

2. Creep relaxation in the tensile stress region appears to be mediated by accumulation of geometrically necessary dislocations (GNDs), which agrees with contemporary literature. More active near-surface restructuring is also observed as characterized by kernel averaged misorientation (KAM) and mean orientation spread (MOS). Creep relaxation in the compressive and neutral stress sites experience a lower accumulation of GNDs and significant twin deformation.
3. A possible explanation for the increased corrosion in the tensile stress region is proposed based on the higher accumulation of GNDs in the tensile stress region. GNDs were observed to accumulate more densely at grain boundaries and closer to the surface where corrosion was most significant. The Cottrell atmospheres around these dislocations create local stress gradients which may promote the preferential diffusion and overall egress of chromium from the sample surface. In contrast, the compressive stress region of the sample alleviated strain primarily through deformation twinning, preventing the accumulation of GNDs and enhanced chromium diffusion.

Evaluation of Corrosion response of Hastelloy N in FLiNaK salt after Proton irradiation

Exposing Hastelloy N to corrosion after irradiation up to 1 local DPA using 2.5 MeV protons is demonstrated to exacerbate corrosion as measured by the increased

depletion of Cr and Mo relative to the control samples. Complex microstructural evolution was identified after irradiation and corrosion steps of the experiment. Widespread dislocation networks which formed after irradiation were shown to facilitate the segregation of Si. After exposing irradiated and control samples to corrosion in static FLiNaK salt for 500 hours, STEM-EDS data revealed that the dislocation networks observed in the irradiated sample were partially replaced with fine grain Mo-Si rich intragranular precipitates. Intergranular precipitates which are typical of aged Hastelloy N were observed in both irradiated and control samples. Cr and Mo suffered greater depletion in the irradiated samples. A ≈6× increase in Cr depletion was measured in the irradiated samples, which represents a significant sensitization. It is hypothesized that the dislocation networks formed during irradiation facilitated the egress of chromium into the fluoride salt through the pipe diffusion phenomenon.

Corrosion in MSR environments is synergistic of several physical processes. These findings help complete the understanding of irradiation-assisted corrosion in Hastelloy N as sensitive to not only embrittlement effects, but also raw radiation damage. The relative importance of this sensitivity will vary depending on the exact location of salt-facing materials in the MSR. Not considering metallurgical design and surface preparation, total dose, dose rate, temperature, salt purity, flow erosion and whether these variables act constantly or cyclically must all be weighed in predicting corrosion sensitivity. Cyclical dose and corrosion exposure presents a particular circumstance to which the present work is especially pertinent. Any circumstance in which a Hastelloy N component is exposed to neutron radiation of energy distribution

excluding serious He transmutation and then immersed in salt could present a special degradation risk to that component. A situation might occur with neutron control or measurement instrumentation constantly exposed to radiation flux in proximity to the core but only occasionally inserted in the melt.

Evaluation of Mechanical Property Evolution in Hastelloy N After Ion Irradiation Via Micropillar Compression

The current study attempts to qualify and quantify ion irradiation responses and mechanical property changes of proton irradiated Hastelloy-N. Post-irradiation characterization was performed on the cross-section of the irradiated sample. A large grain was selected and multiple micron-pillars were prepared by using FIB. Depending on the distance away from the surface, each pillar represented a different local dpa. Compression testing showed that the yield stress of each pillar increased systematically as a function of dpa. At 2.3 dpa, yield stress increased by 60%. TEM and STEM characterization showed that the irradiated sample developed complicated defect structures including interacting dislocation lines, corduroy-like dislocations, and dislocation pileups. EDS mapping showed that silicon atoms diffused towards and decorated dislocations, likely under the influence of Cottrell atmospheres. None of the above dislocation networks and silicon segregation were found in the unirradiated region. The study suggests that irradiation hardening in Hastelloy-N is most likely contributed by synergistic effects from multiple mechanisms.

Radiation embrittlement is a phenomenon with extensive study and operational experience in the nuclear industry. Even so, the degree of embrittlement observed in this study was surprising and raises questions about the long-term mechanical stability of salt facing Hastelloy N components. Sustained ductility is highly important to the performance of metallic structures under any circumstance, especially for mitigating the risk of catastrophic component failure through brittle failure. It has been suggested elsewhere that Hastelloy N may be used as a non-structural container supported by a scaffolding of high-temperature and radiation hardy material. This may reduce stress experienced by salt-facing components so that brittle failure is of negligible probability. It is also possible that the metallurgical variations of Hastelloy N with composition changes sufficiently resist radiation embrittlement and remove serious concern for long term failure. In the shadow of persistent embrittlement through helium gas transmutation and aggregation, as well as fission product uptake, direct radiation damage embrittlement may be a moot concern. It is also worth considering whether radiation embrittlement would be mitigated or accelerated at higher temperatures with greater available energy for defect recombination.

Suggestions for future work

Protective coatings are proven to be an effective method for corrosion mitigation under good application conditions. Evaluation under stress-corrosion or stress-irradiation conditions would further solidify confidence in coating performance for long term MSR applications. These studies could be performed for any alloy but would be especially valuable for expanding data in 316SS or Hastelloy N, which have already demonstrated coating compatibility under neutral stress and irradiation conditions. Stress-swelling response needs further study and the in-situ stress irradiation methodology detailed here can facilitate such work given its simplicity and low cost for laboratory scale experimentation. The three-point bending system described here is robust enough to be modified for the study of other physical processes not explored here. Careful experiment design should be considered, and some recommended changes are listed below for stress-irradiation studies.

- As high of an irradiation energy as possible should be used if implantation is to be done with heavy ions. it may be prudent to move to lighter ions to increase range, but this will severely inhibit the level of damage and swelling which can be achieved. The positive side of this is that doing so will better help isolate void nucleation effects by reducing dose rate and increasing data sampling area
- Partition of the void analysis volume during TEM microscopy after irradiation should be carefully considered to avoid the influence of surface effects. This applies to both heavy and light ion experiments.

- Proton implantation would be an ideal solution to remedy both the tendency of dose rate and surface sinking to adversely affect swelling response. The tradeoff of reduced dose rate may be tolerable if studies are focused on the void nucleation period rather than advanced steady-state swelling.
- Transition to four-point bending is suggested for future studies to eliminate the influence of small but potentially important deviatoric stress components

Access to research facilities with in-situ irradiation-corrosion capabilities will become restricted as demand for these valuable resources increases. This potential bottleneck in MSR development can be somewhat alleviated through ex-situ irradiation corrosion experiments. While not a perfect surrogate for the conditions of an active MSR reactor, this methodology offers a simplified and cost-effective alternative which can serve the needs of a larger number of research efforts. The data collected here for Hastelloy N can easily be replicated for any number of candidates MSR alloys and for a wide variety of relevant temperatures, radiation doses, salts, and corrosion conditions.

References

[1] L. Olson, K. Sridharan, M. Anderson, T. Allen, Nickel-plating for active metal dissolution resistance in molten fluoride salts, Journal of Nuclear Materials 411(1) (2011) 51-59.

[2] H. Yadavalli, C. Jagadeeswara Rao, N. Dr S, T.V. Mohan, S. Rangarajan, S. Albert, Corrosion Behaviour of Plasma-Sprayed Nickel Coating on Type 316L Stainless Steel in High-Temperature Molten FLiNaK Salt, Transactions of the Indian Institute of Metals 74 (2021) 1-13.

[3] H. Zhu, B. Li, M. Chen, C. Qiu, Z. Tang, Improvement of Corrosion Resistance of Hastelloy-N Alloy in LiF-NaF-KF Molten Salt by Laser Cladding Pure Metallic Coatings, Coatings (2018).

[4] W.C. Chengxu Wang, Minghui Chen, Demin Chen, Fuhui Wang, Ni/AlN Composite Coating for Corrosion and Elements Interdiffusion Resistance in Molten Fluoride Salts System, Acta Metallurgica Sinica (English Letters) 34(12) (2021) 1704-1714.

[5] C. Wang, W. Chen, M. Chen, D. Chen, K. Yang, Corrosion behavior and elements interdiffusion between a Ni coating and GH3535 alloy with and without a CrN barrier in molten fluoride salts, Journal of Nuclear Materials 514 (2019) 348-357.

[6] S.J. Zinkle, J.T. Busby, Structural materials for fission & fusion energy, Materials Today 12(11) (2009) 12-19.

[7] H. Kim, J.G. Gigax, J. Fan, F.A. Garner, T.L. Sham, L. Shao, Swelling resistance of advanced austenitic alloy A709 and its comparison with 316 stainless steel at high damage levels, Journal of Nuclear Materials 527 (2019) 151818.
[8] Radiation-induced damage in Austenitic structural steels used in nuclear reactors, Chapter 3.02 in Comprehensive Nuclear Materials second edition, 2020, pp. 57-168.

[1] L. Olson, K. Sridharan, M. Anderson, T. Allen, Nickel-plating for active metal dissolution resistance in molten fluoride salts, Journal of Nuclear Materials 411(1) (2011) 51-59.
[2] H. Yadavalli, C. Jagadeeswara Rao, N. Dr S, T.V. Mohan, S. Rangarajan, S. Albert, Corrosion Behaviour of Plasma-Sprayed Nickel Coating on Type 316L Stainless Steel in High-Temperature Molten FLiNaK Salt, Transactions of the Indian Institute of Metals 74 (2021) 1-13.
[3] H. Zhu, B. Li, M. Chen, C. Qiu, Z. Tang, Improvement of Corrosion Resistance of Hastelloy-N Alloy in LiF-NaF-KF Molten Salt by Laser Cladding Pure Metallic Coatings, Coatings (2018).
[4] W.C. Chengxu Wang, Minghui Chen, Demin Chen, Fuhui Wang, Ni/AlN Composite Coating for Corrosion and Elements Interdiffusion Resistance in Molten Fluoride Salts System, Acta Metallurgica Sinica (English Letters) 34(12) (2021) 1704-1714.
[5] C. Wang, W. Chen, M. Chen, D. Chen, K. Yang, Corrosion behavior and elements interdiffusion between a Ni coating and GH3535 alloy with and without a CrN barrier in molten fluoride salts, Journal of Nuclear Materials 514 (2019) 348-357.

[6] S.J. Zinkle, J.T. Busby, Structural materials for fission & fusion energy, Materials Today 12(11) (2009) 12-19.

[7] H. Kim, J.G. Gigax, J. Fan, F.A. Garner, T.L. Sham, L. Shao, Swelling resistance of advanced austenitic alloy A709 and its comparison with 316 stainless steel at high damage levels, Journal of Nuclear Materials 527 (2019) 151818.

[8] Radiation-induced damage in Austenitic structural steels used in nuclear reactors, Chapter 3.02 in Comprehensive Nuclear Materials second edition, 2020, pp. 57-168.

APPENDIX A

EXAMPLE CORROSION REACTIONS FOR FLUORIDE MELTS

Note: This list is a basic summary of redox reactions in fluoride salt systems and not intended to be comprehensive or complete. For reference purpose only.

Basic modes [1]

- Alloy element removal:

$$Me_{(s)} + MF_{(l)} \rightleftharpoons MeF_{(l)} + M_{(l)} \quad (1.a)$$

  - *Me = alloying element*
  - *M = alkali metal*

- Fuel fluoride reduction:

$$Cr_{(s)} + UF_{4(l)} \rightleftharpoons 2UF_{3(l)} + CrF_{2(l)} \quad (1.b)$$

Impurity driven modes [1]

- Metallic impurity reduction:

$$FeF_{2(l)} + Cr_{(s)} \rightleftharpoons CrF_{2(l)} + Fe_{(s)} \quad (2)$$

- Oxide film dissolution:

$$2Fe^{+++} + Cr_{(s)} \rightleftharpoons 2Fe_{(s)} + Cr^{+++} \quad (3)$$

- Moisture-driven HF production

$$H_2O_{(g)} + 2F^- \rightarrow O^{2-} + 2HF_{(g)} \quad (4)$$

$$MF_{(l)} + H_2O_{(g)} \rightarrow MOH_{(l)} + HF_{(g)}, \; when\; T > T_m \quad (5.a)$$

$$2MF_{(l)} + H_2O_{(g)} \rightarrow M_2O_{(l)} + 2HF_{(g)}\; T < T_m \quad (5.b)$$

$$HF_{(g)} \rightarrow HF_{(l)} \quad (6)$$

$$xMe + yMF_{(l)} \rightarrow Me_xF_y + \frac{y}{2}H_{2(g)} \quad (7)$$

References

[1] W.D. Manly, J.H. Coobs, J.H. DeVan, D.A. Douglas, H. Inouye, P. Patriarca, T.K. Roche, J.L. Scott, Metallurgical Problems In Molten Fluoride Systems, in: R. Hurst, R.N. Lyon, C.M. Nicholls (Eds.), Progress In Nuclear Energy, Pergamon Press, New York, 1960, pp. 201-221.